UNIVERSITÉ DE SHERBROOKE
Faculté de génie
Département de génie civil

BOND PERFORMANCE BETWEEN CONCRETE AND THE FRP TUBE UNDER CYCLIC LOADING; AND DESIGN OF NEW BEAM-COLUMN CONNECTION FOR CONCRETE-FILLED FRP TUBES

PERFORMANCE DE L'ADHÉRENCE ENTRE LE BÉTON ET LE TUBE SOUS CHARGES LATÉRALES CYCLIQUES, EN PRF ET CONCEPTION DE NOUVELLES CONNEXIONS POUTRE-COLONNE POUR TUBES EN PRF REMPLIS DE BÉTON

Thèse de doctorat
Spécialité : génie civil

Ahmed Mohamed Ahmed Ali
(Ahmed Ali)

A dissertation submitted in partial fulfilment
of the requirements for the degree of
Doctor of Philosophy
(Civil Engineering)

Sherbrooke (Québec) Canada
Novembre 2018

MEMBRES DU JURY

Prof. RADHOUANE MASMOUDI
Directeur

Prof. MOHAMMAD IQBAL KHAN
Évaluateur

Prof. RICHARD GAGNÉ
Rapporteur/Évaluateur

Prof. SLIMANE METICHE
Évaluateur

Prof. HAMDY MOHAMED
Évaluateur

DEDICATION

To My Father's Soul, Who Taught Me How to Be an Honest,

Sincere, Ambition Person, He Is the Reason for Who I Am Now and

Tomorrow. I Am Owing to Him All My Life

ABSTRACT

In the last two decades, researchers reported that concrete-filled FRP tube (CFFT) members have a better performance compared to conventional reinforced concrete members (beams or columns) in terms of strength, ductility, and durability in corrosive environments. This superior performance of CFFT returns to many reasons like, the FRP tube provides a longitudinal and transverse reinforcement, serve as a permanent lightweight formwork, and confine the concrete core which increases the concrete compressive strength and provides more ductility for the CFFT structural members. All these advantages provide CFFTs the ability to be used in many structure field applications like marine piles, bridges girders and columns, poles, and overhead sign structures.

Protracted studies are conducted to investigate and evaluate the behavior of CFFT structural members under different type of loading, lateral monotonic or cyclic loads with or without axial loads. Nevertheless, rare researches were investigated the effect of the bond between the concrete core and the FRP tube on the flexural capacity of the CFFT member. The size effect of the FRP tube also needs to be examined.

In addition, this thesis also aimed at answering another question: how to connect CFFT beam to CFFT column? up-to-date, all the previous researches in CFFT domain are studied CFFT beams or CFFT column and there are no previous trials to establish a CFFT beam-column connection.

This thesis is divided into two parts. The first part investigates the interfacial bond performance between the FRP tube and the concrete core. Full-scale specimens were tested under lateral cyclic load. An innovative approach was proposed to assess the bond between the FRP tube and the concrete core by using embedded concrete strain gauges into the concrete core, to study the composite action between the FRP tube and its concrete core effect on the flexural behavior of CFFT. In addition, contribution of sand coating bond enhancer on improving the bond between the FRP tube and the concrete core is also investigated. Four full scale circular CFFT columns were tested in the first part under lateral

cyclic load only to study the bond between the FRP tube and the concrete core, sand-coating effect (two columns have sand-coating and the other two are without) and the tube-size effect (two columns have 305 mm diameter and the other two have 406 mm diameter) on the flexural behaviour of the CFFT members. An analytical model was developed to predict the flexural behavior of the fully bonded CFFT members. This model was established based on layer-by-layer section analysis. The model predicted the failure mode, flexural capacity, curvature, and compression zone depth.

While the second part focused on development and design of a new assembly of CFFT beam-column connection for rectangular CFFT members. The new connection has been studied experimentally, and a new analytical model to predict its structural capacity is proposed. This part also proposes design equations and analytical study to calculate the flexural capacity of rectangular CFFT beams as well as the required embedded depth to achieve its flexural capacity. Four rectangular CFFT beam-column connections were designed, manufactured, assemblage and tested under monotonic load.

The first part results illustrated that the bond significantly influences the flexural strength and stiffness of the CFFT column. Using sand-coating as a bond enhancer improved the bond between the FRP tube and the concrete core, minimize the adverse effect of the interface gap, and increased the flexural capacity and stiffness of tested CFFT columns. This study provides some recommendations required to use unreinforced CFFT members to attain its structural benefits like using non-shrink concrete in the filling the FRP tube is suggested to eliminate generating of the interface gap. In addition, sand-coating or any comparable bond enhancer should be utilized to improve the interfacial bond between the concrete core and the FRP tube. These recommendations are demanded to realize the full composite action in the unreinforced CFFT members. The proposed analytical model estimated the failure mode, flexural capacity, curvature, and compression zone depth with a good agreement comparing by the experimental results.

The second part results showed that the proposed connection successfully transferred the moment from the CFFT beam to the CFFT column. The optimal embedded depth required to induce flexural failure of the CFFT beam is two times the CFFT beam depth (i.e. FRP

tube depth). The proposed theoretical model successfully predicted the flexural strength of the CFFT beam, the failure mode, the optimal embedded depth, and the effect of the embedded depth on the flexural capacity of the connection with high accuracy (maximum difference 10.5%).

Keywords: Fiber-reinforced polymer, Concrete-filled FRP tubes, Cyclic loading, Bond, Composite action, shrinkage gap, Sand-coating, Interface gap, Flexural behavior, CFFT connection, Beam-column connection, Embedment depth.

RÉSUMÉ

Au cours des deux dernières décennies, les travaux de recherche rapportés sur les tubes de polymères renforcés de fibres remplis de bétons (TPRFB) ont clairement démontré une meilleure performance par rapport aux éléments (poutre ou colonne) en béton armé conventionnel : en termes de résistance, ductilité et durabilité dans des environnements corrosifs. Plusieurs facteurs expliquent cette performance supérieure : le tube en (PRF) fournit un confinement parfait pour le béton, particulièrement lorsqu'il est sollicité en traction, fournit également des renforts dans les deux directions longitudinale et transversale de l'élément, et sert de coffrage léger et permanent. La résistance à la compression du noyau de béton est considérablement augmentée et la ductilité/déformabilité des membrures se trouve grandement améliorée. Tous ces avantages confèrent la possibilité aux (TPRFB) d'être utilisés dans de nombreuses applications telles que les pieux marins, les poutres et les colonnes de ponts, les poteaux et les structures de panneaux suspendus.

Plusieurs recherches ont été menées pour étudier et évaluer le comportement des éléments structuraux (TPRFB) sous différents types de chargement : charges latérales monotones ou cycliques avec ou sans charges axiales. Néanmoins, très peu de recherches ont été réalisées pour étudier l'effet de l'adhérence entre le noyau de béton et le tube PRF sur le comportement à la flexion d'un élément TPRFB. L'effet de taille du tube en PRF doit également être examiné.

Par ailleurs, une question que la présente thèse a tenté de répondre est : comment attacher une poutre (TPRFB) à une colonne (TPRFB)? À la lumière de la revue de littérature et aux mieux de mes connaissances, il n'existe aucune étude traitant des connexions poutre/colonne pour TPRFB.

Cette thèse est composée de deux parties. La première partie porte sur l'évaluation de la performance de l'adhérence entre le tube en PRF et le béton. Des prototypes grandeur nature de colonnes TPRFB ont été testés sous charges latérales cycliques. Une approche novatrice pour évaluer la performance de l'adhérence entre le tube de PRF et le noyau de béton en utilisant des jauges de déformation intégrées dans le béton a été développée et utilisée. Cette

technique a permis d'étudier l'action composite entre le tube en FRP et le noyau de béton sur le comportement en flexion des colonnes TPRFB. En outre, la contribution de l'amélioration de l'adhérence à l'aide d'enrobage de sable est également étudiée, et est quantifiée. Quatre colonnes circulaires, grandeur nature, ont été testées dans la partie I sous charge cyclique latérale pour étudier l'adhérence entre le tube en PRF et le noyau de béton. L'effet d'un revêtement de sable (Deux colonnes avec revêtement de sable versus deux colonnes sans revêtement de sable), ainsi que l'effet de la taille des tubes (deux colonnes de 305 mm de diamètre versus deux autres de 406 mm de diamètre) sur le comportement en flexion des membres TPRFB ont été étudiés.

La deuxième partie a porté sur le développement et la conception d'une nouvelle connexion poutre-colonne pour TPRFB de sections rectangulaires. La nouvelle connexion a été étudiée expérimentalement, et un nouveau modèle analytique permettant de prédire sa capacité structurale est proposé. Des équations de conception et des études analytiques pour calculer la capacité en flexion de poutres rectangulaires de TPRFB, ainsi que la profondeur encastrée requise sont également présentées. Quatre connexions poutres-colonnes TPRFB de sections rectangulaires ont été conçues, fabriquées et testées sous charge monotone.

Les résultats de la première partie ont montré que l'adhérence influence significativement la résistance à la flexion et la rigidité de la colonne TPRFB. L'utilisation d'un revêtement de sable améliore l'adhérence entre le tube de PRF et le noyau de béton, minimise l'effet néfaste d'un retrait éventuel du béton. Cette étude fournit quelques recommandations nécessaires pour utiliser les membrures TPRFB non armées, comme l'utilisation d'un béton expansif dans le remplissage du tube en PRF, afin d'éviter toute possibilité de retrait du béton, particulièrement sous charge de flexion. De plus, l'utilisation d'un revêtement de sable ou toute autre technique pouvant améliorer l'adhérence entre le noyau en béton et le tube en PRF est nécessaire sous charge de flexion. Ces recommandations sont exigées pour réussir l'action composite complète dans les membrures TPRFB en béton non-armé.

Les résultats de la deuxième partie ont montré que la connexion proposée transfère avec succès le moment de la poutre TPRFB vers la colonne TPRFB. La profondeur optimale requise pour induire une rupture par flexion de la poutre TPRFB est évaluée à environ deux

fois la profondeur de la poutre TPRFB (c'est-à-dire deux fois la profondeur du tube en PRF de la poutre). Le modèle théorique proposé prédit avec succès et une bonne précision la résistance à la flexion de la poutre TPRFB, le mode de rupture, la profondeur optimale d'ancrage et l'effet de la profondeur encastrée sur la capacité en flexion de la connexion.

Mots clés : Polymère renforcé de fibres (PRF), Tubes en PRF remplis de béton, charge cyclique, adhérence, Action composite, retrait du béton, revêtement de sable, comportement en flexion, connexion TPRFB, connexion poutre-colonne, profondeur d'ancrage.

LIST OF PUBLICATIONS

During this research project at the University of Sherbrooke, the candidate has produced the following publications:

JOURNAL PAPERS:

1. **Ahmed, M. Ali** and Radhouane Masmoudi. "Flexural strength and behavior of circular sand-coated concrete-filled FRP tubes under cyclic load." *ACI Special Publication*, SP-79, (2017), (**Accepted and Under Press**).

2. **Ahmed, M. Ali,** Daniel Robillard, Radhouane Masmoudi, and Mohammad Khan. "Experimental investigation of bond and tube thickness effect on the flexural behavior of concrete-filled FRP tube under lateral cyclic loading." *Journal of King Saud University - Engineering Sciences,*(2017), (**Accepted and Under Press**)..

3. **Ahmed, M. Ali** and Radhouane Masmoudi. "Experimental and analytical investigation of new concrete filled FRP tube beam-column connections", *Journal of Engineering Structures*, Elsevier, (2018), (**Submitted on 30 June 2018, Under review**).

CONFERENCES PUBLICATIONS:

4. **Ahmed, M. Ali,** Radhouane Masmoudi, and Mohammad Khan. "Effect of sand-coating bond performance on the flexural capacity of circular concrete-filled frp tubes." *6th International Conference on Engineering*

Mechanics and Materials, EMM608–(1–10), *Canadian Society for Civil Engineering, Annual Conference – Vancouver, , (2017).*

5. **Ahmed, M. Ali** and Radhouane Masmoudi. "Experimental Investigation of a New Beam-Column Connection for Concrete-Filled FRP Tubes (CFFTs)", *9th International Conference on Fiber-Reinforced Polymer (FRP) Composites in Civil Engineering,* (CICE 2018), PARIS (2018).

Acknowledgment

In the Name of Allah, the Most Gracious, the Most Merciful. All praise is for Allah, Lord of the Worlds. The Most Gracious, The Most Merciful. Master of the Day of Judgment. You (Alone) we worship, and You (Alone) we ask for help. Guide us to the Straight Way, the way of those upon whom You have bestowed Grace, not of those who earned Your Anger, nor of those who went astray (Al-Fatiha, The Holy Quran).

The author wishes to express his deep gratitude to everyone who contribute to make this research possible. The author also expresses his sincere gratitude and appreciation to his supervisor Dr. RADHOUANE MASMOUDI for his guidance, inspiration, and encouragement throughout this research program. Also, sincere thanks to Dr. M.-Iqbal Khan for his contributions to my journal and conference publications, and for accepting to review my thesis.

The author would like to thank the other jury members for accepting to review my thesis and I look forward for their valuable suggestions and comments.

Sincere words of thanks must also go to Dr Jean Proulx, the head of the Civil Engineering department in University of Sherbrooke, for his support. Special thanks are extended to Mr. Steven Maceachern, Mr. Sébastien Rioux, Mr. Claude Aubé, Mr. Nicolas Simard, and Mr. Laurent Thibodeau for their assistance during the experimental phases of this research.

My sincere appreciation and thanks must be expressed to my family (my Mother, my Brothers, my Sisters) for their encouragements, endless love, unlimited bolster, and fascinating moments they've given me.

Words cannot express the author's gratitude and appreciation towards his wife Zeinab for her understanding, encouragement, and support always. No one cannot imagine how much strength her support has given me during this challenging time. Thank you for your thoughtfulness, your words of encouragement, and being there for me through my ups and

downs. I would also like to thank my little daughter Toka, who always stole my heart with her brilliant smile; she is the joy of our lives.

Finally, this thesis is dedicated to the memory of my father, who has been a wonderful parent and has shown a genuine interest in and concern for my life, my work, and my well-being. To whom has sacrificed to give me the ability to do this work and reach this point. To whom I promised to dedicate this dissertation before he left this world, To my father.

Ahmed Ali

November 2018

TABLE OF CONTENTS

LIST OF TABLES

LIST OF FIGURES

1. INTRODUCTION

1.1. General Background

Concrete-filled fiber-reinforced polymer (FRP) tubes (CFFTs) are innovative structural systems, because of its high strength and ductility due to confining the concrete core, durability, and minimal maintenance requirements in corrosive environments. They provide also lightweight permanent formwork and the tubes themselves provide longitudinal and lateral reinforcement. The CFFTs can be used as marine piles, bridges (girders, columns, and piers), poles, and highway overhead signs.

As it is well known, the main assumption of the flexural design of any reinforced concrete section, according to all north American design codes and guidelines, is that strain in concrete and non-prestressed reinforcement shall be assumed proportional to the distance from the neutral axis. It means that the strain distribution is linear over the cross-section and the bond between the concrete and the reinforcement is full-bond under service loads. Consequently, the full composite action should be guaranteed between the tube and concrete core. Fam and Rizkalla (Fam and Rizkalla 2002) tested circular CFFT without internal reinforcement. They reported that, excessive slip occurred between the concrete core and the FRP tube. This slip not only has adverse effect on the composite action of the system but also reduces the stiffness of the CFFT beams, especially with thin tubes. Ahmad (Ahmad 2004) tested short and deep CFFTs beam under flexure and fatigue loads. The author concluded that slippage is mostly the single significant factor that dominates the fatigue behavior and fatigue life of CFFT beams. Fatigue life directly depends on the amount of slippage that occurs between the concrete core and the FRP tube. Slippage reduces the composite action in fatigue loading with a high rate if it is compared to static and quasi-static response (Ahmad 2004). Interfacial bond between FRP tube and the concrete core should be adequate to accomplish the composite action, which is required to promote the strength and stiffness of CFFT members.

Extensive studies have investigated the axial and flexural behavior of CFFTs as columns and beams, but rare studies have investigated how to connect the CFFTs together or to other structural members as slabs, footings, and columns. Zhu (Zhu 2004; Zhu et al. 2004, 2006a; b)and Lai (Lai 2010) presented CFFT footing connections with several configurations as precast CFFT footing connection, post-tensioned CFFT footing connection, cast-in-place CFFT footing connection, and CFFT tube bonded adhesively to a steel-reinforced concrete (RC) stub protruded from the footing top. Zakaib (Zakaib and Fam 2012) presented a moment connection for circular CFFT beams by embedding a steel I-beam into the circular CFFT section to a certain length and the other end of the steel I-beam is welded to steel plate that is fixed to a rigid steel assembly by four steel anchors to provide the end fixation.

Based on many studies, the CFFTs experience high strength and deformability under axial and bending loads. The powerful utilization of the CFFTs in structural buildings cannot be achieved without connecting them safely to other structural members. The connections should have enough strength and stiffness to resist and transfer the applied loads and deformations from the beams to the columns.

1.2. Research Originality and Contribution

This research is divided into two Parts. The originally of the first part is using a novel approach to evaluate the composite action in CFFT members. The principal concept of this approach is depending on measuring the strains inside the concrete core and comparing the interior concrete strains values with the electric strain gauges on the external skin of the tube. While the originality of the second part is introducing a new beam-column connection for rectangular CFFT members. The CFFT beam embedded into a steel connection with different embedded depths. The void between the steel connection and the CFFT beam filled with epoxy grout. The steel connection was bolted to the CFFT column using high strength steel anchors. Based on an extensive review of the previous researches in CFFT domain, this is the first research presents a beam-column connection for rectangular CFFT members.

So, the current doctoral research aims at filling research gabs and investigates experimentally and analytically beam-column connection for rectangular CFFTs to be

utilized in the construction field. In addition, this research also introduces an innovative approach to evaluate the composite action of circular CFFT members besides the effect of using sand-coating as a bond enhancer on the flexure performance of CFFT members under lateral cyclic load.

1.3. Research Objectives

The first part of this study investigates experimentally column-footing connections under lateral cyclic load. While the second part of this study introduces an innovative design of beam-column connections for rectangular CFFTs. The objectives of this study can be summarized as follows:

- To investigate the effect of bond between the concrete core and the FRP tube on the flexural behavior of CFFT members
- To investigate the size effect of the concrete core on the interfacial bond between the concrete core and the FRP tube.
- To evaluate the performance of using sand-coating as a bond enhancer to improve the interfacial bond between the concrete core and the FRP tube.
- To investigate a new rectangular CFFT beam-column connection.
- To investigate the effect of bond between the CFFT beam and the epoxy grout on the presented beam-column connection.
- To determine the optimal embedded depth of the proposed beam-column connection.
- To create an analytical model for the studied CFFT beam-column connection.

1.4. Methodology and Contents

To achieve the objectives of this research, experimental and analytical phases are proposed. The experimental phase includes CFFT column connected to RC footing (four full-scale specimens) and beam-column connections (four specimens). The first part of this study investigates experimentally the effect of the interfacial bond between the concrete core and the FRP tube on its flexural performance under lateral cyclic load. The test parameters are the size of the circular CFFT columns and the interfacial bond between the concrete core and the FRP tube surface. The second experimental phase includes the construction and testing of four beam-column connection specimens having similar dimensions. All beam-column connections are rectangular pulturded GFRP tube filled with concrete as beams connected to rectangular filament wound GFRP tube filled with concrete as columns.

The analytical phase developed an analytical model to analyze and predict the behavior of the beam-column connections. The efficiency and accuracy of the model was verified against the experimental results. Afterwards, the model was used to conduct a parametric study. The conclusions of this study were collected and analyzed to introduce a new study of beam-column connection for CFFTs, which can be used in structures and bridges or ready structural elements industry field.

The contents of this thesis are briefly described in the following:

Chapter 2 presents a general literature review pertinent to concrete-filled FRP tube with more concentration on the previous studies related to bond in CFFT members and the previous proposed CFFT connections.

Chapter 3 (1st article) presents the results of an experimental investigation on the flexural strength and behavior of circular sand-coated concrete-filled FRP tubes (two full-scale) specimens under cyclic load

Chapter 4 (2nd article) presents test results of an experimental program to investigate the composite action of full-scale circular CFFT columns under lateral cyclic load (four full-scale specimens). The size effect of the CFFT column besides the effect of using sand-

coating as a bond enhancer were examined. Recommendations for using unreinforced CFFT members were proposed to ensure the attain of full composite action.

Chapter 5 proposing an analytical model based on the layer-by-layer approach to predict the flexural behavior of the fully bonded CFFT.

Chapter 6 (3rd article) developed a new assembly of CFFT beam-column connection for rectangular CFFT members. The connection was investigated experimentally and analytically to be widely utilized in the practice. Design equations were proposed to calculate the flexural capacity of rectangular CFFT beams and the required embedded depth to achieve its flexural capacity.

Chapter 7 proposing an analytical study of the proposed beam-column connection based on two approaches (stress-block and layer-by-layer). A comparison between two approaches was implemented to evaluate them accuracy comparing to the experimental results. A parametric study has been conducted to investigate the effect of tube thicknesses, the material properties (FRP tube, concrete), and the grout bond strength on the flexural capacity and the optimal embedded depth of the proposed connection.

Chapter 8 provides conclusions and summary of the research with respect to observations and points discussed throughout the thesis in addition to recommendations for future work.

References.

2. LITERATURE REVIEW

2.1. Introduction

Using concrete-filled fiber-reinforced polymer (FRP) tubes (CFFT) has begun for different structural applications in the last twenty years. The CFFTs are involved in various applications as piles in marine structures, bridges (girders, columns, and piers), poles, and highway overhead sign structures. Using FRP tube in this system provides high resistance against corrosion due to the harsh environmental conditions, high strength due to confining the concrete core, durability and requires low maintenance, lightweight permanent formworks and the tube itself provides longitudinal and lateral reinforcement. On the other hand, the concrete core supports the tube walls against the buckling.

The bond between the concrete and the FRP sheet material is the limiting factor for the ultimate strength of the beam (Honickman and Fam 2009). AASHTO (AASHTO 2012) did not provide a specific technic to achieve the full bond in the CFFT design. Very limited studies have been conducted to study the bond between the FRP tube and the concrete. Mirmiran (Mirmiran et al. 1998a) used FRP shear connector ribs on the interior surface of the tube to achieve the full bond between the square tube and the concrete. Belzer (Belzer et al. 2013) investigated the bond between the rectangular FRP tube and concrete by using epoxy coating.

Extensive research was carried out on CFFTs as columns like (Burgueno et al. 1998; Fam and Rizkalla 2003, 2001, Mirmiran et al. 1998b, 2000; Mohamed and Masmoudi 2010a; Ozbakkaloglu 2005), as beams like (Abouzied and Masmoudi 2014, 2015, 2017; Fam and Rizkalla 2002; Helmi et al. 2005; Mohamed and Masmoudi 2010b, 2012). Many CFFT columns with circular or rectangular sections were tested under several types of loading (axial only, axial and lateral, monotonic or cyclic). In addition, many of CFFT beams were tested under flexural to provide flexural design for CFFT beams. The CFFT connections are a vital structure element. They give the ability to use the CFFTs at any structure. The CFFT connections include footing connections and beam-column connections. Limited researches studied the CFFT footing connection as (Lai 2010; Zhu 2004). They presented a CFFT footing connection with several configurations as precast CFFT footing

connections, post-tensioned CFFT footing connections, cast-in-Place CFFT footing connections, and CFFT tube was adhesively bonded to a steel-reinforced concrete stub protruding from the top of the footing. Zakaib (Zakaib and Fam 2012) presented a moment connection for circular CFFT beam by embedding a steel I-beam into the circular CFFT and welded to steel plate from the other side. No research was carried out on the CFFT beam-column connections.

This chapter introduces a literature review on CFFT performance and presents the previous researches on the bond between FRP tube and concrete and the previous trials to make CFFT connections.

2.2. Review on Concrete-Filled FRP Tubes (CFFT) Performance

Most researchers concluded high efficiency of the confinement effect of FRP tube in CFFT system. Mirmiran (Mirmiran et al. 1998b) defined three parameters affect the efficiency of GFPR tubes in confinement. Their experimental program consisted of 101 specimens tested to investigate the column length to diameter ratio, tube cross section shape, and the bond between the inner tube surface and the concrete core. 30 cylindrical specimens with dimensions of 152.5 × 305 mm and 12 square specimens with 152.5 × 152.5 × 305 mm dimensions were tested under concentric loading. This group was divided to three groups varying in the tube wall thickness. The results showed that the effective of circular tube confinement is about twice the square tube confinement it determined according to their ultimate compressive strength as shown in the stress-strain curves in Figure 2.1. The results discussion showed that circular tube confinement produces uniform pressure acting on the concrete core but the pressure produced in the square tube varying from corner to edge. In the second tested group consisted of 24 cylinders with four variations in column length to diameter ratio, the ratio approximately varying from 2:1 to 5:1. In addition, there were three variations in tube wall thickness in each one of four variations in column length to diameter ratio group. The result of this group showed a little reduction in the strength and ductility for the 5:1 specimens comparing by the 2:1 specimens, the redaction was in range 10 – 12 % as shown in the stress-strain curves in Figure 2.2.

The third group investigated the bond between the inner tube wall surface and the concrete core. All circular specimens were fabricated by wrapping concrete cylinders rather than filling prefabricated FRP tubes, with the exception of three-square specimens. Adhesive bonding had little effect on the confining pressure of the circular specimens, whereas mechanical bond (shear connectors) increase the confining effect for square specimens because it helped to distribute pressure more evenly around the square specimens.

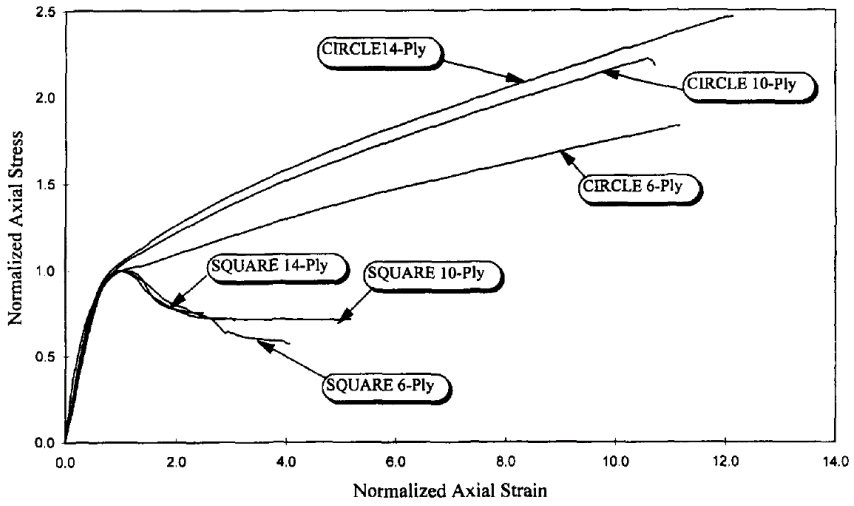

Figure 2.1: Normalized stress-strain curves for the effect of tube cross-section (Mirmiran et al. 1998b).

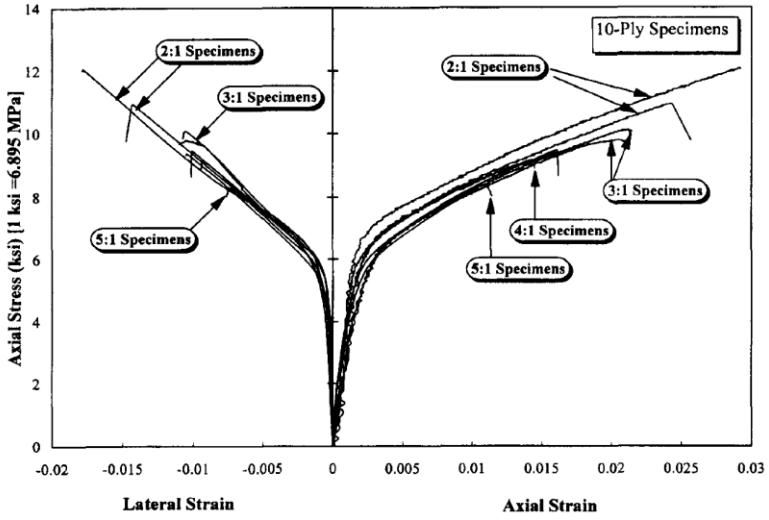

Figure 2.2: Biaxial stress-strain curves for the effect of length to diameter ratio (Mirmiran, et al. 1998a).

Fam (Fam and Rizkalla 2001) tested rectangular CFFTs under eccentric and concentric axial compression loads. The results showed that the columns loaded over the entire cross-section could fail in a brittle manner by fracture of the FRP tube at the round corner, where a high level of bi-axial state of stresses is developed. The round corners of CFFT columns provide confinement initially; however, the flat sides of the FRP tube bend outwards eventually and cause the column to bulge and the concrete core to lose restraint. Consequently, the confinement effect significantly reduced.

Fam (Fam and Rizkalla 2003) tested five and ten concrete-filled FRP tubes (CFFTs) under concentric and eccentric axial compression loads respectively. The parametric studied were the effects of concrete fill, laminate structure of the tube, reinforcement ratio based on the wall thickness. The result showed that ignoring the effect of axial loading of the FRP tube under compression and assuming the development of its full hoop strength overestimate the confinement effectiveness. The totally filled GFRP tubes provide the most effective confinement for columns. The strength of the column was governed by failure of the FRP jacket. Unlike steel tubes, the FRP tubes fracture in a brittle manner. The laminate structure significantly affects the shape and size of the interaction diagram.

Boumarafi (Boumarafi et al. 2015) studied the effect of the GFRP tube thickness on the capacity of square CFFT columns. The test results showed a significant enhancement in the ultimate capacity and ductility due to using thicker FRP tubes. The load-axial displacement curves and stress-axial strain curves of CFFT columns could be considered as bilinear. The gained ductility for CFFT columns was 500% that of unconfined PC columns.

Mirmiran (Mirmiran et al. 2000) tested sixteen specimens with 2.75m long were fabricated from two different tubes (spin-cast or filament-wound). The spin-cast tubes were over-reinforced while the filament-wound were under-reinforced. The samples were loaded axially, and then lateral loads were applied while keeping the axial load constant. The flexural capacity of the spin-cast tubes was twice the filament-wound tubes as shown in Figure 2.3 where type I was the spin-cast CFFT and type II was filament-wound CFFT. The failure of spin-cast tubes was at compression due to the rupture of the tube. The failure of the filament-wound tubes happened due to fracture of the tube along its main winding

axis at low axial loads while compression governed at high axial loads. The observed slippage in the axially loaded columns can neglected. Lateral load capacity was seen to decrease as axial loads increased. Bilinear load-deflection behavior was observed, with the change coming at the cracking of concrete. The spin-cast tubes had lower deflections and higher capacities.

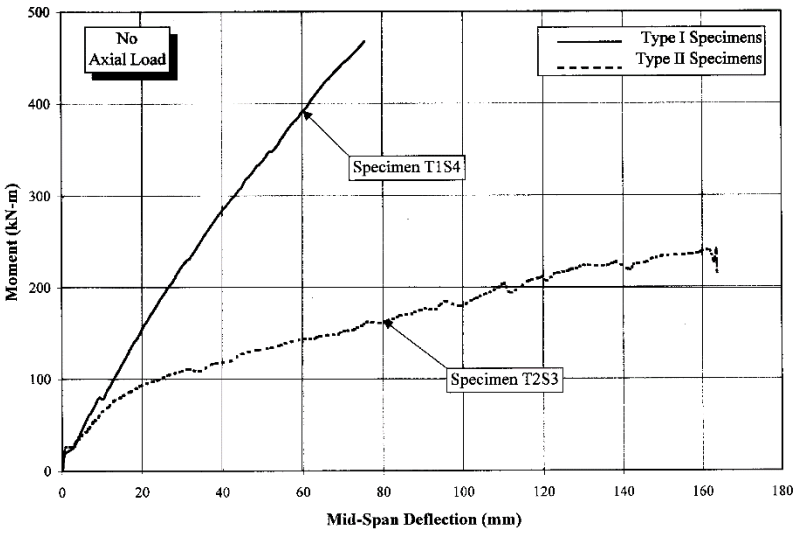

Figure 2.3: Moment–deflection curve for spin-cast and filament-wound CFFTS (Mirmiran et al. 2000).

Fam (Fam et al. 2005) tested three beams and five short columns full-scale rectangular concrete-filled rectangular filament-wound glass fiber reinforced polymer (GFRP) tubes to study the flexural behavior of CFFTs and to obtain their axial load–bending moment interaction diagram. The tubes were manufactured in two different sizes 271 x 164 and 374 x 266 mm as shown in Figure 2.4(a). The stacking sequence for the flanges was [90, 45, -45, 45, -45, 0, 0, 90, 0, 0, 45, -45, 45, -45, and 90], while that of the webs was [90, 45, -45, 45, -45, 90, 45, -45, 45, -45, 90] as shown in Figure 2.4(b). The inner tube surfaces were coated with epoxy resin then coarse silica sand was applied to produce a rough texture as shown in Figure 2.4(c). Figure 2.5 show the tested beams cross sections “a”, “b” and “c” denote totally and partially filled large tube and totally filled small tube respectively. Five short columns consisted of the small GFRP tubes with 680 mm long were filled with concrete. All columns were tested under concentric or eccentric axial compression loads applied at various eccentricities. Columns C1, C3, C4, and C5 were tested using a setup

with free rotation allowed at both ends. Specimen C2 was tested between two fixed platens, without allowing end rotation. All samples details shown in Figure 2.6. Significant nonlinearity observed for Laminates with fibers orientation angle ±45 degrees under tension and compression as shown in Figure 2.7. The capacity of the beam with inner void was smaller than the totally filled tube by 22% but it had 56 % lighter in weight. Totally filled tube failed in tension by rupture of FRP. The partially filled tube failed in compression due to the buckling and fracture of the concrete compressive flange as shown in Figure 2.10. The depth of compression zone in CFFT beams after cracking was ranged from 20 to 30% of the section depth and linear strain distribution was observed as shown in Figure 2.8. Increasing the reinforcement ratio by 55%, it leads to increase in the flexural strength by 41%. The confinement effect in CFFTs columns was reduced due to bend of the flat sides of the FRP tube bend outwards then the concrete core loose restraint. All columns failed in brittle manner by fracture of the FRP tube at the round corner. Figure 2.9 show the effect of eccentricity in the axial capacity of CFFTs.

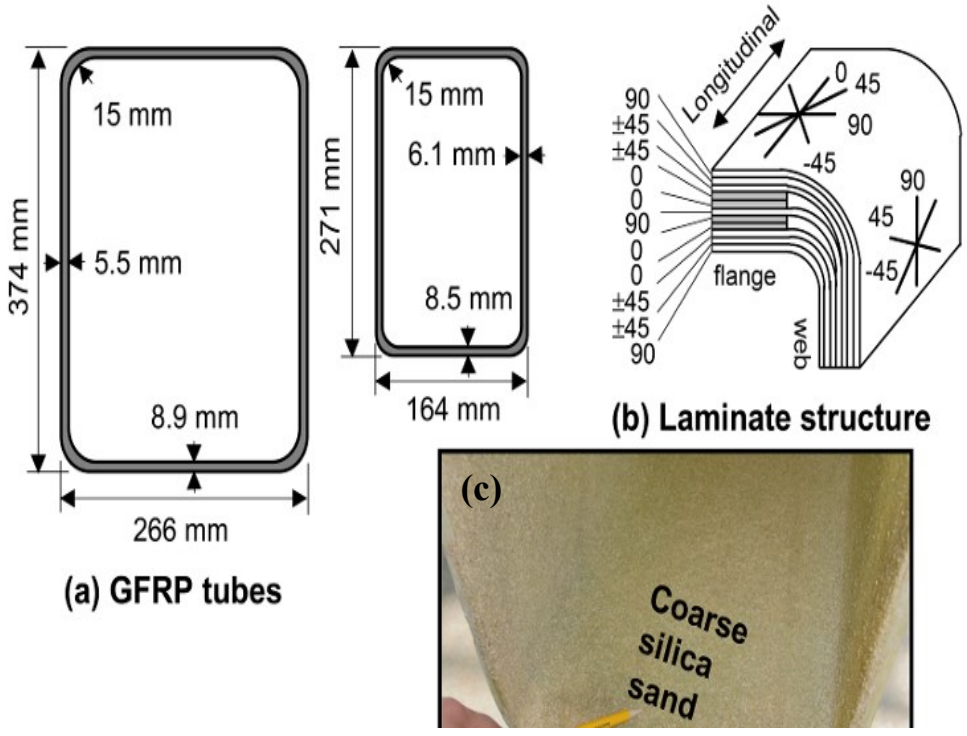

Figure 2.4: Details of GFRP tubes tested by (Fam et al. 2005).

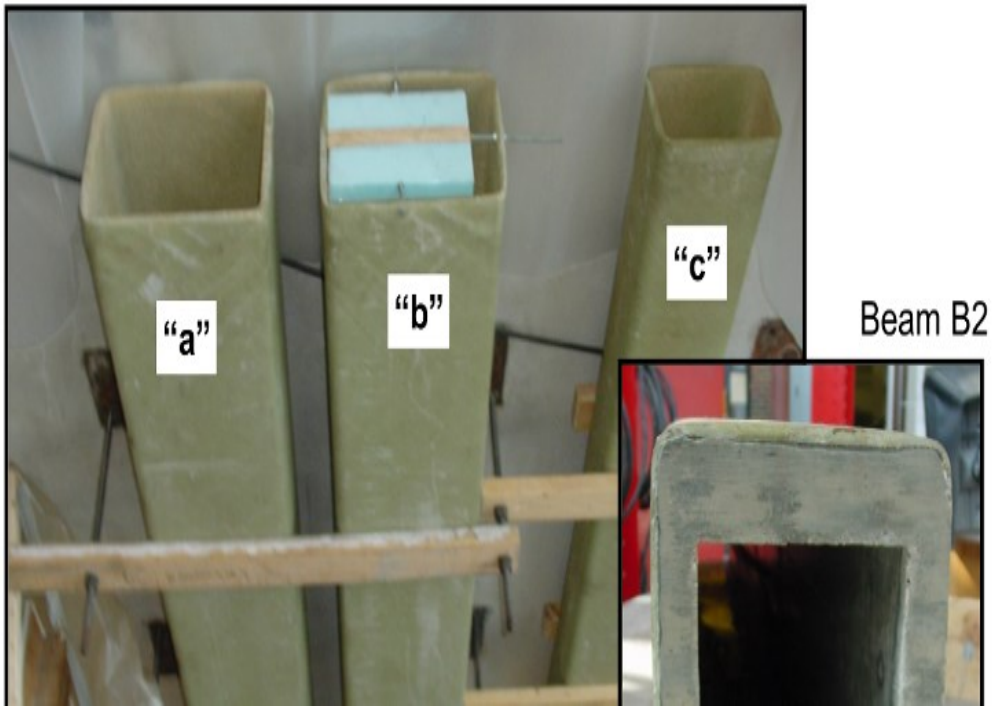

Figure 2.5: Casting setup of CFFT beams tested by (Fam et al. 2005).

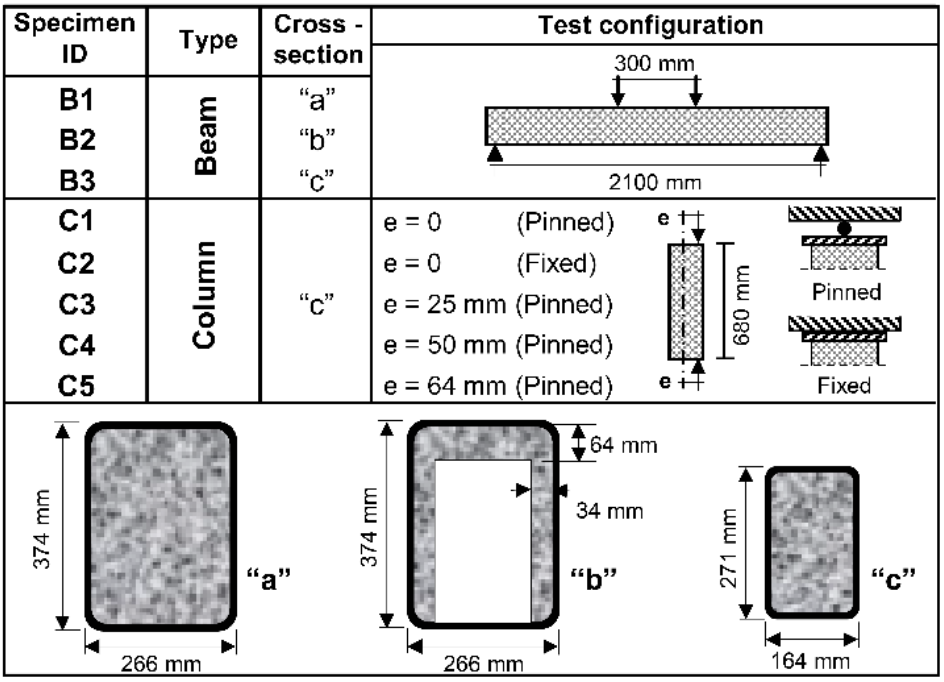

Figure 2.6: Specimens Details tested by (Fam et al. 2005).

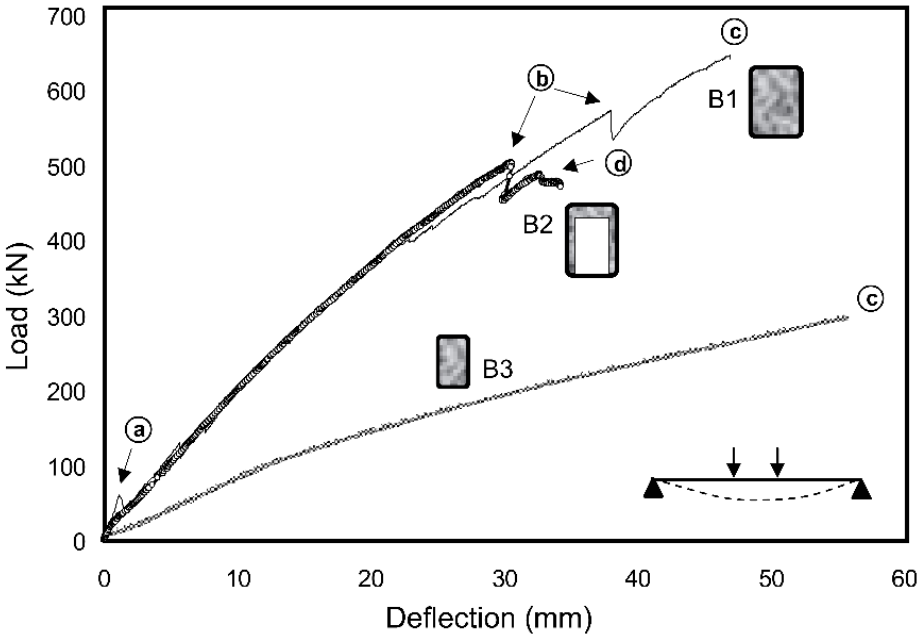

Figure 2.7: Load-deflection behavior of tested beams by (Fam et al. 2005).

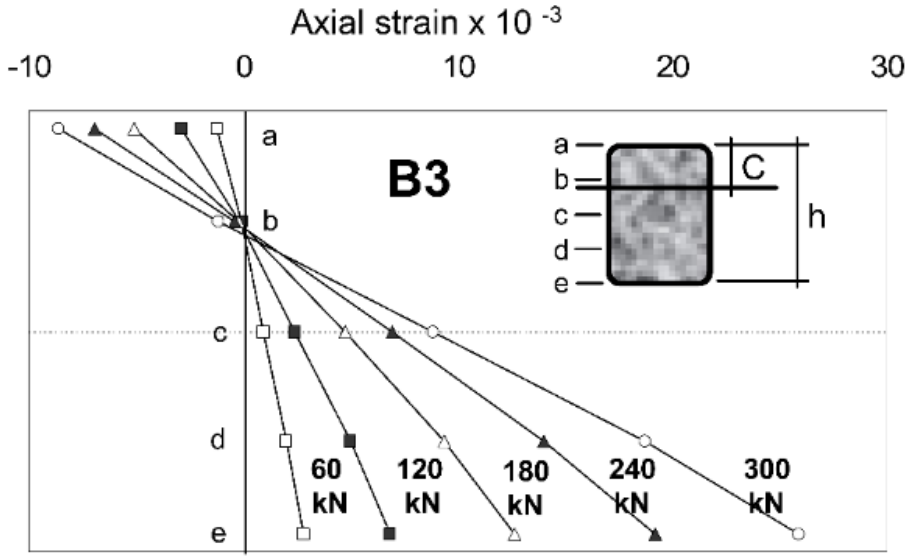

Figure 2.8: Variation of neutral axis of tested beams by (Fam et al. 2005).

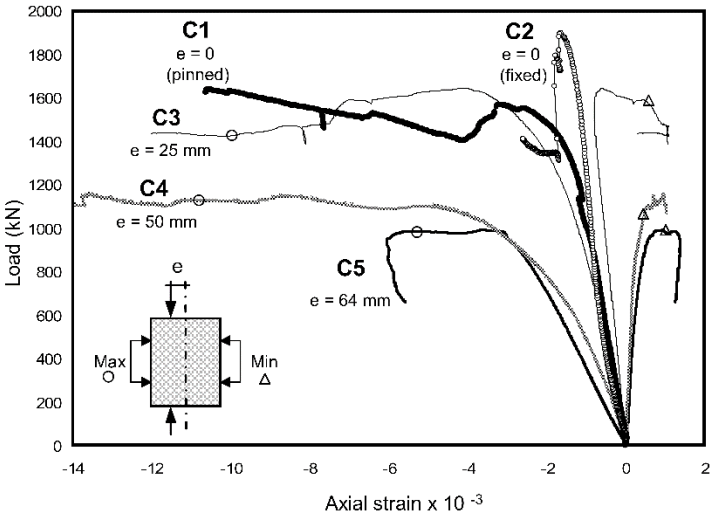

Figure 2.9: Load-axial strain behavior of tested columns by (Fam et al. 2005).

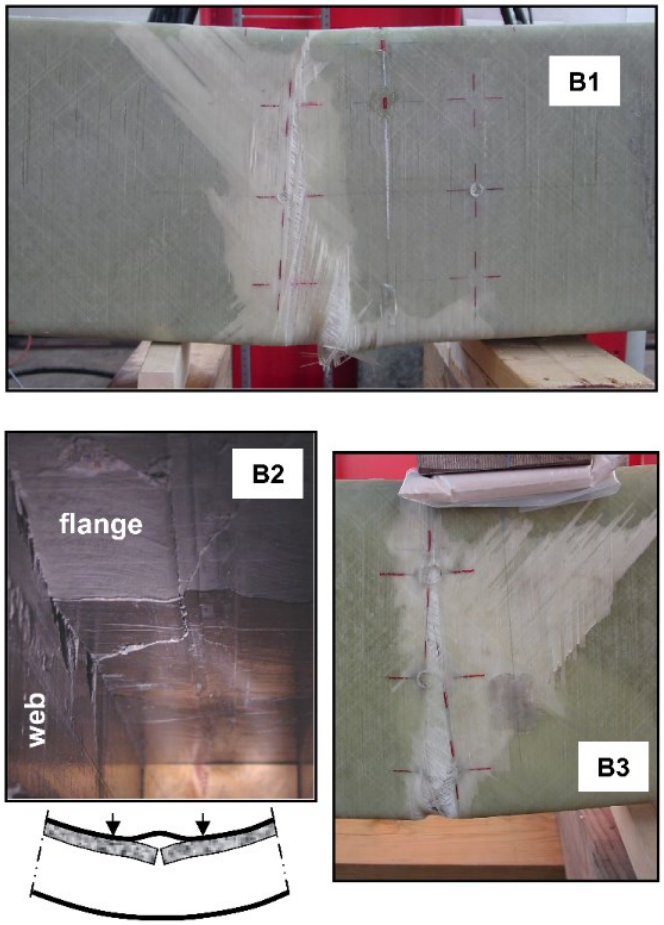

Figure 2.10: Failure mode of tested beams by (Fam et al. 2005).

Mohamed (Mohamed and Masmoudi 2010c) tested ten circular CFFTs under four-point bending load with 213 mm diameter and 2000 mm length. The studied parameters were the FRP tube thickness, concrete compressive strength, type of internal reinforcement (steel or FRP bars), and type of transverse reinforcement (spiral steel or FRP tube). The results showed that the reinforced concrete filled GFRP tubes (RCFFT) had higher strength, ductility, stiffness, and cracking load than the beam reinforced with a spiral steel. The deflection for RCFFTs was lower than the deflection for the beam reinforced with a spiral steel. Insignificant effect observed between using 30 and 45 MPa concrete compressive strength. The axial stiffness of the FRP tubes had significant effect in the strength, ductility, and deflection of RCFFTs. An acceptable theoretical analysis was presented to predict the ultimate and yield moment capacities of FRP or steel–RCFFT beams**.**

2.3. Bond in Concrete Filled FRP Tubes

Bond development is one of the first fundamental requirements for any concrete structure, loads transfer from concrete to the reinforcement by bond. Therefore, the bond quality has a notable effectiveness on crack formation according to that it will also effects on the spacing between cracks and crack width.

The FRP tube in the case of concentrically loaded column provides hoop confinement, and therefore, the mechanical bond between FRP and concrete is not important. For flexural loads, the FRP tube plays a significant role. It confines the concrete in the compression zone and acts as the flexural and shear reinforcement at the same time. This requires development of the full composite action between FRP tube and concrete. Therefore, a mechanical bond is necessary (Samaan 1997). There are many ways to enhance the mechanical bond between the FRP tube and concrete like sand coating, resin ribs, shear connector, and internal crossing bars.

When flexural tests on CFFTs (without internal reinforcement) are carried out, excessive slip may occur between the concrete core and the FRP tube. This slip may adversely affect the composite action of the system unless special measures are taken, such as roughening the inner surface of the tube (Fam and Rizkalla 2002). If internal rebar reinforcement is

used and no bond enhancing is done, slip measured at both ends may be very small and can be neglected (Cole and Fam 2006).

Mirmiran (Mirmiran et al. 1998a) used interior shear ribs to enhance the mechanical bond between square FRP tube and concrete as shown in Figure 2.11. The results showed the presence of shear ribs could arrest any separation or slippage. The shear ribs allowed full utilization of the tube. The shear ribs provided high efficiency in transferring the load between the tube and the concrete core.

Figure 2.11: Interior shear ribs of the FRP tubes (Mirmiran et al. 1998a).

Mirmiran (Mirmiran et al. 1998a) tested thirty-five CFFT columns to study the effect of using adhesive bond and the mechanical bond between square FRP tubes and concrete in square CFFT columns. Three CFFTs were made using special collapsible mandrel with interior shear ribs. Thirty-two CFFT with and without interface bond were tested, two methods used to fabricate the FRP jacket (multi-layered and single-warp) for adhesive bonded samples. Polyester resin was used to adhesive the FRP layers to the concrete columns after 28-day form concrete casting in the adhesive bonded samples. The authors reported that the adhesive bond did not affect the capacity of the columns. The mechanical

bond (shear ribs) improved the performance of the section by distributing the confinement more efficient around the tube perimeter.

Ahmad (Ahmad 2004) tested CFFTs as deep beam and short beam under flexure and fatigue. He concluded that slippage is probably the single most important factor that dominates the fatigue behavior and fatigue life of CFFT beams. Fatigue life is directly related to the amount of slippage that occurs between the concrete core and the FRP tube. Slippage reduces the composite action in fatigue loading at a much greater rate when compared with static and quasi-static response.

Nelson (Nelson et al. 2008a) tested six push-through CFFT specimens embedded into concrete footings under axial compression load as shown in Figure 2.12. The aim of their tests was determining the interfacial shear strength (bond) between the GFRP tube and concrete.

Based on the experimental results for this type of tubes the average ultimate bond strength between the GFRP tube and the concrete is 0.75 MPa this value can be changed according to the surface texture, preparation of the FRP tube, concrete rupture modulus, and confining steel reinforcement in the footing. Once the bond reached the ultimate strength, it dropped to a level of about 50 to 60 percent of the ultimate bond strength as shown in Figure 2.13.

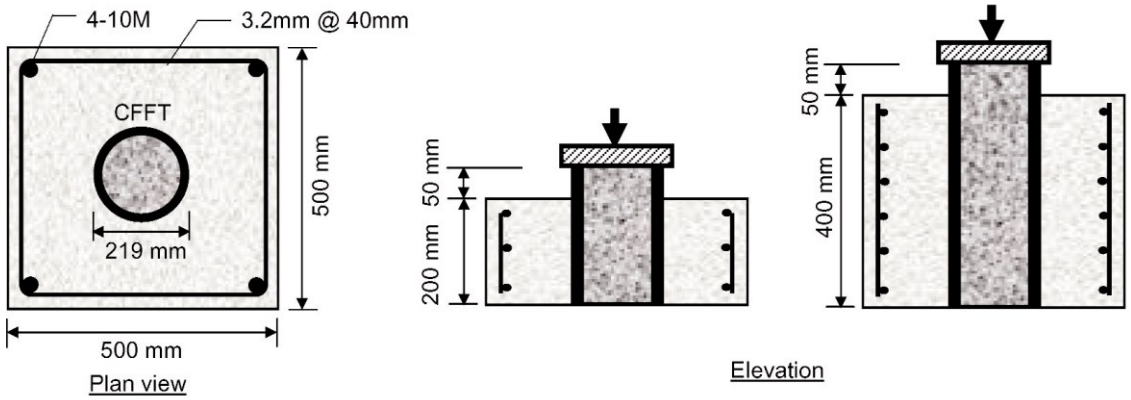

Figure 2.12: Push-through Specimens (Nelson et al. 2008a).

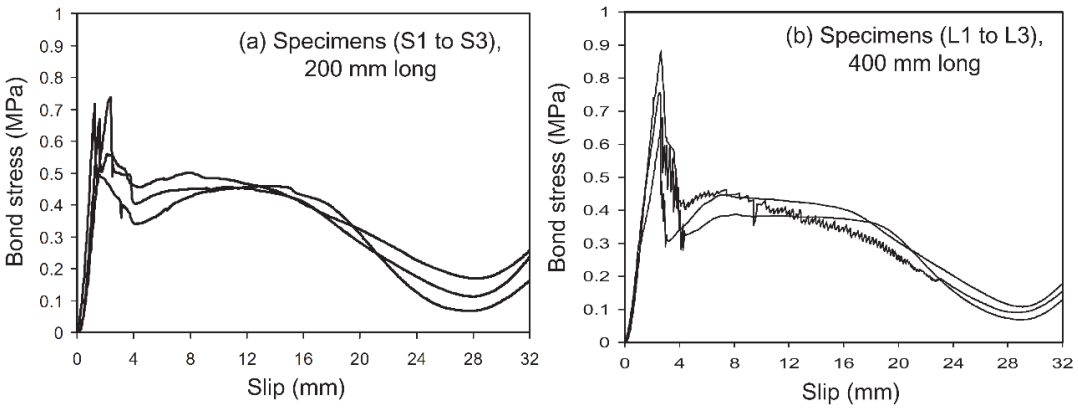

Figure 2.13: Bond stress – slip behavior of push-through specimens (Nelson et al. 2008a).

Ji (Ji et al. 2009) investigated the effect of the thickness of the FRP ribs and FRP skin on the interfacial bond strength. Five groups of specimens tested under push-out test. The specimens Group "A" and "B" were a normal FRP tube filled with concrete with variation on the thickness of the tube wall. Groups "C", "D", and "E" were a FRP tubes with FRP ribs with variation on the ribs thickness as shown in Figure 2.14. The results were opposite to the common belief, the interfacial shear strength decreases as the rib thickness increases. The authors reasoned that to the lower of concrete strength used. The Results also showed that the increasing the tube skin thickness increases the interfacial bond in the normal FRP tubes.

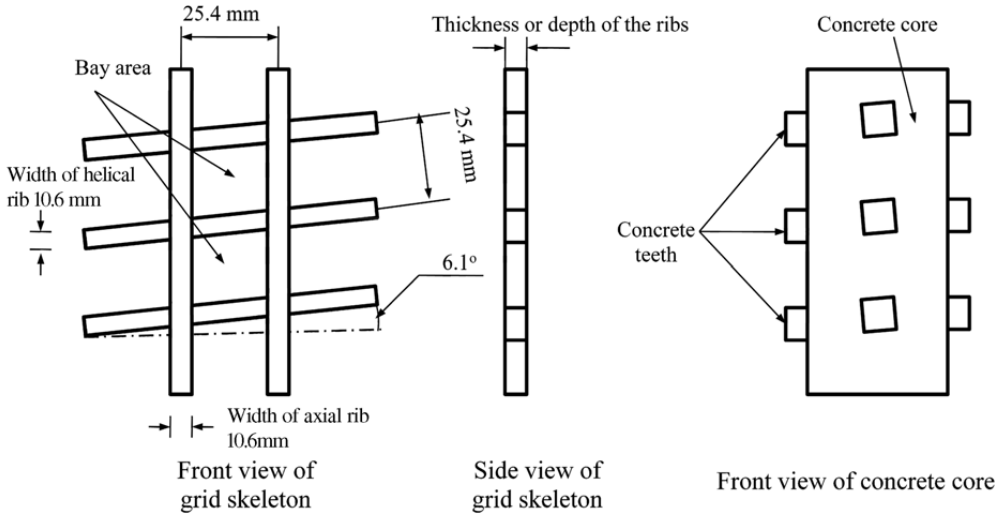

Figure 2.14: Schematic of rib width, thickness, bay, and concrete teeth (Ji et al. 2009).

Belzer (Belzer et al. 2013) investigated the degree of composite action between rectangular pultruded GFRP tube and concrete. The objective of this research was done by testing twelve beam specimens under four-point flexural loads. The specimens were classified to four different configurations, three beams for each configuration type. The first configuration was an empty GFRP tube (A); the second configuration was concrete filled GFRP tube (B); the third configuration was concrete filled GFRP tube with epoxy bonding of the flanges (C); the fourth configuration was concrete filled GFRP tube with epoxy bonding all interior surface (D) as shown in Figure 2.15. All specimens had the same dimensions 3.5 m long with 3.05 m clear span, 152 mm width and 203 mm depth. The tube flange thickness was 9.5 mm and the web thickness was 6.4 mm.

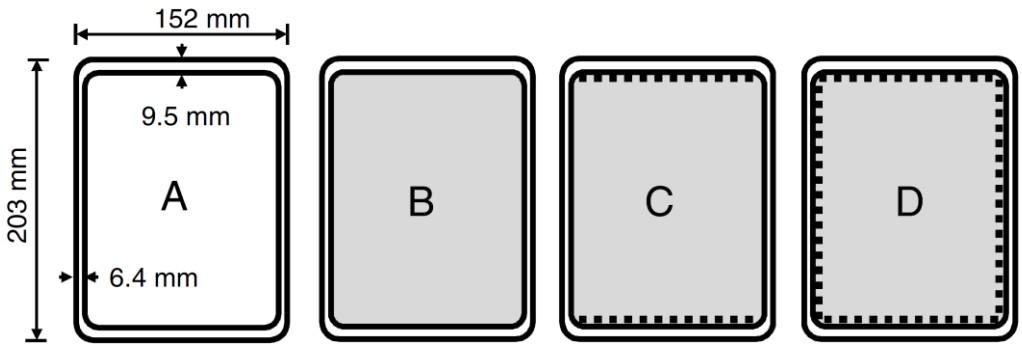

Figure 2.15: Beam configurations (Belzer et al. 2013).

The results indicated that using epoxy to bond the FRP tube to concrete increases the flexural capacity and stiffness significantly. The load-deflection curves for the four beams are shown in Figure 2.16. The curves show the significant effect of bond between the FRP tube and concrete on the flexural capacity and stiffness of rectangular CFFTs. Based on the results of strength, stiffness, slippage between the FRP tube and concrete and the neutral axis location, the authors reported that the fully bonded and partially bonded achieve acceptable composite action performance more than the other beam configurations. An analytical model was developed to predict the behavior of the fully bonded composite CFFTs (D). The model results agreed well with the experimental results for the fully bonded beam (D).

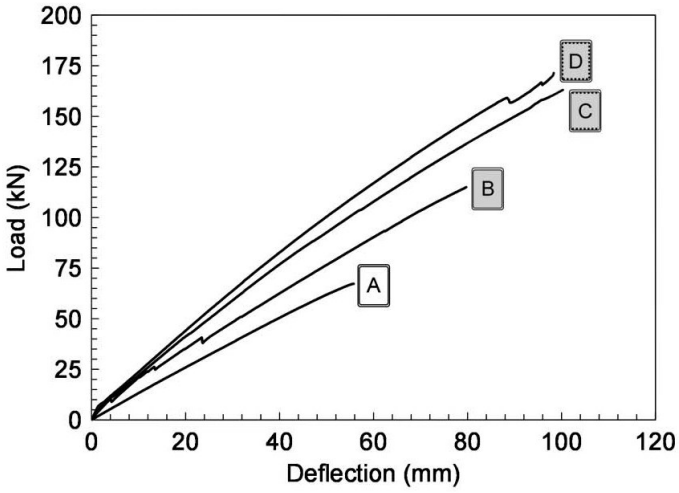

Figure 2.16: Load deflection curves for beams (Belzer et al. 2013).

2.4. Concrete Filled FRP Tubes (CFFTs) Connections

The CFFT connections are classified to two types, joints between members and splices in the same member. The previous research about CFFTs connections is very limited. Lai (Lai 2010)studied connections between CFFT columns and footings. Four types of connections were studied by Zhu (Zhu 2004) splices, beam to column connections, column to RC pier caps, and column to RC footings. Zakaib (Zakaib and Fam 2012) studied a moment CFFT connection.

Zhu (Zhu 2004) studied an innovative modular bridge pier system using stay-in-place FRP forms filled with concrete as shown in Figure 2.17. Four different CFFT connections were investigated in this study. A Male-Female connection without dowel bars was used to connect one CFFT to the pier caps, while dowel bars without embedment was used to connect it to the RC footing (Frame 1). The second column was connected to the pier cap by male-female connection with dowel bars, and dowel bars with embedment into the RC footing was used to connect it to the footing (Frame 2). The pile cap was a stay-in-place form also made of FRP sheets and attached with an extra sheet on top for negative moment continuity. A bonding agent was used in all connections also the gap between the tube and the RC footing were filled with a cement grout mixed with the same bonding agent. It was observed that the male-female joints lacked the structural integrity necessary for this

application. (Frame 1) had higher initial stiffness despite the absence of dowel bars and embedment. Embedding the CFFT into the RC footing produced a beneficial effect for the connection. The study also showed that the internal reinforcement outside of the connection area is not necessary.

Zhu (Zhu 2004) also tested four columns to footing connections under cyclic load, three CFFT columns and a control RC column, all with similar RC footings. The three CFFT specimens included a cast-in-place CFFT column with starter bars from its RC footing, a precast CFFT column with starter bars from its RC footing and grouted ducts, and a precast CFFT column post-tensioned to its RC footing as shown in Figure 2.18. The reinforcement in all specimens was four 16 mm and four 19 mm diameter of Grade 414 MPa mild steel, expect for the post-tensioned CFFT column, which had eight 19.0 mm Grade B-7 high strength threaded rods with a yield strength of 724 MPa. The CFFT columns did not fail up to the displacement of 180 mm. Therefore, they were pushed monotonically to a displacement of 300 mm, equivalent to a 13.3% drift ratio. The loading rate for the monotonic loading phase was kept the same as that for μ of six, which was 36.6 mm/min. Separation between the FRP tube and footing was observed at high displacements, but the load was still transferred effectively as sown in Figure 2.19. All three joint methods performed in a very similar manner and were much more ductile than the control RC column as shown in Figure 2.20. The development in the performance was a result due to the confinement of the concrete core by the tube.

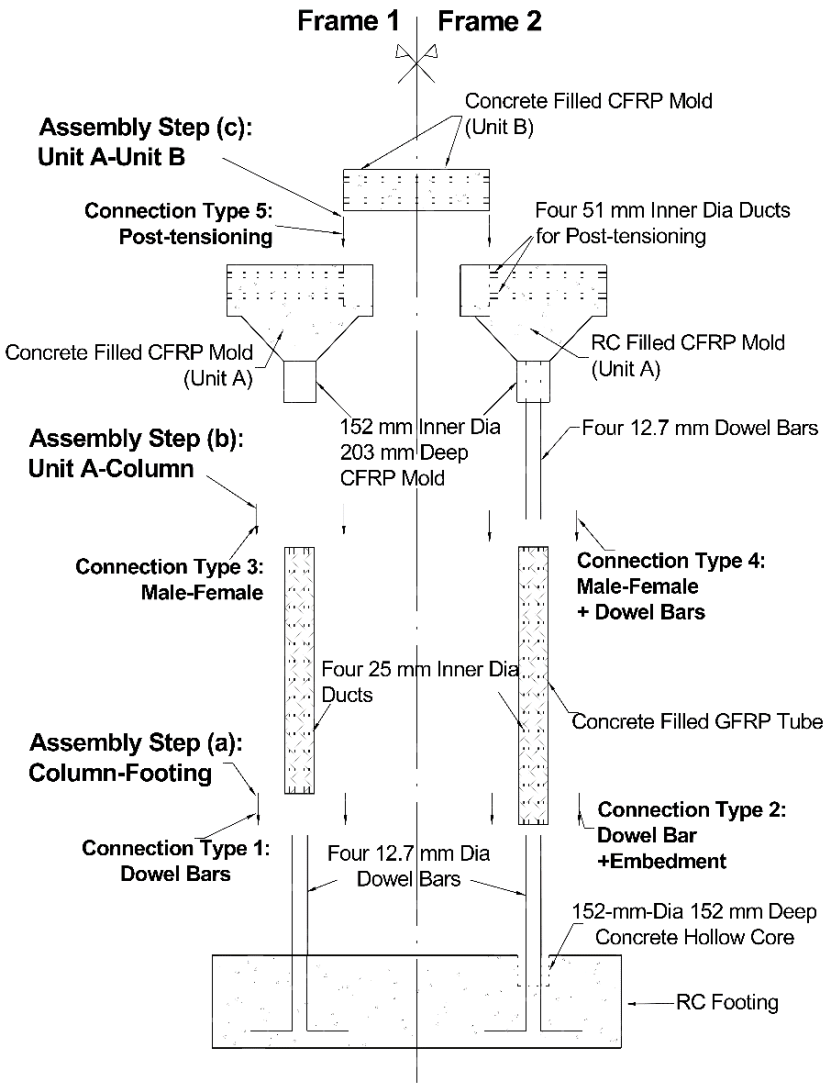

Figure 2.17: CFFTs connections studied by (Zhu 2004).

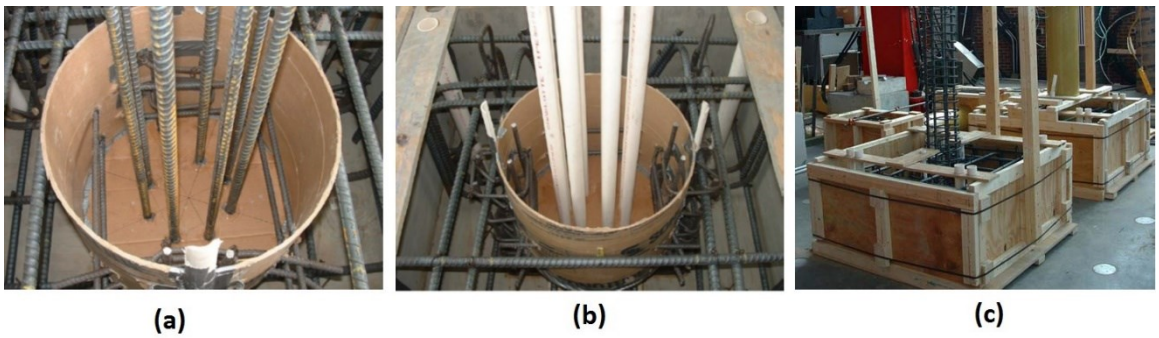

Figure 2.18: CFFT Column- footing connections studied by (Zhu 2004)(a): for precast CFFT, (b): for post-tensioned CFFT, (c): for Cast-in-Place Columns.

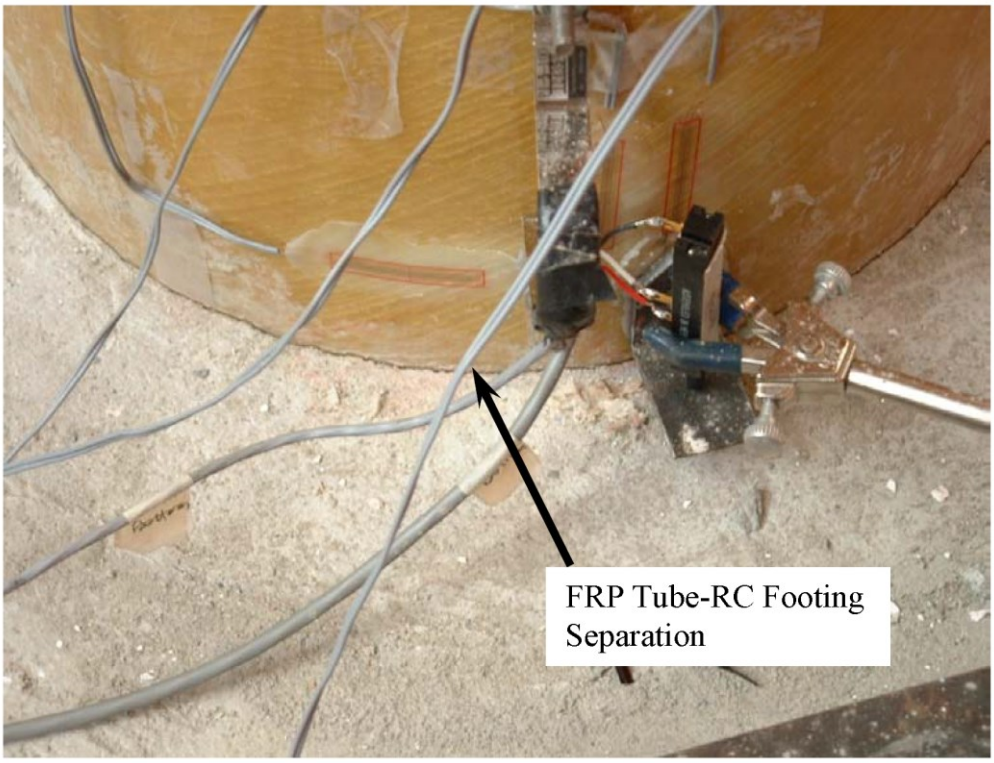

Figure 2.19: Separation between FRP Tube and RC Footing (Zhu 2004).

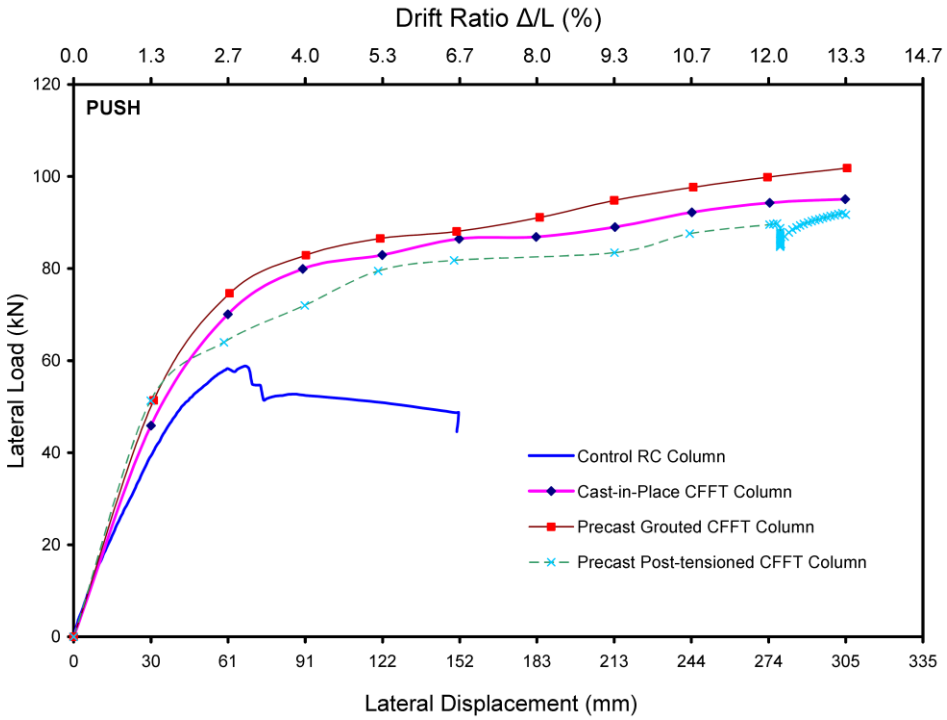

Figure 2.20: Lateral Load-Deflection Envelope Curves of Tested Columns (Zhu 2004).

Zhu (2004a) also investigated four techniques for CFFTs splices, grouted steel bars, grouted FRP bars, un-bonded post tensioning bars and FRP sockets as shown in Figure 2.21. A control un-spliced CFFT section was also prepared for comparison. The five specimens were tested under a four-point bending test. The post tensioning beam recorded higher strength than the other spliced beams but less than the un-spliced beam by 30 %. The Failure of the two bar-spliced beams was similar, failure was determined based on excessive bar slippage and joint opening, but with more sharp load drops. Figure 2.22 shows the load-deflection curves for the tested CFFT beams.

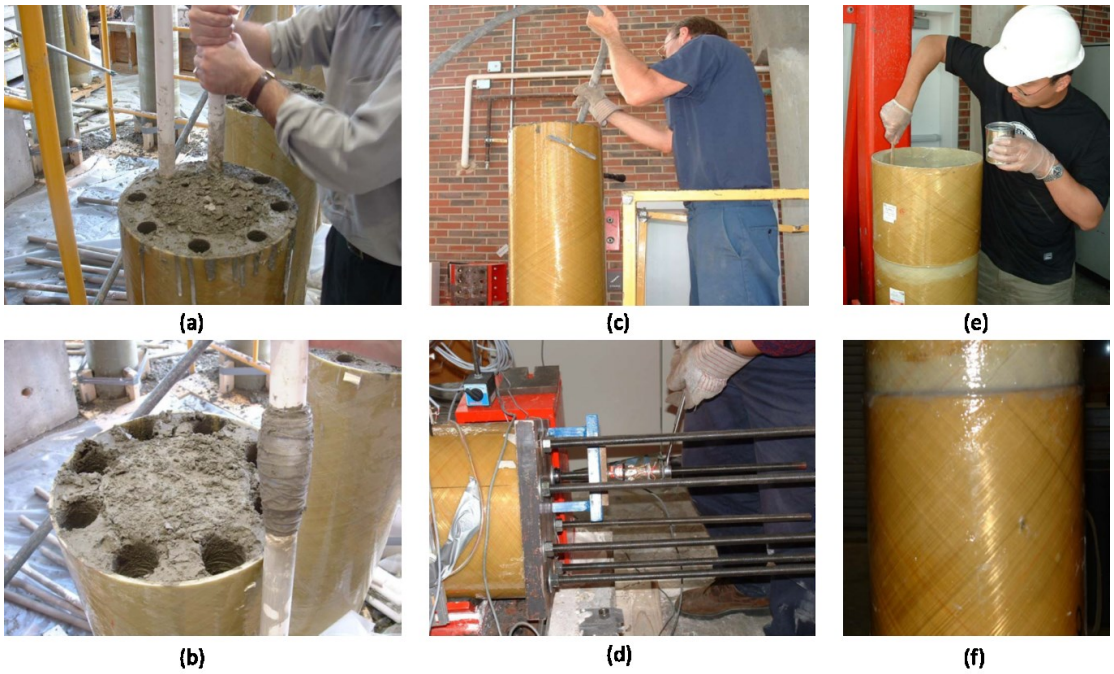

Figure 2.21: Specimen Casting and assembly: (a) PVC Pipes Being Pulled Out After Partial Setting of Concrete, (b) Enlarged Ducts Made by PVC Pipes, (c) Consolidating Grout in Steel Bar Spliced CFFT Beam, (d) Post-Tensioning Procedure, (e) Applying Epoxy to Inside Surface of FRP Socket Spliced Beam, (f) Close-up View of FRP Socket Spliced CFFT Beam Joint (Zhu 2004).

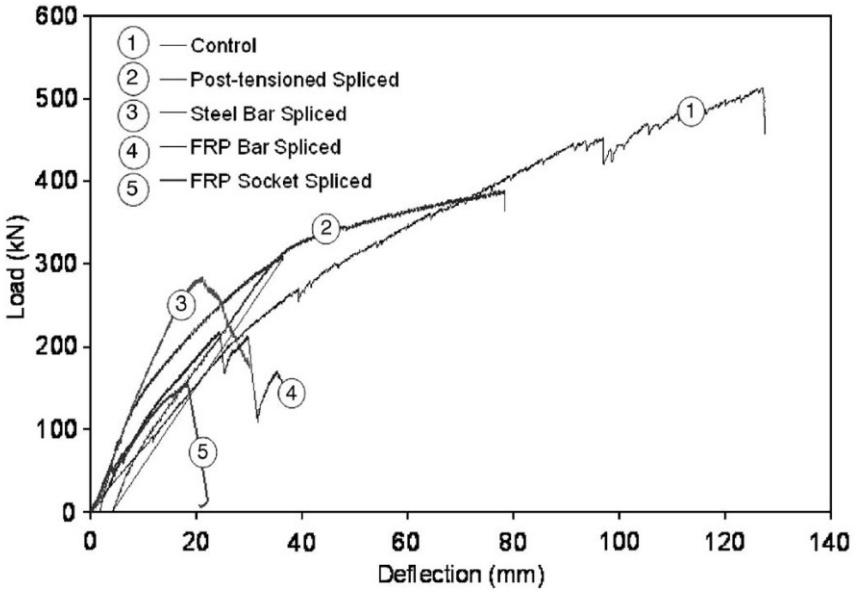

Figure 2.22: Comparison of load-deflection responses of CFFT beams (Zhu 2004)

Lai (Lai 2010) tested two types of moment connections between an unreinforced CFFT and a reinforced concrete footing. The first type was direct embedment of the precast CFFT into the footing as shown in Figure 2.23. The second type was the tube was adhesively bonded to a steel-reinforced concrete stub and was protruded from the top of the footing as shown in Figure 2.24. The aim of the research was determination of the minimum required embedded length and minimum required stub height to achieve the strength of the CFFT members. Five cantilever samples were tested with the first type of connection as shown if Figure 2.25. The Results showed that the optimal embedment length of the CFFT into RC footing is 0.73 times the diameter of the CFFT. Pseudo-ductility was observed in flexure for the CFFT embedded into the RC footings with at least the optimal length. Radial cracks in the footings were observed in all specimens. These cracks were fine in the specimens with embedment lengths equal to or greater than the optimal length as shown in Figure 2.26. Figure 2.27 shows the effect of embedment length into footing on ultimate load capacity of CFFT. In the second type of connections, eight cantilever specimens were tested. A short reinforced concrete stub was cast as part of the footing. Four samples tested with varying stub lengths, two with different steel reinforcement ratios in the stub, and two were tested in low-cycle fatigue. The Results showed that the optimal RC stub height is about 1.1 times the diameter of the CFFT and the minimum longitudinal steel

reinforcement ratio of 3.4% was required in the RC stub to achieve the flexural strength of the CFFT. Figure 2.28 shows the failure of the CFFT beams which, depending on the RC stub height. The responses of specimens with different RC stub lengths with load-deflection; load-slip plus crack opening; and load-longitudinal strain at stub end were showed in Figure 2.29.

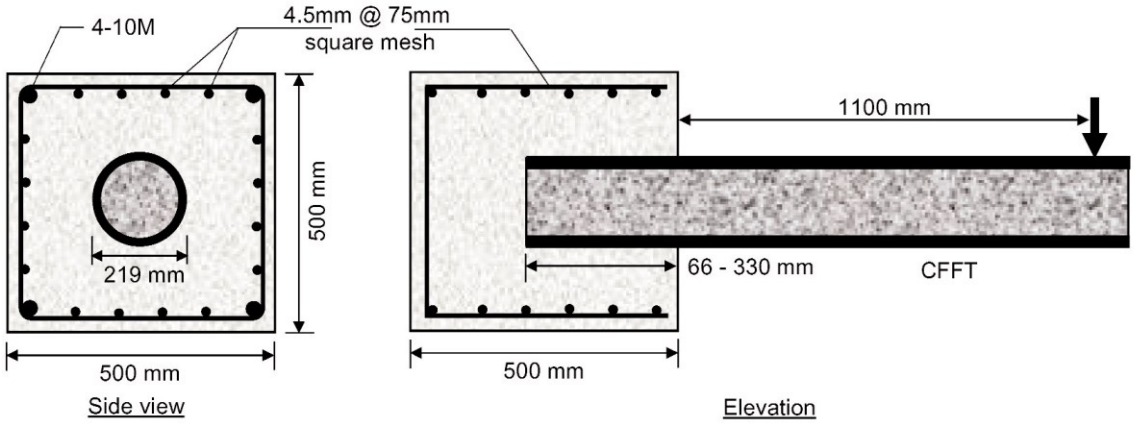

Figure 2.23: First connection type: direct embedment of the precast CFFT into the footing (Nelson et al. 2008a).

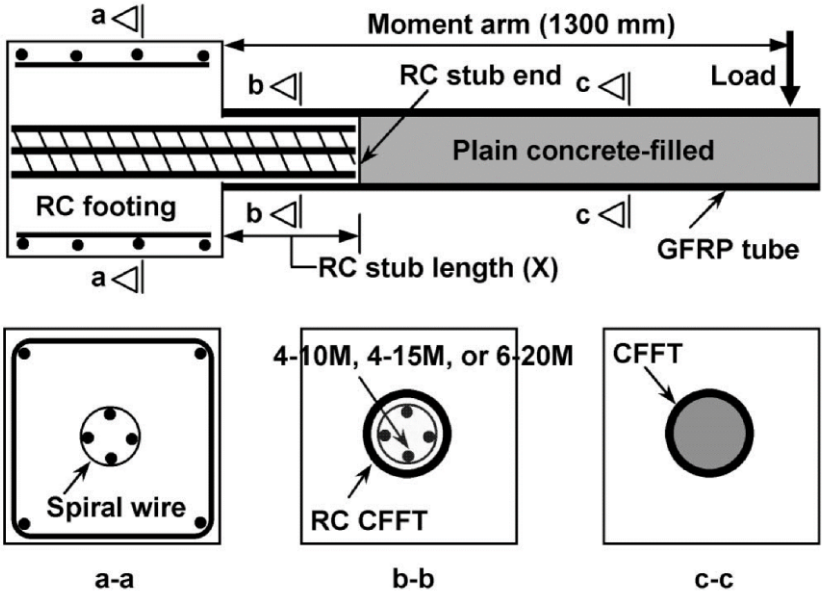

Figure 2.24: Second connection type: direct embedment of the precast CFFT into the footing (Sadeghian et al. 2011).

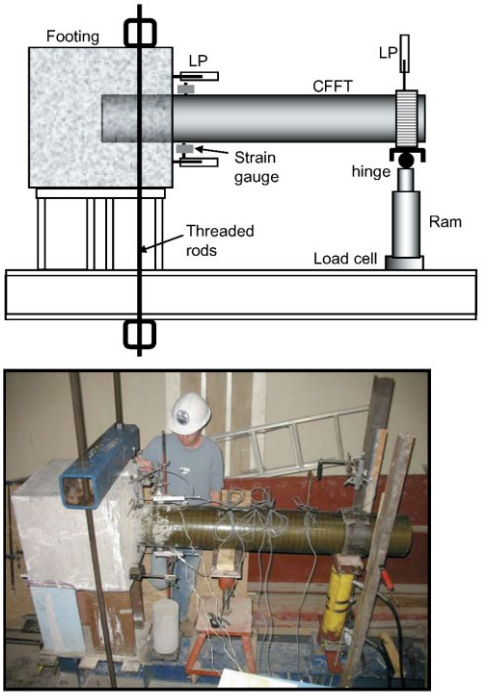

Figure 2.25: Test Setup for the direct embedment precast CFFT into the footing (Nelson et al. 2008a).

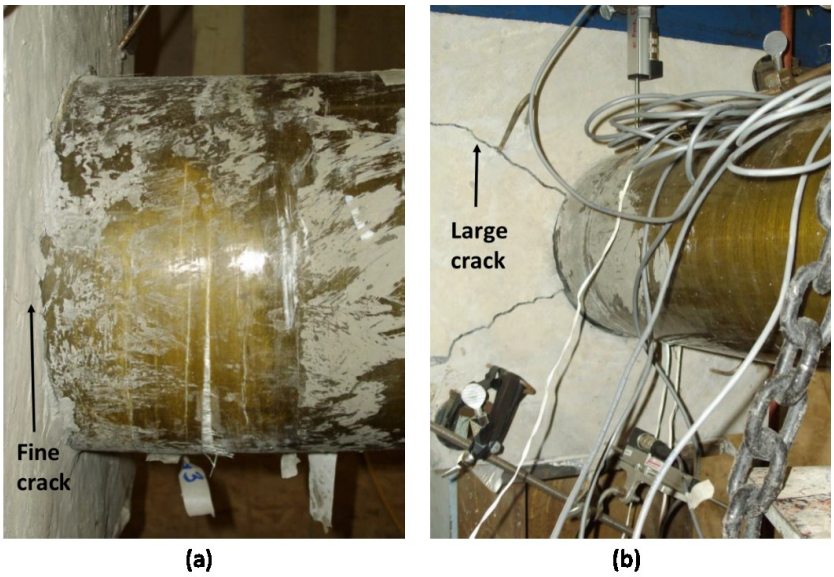

Figure 2.26: Failure mode: (a) fine cracks in the specimens with embedment lengths equal to or greater than the optimal length (CFFT tension failure), (b) excessive slip/bond failure in the specimens with embedment lengths smaller than the optimal length. (Lai 2010).

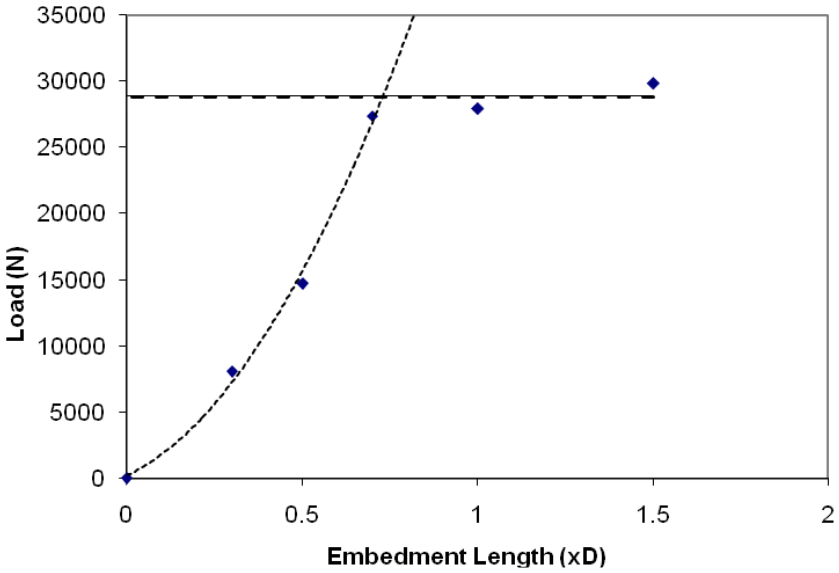

Figure 2.27: Effect of embedment length into footing on ultimate load capacity of CFFT (Lai 2010).

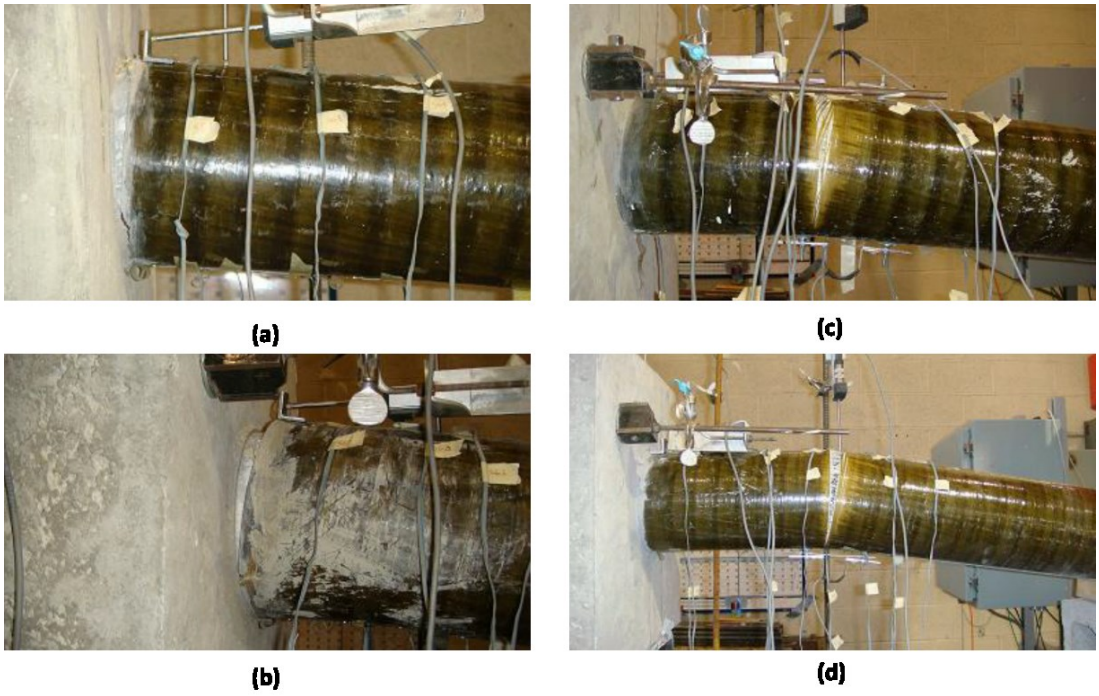

Figure 2.28: Failure modes: (a) Bond failure of specimen 0.5D, (b) bond failure and hoop fracture of tube in specimen 1.0D, (c, and d) tensile rupture failure of tube in specimens 1.5D and 2.0D respectively. (Lai 2010).

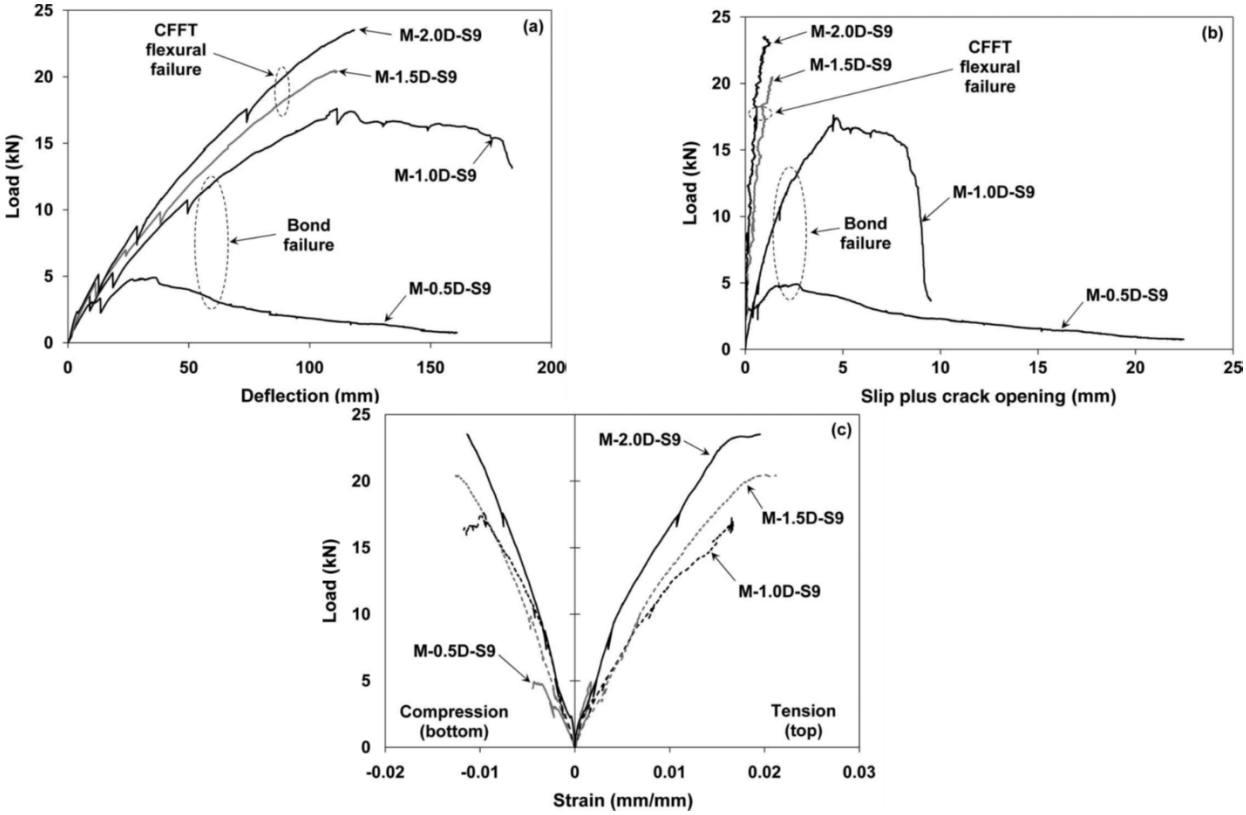

Figure 2.29: Responses of specimens with different RC stub lengths: (a) load-deflection; (b) load-slip plus crack opening; (c) load-longitudinal strain at stub end (Sadeghian et al. 2011).

Sadeghian (Sadeghian and Fam 2010, 2011) produced an analytical model and parametric study on the CFFT footing connections by direct embedment based on Lai (Lai 2010) results. This model takes into account several factors as tube lamination structure, moment, axial loads, concrete strength, interfacial shear (bond) between the tube and concrete, tube thickness, and tube diameter. This model presented the minimum embedded length for the FRP tube into the reinforced concrete footing to achieve the full fixation between the CFFT and the footing. The parametric study showed that the minimum required embedment length decreases with increasing the tube diameter, interfacial shear (bond), and the concrete strength. Presence of axial compression load decreases the minimum required embedded length, also presence of axial tension load increases the minimum required embedment length. All the factors that affect the flexural capacity of the CFFT affect also

the embedment length because the applied moment is one of the main parameters that affect the embedment length, increasing the moment lead to increasing the embedded length.

Helmi (Helmi et al. 2005) investigated the CFFTs splicing by testing four piles of 357mm diameter and 13.7m length driven and then extracted to examine for any damage. The extracted piles were then tested in bending. The splice consisted of two steel plates with threaded rods connecting the two plates as shown in Figure 2.30. Each plate had four small T shaped grooves around the outside, which were matched and then connected with an I-shaped key. This connection was 7% stronger than the un-spliced tubes when tested, which can be partially attributed to the presence of the rebar used to connect the plates.

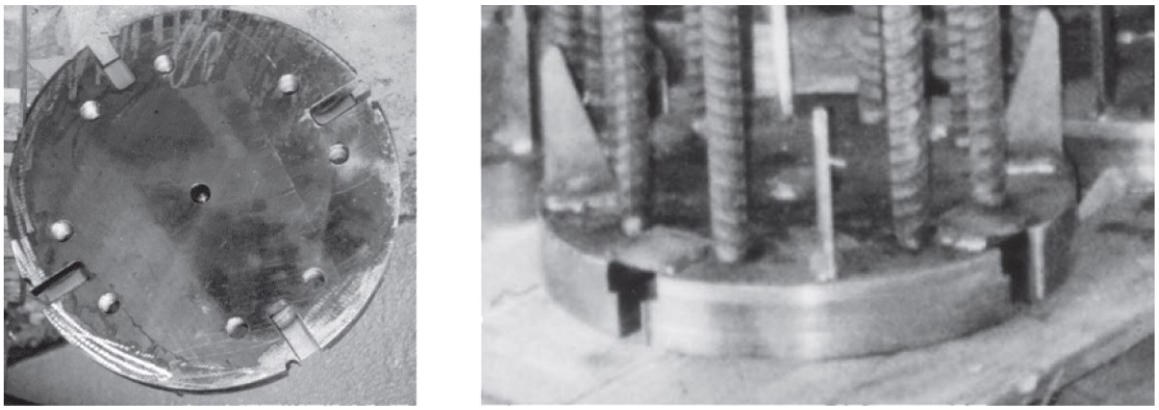

Figure 2.30: Splice details (Helmi et al. 2005).

Zakaib (Zakaib and Fam 2012) tested a moment connection through five cantilever tests. The connections consisted of steel base plates welded to steel sections embedded into the CFFT members at various length (Ls)-to-span-length (L) ratios ranging from 0.1 to 1.0 as shown in Figure 2.31. The results showed that the minimum embedment length of the steel section, measured from the base plate, and required the CFFT member to reach its flexural strength, was 17% of the CFFT span. Failure in this case occurs at the free end of the steel section. Shorter embedment results in premature bond failure of the steel section. The minimum embedment length required to reach the full plastic capacity of the moment connection at the fixed end is 48% of the CFFT span. The failure mode was depending on the embedment length of the steel I-beam section into the CFFT cantilevers as shown in Figure 2.32. Figure 2.33 shows the load-deflection curves for the tested cantilevers. This connection was successfully modeled analytically as shown. The model was established to

predict the ultimate moment capacity of the CFFT-encased steel section based on the moment connection, the failure envelope illustrated in Figure 2.34, for the full range of (Ls/L) ratios. The failure envelope can be characterized by three distinct regions, namely, a bond failure region at the connection at small (Ls/L) ratios, a CFFT flexural failure at the end of steel section, for moderate (Ls/L) ratios, and a plastic hinge flexural capacity at the fixed end for large (Ls//L) ratios. Figure 2.35 shows the failure envelope based on different failure modes according to steel section length.

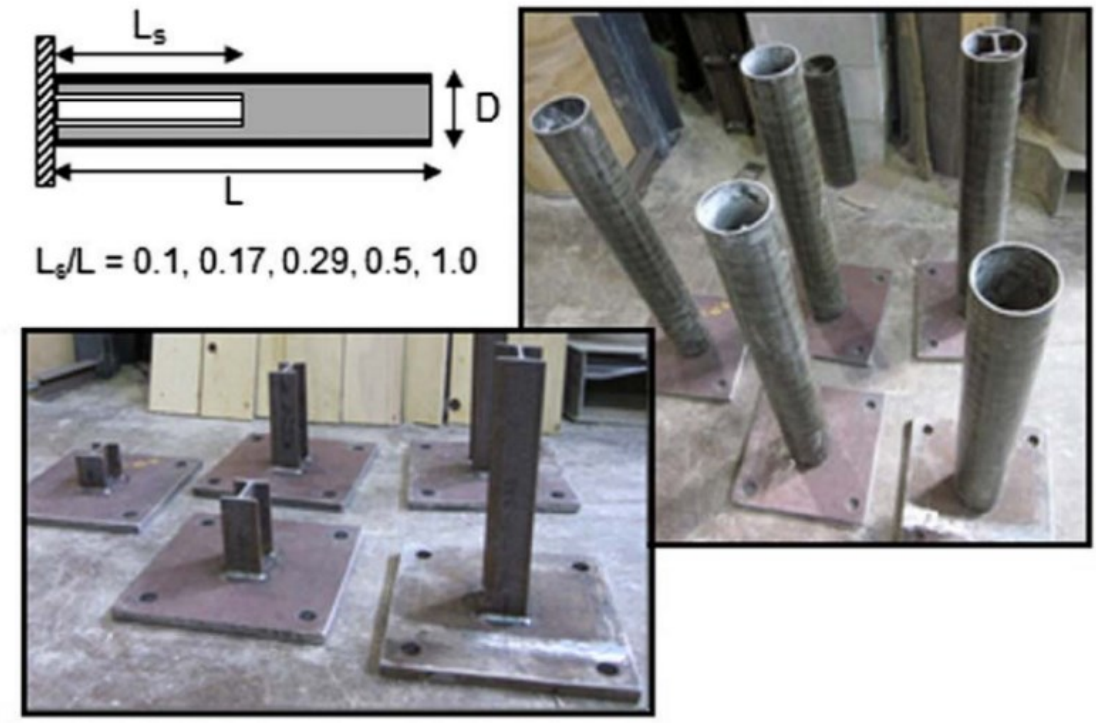

Figure 2.31: Test specimens (Zakaib and Fam 2012).

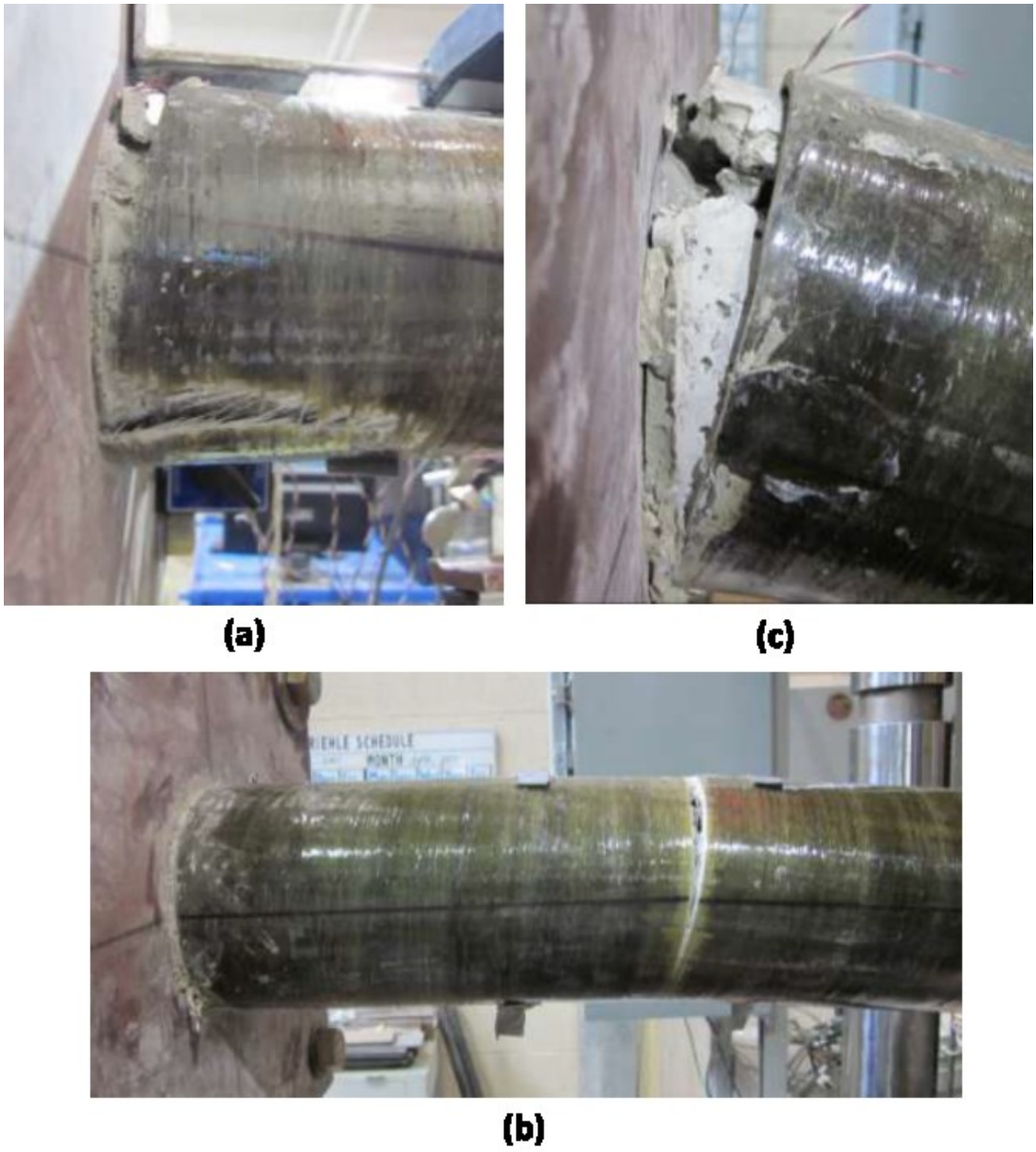

Figure 2.32: Failure Modes: (a) Tension slip and compression GFRP tube splitting in CS1 and CS2, (b) CFFT tension failure at end of steel section in CS3, (c) Excessive yielding of the steel in CS4 and CS5 (Zakaib and Fam 2012).

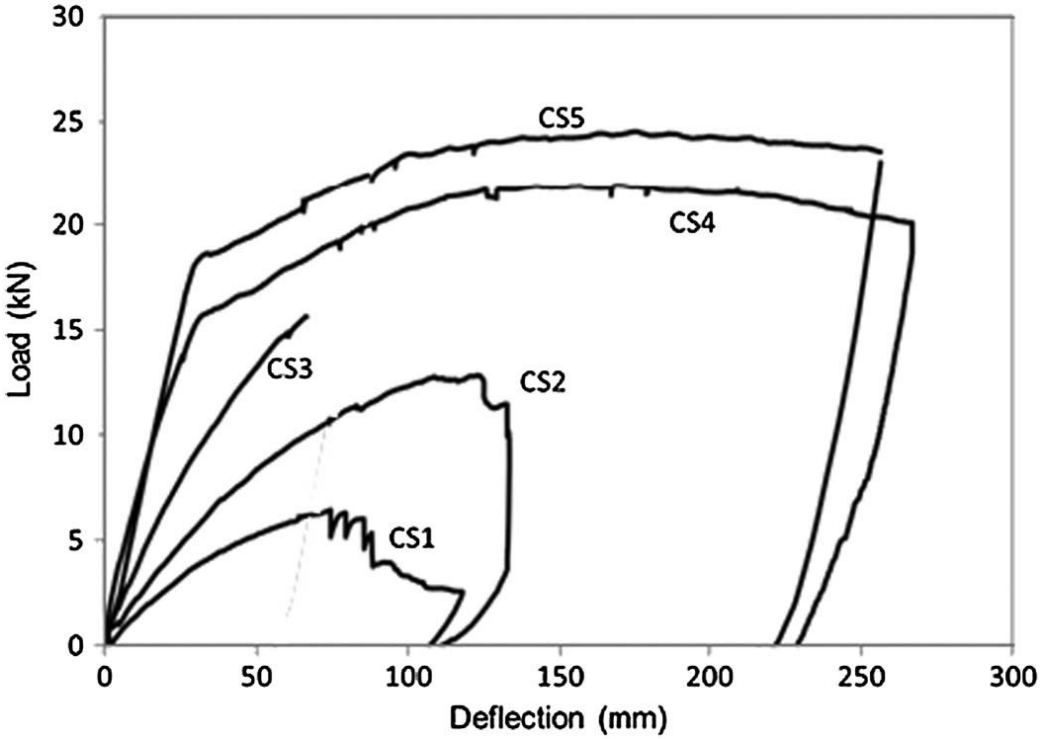

Figure 2.33: Load-deflection responses of cantilever specimens (Zakaib and Fam 2012).

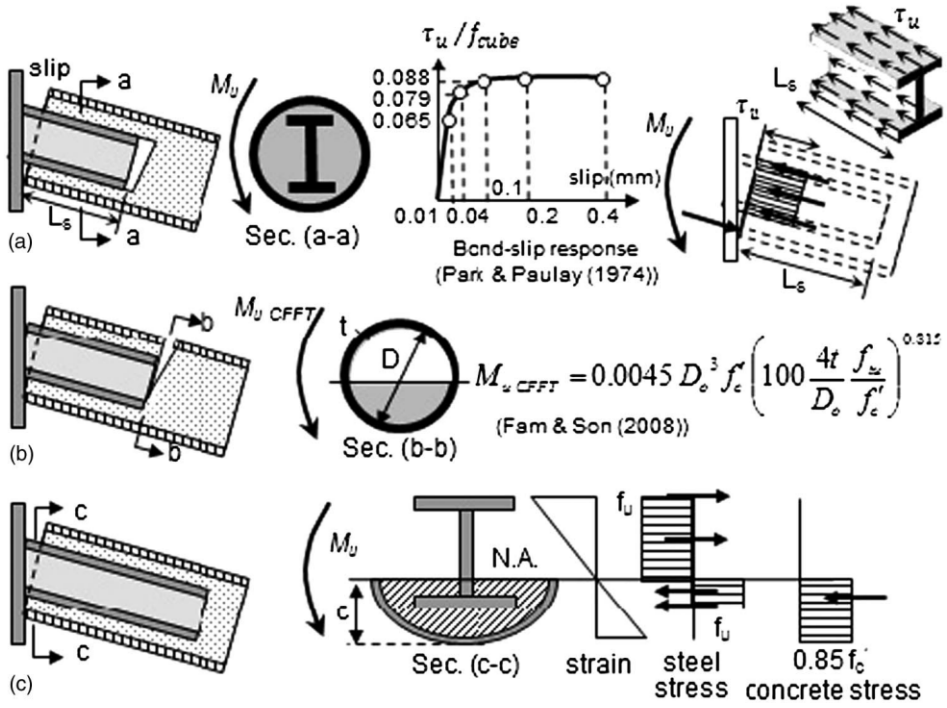

Figure 2.34: Summary of the analytical model: (a) slip of steel section; (b) flexural failure of CFFT at the end of steel section; (c) plastic hinge development at fixed end (Zakaib and Fam 2012).

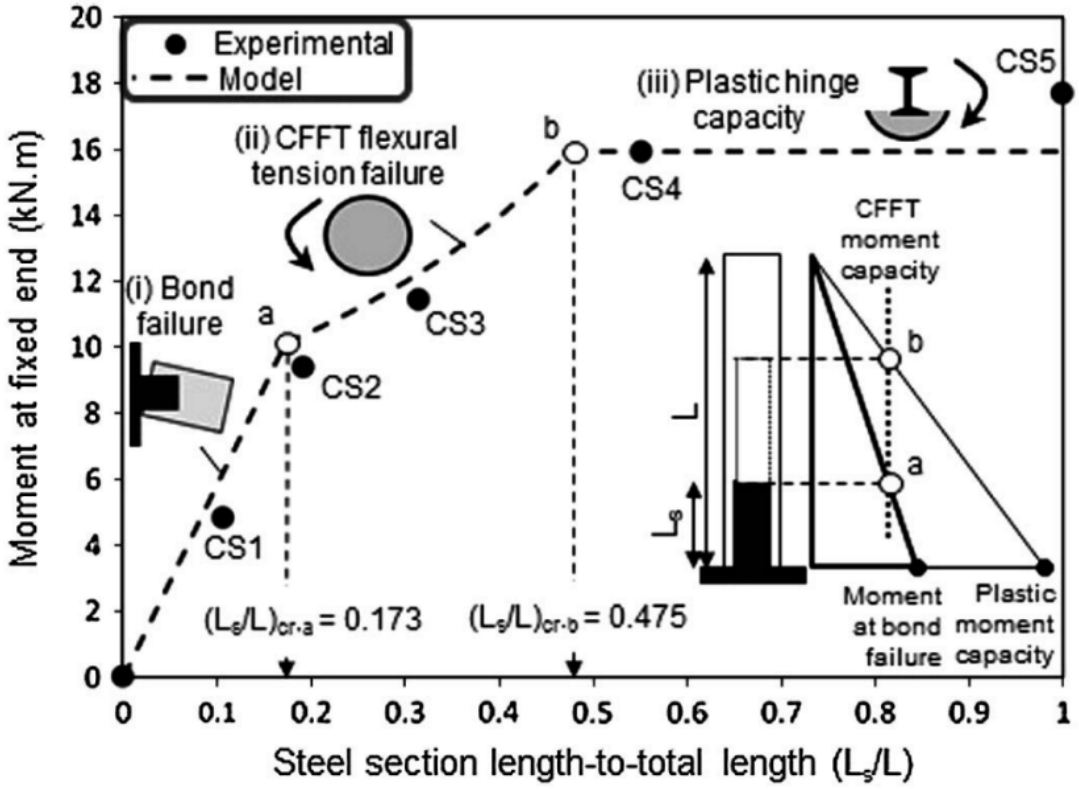

Figure 2.35: failure envelope based on different failure modes according to steel length compared to experimental results (Zakaib and Fam 2012).

Youm (Youm et al. 2013) tested circular segmental modular CFFT columns and cast-in-place CFFT columns under quasi-static cyclic loading. The CFFT segments were manufactured with holes for the longitudinal steel bars transmitted from the reinforced concrete footing as shown in figure 2.36. |Mortar was used to fill the holes after the steel bars had been inserted. All columns were designed to have the same aspect ratio. The columns had 300(s), 600(M), 1000(L) mm diameter where S, M, L used to define the column and 2.5, 3, 4 mm tube thickness respectively. The authors named "MC" for modular CFFT columns, "CC" for the cast-in-place CFFT columns and "C" for conventional reinforced concrete columns. The longitudinal steel reinforcement ratios were 2.41%, 1.41%, and 2.33% for S, M, and L respectively. The results showed that the performance of the modular CFFT columns was comparable to the cast-in-place CFFT

column and superior to the conventional reinforced concrete column a shown in Figure 2.37. Figure 2.38 show the failure modes for the tested CFFT columns.

Figure 2.36: Description of the modular CFFT columns to show (a) formwork for the CFFT segment, (b) manufactured segment, (c) epoxy application, and (d) installation of the segment (Youm et al. 2013).

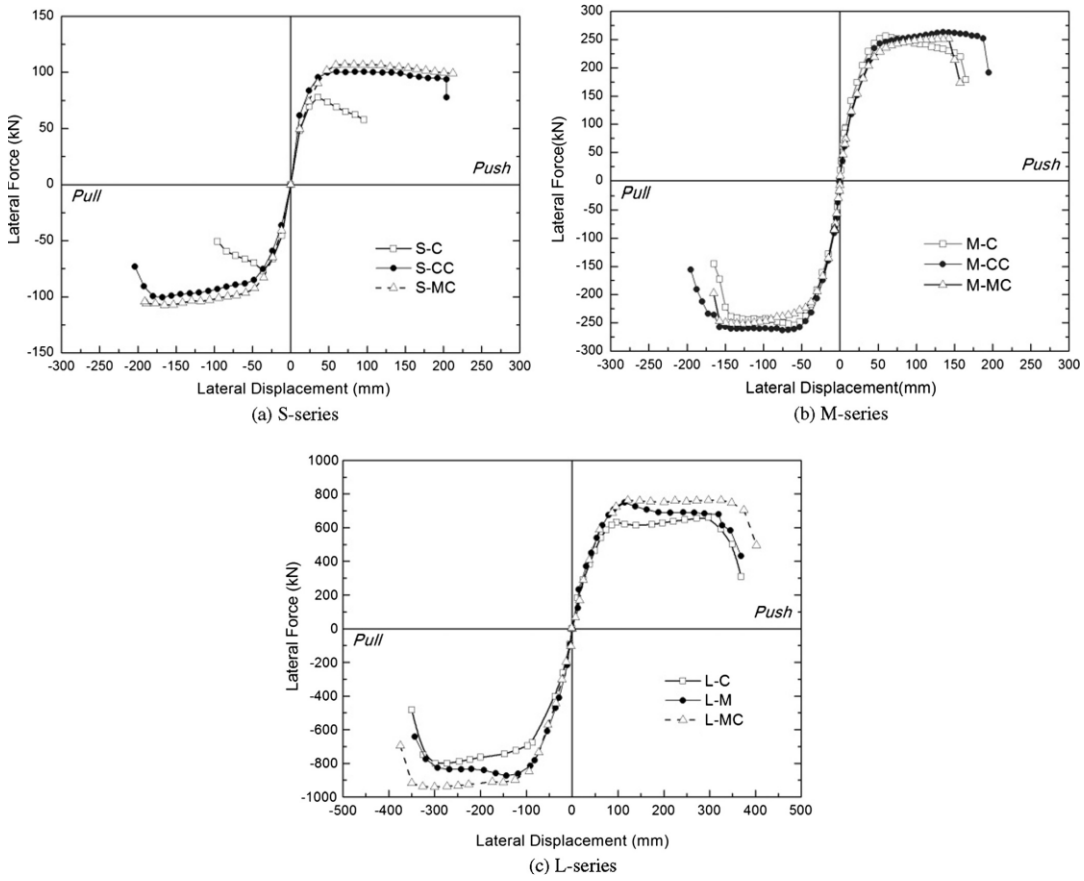

Figure 2.37: Lateral force–displacement envelope curves for the columns in: (a) S-series, (b) M-series, and (c) L-series (Youm et al. 2013).

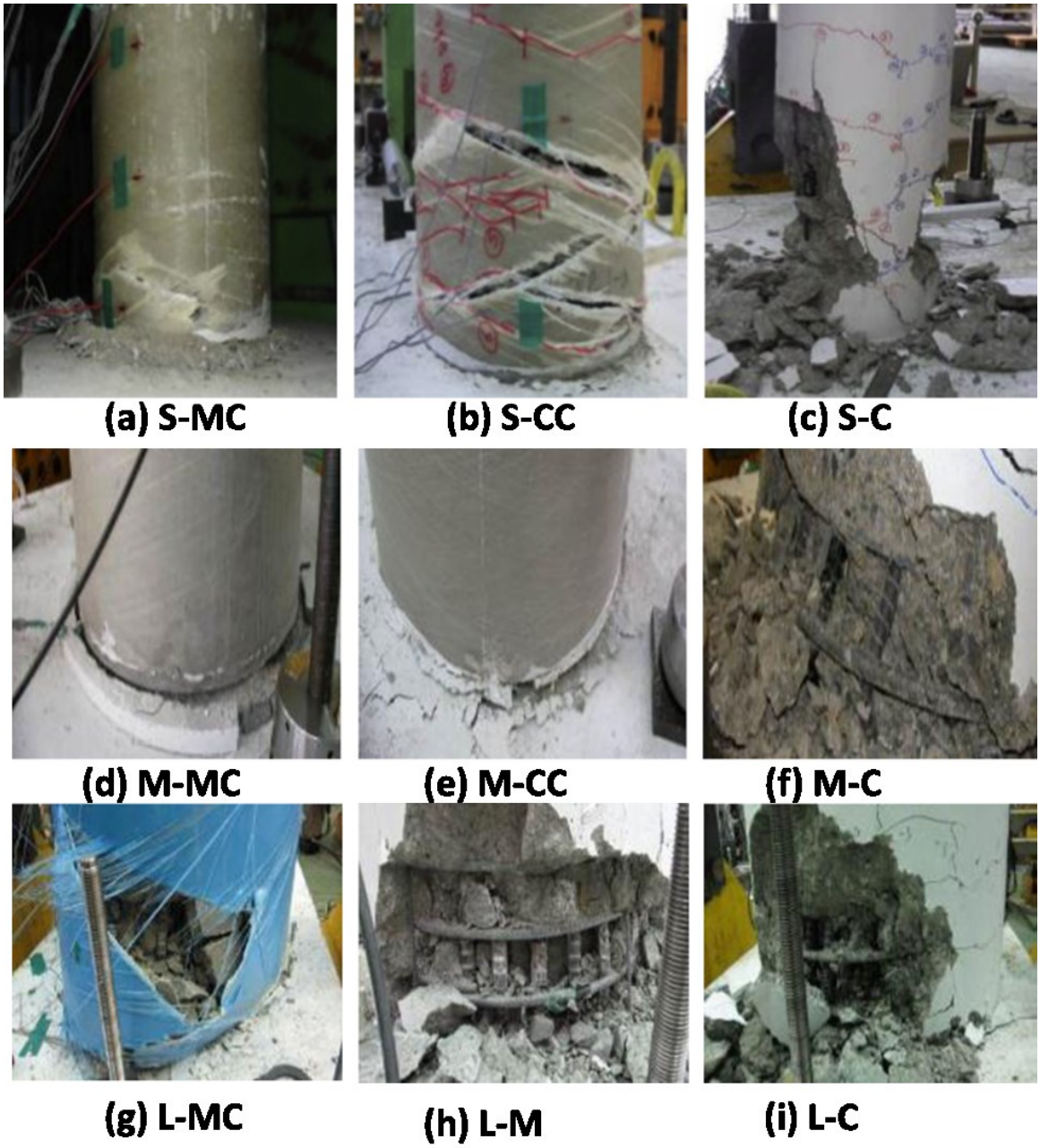

Figure 2.38: Failures at the plastic hinge zone for the columns: (a) FRP tube crack in specimen of S-MC (modular CFFT) column, (b) FRP tube diagonal cracks of S-CC (cast-in-place CFFT) column, (c) spalling of concrete cover of S-C (cast-in-place) column, (d) gap opening at the base of the column M-MC, (e) gap opening at the base in of the column M-CC, (f) buckling of longitudinal bars in the column M-C, (g) FRP tube rupture in the column L-MC, (h) longitudinal bar buckling after in the column L-M (modular RC column) and (i) the column L-C (cast-in-place RC) column (Youm et al. 2013).

3. FLEXURAL STRENGTH AND BEHAVIOR OF CIRCULAR SAND-COATED CONCRETE-FILLED FRP TUBES UNDER CYCLIC LOAD

Foreword

Authors and Affiliation

- **Ahmed M. Ali:** Ph.D. candidate in the Department of Civil Engineering at Sherbrooke University, Sherbrooke, J1K 2R1, Quebec, Canada.
  E-mail: Ahmed.Ali3@usherbrooke.ca

- **Radhouane Masmoudi:** Professor at the University of Sherbrooke, Sherbrooke, J1K 2R1, Quebec, Canada.
  E-mail: Radhouane.Masmoudi@usherbrooke.ca

Journal Title: ACI—Special Publication
Acceptance Status: Accepted for Publication.
Reference: A. M. Ali and R. Masmoudi, (2017). "Flexural strength and behavior of circular sand-coated concrete-filled FRP tubes under cyclic load", *ACI—Special Publication, SP-79*.

Journal Title: Elsevier— Journal of King Saud University - Engineering Sciences
Acceptance Status: In Press
Reference: Ali, A.M., et al. Experimental investigation of bond and tube thickness effect on the flexural behavior of concrete-filled FPR tube under lateral cyclic loading. *Journal of King Saud University – Engineering Sciences*, Elsevier, (2017).
https://doi.org/10.1016/j.jksues.2017.09.005

3.1. Synopsis

This chapter investigates experimentally the effect of sand coating bond enhancer on the flexural behavior of circular concrete-filled FRP tube (CFFT) by testing two full-scale CFFT cantilevers under lateral cyclic load. The full-bond between concrete and any kind of reinforcement is one of the main factors affecting on its flexural behavior. Limited research has investigated the bond effect on CFFT flexural behavior. The bond between the concrete core and the interior surface of the FRP tube is the main parameter of this study. Embedded-concrete strain gauges were used to measure the strain values inside the concrete core, then compared with the strain values measured from the electric strain gauges installed on the tube outer surface. The observed experimental results illustrate that the sand coating increases the flexural strength and stiffness of circular CFFT members. No slippage was observed on the sand-coated specimen; while 6 mm (0.24 in) slippage was measured on the specimen without sand coating. The internal and external strain curves are identical for the sand-coated specimen; while these curves are incompatible for the specimen without sand coating. The experimental results demonstrate the significance of investigating the bond effect and the sand coating contribution to improve the bond between the concrete core and the FRP tube, in addition to assure a good composite action under flexural loads.

Keywords: Bond, Sand coating, Flexural behavior, Fiber-Reinforced Polymer, Concrete-filled FRP tubes (CFFT), Composite action, Lateral cyclic load.

3.2. Introduction

Concrete-filled fiber-reinforced polymer tubes (CFFTs) have been used effectively in the last two decades because of its strength and ductility. Besides the confinement advantage, which provides its high strength and ductility, the tube serves as a lightweight permanent formwork, protects the concrete from the harsh environmental conditions and provides a longitudinal and lateral reinforcement. The most common structural applications for CFFT are piles, bridges girders and columns, poles, and overhead sign structures.

The main assumption of the moment design of any reinforced concrete section, according to ACI-318-14 (ACI Committee 318 2014) is that strain in concrete and nonprestressed reinforcement shall be assumed proportional to the distance from the neutral axis. It means that the strain distribution is linear over the cross-section and the bond between the concrete and the reinforcement is full-bond under service loads. In the case of CFFT, the FRP tube is surrounding the concrete not embedded inside the concrete as the steel reinforcement. Additionally, the surface of the FRP tube is smoother than the steel reinforcement, which renders the bond between the FRP tube and the concrete core becomes weaker than the bond between the steel reinforcement and concrete.

Cyclic behavior of CFFT has been investigated by (Idris and Ozbakkaloglu 2013; Ozbakkaloglu 2005; Ozbakkaloglu and Idris 2014; Ozbakkaloglu and Saatcioglu 2004, 2006; Shao and Amir Mirmiran 2005), however, limited studies investigated the effect of the bond between the tube and the concrete (Belzer et al. 2013; Mirmiran et al. 1998a). The CFFT shall be detailed, fabricated and constructed such that full composite action is achieved between the tube and concrete (AASHTO 2012). Fam (Fam and Rizkalla 2002) tested circular CFFT without internal reinforcement. They reported that, excessive slip occurred between the concrete core and the FRP tube. This slip not only has adversely affect on the composite action of the system but also reduces the stiffness of the CFFT beams, especially with thin tubes. Iftekhar (Ahmad 2004) tested short and deep CFFTs beam under flexure and fatigue loads. The author concluded that slippage is mostly the single significant factor that dominates the fatigue behavior and fatigue life of CFFT beams. Fatigue life

directly depends on the amount of slippage that occurs between the concrete core and the FRP tube. Slippage reduces the composite action in fatigue loading with a high rate if it is compared to static and quasi-static response (Ahmad 2004). Belzer (Belzer et al. 2013) investigated the degree of composite action between rectangular pultruded GFRP tube and concrete. The experimental results indicated, that using epoxy to increase the bond between the FRP tube and concrete significantly increases the flexural capacity and stiffness of CFFT. Abouzied (Abouzied and Masmoudi 2014, 2015, 2017) investigated the flexural behavior of the sand-coated rectangular CFFT beams. Authors reported that no slippage was observed between the tube and the concrete core.

3.3. Research Significance

The effect of bond performance on the flexural behavior of CFFT is very important to be investigated. It has a significant effect on the flexural capacity and stiffness of the CFFT members. This research is focused on the experimental evaluation of the effect of bond performance on the flexural behavior of CFFT under lateral cyclic load. The performance of sand coating bond enhancer on the composite action between the FRP tube and concrete is presented. This study not only provides a new experimental data that could be used to improve the flexural design of CFFT but also presents a new way to measure the strain inside the concrete core. This new way depends on using embedded-concrete strain gauges to evaluate the impact of bond on the CFFT flexural behavior.

3.4. Experimental program

3.4.1. Material properties

The tubes are manufactured using the Pultrusion process and are mainly composed of E-Glass fibers and vinyl ester and phenolic resins, according to the manufacturer datasheet. The average modulus of elasticity of the tube (E_f) is equal to 41 GPa (5.91E+06 psi) and the average flexural strength of the tube is equal to 480 MPa (69658 psi), also according to the manufacturer datasheet. The average moment capacity of the empty tube is equal to 392 kN.m (289 kip-ft). The mechanical properties of the tube are presented in Table 3.1, which

was provided by the tube manufacturer. The tubes were filled with a commercial normal weight concrete, with a target compressive strength 35 MPa (5076 psi) after 28 days. Steel bars with size M10 and M15 with a modulus of elasticity (E_s) 200 GPa (29E+06 psi) and yield stress (f_y) 460 MPa (66750 psi) were used as reinforcement in the concrete footing block.

Table 3-1: Material mechanical properties of GFRP tubes*

Average Flexural Strength	480 MPa	69,658 psi
Average Axial Compression Strength	480 MPa	69,658 psi
Average Modulus of Elasticity	40.7 GPa	5.91E+06 psi
Bending Stiffness (EI)	5.17E+11 kg.mm^2	5.17E+11 lbs.in^2
Average Moment Capacity	392 kN.m	289 kip-ft

* provided by the manufacturer

3.4.2. Test specimens

In this experimental study, two full-scale circular concrete-filled FRP tubes cantilever columns were tested under lateral cyclic load. Figure 3.1 shows the specimen shape. One of the two specimens, which is called “C12S”, had sand coating applied on the internal surface of the FRP tube. The other specimen, which is called “C12”, was fabricated without sand coating. Vinyl ester resin was used to adhere the sand particles to the internal surface of the tube. Sand coating was fabricated by applying a layer of vinyl-ester resin on the internal surface of the tube using paint-rolls. The vinyl-ester resin layer was covered with large-size sand particles, as shown in Figure 3.2. Sand coating provides more roughness to the internal surface of the tube, which leads to enhance the bond performance.

Figure 3.1: Specimen shape

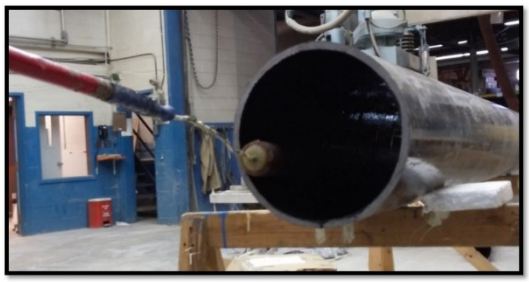

Applying the epoxy resin using paint roller

Covering the epoxy layer with coarse sand particles

Figure 3.2: Sand-coating Process

The columns were connected to rigid reinforced concrete footings. The FRP tubes had the same outer diameter and thickness 305 mm (12 in) and 12.7 mm (0.5 in) respectively. A wooden plate closed the bottom end of the tubes. That gains the column the advantage of the precast element. The embedded-strain gauges were installed in steel holders with 3.2 mm (1/8 in) diameter, as shown in Figure 3.3(a). The steel holders were fixed to the wooden plate and were inserted in the bottom end of the FRP tube, as shown in Figure 3.3(b and c). No holes were made in the FRP tube wall and the footing reinforcement was surrounding the tube.

The FRP tubes had 1930 mm (76 in) shear span as well as were embedded 500 mm (19.7 in) into the footing. The footing was reinforced with M10 and M15 steel bars. The tube was embedded into the steel cages before the concrete casting, as shown in Figure 3.3(d). The specimens had the same fiber reinforcement ratio of 16.7 %. The exterior surface of the embedded part of the two tubes was prepared with sand coating to enhance the bond between the tube and the footing. Table 3.2 presents a summary of the test specimens.

Table 3-2: Summary of the test specimens

CFFT ID	Concrete compressive strength (MPa)	FRP Reinforcement Ratio (%)	Shear span (mm)	Embedment depth into the footing (mm)	Inner surface condition	Studied Parameter
C12	35 (5076 psi)	16.7	1930 (76 in)	500 (19.7 in)	…….	Effect sand coating on the bond between concrete and the FRP tube. Effect of bond on the flexural behavior
C12S	35 (5076 psi)	16.7	1930 (76 in)	500 (19.7 in)	sand coating	

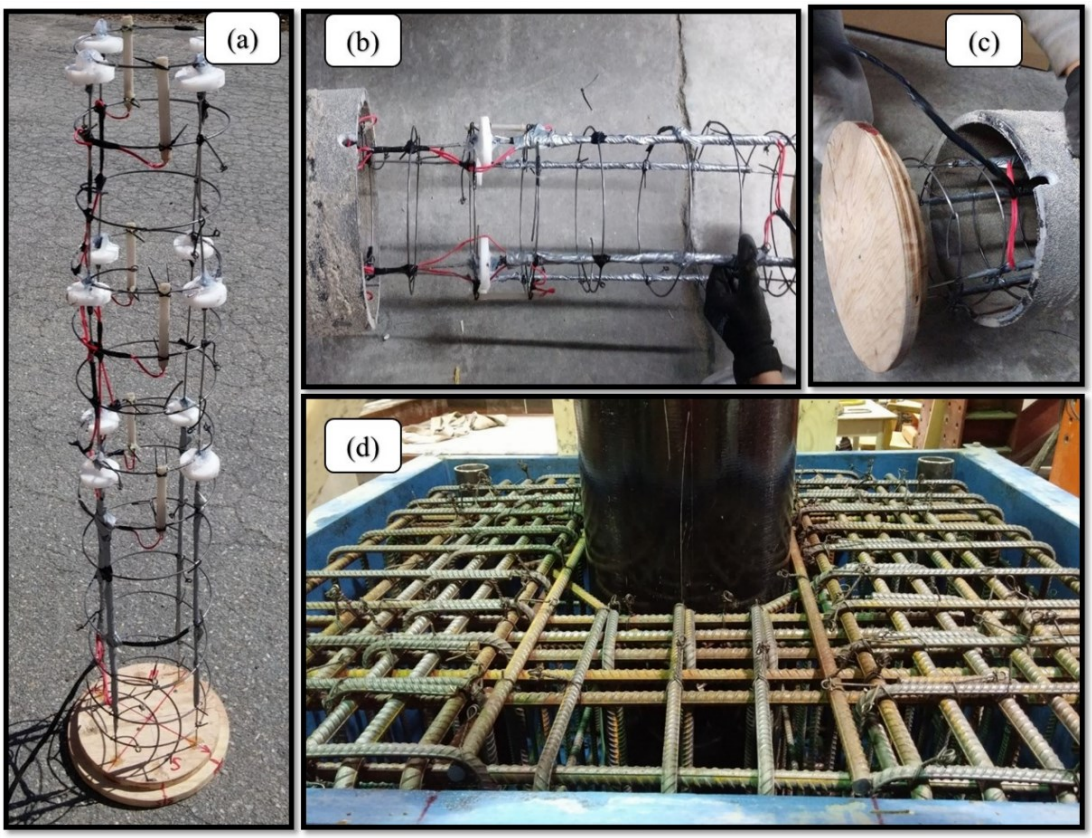

Figure 3.3: Specimen preparation, (a): Establish of the steel holder with the embedded strain gauges and wood end-plate., (b) and (c): inserting of the steel holder inside the tube and the strain gauges aligned with north and south of the specimen, and (d): Inserting of the column into the footing steel cages.

3.4.3. Test setup

The specimens were tested by using the test setup shown in Figure 3.4. Two rigid steel frames were connected together by two rectangular steel beams. These two rectangular steel beams serve as a lateral guiding system for the specimens to prevent any out of plane movement. A hydraulic actuator with 500 kN (112.4 kip) capacity was attached to the main frame and was attached to two high strength cables from the other side. Four inclined steel members were used to prevent any undesirable deflection or movement of the main frame. A steel column head was used to apply the load to the column. The steel-head was prepared with four high strength plastic cylinders, which were in direct contact with the lateral guide

beams, as shown in Figure 3.5. These four cylinders were covered with grease to minimize the friction with the lateral guide beams. The footing was bolted at its corners to the laboratory structural floor using four high strength threaded Dywidag bars. These threaded steel bars were loaded by 400 kN (89.9 kip) tension force to prevent any sliding or overturning of the footing.

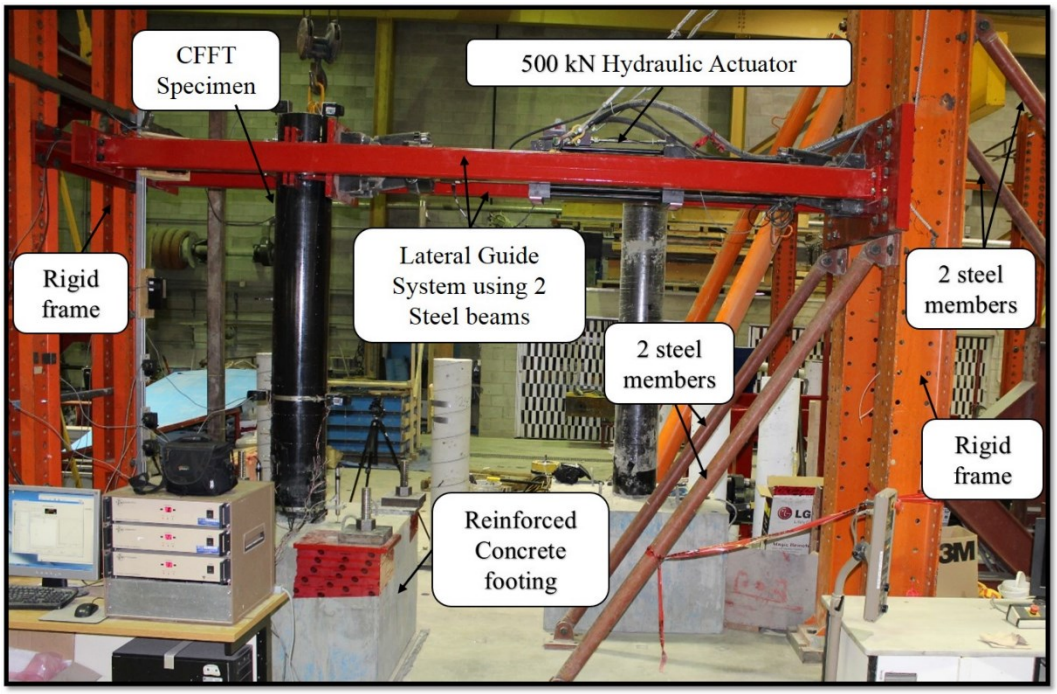

Figure 3.4: Test setup

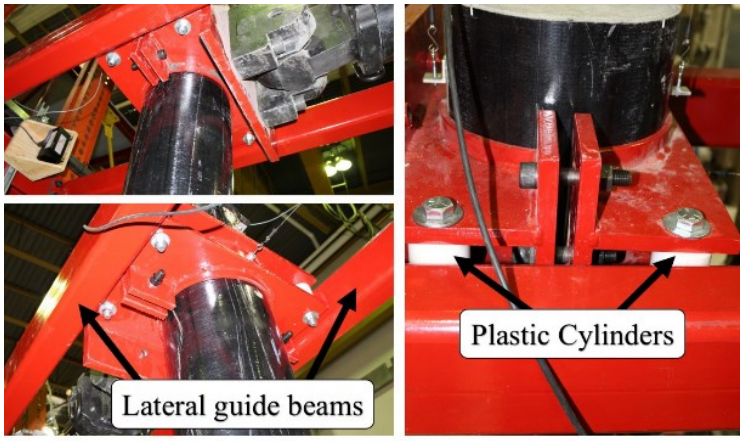

Figure 3.5: Column head details

3.4.4. Instrumentation and test procedure

3.4.4.1. Instrumentation

The instrumentation layout is shown in Figure 3.6. The lateral displacement was measured by using potentiometers at heights 120 mm (4.7 in), 350 mm (13.8 in), 500 mm (19.7 in), 800 mm (31.5 in), and 1930 mm (76 in) above the footing surface. One potentiometer was attached to the footing to measure any footing movement. Another two potentiometers were used at the top of the specimen to measure the slippage between the tube and the concrete core. Two metal rings were installed on the column at the height 100 mm (3.94 in) and 710 mm (27.95 in) above the footing level. The two rings had two potentiometers to measure the rotation at the plastic hinge zone and two LVDTs to measure the slippage between the column and the footing, as shown in Figure 3.7. Strain gauges were installed in six sections distributed in the column critical zone, sections one to six were positioned at height 50 mm (1.97 in), 152.5 mm (6 in), 305 mm (12 in), 457.5 mm (18 in), 610 mm (24 in), and 762.5 mm (30 in), respectively above the footing level. Six embedded concrete strain gauges were placed inside the column before the concrete casting at the sections 2, 4, and 6. In each section, two embedded concrete strain gauges were positioned at 30 mm (1.2 in) from the interior tube wall in the loading directions. Vertical surface electric strain gauges were placed on the tube surface at the same height and were aligned with the embedded concrete strain gauges. The embedded and electrical surface strain gauges were at the same position to be able to compare the strain measurements together. Vertical and horizontal surface electric strain gauges were installed on the tube surface at the maximum tension and compression of the six sections to measure the vertical and the hoop strains in the plastic hinge zone. The data of load and displacement from the controller, potentiometers, LVDTs, and strain gauges were recorded using three synchronized high-speed data acquisition systems.

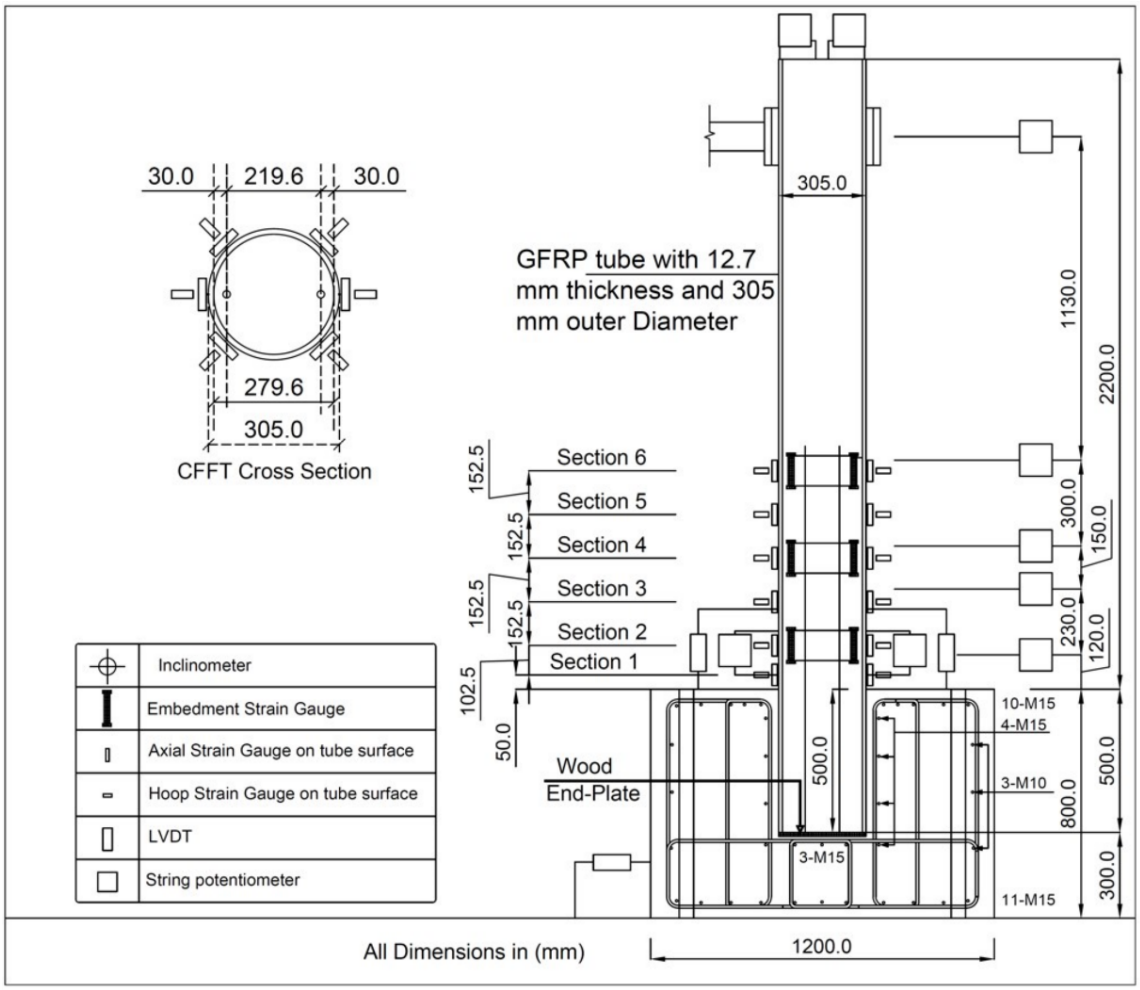

Figure 3.6: Layout of the specimen instrumentation

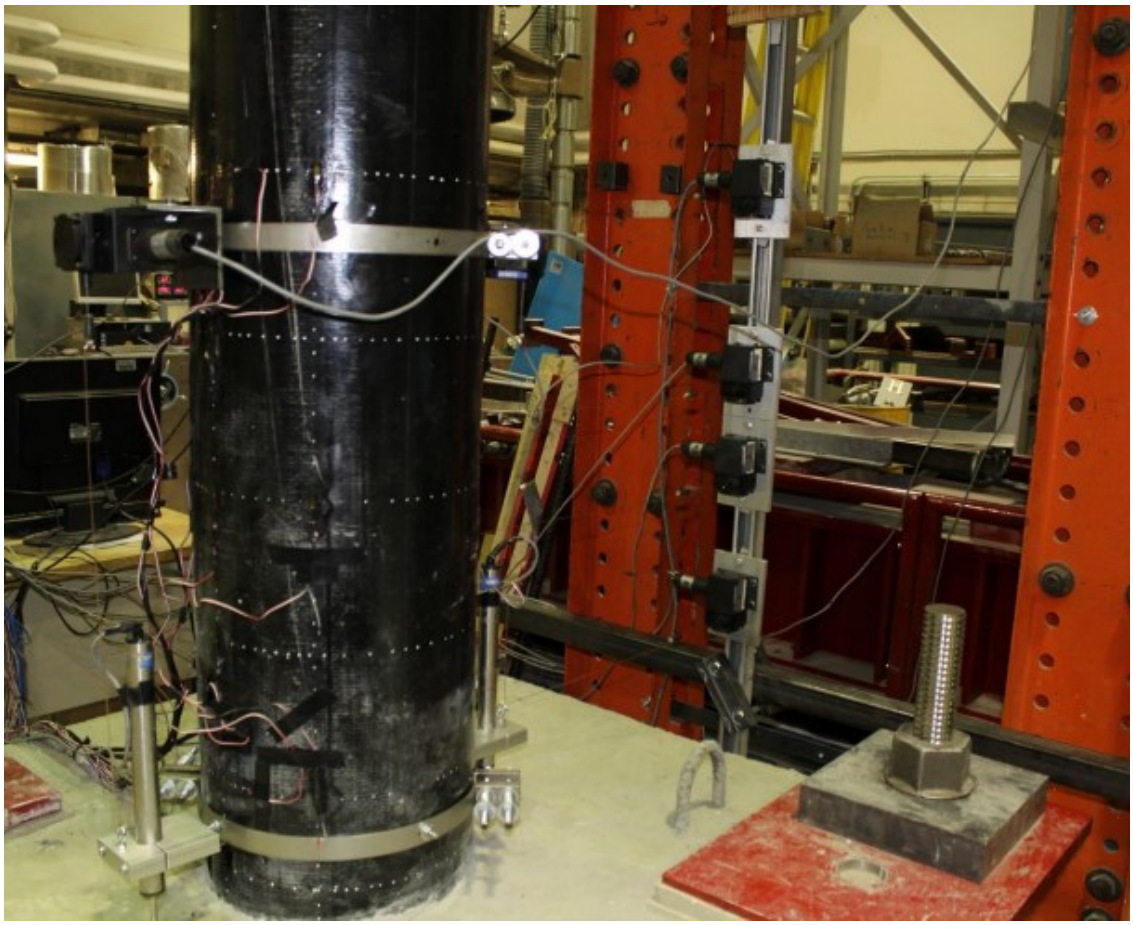

Figure 3.7: Instrumentation of the plastic hinge zone

3.4.4.2. Test procedure

A hydraulic actuator with 500 kN (112.41 kip) capacity was used to apply the lateral cyclic load on the specimens, as shown in Figure 3.4. The cyclic lateral load was applied by displacement control up to the failure of the specimen using a displacement rate of 0.4 mm/s (0.945 in/min). Two complete cycles at the same amplitude, were applied with increment 0.25% drift to reach 1% total drift. After that, the drift increment was increased up to the failure of the specimens with two complete cycles at the same amplitude. Figure 3.8 shows the loading pattern as a relationship between the drift ratio and the number of cycles.

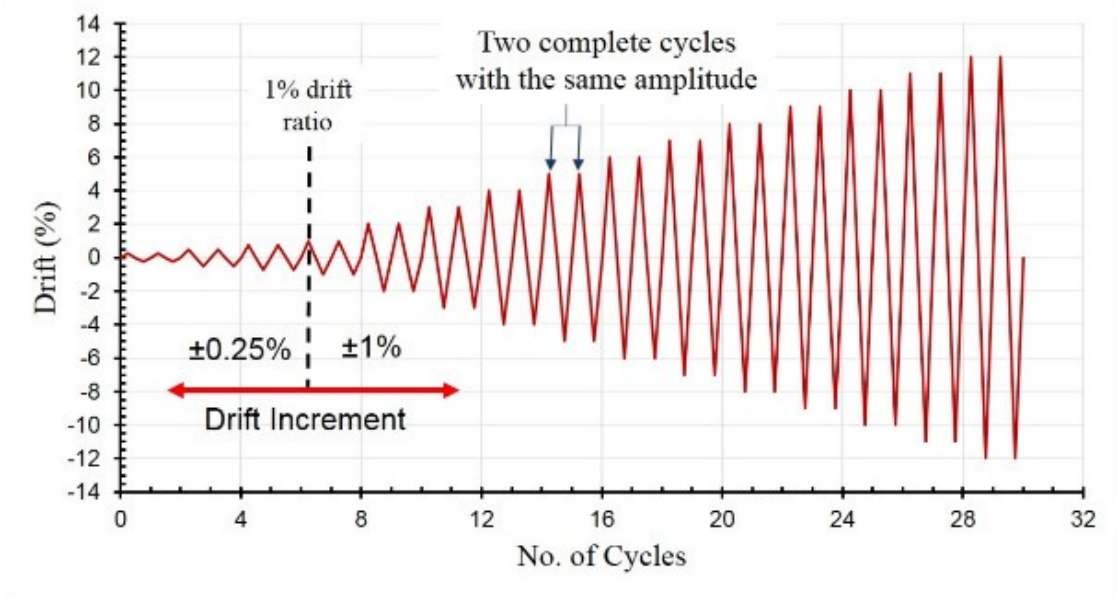

Figure 3.8: Schematic descriptions of cyclic loading regime

3.5. Experimental Results

3.5.1. Hysteretic response and failure mode

The relationships between the lateral load, the lateral top displacement, and the lateral drift ratio are shown in Figure 3.9. It is clear that the loops of the hysteretic curves are identically typical flexural loops up to the failure of the specimens. The recorded lateral load of the second run was lower than the lateral load of the first run. This was attributed to the stiffness degradation of the column due to the loading and unloading cycles. Figure 3.10 shows the deflection of the specimens before the failure. The stiffness degradation of the column C12 was eminently observed more than C12S, as shown in Figure 3.9. No failure was observed in the footings; however radial fine cracks were observed in the top surface at lateral drift ratio of 4%, as shown in Figure 3.11(a).

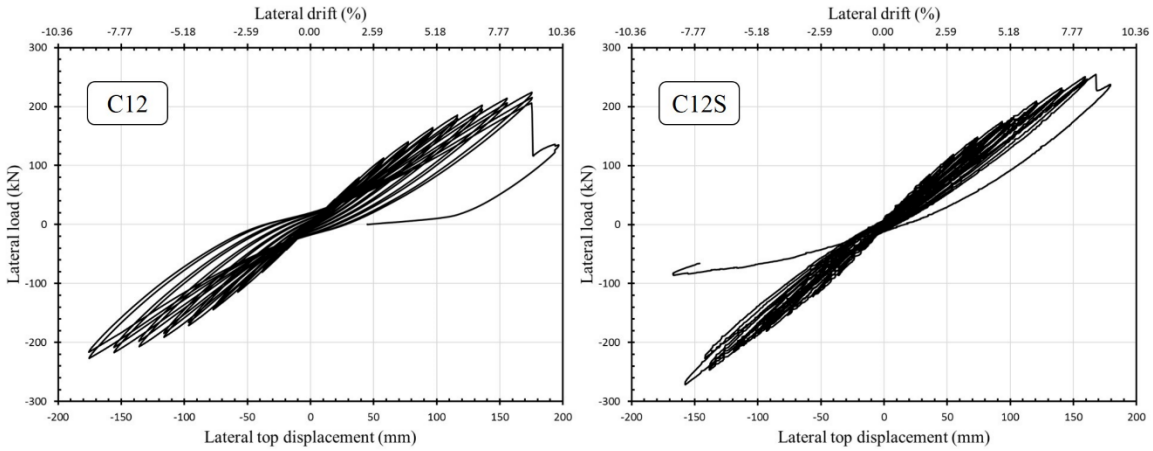

Figure 3.9: Experimental Hysteretic lateral load-lateral displacement relationship

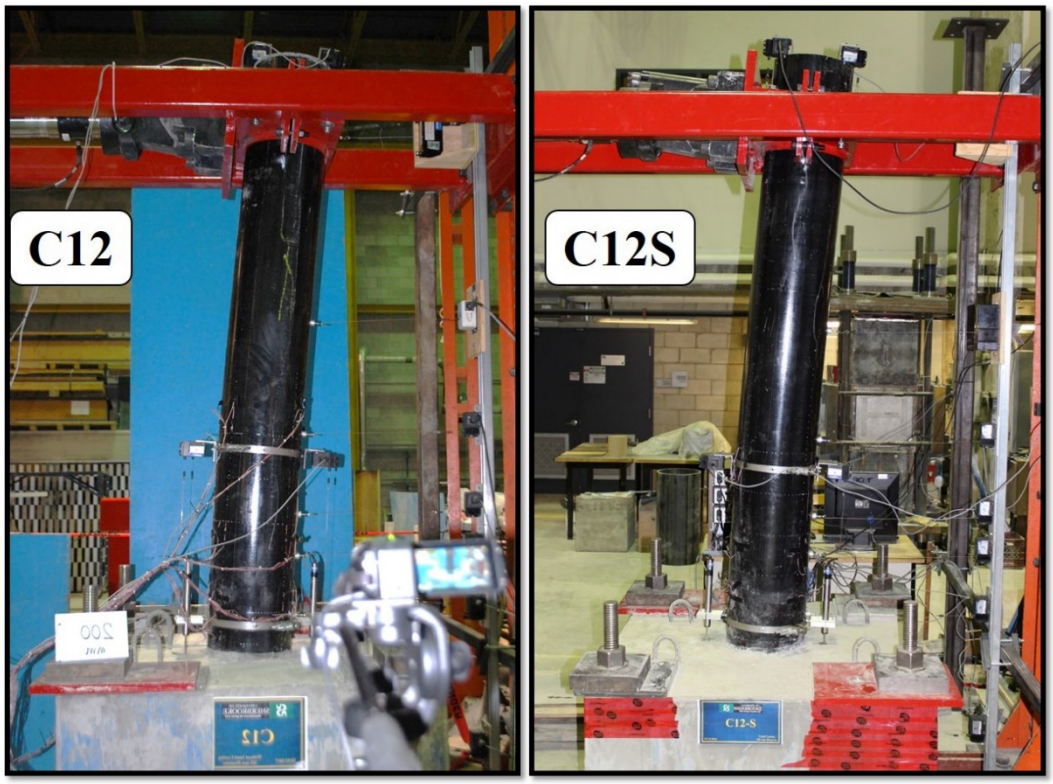

Figure 3.10: Deflection of the specimens before the failure

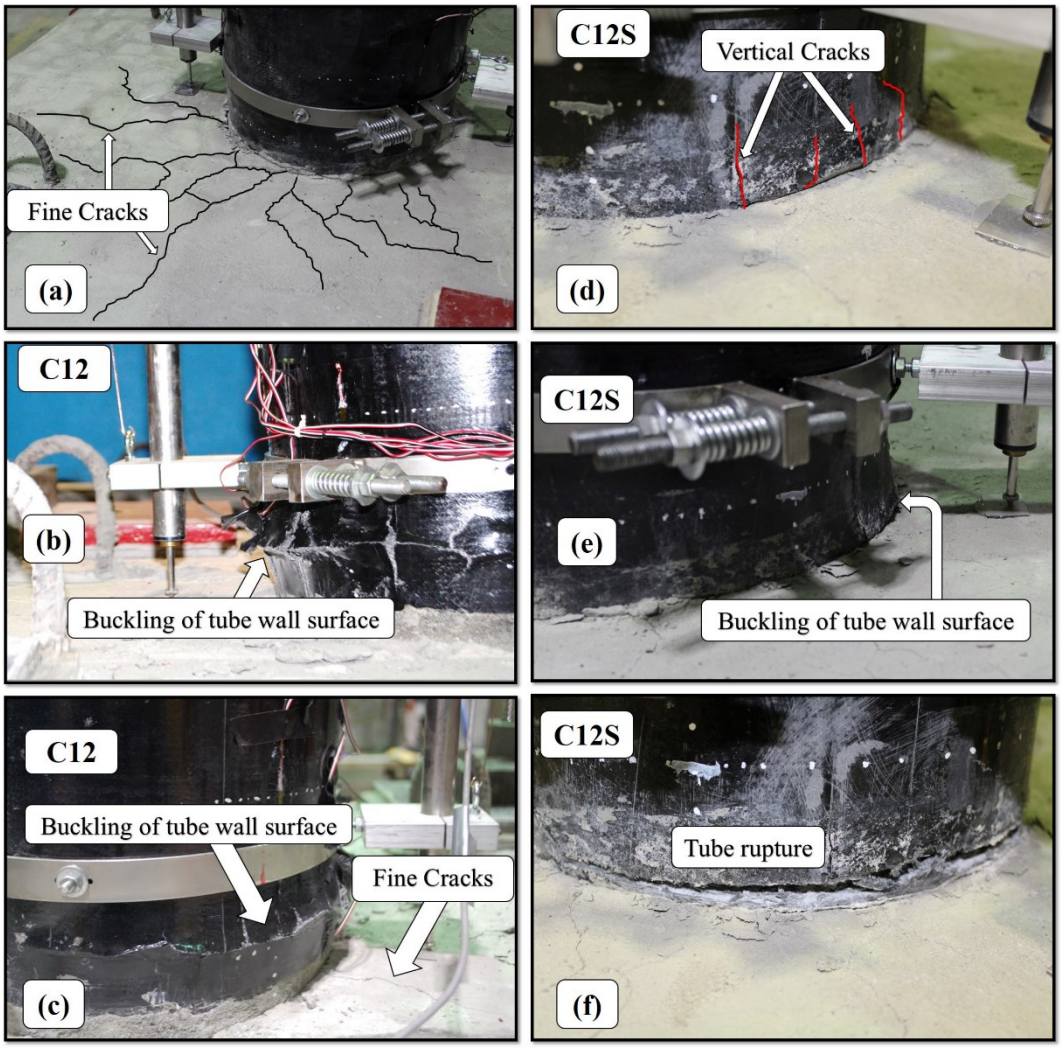

Figure 3.11: Failure mode of the specimens

The maximum recorded drift ratios reached by C12 and C12S were + 9.3 % and + 8.7 % in the pushing direction and - 9.3 % and - 8.3 % in the pulling direction, respectively. The specimen C12 failed in the first cycle of + 10.36 % programmed-drift ratio, at + 8.75 % drift ratio, although it has reached + 9.3 % in the previous cycle. This failure is attributed to the significant effect of the stiffness degradation on the flexural behavior of this specimen. The specimen C12S failed in the first cycle of + 9.3 % programmed-drift ratio amplitude, at + 8.7 % drift ratio. It was the maximum drift value achieved in the pushing direction for the specimen C12S. The summary of the test results is shown in Table 3.3. The specimens failed on the same side in compression failure mode. The failure occurred due to the local buckling

of the tube thickness on the compression side at different loading levels. The failure of the specimen C12 took place suddenly with a strong explosive sound due to the local buckling of the tube thickness at + 205 kN (46.01 kip) lateral load in the pushing direction, as shown in Figure 3.11(b) and (c). The test was completed until the lateral load reached zero, and consequently, the test was halted. The specimen C12S failed also in compression mode due to the local buckling of the tube thickness in the compression side. Unlike specimen C12, the failure did not occur suddenly, and the sound was lower than the C12. This was attributed to the composite action, which assures a more gradual failure with the contribution of the concrete deformability at ultimate crushing. The failure of C12S initiated by vertical cracks in the tube wall, as shown in Figure 3.11(d), then local buckling of the FRP tube thickness took place, as shown in Figure 3.11(e). The test was not stopped after the local buckling of the tube; furthermore, the loading direction was reversed. Complete rupture of the tube occurred due to the applied tension on the surface, which suffered from local buckling, as shown in Figure 3.11(f). The local buckling damage of C12 was significantly observed more than C12S, as shown in Figure 3.11(c) and (e). The envelopes of lateral load-deflection relationships for the specimens are shown in Figure 3.12. The stiffness degradation and the strength of the specimens can be observed well in the envelope load-displacement curve.

Table 3-3: Summary of the test results

CFFT ID	Failure			Maximum at Pushing			Maximum at Pulling		
	Δ	P	Cycle ID	Δ	P	Cycle ID	Δ	P	Cycle ID
C12	+169 mm	205 kN	1st cycle of +200mm	+180 mm	224 kN	1st cycle of +180mm	-180 mm	-227 kN	1st cycle of -180 mm
C12S	+168 mm	255 kN	1st cycle of+180 mm	+168 mm	255 kN	1st cycle of +180mm	-160 mm	-272 kN	1st cycle of -180 mm

Where, Δ = Lateral Top displacement and P = Lateral Force.

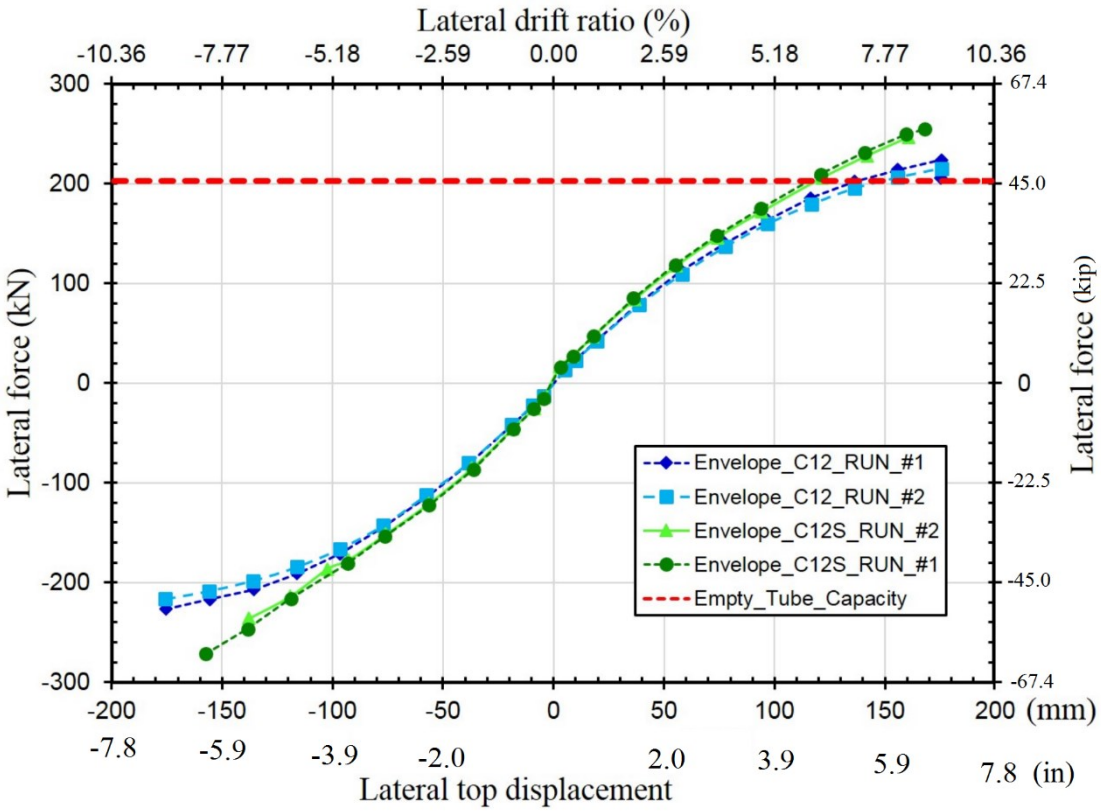

Figure 3.12: Experimental Envelope lateral load-lateral displacement relationship

3.5.2. Flexural strength

The flexural capacity of C12S was higher than C12 by 24%, as shown in Figure 3.12. It is considered as a direct result of using sand coating to improve the composite action in CFFT members. Note that the shear span, concrete properties, and the FRP tube were identical for the two specimens. The flexural capacities of C12 and the empty FRP tube were 395.65 kN.m (291.8 kip-ft) and 392 kN.m (289.1 kip-ft), respectively. That means the contribution of concrete is less than 0.1% of the flexural capacity. There was no composite action between the concrete core and the tube; consequently, the failure of C12 was associated with the tube flexural strength. Specimen C12S failed at 492 kN.m (362.9 kip-ft) with 24 % higher than C12. The contribution of concrete was 20% of the flexural capacity of C12S.

3.5.3. Initial stiffness

Figure 3.13 illustrates the deflection-lateral load relationship at the first cycle. The initial stiffness depends on the elastic modulus of the materials and the section inertia. It was determined by calculating the slope of the load-deflection curve before the cracking of the concrete. The initial stiffness of C12 and C12S were 2.55 kN/mm (14.56 kip/in) and 4.45 kN/mm (25.41 kip/in), respectively. The initial stiffness of C12S was higher than C12 by 74%. This is attributed to the separation between the concrete core and the tube in the specimen C12. Furthermore, the sand coating enhanced the bond performance of the specimen C12S.

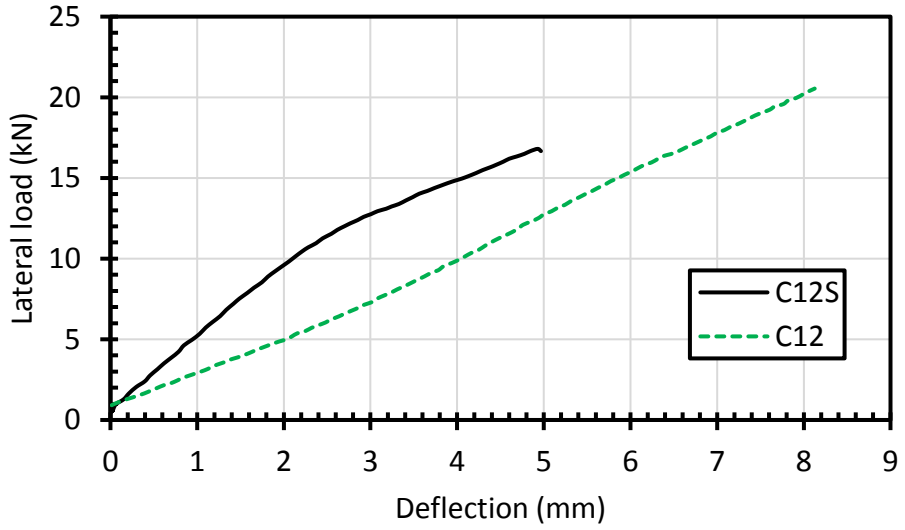

Figure 3.13: Experimental lateral load-lateral displacement relationships at the first cycle

3.5.4. CFFT measured column stiffness

The lateral deflection of any structural member consisted of bending deformation and shear deformation. In case of cantilever columns, it was found that, the value of the shear deformation was very small if it compared with the bending deformation, so that the lateral deformation of cantilever columns equal to the bending deformation and neglect the shear deformation. The cantilever column bending deformation depends on the applied load value

and structural bending stiffness of the element. According to the basics of the structure analysis, the bending stiffness of the cantilever calculated from ($K = (3EI)/(L^3) = P/\Delta$), where "K" is the cantilever stiffness, "E" is the young's modulus of the composite section, "I" is the moment of inertia of the hybrid section, "L" is the shear span of the cantilever, "P" is the applied lateral load, and "Δ" is the lateral displacement at the loading point. "I" depends on many parameters like the cracking of the section and the composite action between the tube and the concrete core. The value of "K" can be extracted from the experimental measured results of the lateral displacement as illustrated in the previous equation. Figure 3.14 shows the relation between the stiffness of the columns "pulling and pushing" and the average measured lateral displacement. The columns started approximately with the same stiffness, then the stiffness of the "C12" decreased more than "C12S" with the increasing of the lateral displacement. Sand-coating increases the stiffness of the column, which mean decreases of deformation as shown in figure 3.14.

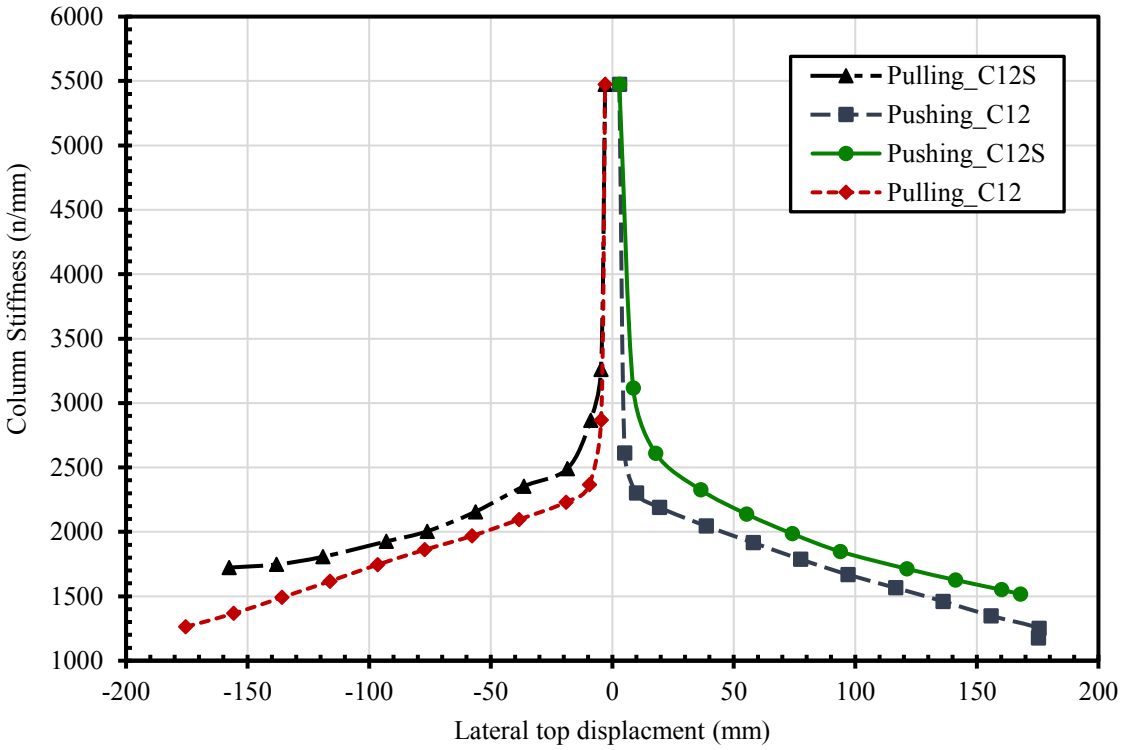

Figure 3.14: Average columns stiffness (pulling and pushing) -lateral displacement relationship

3.5.5. Strain compatibility analysis

The measurements of the embedded-concrete strain gauges and the electric surface strain gauges were illustrated in Figure 3.15 as envelope relationship between the load and the strain. The compression concrete and tube strains of the column C12 are not matched together in section 2 and 6. That means the strain distribution in the concrete core was different from that of the tube. The strains at section 4 were closed due to the excessive compression in this plastic hinge zone. Little of concrete strain responses are not complete up to ultimate failure. This is attributed to some of the out of range of some strain gauges. On the other hand, the strains of C12S are matched together in the three sections. There is a little difference appeared only on the ultimate failure stage in section 2, which is considered the maximum critical section location. This strain analysis proves the high efficiency of using sand coating as a bond enhancer in CFFT.

3.5.6. Slippage observation

CFFTs (without internal reinforcement) are carried out excessive slip may occur between the concrete core and FRP tube [11]. Slippage has adversely affect on the flexural behavior of CFFT members. Therefore, it is important to evaluate the slippage performance of sand-coated specimen. The slippage between the concrete core and the tube was measured by using two potentiometers at the top of the column. The recorded slippage value was 6 mm (0.24 in) for C12 and no slippage was recorded for C12S, as shown in Figure 3.16. This observation revealed that the sand coating prevents or reduces the slippage of the unreinforced CFFT members.

The slippage between the footing and the column was measured by using two LVDTs. The envelope slippage- deflection responses for C12 and C12S are shown in Figure 3.17. The specimens had sand coating on the outer surface, which embedded into the footing so the footing-slippage behavior has approximately the same response.

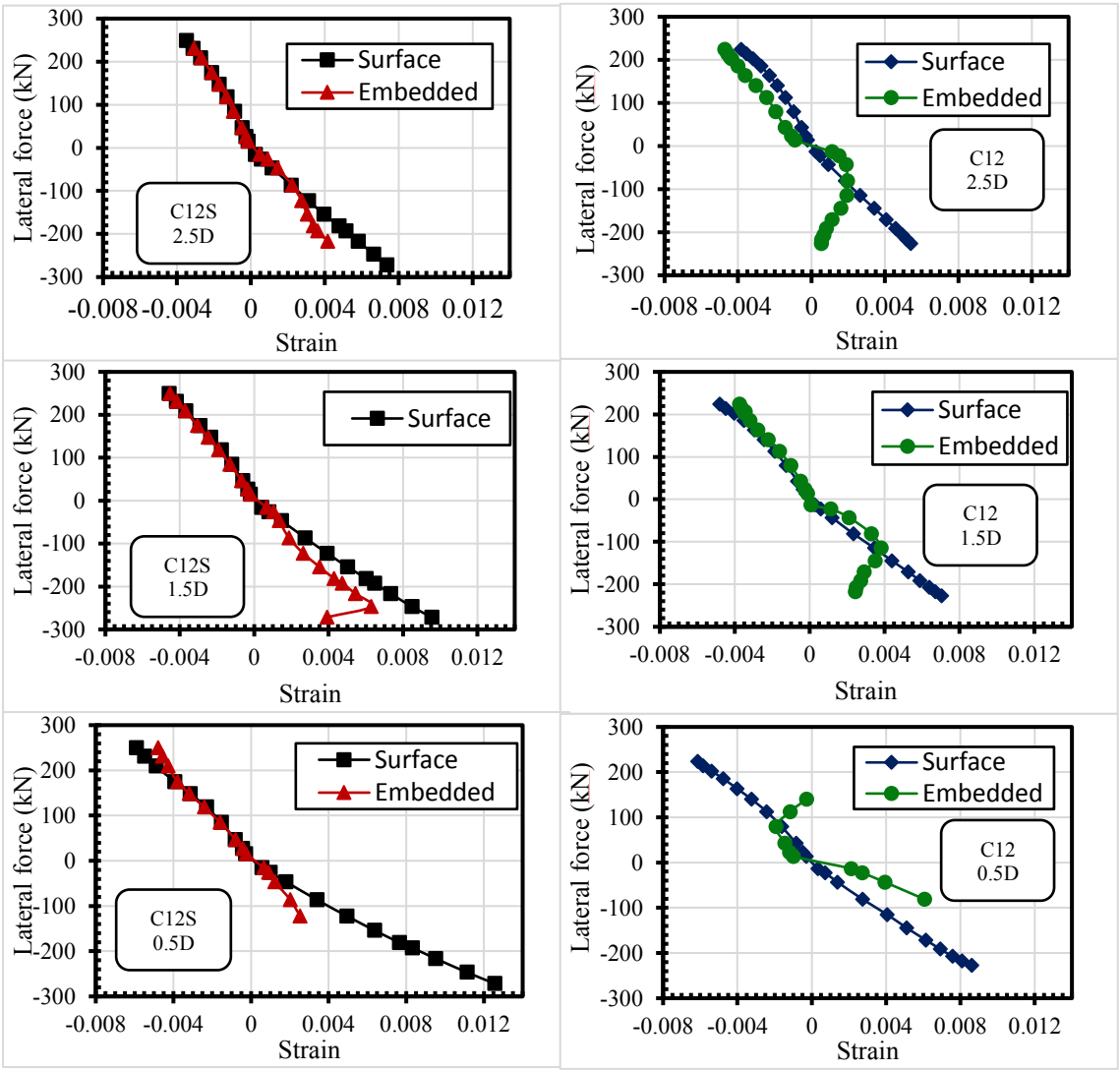

Figure 3.15: Lateral load-strain envelope curves

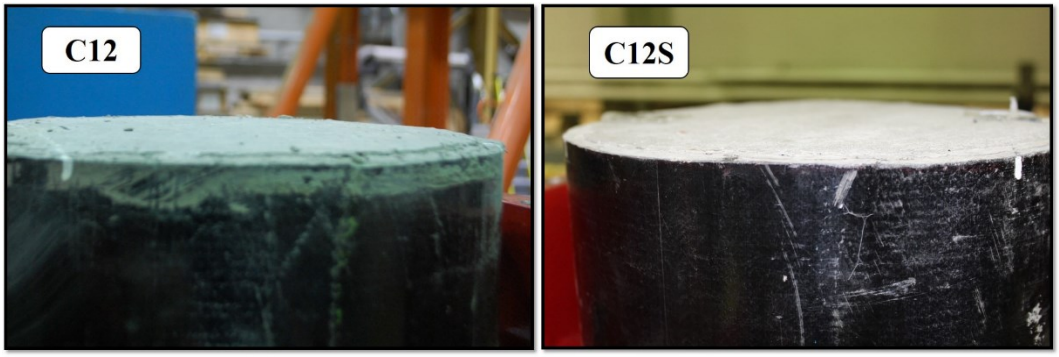

Figure 3.16: Slippage between the tube and the concrete core

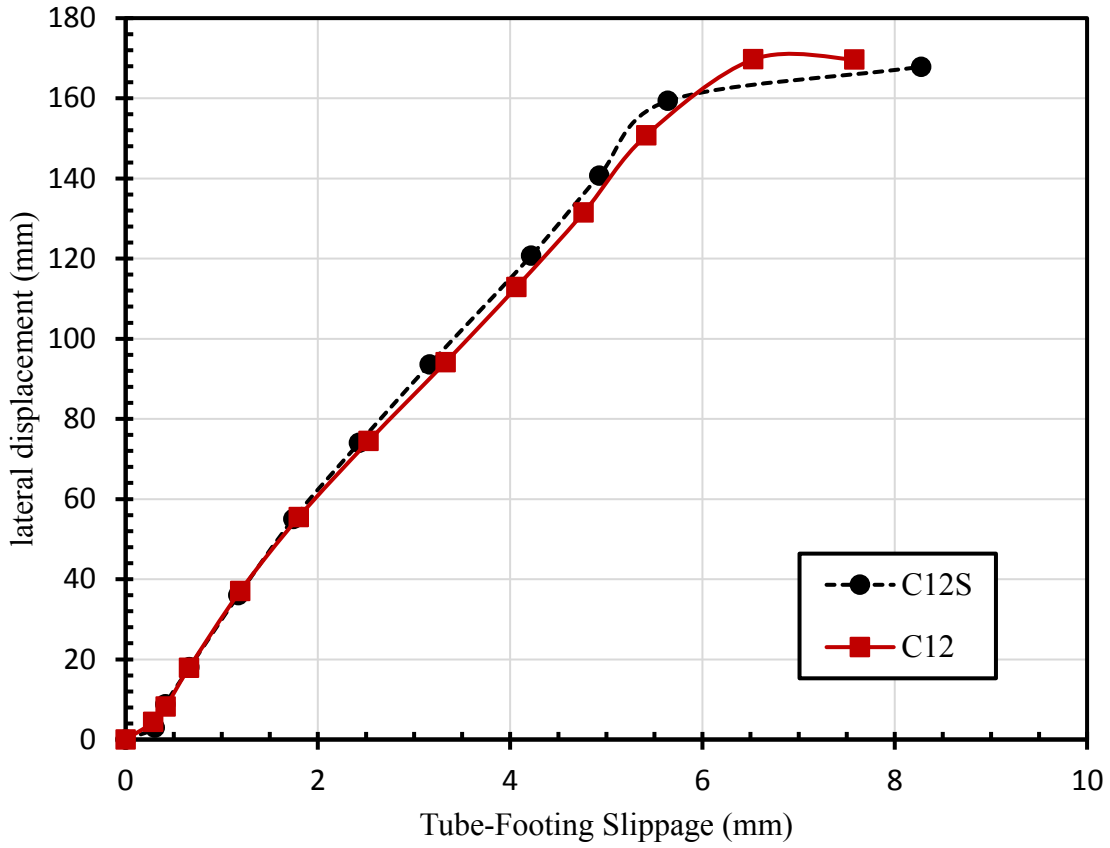

Figure 3.17: Slippage between the tube and the footing

3.5.7. Embedded depth

Sadeghian (Sadeghian and Fam 2010, 2011) presented analytical study based on the experimental work of Nelson (Nelson et al. 2008b). This study derived an analytical equation to calculate the minimum embedded length, which fulfills the flexural capacity of the CFFT member without any slippage failure. According to Sadeghian's simplified equation, which is shown in equation 3.1, the embedded length X_{cr} depends on the column diameter D, concrete compressive strength f_c', the bond between the tube and the concrete τ_{max}, and the moment capacity of the section M_{max}. The value of the τ_{max} measured by Nelson et al. [19] for the FRP tube and the concrete (τ_{max}= 0.75 MPa = 108.7 psi).

$$M_{max} = D^3 \left[\frac{f_c'}{3\pi}\left(\frac{X_{cr}}{D}\right)^2 + 0.375\pi\tau_{max}\left(\frac{X_{cr}}{D}\right)\right] \quad (3.1)$$

According to the maximum achieved moments by C12 and C12S, which were 395.65 kN.m (291.8 kip-ft) kN.m and 492 kN.m (362.9 kip.ft), the required embedment lengths are 556 mm and 624 mm, respectively. The embedded length of the specimens was only 500 mm (19.7 in), which means sand coating on the exterior surface of the embedded part of the tube decreased the required embedment length. The calculated bond strength from the equation is equal to $\tau_{max} = 3.81$ MPa (552.6 psi) based on the maximum moment $M_{max} = 492$ kN.m (362.9 kip-ft) and the real embedded length $X_{cr} = 500$ mm (19.7 in). The maximum value of the bond between concrete and any reinforcement type cannot be higher than the tensile strength of the concrete, which equals to 4.0 MPa (580 psi). Sand coating improves the bond strength to be 95% of the maximum value of the bond can be achieved between the concrete and the FRP tube.

3.6. CONCLUSIONS

The effect of the bond between the FRP tube and the concrete core on the flexural behavior of unreinforced concrete-filled FRP tubes was experimentally investigated. Two full-scale specimens were tested under lateral cyclic loading. This investigation can be summarized in the following conclusions:

- The comparison between the embedded concrete strain gauges and the tube surface strain gauges illustrated that the strain responses were inharmonious for the specimen without sand coating (C12). On the other hand, the strain responses of the sand-coated specimen (C12S) were identical. This result reveals the high efficiency of sand coating on achieving the composite action of the CFFT members.
- The failure load of C12 was approximately equal to the failure load of the empty FRP tube, which proves that the bond has a significant effect on the flexural behavior of the unreinforced CFFT members.
- Use of sand coating as a bond enhancer increases the flexural capacity and stiffness of the unreinforced circular CFFT section.

- Use of sand coating leads to decrease the effect of the stiffness degradation due to loading/unloading which was clear from the comparison between the first and the second loading cycles at the same amplitude.
- Improving the bond delays the local buckling of the FRP tube thickness, which means improving the flexural behavior.
- Sand coating improves the bond between the tube and the concrete up to 95% from the maximum bond value.
- Sand coating bond enhancer reduces the slippage between the concrete core and the FRP tube at ultimate failure.
- The required embedded length into the footing decreased by 25% because of using sand coating on the exterior surface of the tube-embedded part.
- The bond condition between the concrete and the FRP tube should be considered in the design of the unreinforced CFFT and should be involved in the flexural design equations.

4. INNOVATIVE APPROACH TO INVESTIGATE THE COMPOSITE ACTION OF FULL-SCALE CFFT COLUMNS UNDER CYCLIC LOAD

4.1. Abstract

Concrete filled fiber-reinforced polymer (FRP) tube (CFFT) elements are a praiseworthy competitor to replace the conventional reinforced concrete (RC) members in severe environmental conditions. This chapter investigates the effect of the bond between the FRP tube and its concrete core on the flexural behavior of CFFT members. Four full-scale CFFT columns associated with RC footings were tested under lateral cyclic load without axial load. Two different diameters of CFFT columns were tested to study the size effect on the bond performance then consequently on the flexural demeanor of the CFFT column. Two FRP tubes possessed sand coating on its interior skin to improve the interfacial bond between the FRP tube and the concrete core. An original approach was proposed to study the composite action between the FRP tube and the concrete core based on measuring the strains inside the concrete core by using embedded concrete strain gauges. The assessment of the composite action between the FRP tube and the concrete core was implemented by comparing the interior concrete strains and the corresponding strains on the external tube skin. The experimental results illustrated that the bond significantly influences the flexural strength and stiffness of the CFFT column. Using sand-coating as a bond enhancer improved the bond between the FRP tube and the concrete core, minimize the adverse effect of the interface gap, and increased the flexural capacity and stiffness of tested CFFT columns.

Keywords:

Fiber-reinforced polymer, Concrete-filled FRP tubes, Cyclic loading, Bond, Composite action, shrinkage gap, Sand-coating, Interface gap, Flexural behavior

4.2. Introduction

Over the past two decades, concrete-filled fiber-reinforced polymer (FRP) tube (CFFT) members were investigated extensively to understand their behavior under several loading types (Abouzied and Masmoudi 2017; Ali and Masmoudi 2017; Boumarafi et al. 2015; ElGawady and Dawood 2012; Mohamed and Masmoudi 2010d; a; Youssef and Hadi 2017). CFFT was developed as a flourishing substitute for several structural elements in the construction domain due to its high performance and durability (Abouzied and Masmoudi 2015; Ali and Masmoudi 2017; Hadi et al. 2016; Mohamed and Masmoudi 2010b). Besides its high strength, the FRP tube considers as a light-weight permanent formwork, noncorrosive longitudinal and transverse reinforcement, and confines the concrete core.

As is well known, slippage between the FRP circular tube and the concrete core adversely influences the flexural strength and stiffness (Ali et al. 2017b; a); so, developing an approach to assess and improve the bond between the tube and the concrete core is required. In addition, north-American design codes and guidelines prevent slippage in flexural-members and considered it as a fundamental demand in the flexural design assumptions.

Abouzied (Abouzied 2016) created a rough texture on the inner surface of the FRP tubes to improve the bond between the tube and the concrete core. The texture roughness technique was implemented by applying a thin layer of epoxy to the inner skin of the tubes thereafter it was covered by silica sand; that is known nowadays as sand-coating technique. The author reported that no slippage was observed on the ends of specimens with sand-coating.

Belzer (Belzer et al. 2013) investigated the degree of composite action between rectangular pultruded glass fiber-reinforced polymer (GFRP) tube and concrete. The experimental results of Belzer (Belzer et al. 2013) showed that using epoxy to bond the FRP tube to concrete significantly increases the flexural capacity and stiffness of the rectangular CFFT.

The previous researches on the composite action between the FRP tube and its concrete core established their analysis mainly on slippage measurements between the concrete core and the FRP tube at ends of the CFFT-member. Authors believe that; the degree of the bond between the FRP tube and the unreinforced-concrete core differs along the unreinforced-CFFT member span

according to the bending-moment distribution. The debonding primarily transpires in the maximum moment point. Thereafter, the debonding propagates along the element span. Researchers capture the slippage at the ends of the CFFT, this slip value is representing the cumulative slippage occurring along the CFFT span. So, the debonding may occur at the maximum moment zone only and due to the remaining bond resistance straight the CFFT span; the slip may not be observed at the end of the CFFT. Therefore, no-slip is not an authentication of full bond and cannot consider as an evidence of the full composite action between the FRP tube and its concrete core.

This research introduces a unique approach to assess the bond between the FRP tube and the concrete core by using embedded concrete strain gauges into the concrete core. The principal concept of this technique is comparing the interior concrete strains values with the electric strain gauges on the external skin of the tube. The interior and exterior strain gauges were adjusted together at the same position and height. In case of the interior concrete strain equals to the exterior strain gauge on the tube surface, it means a full composite action was accomplished. Otherwise, the tube and its concrete core are functioning individually.

This chapter aims at studying the composite action between the FRP tube and its concrete core and composite action effect on the flexural behavior of CFFT. In addition, the contribution of sand coating bond enhancer on improving the bond between the FRP tube and the concrete core is also investigated.

4.3. Experimental Program

The experimental program; that was characterized in this section; accommodates the material properties details (FRP tubes, concrete, steel reinforcement), preparation of specimens (sand coating procedure, test specimens, assembling of the specimens), test setup, instrumentation, and test procedure.

4.3.1. Material properties

4.3.1.1. FRP tubes

The FRP tubes are circular pultruded tubes. All tubes are manufactured with electrical grade E-glass reinforcements in the form of unidirectional roving, Continuous Filament Mat (CFM) and stitched fabric mats (Creative Pultrusions Inc. 2015). The tubes are pultruded with high-performance Vinyl Ester (VE) and Polyurethane resins, VE resins are ideal for long-term performance in harsh marine environments, Polyurethane resins provide all the performance of VE resins in addition to optimal strength, toughness and impact resistance (Creative Pultrusions Inc. 2015).

Two different tube diameters were used in this research; 305mm and 406mm (C12 refer to tubes with 305mm diameter while C16 implies tube with 406mm diameter). The tube thickness is constant in all tubes and equals 12.7mm. For each category of tubes, twelve coupon specimens were tested under axial tension and compression to determine the tubes mechanical properties on the longitudinal direction following the ASTM D3039/D3039M (ASTM D3039 2014) and ASTM D695 (ASTM D695 2010), respectively. The manufacturer provided the tubes mechanical properties based on testing of the full section and following ASTM D6109 (ASTM 2013). Table 4-1 illustrates the dimensions and the mechanical properties of both tubes in the longitudinal direction, where D is the tube outer diameter, t is the tube thickness, f is the average flexural strength, f_{cl} is the average compressive strength, f_{tl} is the average tensile strength, E_l is the Modulus of elasticity, EI is the bending stiffness, and M_f is the average moment capacity.

Table 4-1: Mechanical Properties of GFRP Tubes

	C12		C16	
	Measured	Provided*	Measured	Provided*
D *(mm)*	305	305	406	406
t *(mm)*	12.7	12.7	12.7	12.7
f *(MPa)*	NM	480	NM	395
f_{cl} *(MPa)*	555	480	572	395
f_{tl} *(MPa)*	665	NP	711	NP
E_l *(GPa)*	36.5	40.7	38	41.3
EI ($kg.mm^2$)	NM	5.17E+11	NM	1.28E+12
M_f *(kN.m)*	NM	392	NM	592

* *Provided by the manufacturer, NM = Not Measured, NP =Not Provided*

4.3.1.2. Concrete

Ready-mixed normal weight concrete of 35 MPa target compressive strength; with aggregate size between 5-20 mm and slump of 80 ± 20 mm; was appropriated to fill the tubes. The tubes were decanted vertically. The casting of the specimen started with filling the footing up to the bottom end of the FRP tube then the tubes filled wholly. Thereafter, the footing was completed. For each specimen, nine cylinders and six prisms were prepared and tested on the same day of the test to determine the concrete compressive strength and the concrete modulus of rupture, respectively. The measured concrete properties of the four patches were approximately identical, the concrete compressive strength of the cylinders was 35 MPa ± 2 MPa and the modulus of rupture of prisms was 4.0 MPa ± 0.3 MPa.

4.3.1.3. Steel reinforcement

Two varied sizes of steel reinforcement, M15 (15 mm diameter) and M10 (10 mm diameter) were used to reinforce the footing. The footing was designed to be an over-reinforced concrete element to avoid its failure during the test. Based on the data provided by the manufacturer, the steel reinforcement bars have a modulus of elasticity and yield strength equal to 200 GPa, 420 MPa, respectively.

4.3.2. Preparation of specimens

4.3.2.1. Sand-coating procedure

The essential purpose of using sand-coating is to establish a rough texture on the internal skin of the tube. The sand-coating process comprises three stages, the first stage is the coating of a VE resin layer on the interior skin of the FRP tube using paint-rollers. While the second stage is the covering the VE resin layer by using a coarse silica sand (Atlantic silica, quartz sand, #0 sand) before the hardening of the VE resin. The third stage is the curing of the resin, which materializes by preserving the tubes in a curing room for three days at a constant temperature of 60-degree Celsius. Figure 4.1 shows the sand coating process.

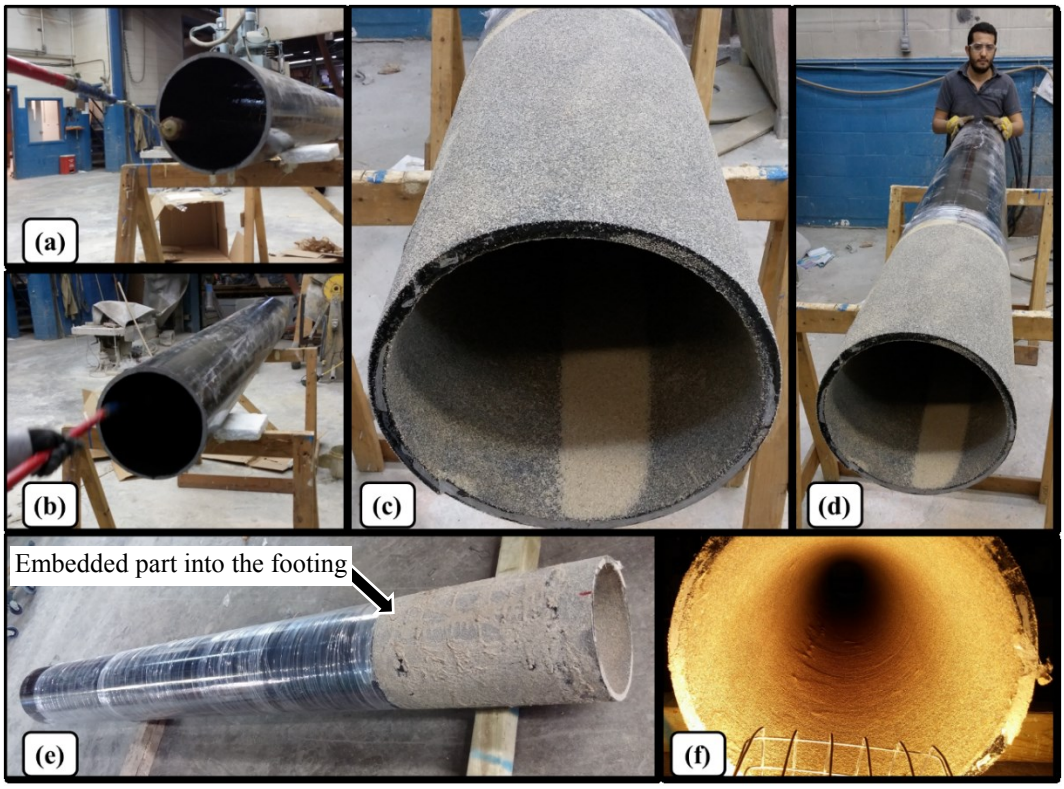

Figure 4.1: Sand-coating creation details

4.3.2.2. Test Specimens

Four full-scale circular CFFT columns were tested under cyclic lateral load; two columns had 305 mm external diameters, and the other two columns had 406 mm external diameters. For each size, one column has a sand-coating bond-enhancer on the internal skin of the FRP tube. The identification of the specimens refers to the column diameter (C16 for the column with 406 mm diameter and C12 for the column with 305 mm diameter) and the presence of the sand-coating on the interior skin of the FRP tube (S for sand-coating bond enhancer). For example, if the tube diameter is 305 mm with a sand-coating bond-enhancer, the ID will be "C12S". The embedded depth of columns into the rigid RC footings was 500 mm and 600 mm for the columns with 305 mm and 406 mm diameter, respectively. Two square-footing sizes of (1.2 m ×1.2 m ×0.8 m) and (1.4 m ×1.4 m ×0.8 m) were utilized for C12/C12S and C16/C16S, respectively. Table 4-2 shows the details of the test specimens, where f_c' is the concrete compressive strength, ρ_f is the fiber reinforcement ratio, L_s is the shear span, and d_f is the embedded depth into the RC footing. For all specimens, the embedded part of the tube into the footing was sand-coated on its exterior skin

to produce a rough texture. This rough texture enhances the bond between the concrete of the footing and the tube; as shown in Figure 4.1.

Table 4-2: Columns details

Column ID	D (mm)	f_c' (MPa)	ρ_f $(\%)$	L_s (mm)	d_f (mm)	Footing dimensions	Tube inner surface condition
C12	305	35	16.7	1930	500	1.2 m×1.2 m×0.8 m	…….
C12S	305		16.7		500	1.2 m×1.2 m×0.8 m	sand coating
C16	406		12.5		600	1.4 m×1.4 m×0.8 m	……..
C16S	406		12.5		600	1.4 m×1.4 m×0.8 m	sand coating

4.3.2.3. Assembling of the specimens

The FRP tubes were cut in the required length 2700mm and 2800mm for C12 and C16, respectively. The sand coating was done on the internal and externally pursuant to the test matrix. During the curing time of sand coating, over-reinforced steel cages were manufactured for the RC footings. The internal concrete strain gauges were attached to steel holders; as shown in Figure 4.2(a) and 2(b). These steel holders (3.2mm diameter) were used to install the internal strain gauges at the required locations. The steel holders were fixed to a wooden plate. Steel holders were inserted to the bottom end of the tube. The wooden plate was utilized to seal the tube bottom end; as shown in Figure 4.2(c) and 2(d). By closing the tube bottom, the column considers as a precast column. The steel cage was installed on a wooden formwork; as shown in Figure 4.2(e). The steel cage was assembled with a void on its center. This void was formed for the FRP tube, so no holes were created on the wall of the tube to pass the top reinforcement of the footing. Thereafter, the closed end of the tube was implanted in the steel cage. The wooden plate was rested on the steel reinforcement bars of the footing. The column was aligned to be in a vertical position and in the center of the four corners holes of the footing, which are used to fix the footing to the laboratory floor. Figure 4.3 shows the specimen-adjustment on the formwork and the concrete pouring process.

`

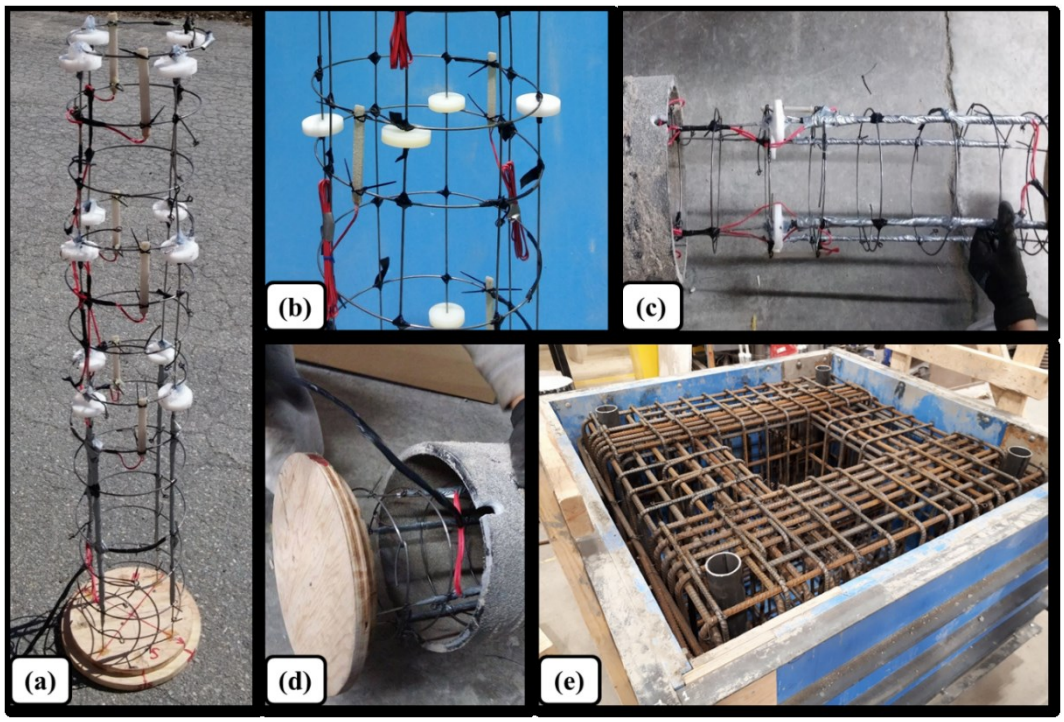

Figure 4.2: Preparation of specimens

4.3.3. Test setup

All specimens were tested on the typical test setup that is shown in Figure 4.4. A hydraulic actuator with the capacity of 500 kN was used to apply the lateral cyclic load. The RC footing was attached to the laboratory floor by using 4 high strength Dywidag bars on its corners. Each Dywidag bar was tensioned by 400 kN (for specimens C12 and C12S) or 500 kN (for specimens C16 and C16S) to avoid the sliding and the overturning of the RC footing. Two rigid steel frames were used to establish the test setup and to ensure the overall test setup stability. The hydraulic actuator was attached to the main-frame. The main-frame was supported by four inclined steel truss members. The secondary frame was used to support the lateral guide system. The lateral guide system prevented any out-of-plan deformation of the column. This system consisted of two HSS steel beams supported on the two rigid frames. Two steel column heads were designed for the two column sizes. The column head used to transmit the load from the actuator to the column. Each steel column head has four rigid plastic cylinders, which were in direct contact with the lateral guide beams. Grease layer covered the plastic cylinders surface to eliminate friction with the lateral guide beams. Figure 4.5 presents the details of the steel column head.

Figure 4.3: Adjustment and casting of specimens

`

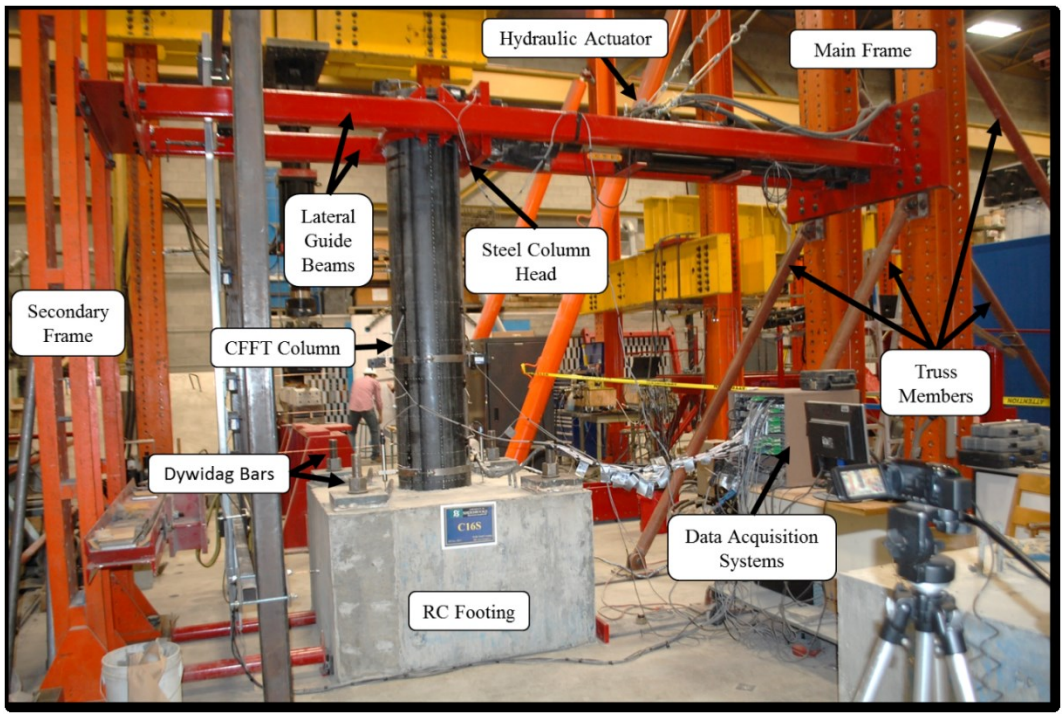

Figure 4.4: Typical test setup

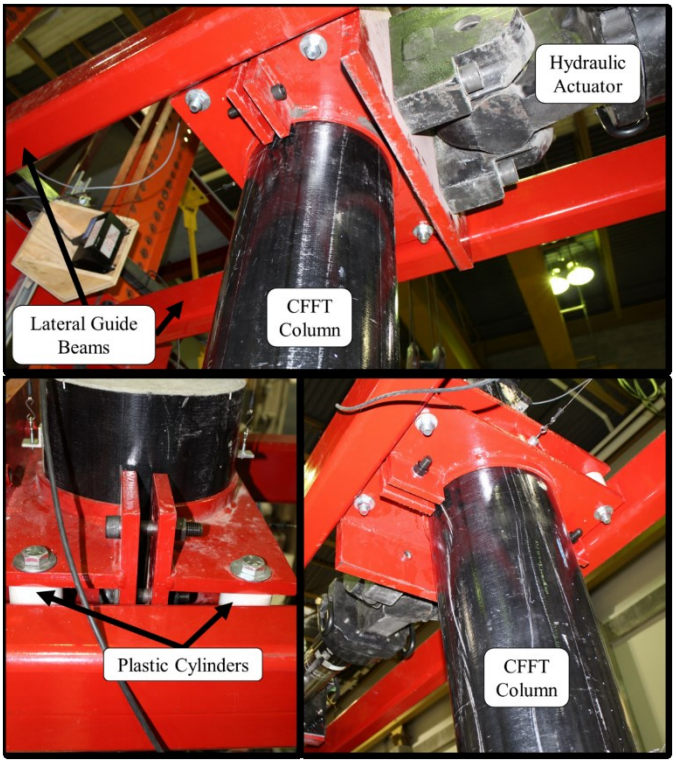

Figure 4.5: Details of the steel column head

4.3.4. Instrumentation and test procedure

Axial and hoop strains were measured on the tube outer skin at six different sections along the column height using electrical strain gauges of 350-ohm resistance. These sections were chosen at 50 mm (section 1), 0.5D (section 2), D (section 3), 1.5D (section 4), 2D (section 5), and 2.5D (section 6) above the top surface of the footing; where "D" is the column diameter, to cover the plastic hinge zone. The instrumentation plan is shown in Figure 4.6.

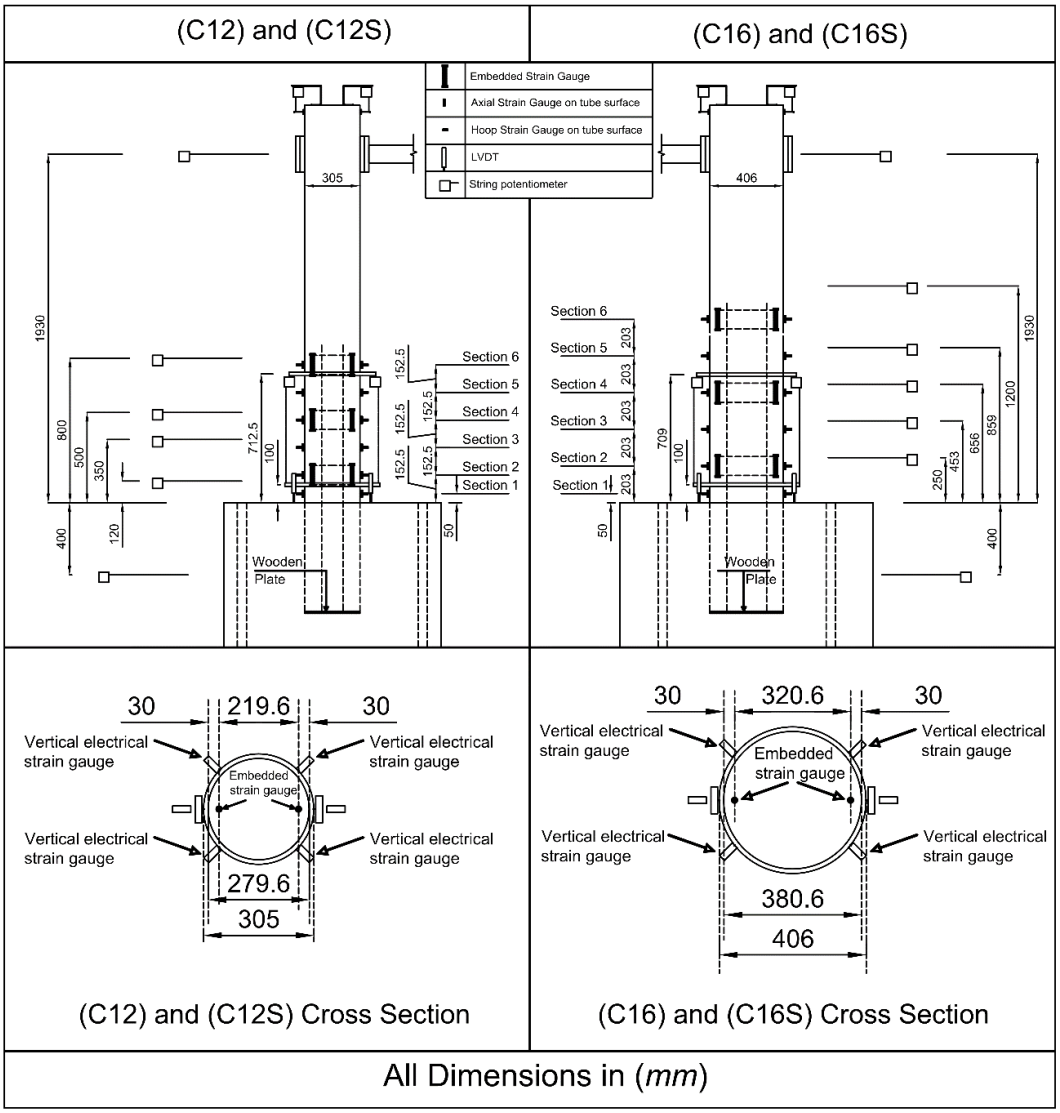

Figure 4.6: Instrumentation layout

Six internal concrete strain gauges were attached to the steel holders at sections 2, 4, and 6, three on the pushing side and the others on the pulling side. The internal strain gauges were positioned at 30 mm far away from the internal surface of the tube. Thin plastic cylinders were attached to the steel holder to maintain the 30mm distance of the internal strain gauges constant along the steel holders; as shown in Figure 4.2(a) and 2(b). Another vertical electrical strain gauges were aligned with the internal strain gauges on the tube surface. Five linear string potentiometers were used to measure the lateral displacement of the column at different heights along the columns height. One potentiometer was attached to the RC footing to record any footing sliding that may occur during the test. Two potentiometers were attached to the top of the column to measure any slippage between the concrete core and the FRP tube.

Another two potentiometers were used to record the curvature of the column in the plastic hinge zone. These potentiometers were fixed to steel ring at a height of 712.5 mm above the footing top surface for C12/C12S or at a height of 709 mm above the footing level for C16/C16S. The wires of these two potentiometers were attached to another steel ring at height 100 mm above the top surface of the footing. Two linear variable differential transformers (LVDTs) were attached to lower steel ring to capture the slippage between the column and the RC footing. Figure 4.7 shows the instrumentation details of the plastic hinge zone of the CFFT column.

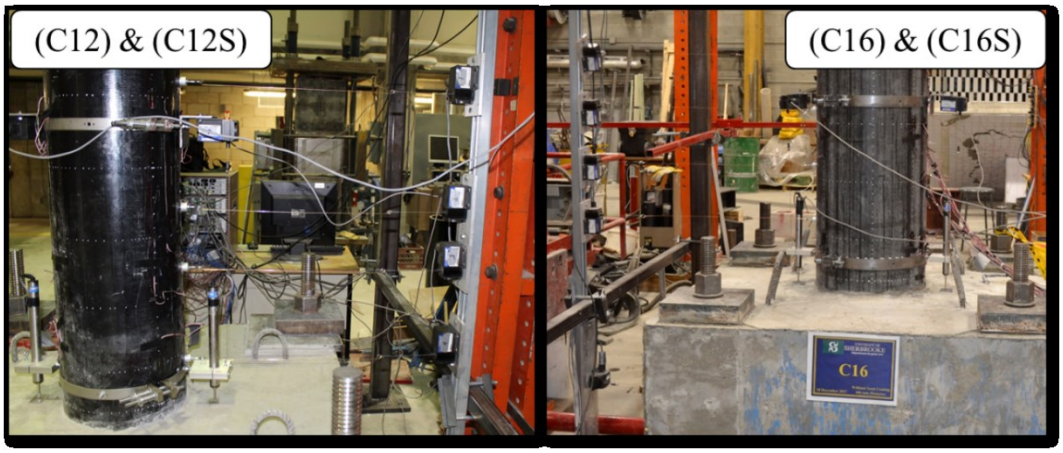

Figure 4.7: Instrumentation of the plastic hinge zone

The lateral loading regime was performed by displacement control with a loading rate of 0.4 mm/s up to the failure of the specimens. Two complete cycles for each drift ratio was implemented to

illustrate the stiffness degradation of the CFFT columns. The loading increment rate was initiated with ± 0.25% drift up to realize total drift equal ± 1%. Posteriorly, the loading increment rate increased to be ± 1%. Figure 4.8 presents the cyclic loading regime description.

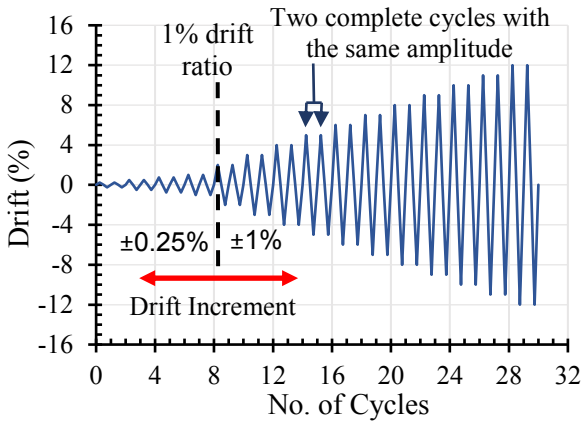

Figure 4.8: Reverse cyclic loading regime

4.4. Experimental Results

This section presents the experimental results and the test observations of the tested specimens. The following definitions are established to illustrate the results simply, the negative sign of force, displacement, and moment is describing the pulling direction; while, the positive sign is used to state the pushing direction. Tensile stresses/strains are called to be positive whereas compressive stresses/strains are defined to be negative.

4.4.1. Test observations

In general, each column demonstrated a sensibly lateral load-top displacement response in the pushing and pulling directions until the rupture of the FRP tube occurred. No evidence that sliding or overturning of the footing was detected. Fine cracks were observed on the top surface of RC footings of specimens C12 and C12S at the lateral drift ratio of 4% until the failure while spalling of the concrete cover of the top surface of RC footings of specimens C16 and C16S was noticed. The spalling of the footing concrete cover accompanied a sudden plummet in the lateral load-top displacement response. LVDTs were removed after the spalling of the concrete cover materialized. Under heightened displacement, the spalling of the footing concrete and the plummet in the lateral load-displacement response increased and became more significant. Table 4-3 shows a summary of experimental results. The following sections present more detailed data on failure mode,

`

hysteretic response, envelope response, cracking moment, slippage observation, composite action analysis, flexural strength, flexural stiffness, and energy dissipation of the tested specimens.

Table 4-3: Experimental Results Summary

CFFT ID	Failure			Maximum at Pushing			Maximum at Pulling		
	Δ (*mm*)	P (*kN*)	Cycle *ID*	Δ (*mm*)	P (*kN*)	Cycle ID	Δ (*mm*)	P (*kN*)	Cycle *ID*
C12	+169	+205	1st cycle of +200 *mm*	+180	+224	1st cycle of +180 *mm*	-180	-227	1st cycle of -180 *mm*
C12S	+168	+225	1st cycle of +180 *mm*	+168	+255	1st cycle of +180 *mm*	-160	-272	1st cycle of -180 *mm*
C16	+137	+180	2nd cycle of +160 *mm*	+115	248	1st cycle of +120 *mm*	-134	-286	1st cycle of -140 *mm*
C16S	+180	+240	1st cycle of +200 *mm*	+154	+307	1st cycle of +160 *mm*	-154	-299	1st cycle of -160 *mm*

Note: Δ = *Lateral top displacement,* P = Lateral load.

4.4.2. Failure mode

The failure of unreinforced CFFT columns often happens when the rupture of the FRP tube developed. The failure of column C12 materialized due to the suddenly buckling of the FRP tube-wall on the compression side at section located approximately 50-60 mm above the footing top surface in the first pushing cycle of + 200 mm. The failure of column C12S, C16, C16S began as fine vertical cracks on the FRP tube-wall then transformed to buckling of the FRP tube-wall on the compression side. Failure of C12S observed at 10-20 mm above the column-footing interface in the first pushing cycle of +180 mm amplitude while the failure of C16 and C16S materialized at 100-150 mm below the column-footing interface. Tests were continued after the buckling of the columns tube-wall and the load direction was reversed, which applied a tension force on the buckled tube-wall. Eventually, full rupture of the buckled tube-wall was developed. Specimens C16 and C16S suffered from high slippage between the CFFT column and the RC footing. Besides the high slippage, the spalling of the footing concrete cover affected the behavior of the columns, these reasons adversely effected the total behaviour of the columns C16 and C16S. Figure 4.9 shows the extent of damage to the tested specimens.

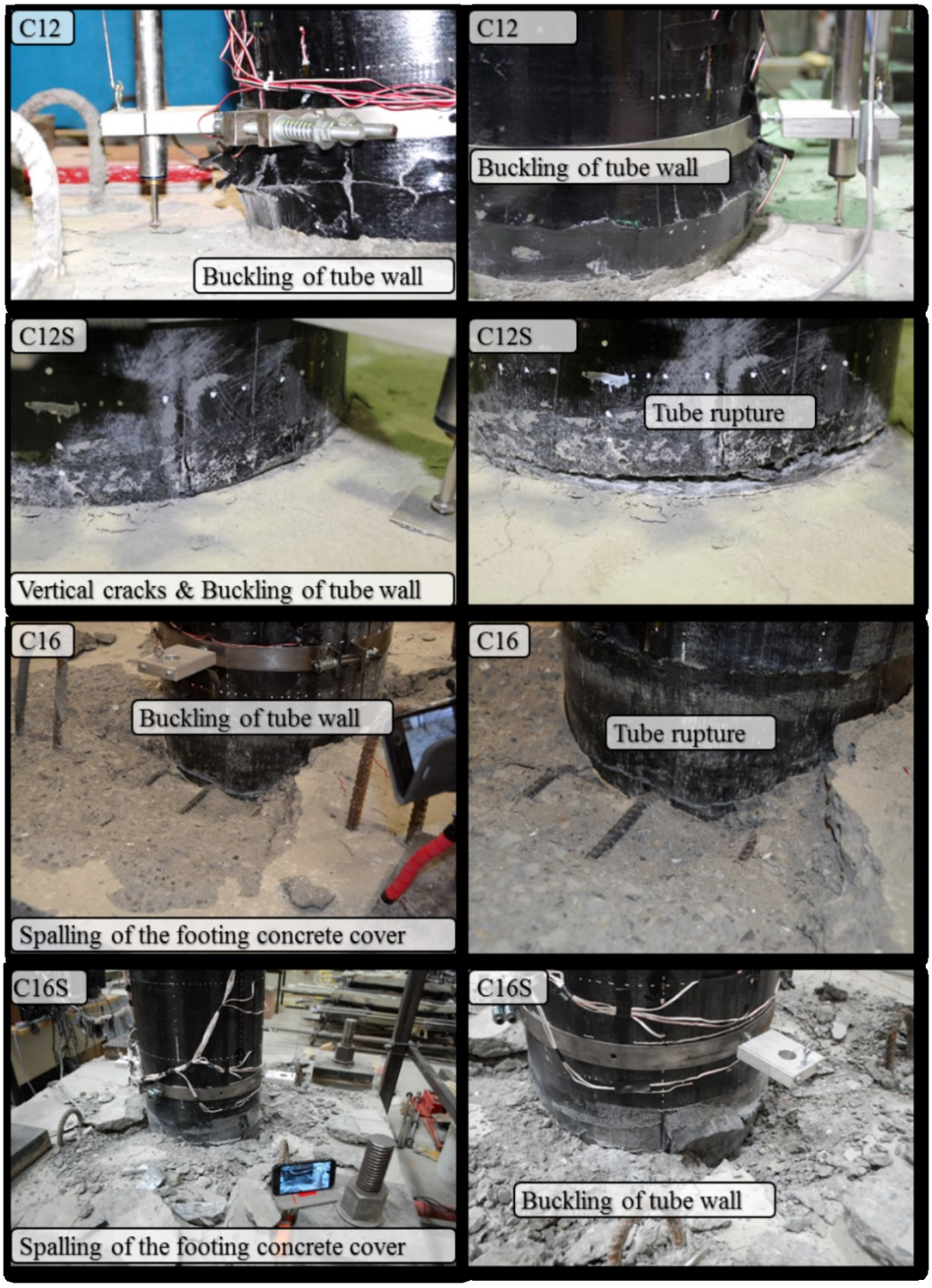

Figure 4.9: Failure mode of columns

4.4.3. Hysteretic responses

Lateral load-top displacement responses of all the tested columns are displayed in Figure 4.10. The lateral top displacement values of the linear potentiometer attached to the column head and the

`

hydraulic actuator were identical. The recorded data of the actuator were used to plot the hysteric response because it was more smooth and stable than the linear potentiometer. Sub-figures in Figure 4.10 have the same drawing scale for facilitating of comparison. The points corresponding to the failure (fracture of the tube) and the maximum achieved load are identified on each curve.

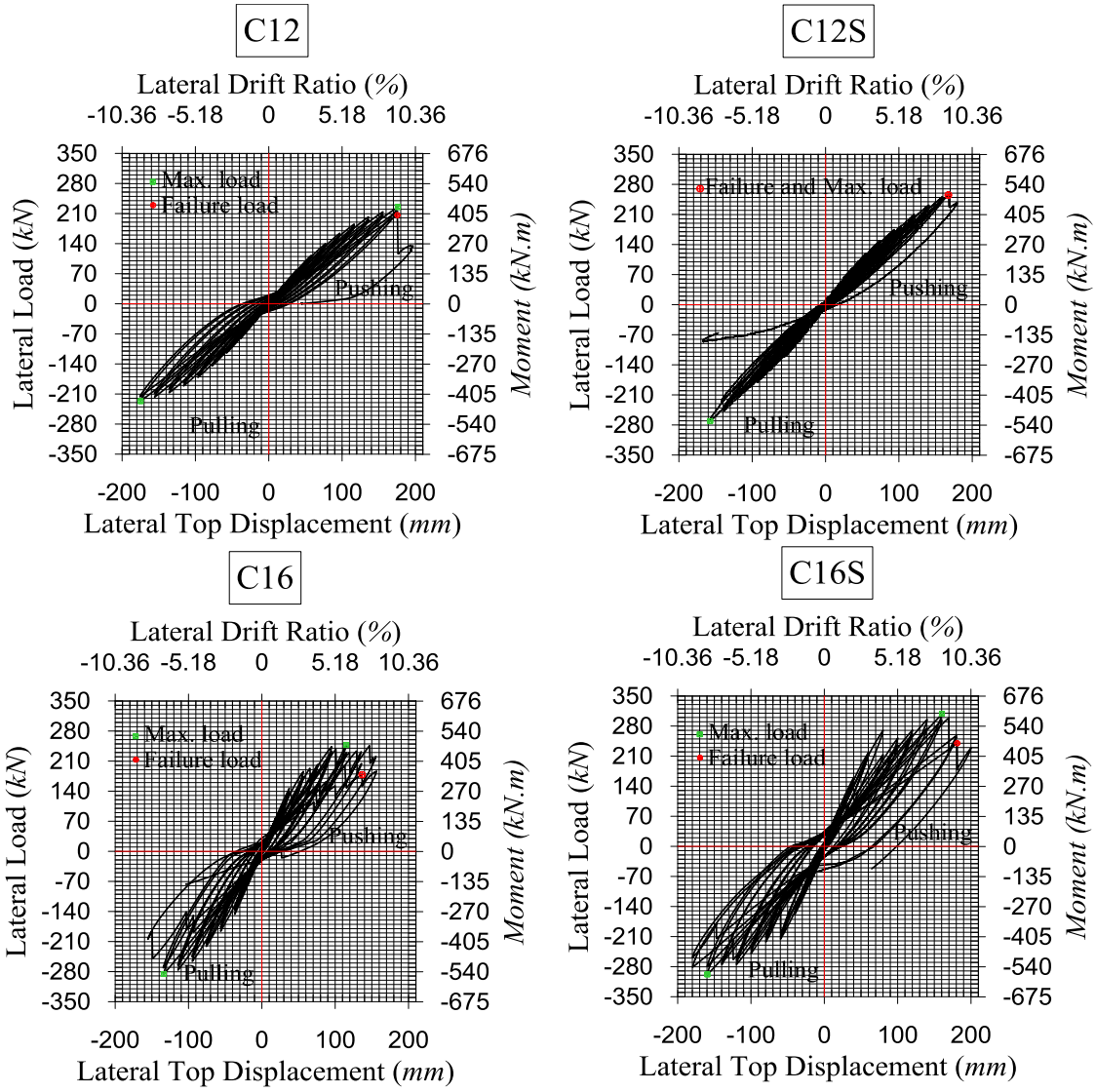

Figure 4.10: Hysteretic load/moment-top displacement responses

Hysteretic responses of columns C12 and C12S are ideal flexural loops until the failure of the columns. As mentioned previously, each cycle was applied two times to investigate the effect of stiffness degradation of columns under the cyclic load. Consequently, the response of the second cycle is lower than the recorded response of the first cycle for the same cycle amplitude. Column C16 showed identical flexural loops until the slippage between the CFFT column and the footing

started in the first cycle of +80 mm. A sudden drop of C16 response was developed in the first cycle of +80 mm and repeated also in the first cycle of (+120, +140, and ±160 mm) and in the second cycle of (+120, ±140, and +160). Figure 4.11 shows the response decay of C16 for each cycle separately while the footing damage corresponding to each cycle is shown in Figure 4.12.

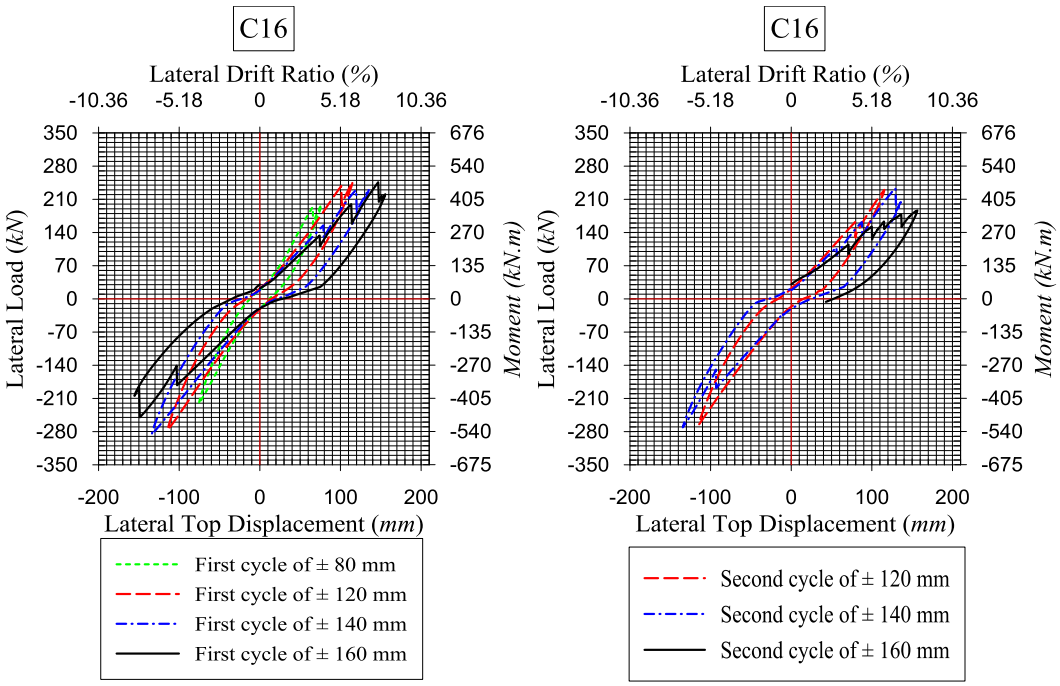

Figure 4.11: Individual loops of C16

Column C16S behaved like C16 in term of the sudden response drop. The first response impairment of C16S monitored at the first cycle of -80 mm and recurrent also in the first cycle of (-140mm, +180mm, and +200mm) and in the second cycle of -180mm. Figure 4.13 and Figure 4.14 show the response decay of each cycle individually and the damage of the RC footing for C16S, respectively. The slope of C16S response decreased significantly after the first response decay (first cycle of -80 mm) ensued.

`

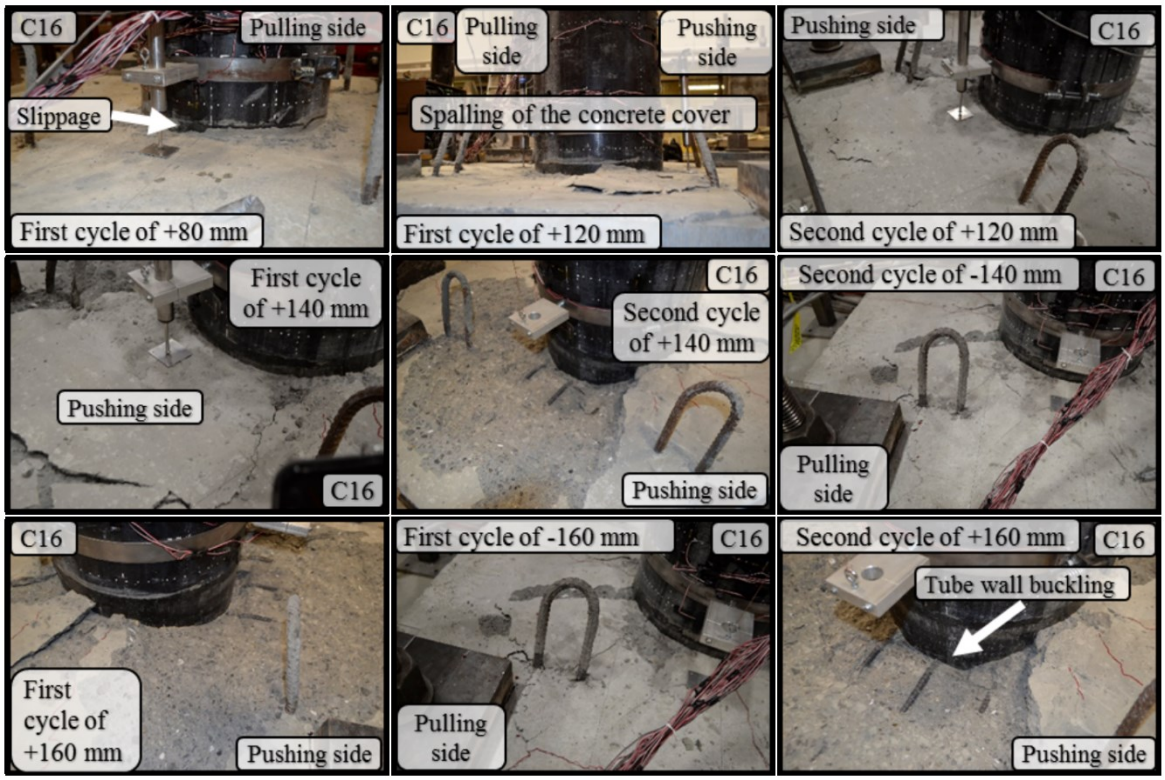

Figure 4.12: Stages of the damage of C16-footing

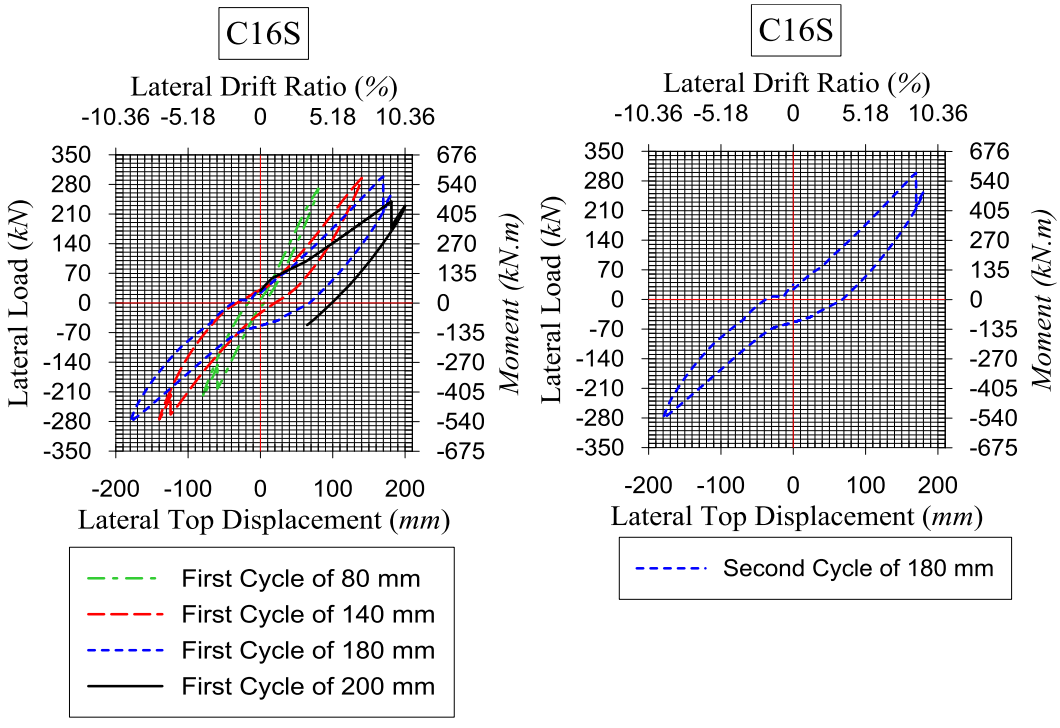

Figure 4.13: Individual loops of C16S

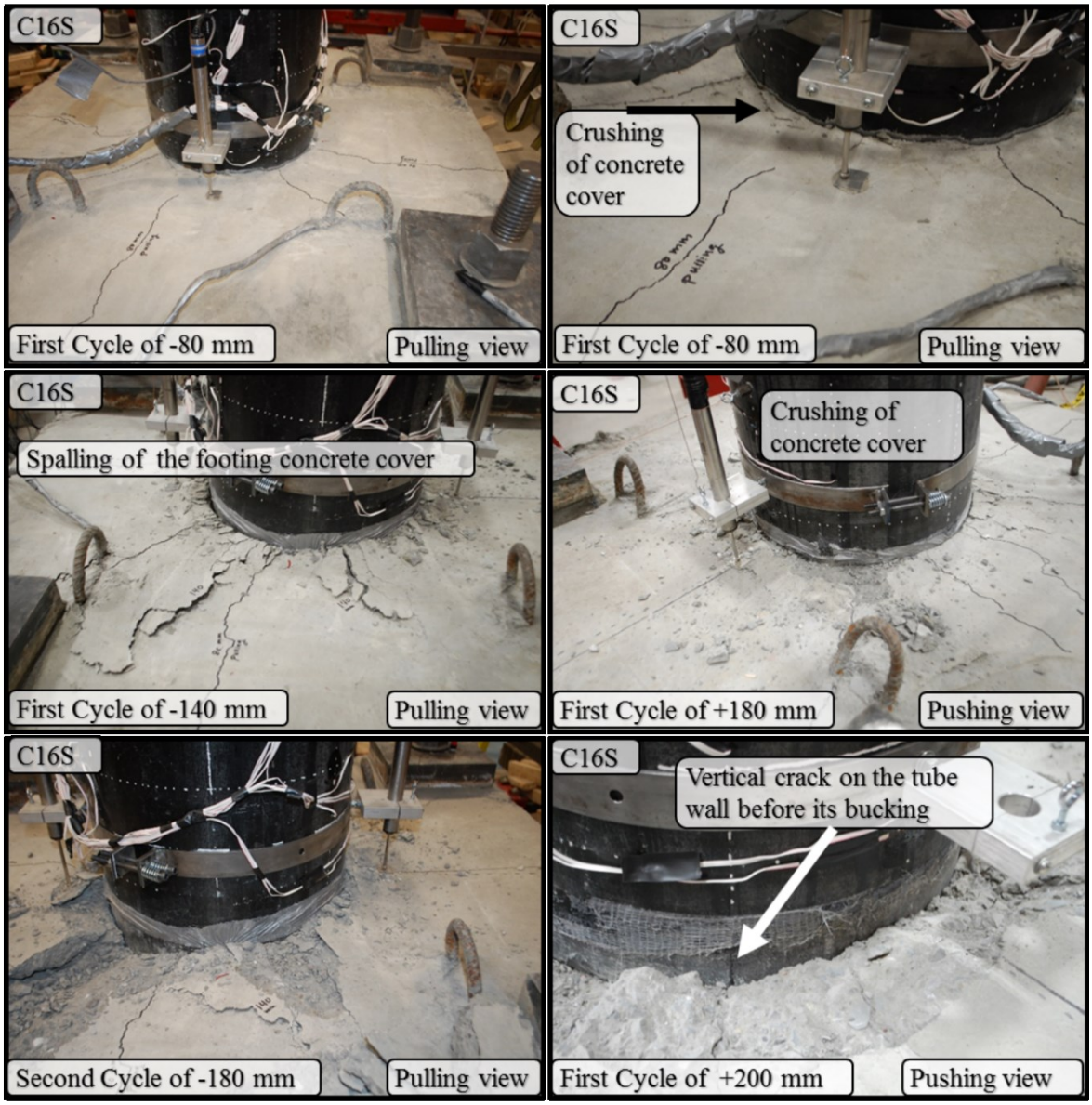

Figure 4.14: Stages of the damage of C16S-footing

4.4.4. Envelope load-displacement responses

The maximum recorded load on each cycle and its corresponding top displacement value are used to plot the envelope lateral load- top displacement response. Where the first cycle and the second cycle with the same amplitude are called the first run and the second run, respectively. Figure 4.15 presents the envelope load/moment-top displacement responses of all tested columns. Based on the data provided by the GFRP tube manufacturer, the flexural capacities of C12 and C16 empty tubes are also illustrated in Figure 4.15. Generally, recorded loads of the second run are a little

`

lower than recorded loads in the first run. Column C12S achieved a maximum-load higher than C12 and the C12-empty tube by 14% and 26%, respectively, in the pushing direction while 20% and 34%, respectively, in the pulling direction. The failure load of C12 is approximately the same as the C12 empty tube. Column C16S reached a maximum-load higher than C16 in the pushing direction by 24% and in the pulling direction by 5%. The maximum load achieved by C16S has approximately equaled the flexural capacity of the C16 empty tube.

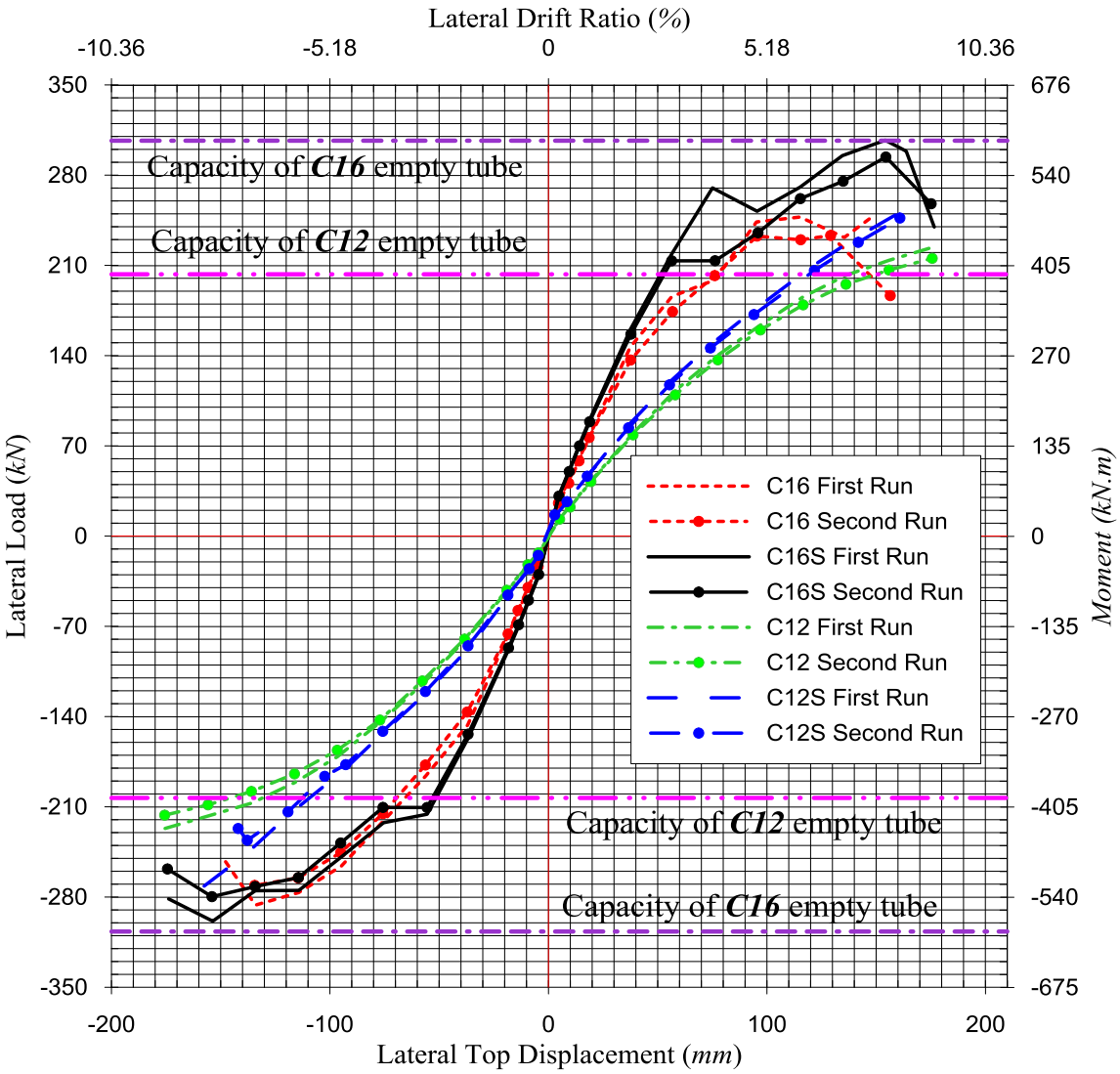

Figure 4.15: Envelope load/moment-top displacement responses

4.4.5. Column-footing slippage

Slippage between the CFFT column and the RC footing was captured using two LVDTs, one in the pushing direction and the other one in the pulling direction, as explained in the instrumentation details section. Figure 4.16 shows the column-footing slippage of all specimens. Slippage occurs on the opposite side of the loading direction, for example, slippage happened on the pulling-side when the loading direction was in the pushing-side. Generally, all column-footing slippage responses behave linearly at the beginning of the test. A nonlinear gradual change in all responses was observed, especially in C12, C16, and C16S. The responses of C16 are not completed due to the early spalling of the concrete cover of the top surface of the RC footing. The maximum column-footing slippage of all specimens was recorded on the pushing side in the second run; that was equal 12.4 mm, 6.5 mm, 25 mm, and 44 mm for C12, C12S, C16, and C16S, respectively.

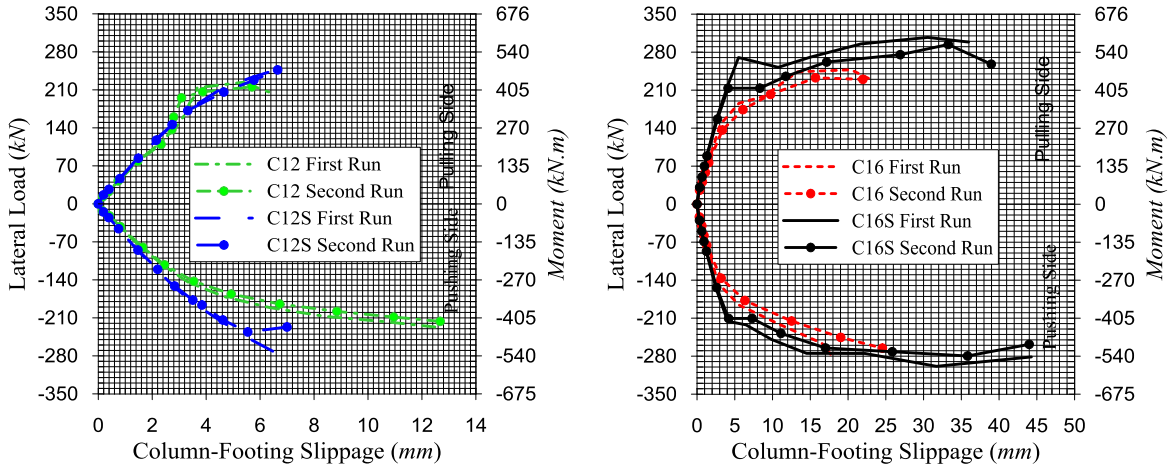

Figure 4.16: Column-footing slippage

4.4.6. GFRP tube-concrete core slippage

Slippage between the GFRP tube and the concrete core was measured on the top end of the CFFT column in the pushing side and pulling side using two linear potentiometers. The captured values of slippage before the failure of columns are equal to 0.4 mm, 0.26 mm, and 2.1 mm for C12, C12S, and C16, respectively. For C16S, the potentiometers were broken after the starting of the test. These values had a rapid change during the failure of the specimens, which reached 6 mm, 0.46 mm, and 3 mm for C12, C12S, C16, respectively, after the failure.

`

4.4.7. Interior and exterior axial strains comparison

Axial strains inside the concrete core were measured by embedded concrete strain gauges. Axial strains on the external tube surface, which are adjusted to the internal strains, were also measured using electrical strain gauges. Figure 4.17 to Figure 4.19 show the internal and external strains-lateral top displacement responses of the tested columns in section 2, section 4, and section 6, respectively. It is clear in all responses, concrete-tensile strains are not in harmony with the tube-tensile strains in all responses of the tested specimen. As it is commonly known, Concrete is cracking when exposed to tensile stresses, which explains the non-harmony between the concrete and the FRP tube in tension.

The following observations describe the comparison between interior and exterior stains in compression. Interior concrete strains of C12 behave non-linearly while the exterior trains are linear up to the failure of the column in sections 2, 4, and 6. On section 2 of C12, the interior strain was transformed to positive at the last cycles, which means tensile stresses were applied to concrete and the tube still exposed to compressive stresses at the same position. This result considers as an evidence of debonding between the tube and the concrete core.

Compressive interior and exterior strains of C12S were typical identicals on all sections; as shown in Figure 4.17 to Figure 4.19. Five from six interior strain gauges of C16 became out of range measurements after a brief time from the beginning of the test. The remaining interior strain gauge of C16 was in section 2 on the pulling side. Interior strain of C16 was nonlinear, not compatible with exterior strain, and changed to positive strain at the last cycles as column C12, as shown in Figure 4.17. In column C16S, one interior strain gauge in section 6 on the pushing direction was broken. The comparison of interior and exterior strains of C16S indicates a harmony between strains until certain level then transformed to incompatible strains. This divergent appeared at the cycles of +20 mm and -60 mm and varying strains from -0.002 to -0.0025 in pushing side. It deduced that the debonding of C16S accomplished between +1% to -3% drift ratio.

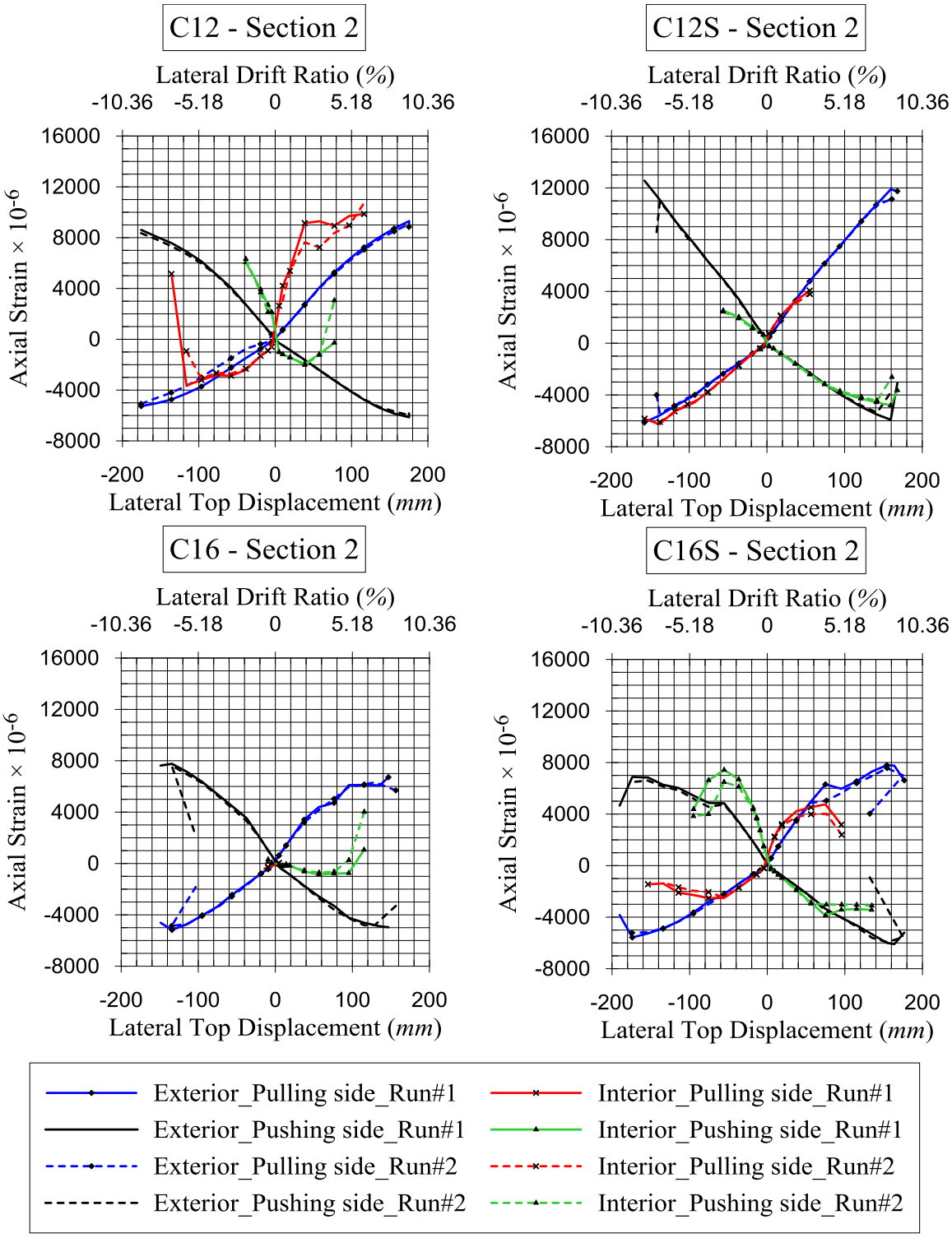

Figure 4.17: Comparison of interior and exterior strains at section 2

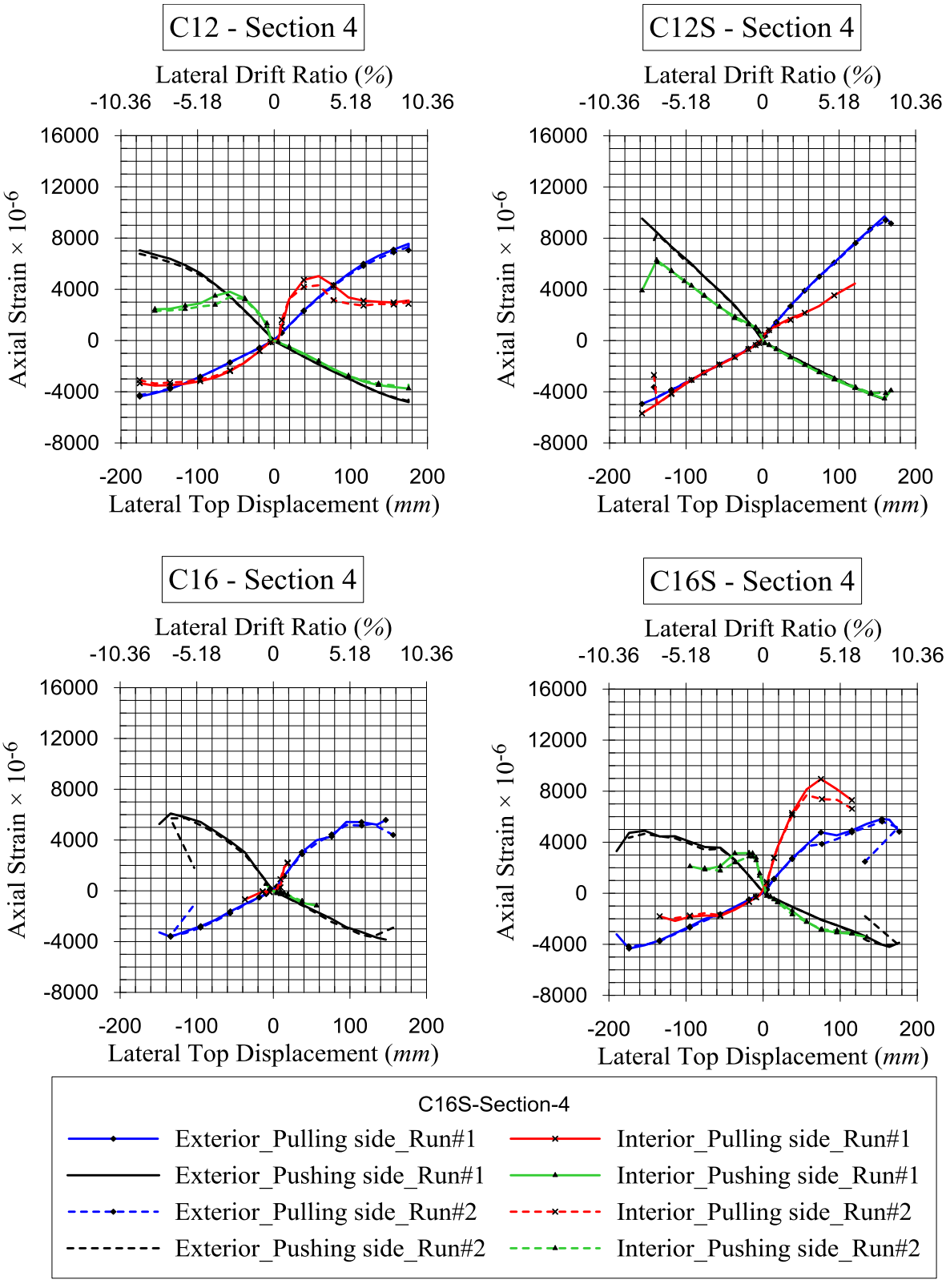

Figure 4.18: Comparison of interior and exterior strains at section 4

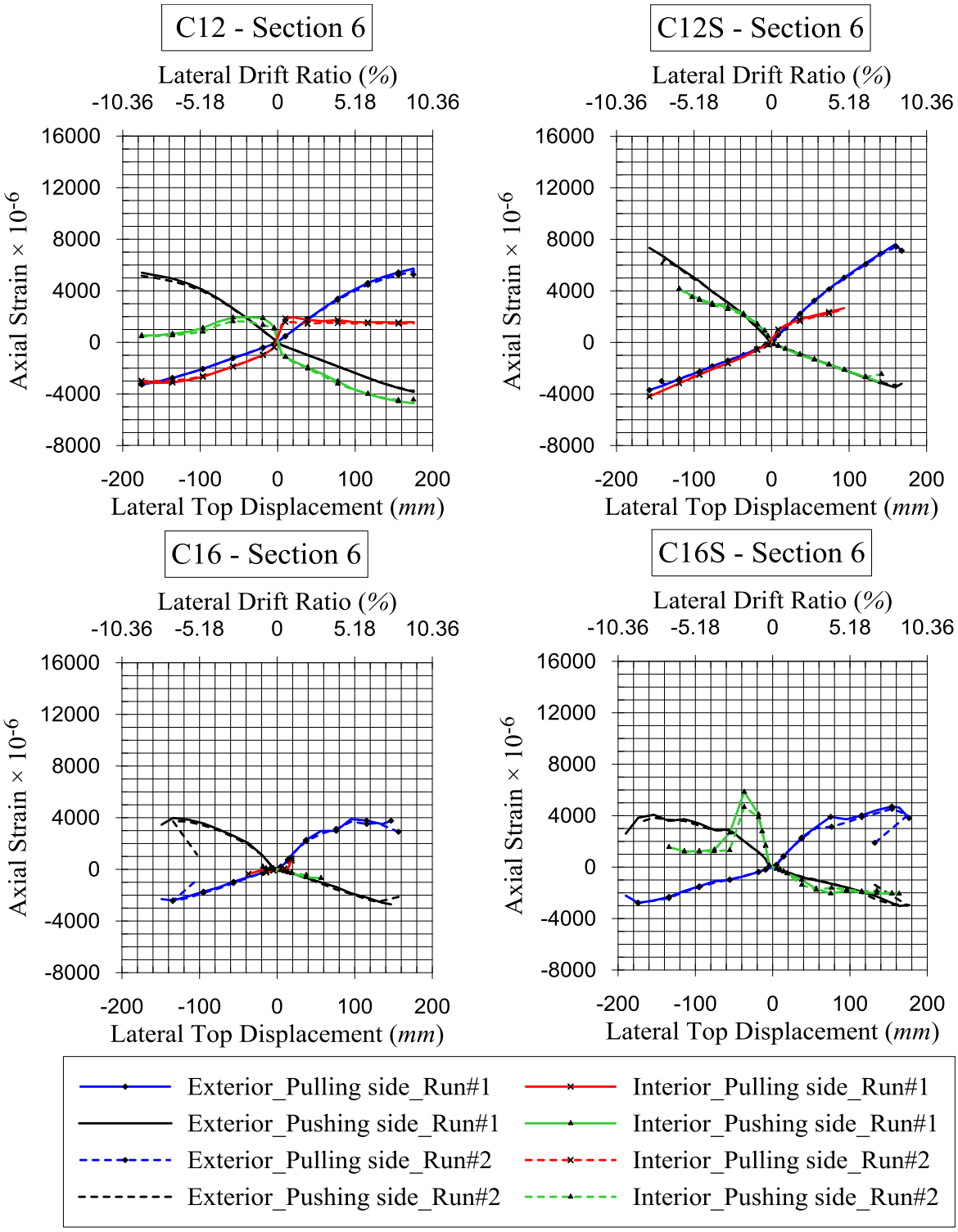

Figure 4.19: Comparison of interior and exterior strains at section 6

4.4.8. Curvature distribution over the column height

Axial strains on the tube exterior skin were used to calculate the curvature of each section by dividing the absolute summation of tensile and compressive strains on the outer diameter of the column. Figure 4.20 shows the curvature distribution over the column plastic hinge zone of the tested specimens. Responses of Columns C12 and C12S behaved linearly over the column height until 2% drift ratio. The slope of curves is gradually increased especially on column C12S, this is evidence on reaching the plastic stage. The plastic hinge length of C12 and C12S is 457.5 mm which is equal to 1.5D. While; columns C16 and C16S behaved approximately linear until the failure. Because of occurrence high slippage between the column and the footing, determination of the plastic hinge of C16 and C16S is inaccessible.

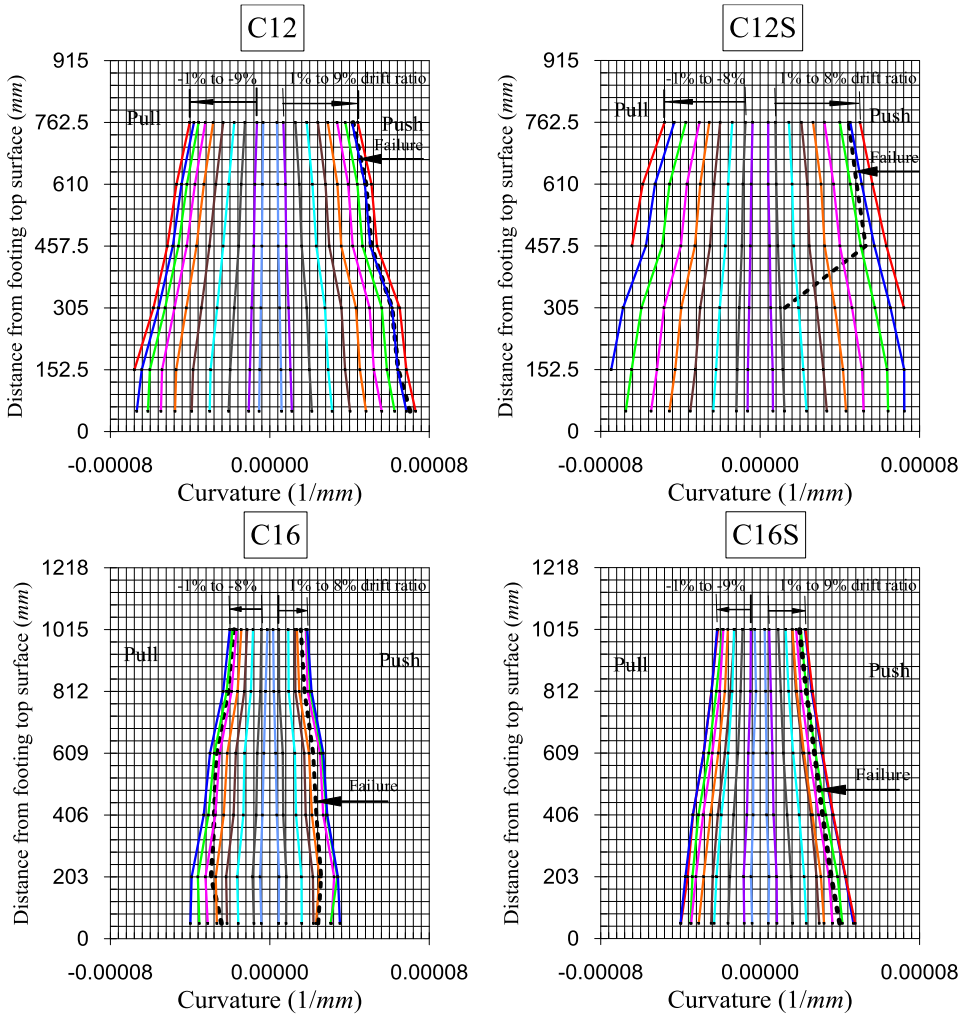

Figure 4.20: Curvature distribution along the column height

4.4.9. Moment-curvature responses

The moment-curvature response is a practical approach to evaluate the flexure stiffness for any structural member. Figure 4.21 presents the moment-curvature responses of the tested-columns. The flexure stiffness of specimens C16 and C16S is higher than the flexure stiffness of specimens C12 and C12S, which was predicted due to the column diameter effect on the flexural stiffness. The response of column C12 has behaved initially like the response of C12S. Thereafter, it started to decline due to the deterioration in the bond between the concrete core and the FRP tube. Responses of columns C16 and C16S have the same behavior until the spalling of the footing concrete cover occurred.

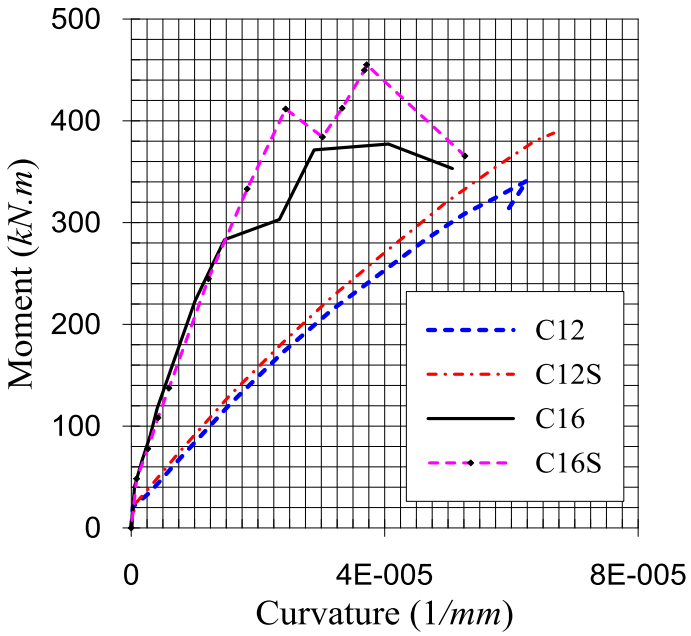

Figure 4.21: Moment-curvature response

4.4.10. Hoop strains distribution over the column height

Hoop strains of the tube were measured on tension and compression sides at different height using hoop strain gauges. Distributions of the hoop strain over the column height are presented in Figure 4.22 and Figure 4.23. In the measured locations, all gauges on the pushing-side and pulling-side of the tube exhibited tensile strain during the pushing-cycles and the pulling-cycles, respectively. The maximum tensile hoop strains were recorded at section 2 for C12 and C12S and at section 1 (located at 50mm above the column-footing interface) for C16 and C16S on the pushing-side in

`

the pushing cycles. The maximum tensile hoop strain for C12S was 5309 micro-strain and higher than C12 by 17%. Hoop strain considers as an indicator for the confinement performance of CFFT columns. It is clear, C12S generated the most effective confinement performance among all specimens.

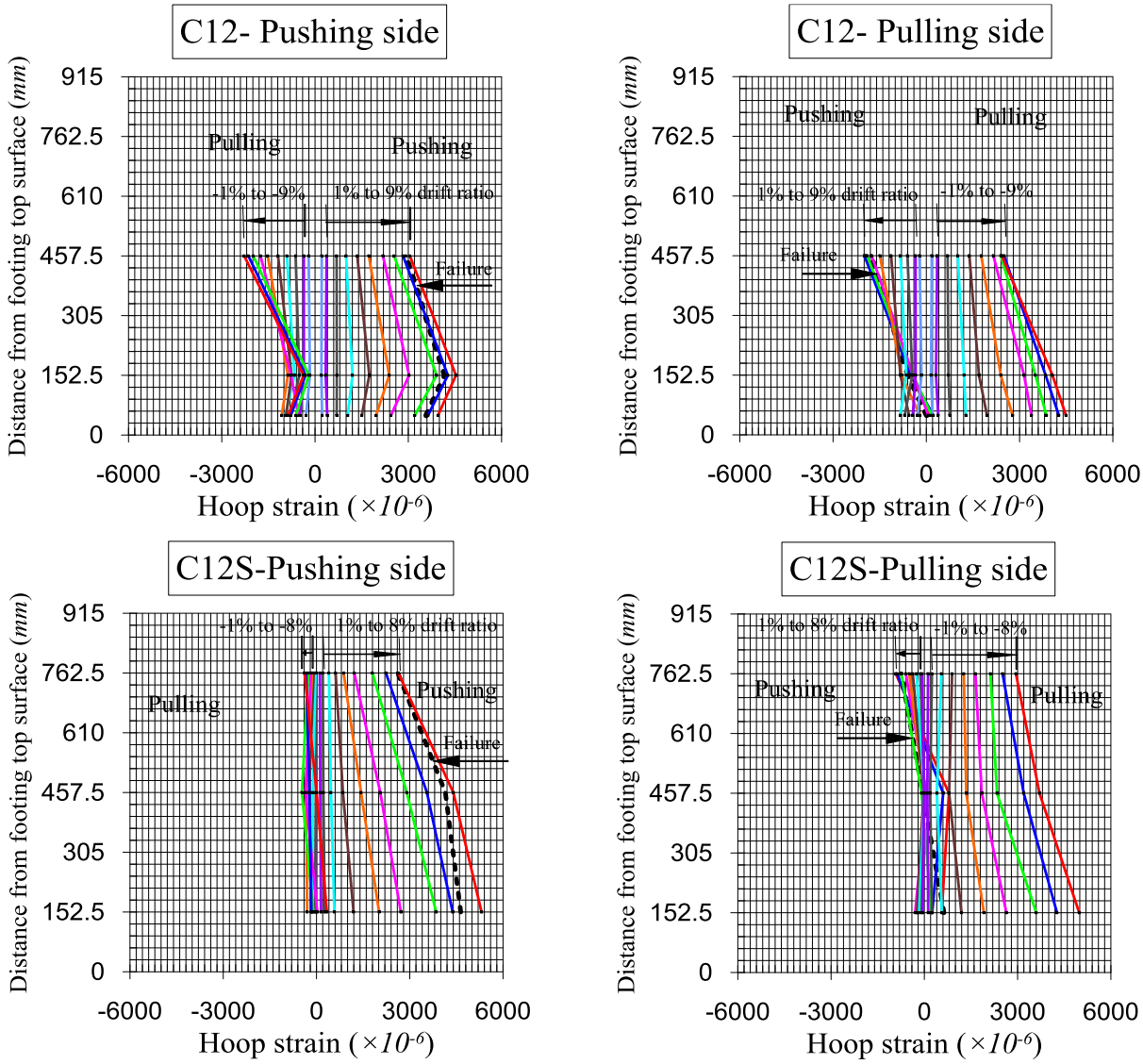

Figure 4.22: Hoop strain distribution along the column height of C12 and C12S

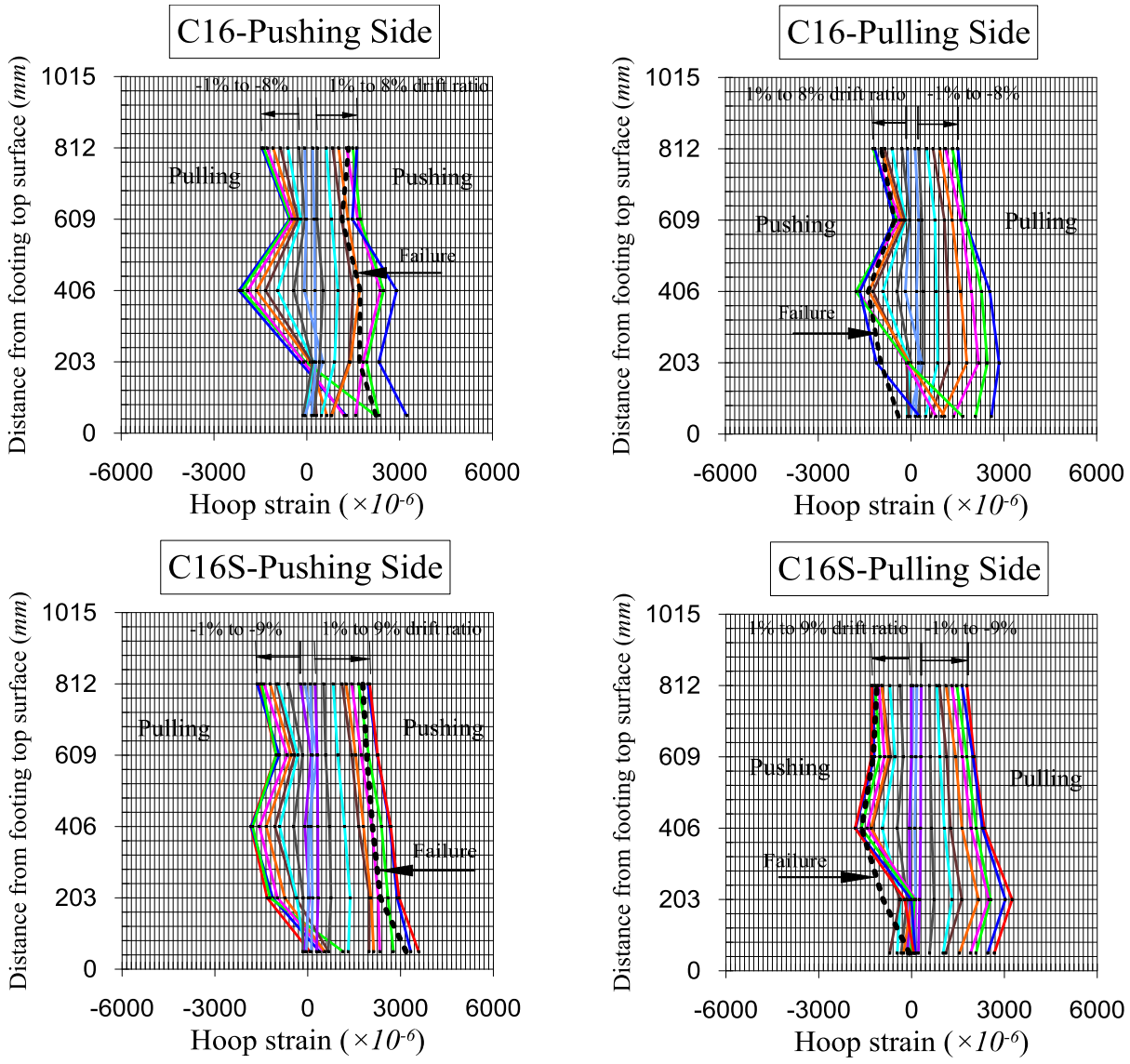

Figure 4.23: Hoop strain distribution along the column height of C16 and C16S

4.4.11. Initial stiffness and cracking moment

The initial stiffness is determined as the inclination of the elastic response (before the cracking of the specimen). Figure 4.24 presents moment-curvature relationships of the columns at the first cycle (cracking cycle). The initial stiffness of C12S and C16S was higher than C12 and C16 by 66% and 27%, respectively. The cracking moment was detected at the point of slope-changing at the moment-curvature relationship in Figure 4.24. Cracking point of C12 was not obvious at the moment-curvature response. Therefore, the moment-axial strain of C12 was utilized to determine the cracking point, as shown in Figure 4.24 (up-right). The cracking moment of C12, C12S, C16,

`

and C16S was 15 kN, 22 kN, 31 kN, and 31.5 kN, respectively. In C12S, sand coating improved the initial stiffness and the cracking moment, while; in C16S, enhanced the initial stiffness only.

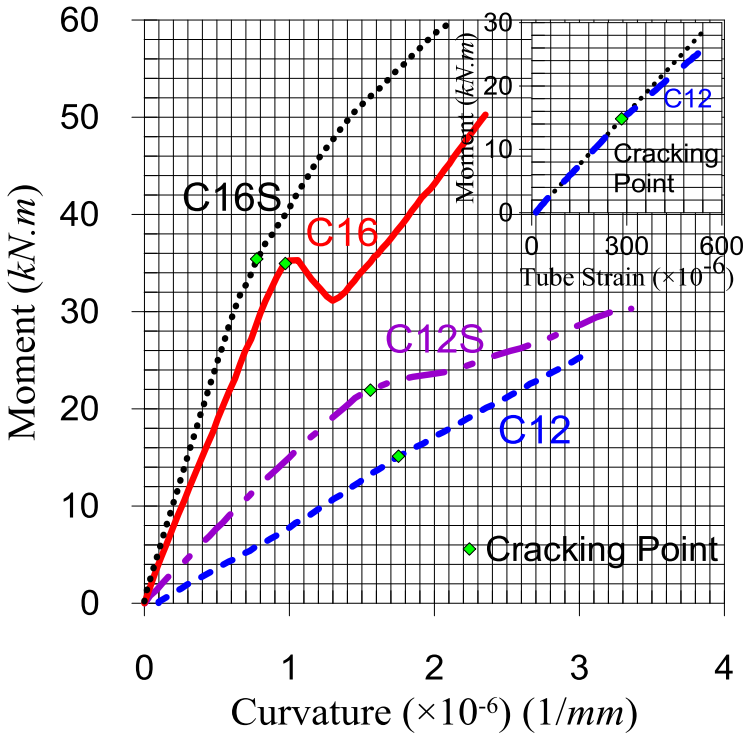

Figure 4.24: Moment-curvature response at the cracking cycle

4.4.12. Dissipated energy and damping ratio

For each cycle, the cumulative dissipated energy is calculated as the enclosed area within the hysteretic loop (Chopra 2007; Priestley et al. 1996). Figure 4.25 shows the cumulative dissipated energy-lateral drift responses for each specimen. Dissipated energy response of C12 was like C12S until 5% drift ratio after that C12 response increased significantly. Dissipated energy responses of C16 and C16S were identical until the specimen failure.

The dissipated energy was used to calculate the damping ratio ξ of each column. The damping ratio was determined as "$\xi = E_h$ / (4π Ee)" (Chopra 2007; Priestley et al. 1996), where "E_h" is the energy dissipation and "E_e" is the elastic strain energy stored in an equivalent linear elastic system under static conditions. The elastic strain energy was calculated as "$E_e = 0.5\ V_m\ \Delta_m$", where "V_m" and "Δ_m" represent the average peak force and displacement values, respectively (Clough and Penzien 2013). Figure 4.26 illustrates the damping ration-drift ratio relationship for

each column. The calculated damping ratios at 0.25% drift ratio were 5.7%, 10.67%, 6%, and 6.75% for C12, C12S, C16, and C16S, respectively. The damping ratio of C12 decreased from 5.7% to 2.62% in 3%-drift ratio posteriorly, increased continuously to 5% in 9%-drift ratio. Column C12S has recorded the minimum damping ratio of 2.11% at 6.25%-drift ratio. Generally, the minimum damping ratio is preferable in the seismic design and CFFT columns indicated a small damping ration comparing to the reinforced concrete columns.

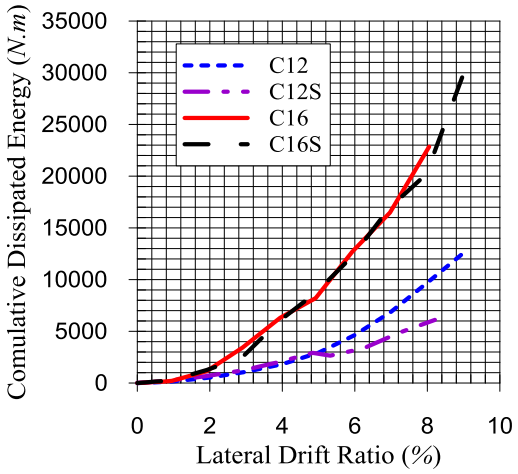

Figure 4.25: Cumulative dissipated energy versus drift ratio

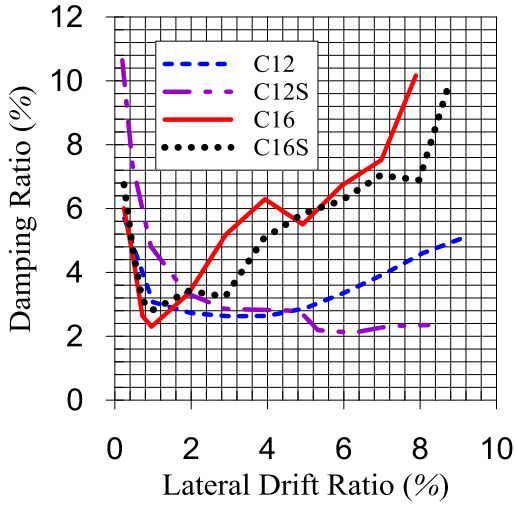

Figure 4.26: Damping ratio versus drift ratio

4.4.13. Residual displacement

For all columns, Figure 4.27 presents the average residual displacement-drift ratio responses. The residual displacement was captured at the end of each cycle as the displacement of the column at zero loading (Priestley et al. 2007). Column C12S exhibited the lower residual

`

displacement response as compared to the other columns. The residual displacement responses of C16 and C16S were significantly increased because of the high slippage between column and footing in addition to the earlier spalling of the footing concrete cover.

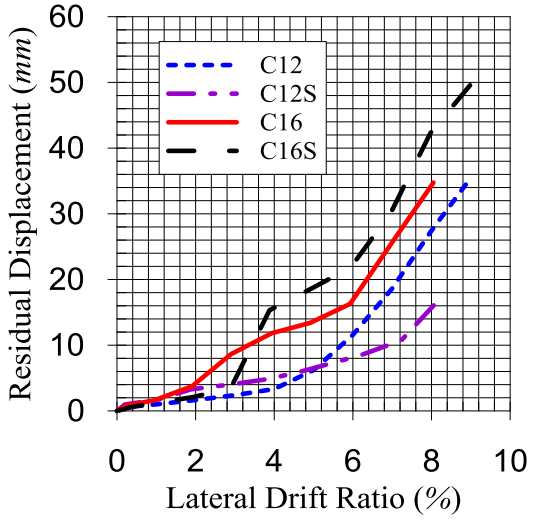

Figure 4.27: Residual displacement versus drift ratio

4.5. Discussion

4.5.1. Composite action of CFFT columns

This section introduces an evaluation of the composite action performance between the FRP tube and the concrete core based on the previous results. Columns C12 and C16 exhibited debonding between the tube and the concrete core that was confirmed by the internal and external strains comparison. In addition, the high slippage values between the concrete core and the FRP tube of C12 substantiated also the debonding. Additionally, the initial stiffness of C12 and C16 was lower than C12S and C16S, respectively. The initial stiffness illustrated that the debonding of C12 and C16 occurred before the testing. The debonding was developed as a result of the autogenous shrinkage of the concrete core. The autogenous shrinkage of the concrete core generated a gap between the concrete core and the FRP tube. The interface gap in CFFT members was mentioned before in researches related to the composite action of concrete-filed steel tubes (Roeder et al. 1999).

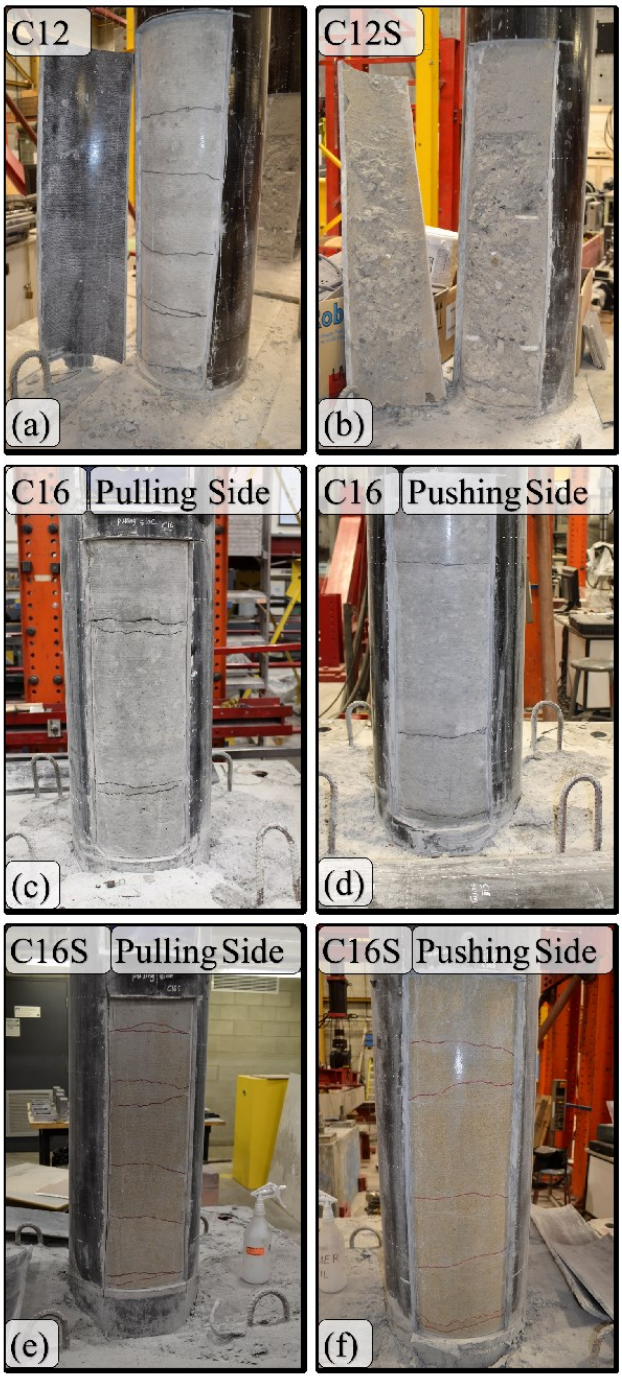

Figure 4.28: Damage of the concrete core after removing the GFRP tube

Column C12S attained a full composite action that was proved also by the strains comparison and the slippage observation. A partially composite action was detected in column C16S. C16S demonstrated full composite action until the debonding materialized between +1%

`

to -3% drift ratio. The debonding was detected in the exterior and interior strains comparison of C16S (Figure 4.17 to Figure 4.19).

The FRP tubes were removed above the footing surface to realize the damage in the concrete core; as shown in Figure 4.28. Parts of the concrete core of C12S were stuck on the removed part of the tube, as shown in Figure 4.28(b), which proves the composite action between the concrete core and the tube. On the other hand, the concrete core-tube interface of C12 and C16 was smooth, as shown in Figure 4.28(a, c, and d). In column C16S, the sand coating has abandoned the tube and stuck to the concrete core, as shown in Figure 4.28(e and f). Accordingly, the debonding of C16S occurred in the epoxy layer.

4.5.2. Effect of tube size on the interface gap size

Concrete shrinkage depends on the environment and on the configuration and size of the specimen. Generally, Shrinkage strain is usually adversely proportional to the ratio of the volume of the specimen to its surface area (Bažant and Sandeep 1995). The shrinkage stain of C12 is equal to the shrinkage strain of C16, but the absolute shrinkage value of C16 will be higher than C12. Consequently, the concrete core of C16 shrank more than C12 by 36%. Therefore, the interface gap size of C16 was higher than C12 also by the same percent. The interface gap size of C12S was zero. That is also confirmed by the previous results for concrete filled steel tube. The experimental results of (Roeder et al. 1999) reported that concrete core shrinkage could lead to very little bond in large diameter tubes.

4.5.3. Effect of interface gap size

It is clear from the interior compressive strain response of the specimens (Figure 4.17 to Figure 4.19), interface gap size affected on the confinement performance of columns. In column C16 has the largest interface gap, the concrete core behaved as unconfined concrete; as shown in Figure 4.17. While the concrete cores of C12 and C16S performed as partially confined concrete (Figure 4.17 to Figure 4.19). Concrete core of column C12S who accomplished the full composite action, interacted as confined concrete (Figure 4.17 to Figure 4.19). This analysis is confirmed by the results of the hoop strain; where C12S attained the maximum hoop strain in all columns; as shown in Figure 4.22.

The cracks distribution of the concrete core along the column height was affected by the interface gap size. All observed cracks were horizontal. There was a convergence between the cracks in columns C12 and C16S; as shown in Figure 4.28(a, e, and f); while divergence of the cracks of C16 was noticed; as shown in Figure 4.28(c and d).

As observed in specimens C12 and C16, increasing the interface gap led to decrease the flexural capacity and stiffness. Flexural strength of C12 has equaled the flexural capacity of the empty tube approximately; while the flexural strength of C16 was lower than the capacity of the empty tube; as shown in Figure 4.15. Presence of the interface gap eliminated the utility of filling the FRP tube by concrete. Consequently, using large-scale FRP tubes without any bond enhancer and filled with unreinforced normal concrete, had adversely affected on CFFT members.

4.5.4. Effect of sand-coating

Sand–coating attained the full composite action in column C12S, while minimized the interface gap effect in specimen C16S. Utilizing sand-coating as a bond enhancer improved the interfacial bond between the FRP tube and the concrete core. In addition to increasing the flexural strength and stiffness of CFFT members; although the negative effect of the interface gap; as shown in Figure 4.21.

4.6. Conclusions and recommendations

An experimental investigation was incurred to study the effect of the interfacial bond between the FRP tube and the concrete core on the flexural behavior of CFFT columns under lateral cyclic load. The tested columns consisted of two different sizes to examine the column size effect on the tube-concrete interfacial bond performance. The evaluation of the composite action was established based on a novel approach rather than the previous imprecisely approaches, which depended only on the slippage between the concrete core and the FRP tube. This novel approach mainly relies on comparing the strains inside the concrete core with its corresponding strains on the tube skin at the same alignment. Composite action analysis of four full-scale CFFT columns demonstrated the following points:

1. Failure of all columns was detected by FRP tube rupture at the column base on the compression side due to the buckling of the FRP tube-wall. The slippage of the

`

columns out the footings was significantly observed for the specimens with 406 mm diameter.

2. Increasing column size increased the interface gap size. The interface gap generated on the contact between the concrete core and the FRP tube due to the shrinkage of the concrete core and the deficiency in the bond between the FRP tube and its concrete core.
3. Absence of the interfacial bond between the FRP tube and its concrete core increased the interface gap, reduced the flexural strength and stiffness of CFFT columns. In addition, the confinement of the concrete core squandered. The flexural strength of the CFFT column without sand-coating was approximately equal to the flexural capacity of the empty tube.
4. Slippage between the FRP tube and the concrete core at the ends of the CFFT member considers an evidence of the debonding has occurred. On the other hand, no-slippage at the ends of the member cannot be considered as a confirmation for achieving the full composite action in CFFT members.
5. Columns without sand-coating suffered from early debonding before the testing due to the shrinkage of the concrete core that was confirmed by the initial stiffness of the tested columns.
6. The column “C12S” (with 305 mm diameter and sand-coating) achieved the full composite action until the failure, while the column C16S achieved full composite action until (+1% to -3%) drift ratio after that the debonding ensued. So that using sand-coating as a bond enhancer improved the flexural strength, stiffness, initial stiffness, and cracking moment of the tested-columns. Sand-coating achieved full composite action in the column with 305 mm diameter, while minimized the adverse effect of the interface gap in the column with 406 mm diameter due to the large size of its concrete core.
7. The results of the analysis were supported by cutting of the FRP tube after the test to examine the interface between the FRP tube and the concrete core. Some parts from the concrete core stuck on the removed part of the tube in the column who accomplished the full composite action. While the removed parts of the tubes from the other columns were smooth without any stuck concrete.

8. In the column with sand-coating and 406 mm diameter, sand-coating abandoned the FRP tube and stuck on the concrete core.

`

5. ANALYTICAL MODEL TO ESTIMATE THE FLEXURAL BEHAVIOR OF THE FULLY-BONDED CFFT

5.1. Introduction

This chapter proposing an analytical model to predict the flexural behavior of the fully-bonded CFFT. In the previous chapter, column C12S accomplished a full composite action between the FRP tube and its concrete core due to using sand-coating as a bond enhancer. Full composite actions mean the strain distribution over the cross-section is linear and the strain is linearly proportional to the distance away from the neutral axis of the cross-section. This model was implemented based on a section analysis to calculate the internal forces in the concrete using numerical integration (layer-by-layer). The assumptions of this model are the first principle design assumptions for reinforced concrete section under flexural and can be summarized as; the plain section remain plain after deformation and the strain distribution over the cross-section is linear (no slip ensues). This model has considered the concrete tension stiffening effect in the tension zone. This model was established based on trials and errors by assuming the compression zone depth and the tube strain to calculate the internal forces. The actual compression zone depth is reached when the equilibrium of forces occurs.

5.2. Materials Constitutive Models

5.2.1. FRP tube material model

The FRP tube material is considered a linear elastic material in tension and compression and has a constant modulus of elasticity (Young's modulus) E_l. Both stress and strain distribution along the cross-section are linear and proportionate together. Figure 5.1 shows the utilized constitutive model for the FRP tube; where f_{cl} and ε_{fuc} are the ultimate compressive strength and strain, respectively. The ultimate tensile strength and strain are expressed using f_{tl} and ε_{fut}, respectively.

Due to the linear stress strain relationship of the FRP tube, stress at any point is calculated as: $f_i = E_l \, \varepsilon_i$.

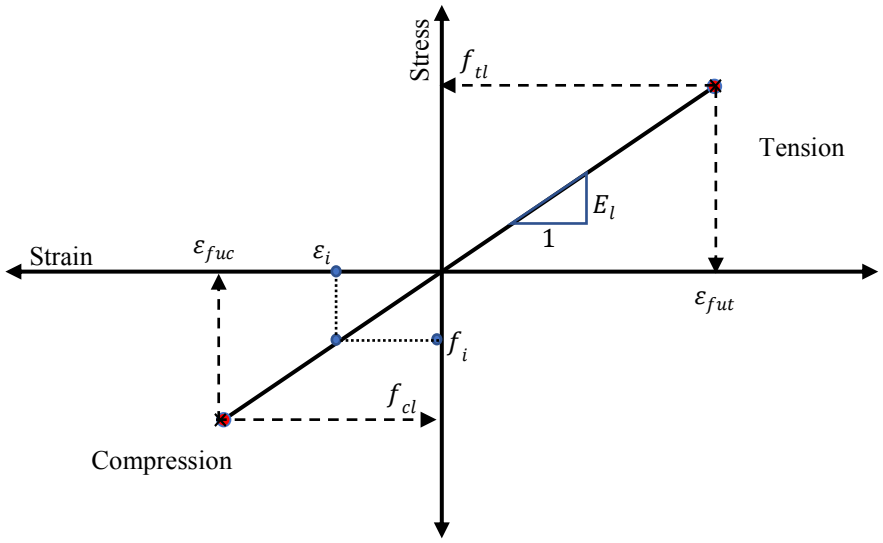

Figure 5.1: Material constitutive model of FRP tube

5.2.2. Concrete material model

The partially confined concrete model is used as proposed by (Abouzied and Masmoudi 2017). For concrete in compression, the model is established from the Popovics's model until the compressive stress f_c reaches f_c' pursued by plastic behavior with constant compressive strength equals f_c'; as shown in Figure 5.2. This model is nominated to provide an intermediate confinement level, that is appropriate for CFFT beams. The model is described in Eqns. (5.1) and (5.2). ε_c presents the compressive strain at any point along the cross-section. Where f_c' and ε_c' are the maximum compressive strength and its corresponding strain, as shown in Figure 5.2. The tangent modulus $E_{co} = 5000\sqrt{f_c'}$ and the secant modulus of concrete $E_{sec} = \frac{f_c'}{\varepsilon_c'}$ are required to calculate the factor r in Eq. (5.3).

$$f_c = f_c' \qquad \text{For } (\varepsilon_c \geq \varepsilon_c') \tag{5.1}$$

$$f_c = \frac{f_c' \, (\varepsilon_c/\varepsilon_c') \, r}{r-1+(\varepsilon_c/\varepsilon_c')^r} \qquad \text{For } (0 \leq \varepsilon_c \leq \varepsilon_c') \tag{5.2}$$

$$r = \frac{E_{co}}{E_{co} - E_{sec}} \tag{5.3}$$

Where f_c' and $\varepsilon_c' = \frac{2f_c'}{E_{co}}$ are the maximum compressive strength and its corresponding strain, as shown in Figure 5.3.

While the model represented by Vecchio and Collins (Collins and Mitchell 1997) used to model the participation of concrete in tension in Eqns. (5.4) and (5.5). Where ($f_{cr} = 0.62\sqrt{f_c'}$) and ($\varepsilon_{cr} = \frac{f_{cr}}{E_{co}}$) are the tensile strength of the concrete and the corresponding tensile strain.

$$f_c = \frac{f_{cr}\,\varepsilon_t}{\varepsilon_{cr}} \quad \text{For } (0 \le \varepsilon_t \le \varepsilon_{cr}) \tag{5.4}$$

$$f_c = \frac{\alpha_1\,\alpha_2\,f_{cr}}{1+\sqrt{500(\,\varepsilon_t - \varepsilon_{cr})}} \quad \text{For } (\varepsilon_t \ge \varepsilon_{cr}) \tag{5.5}$$

Where ε_t presents the tensile strain at any point along the cross-section; (α_1) is a factor accounting for the bond characteristics. The bond factor ranges in value from zero to 1.0, (α_2) is a factor accounting for the nature of loading and was taken as 0.7 for cyclic loading.

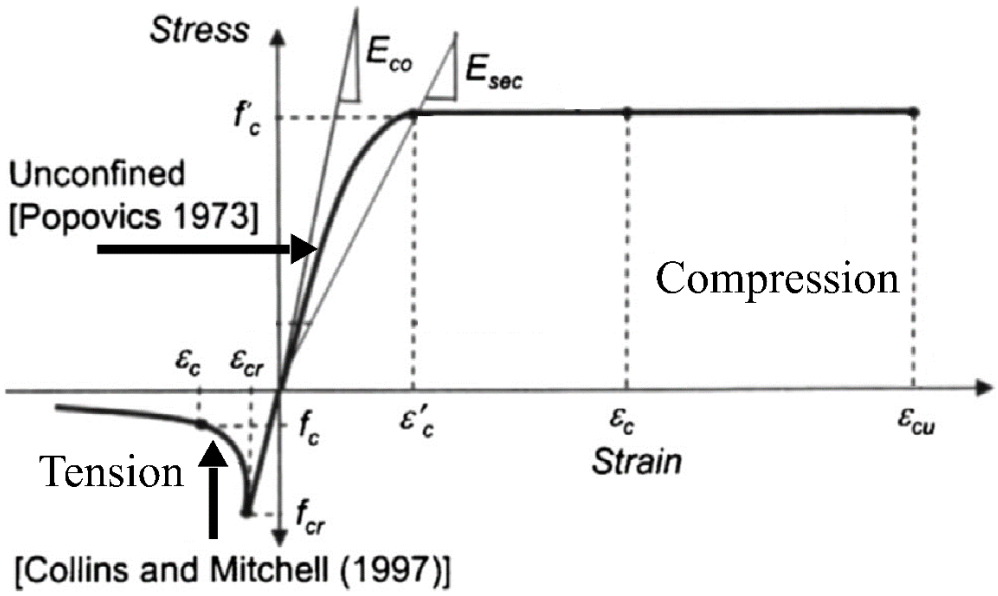

Figure 5.2: Material constitutive model of concrete

`

5.3. Geometry of the CFFT Cross-Section

The proposed model divides the cross-section of the circular CFFT member under flexural load into three zones based on the concrete core condition. The first zone is the concrete subjected to compression (compression zone), the second zone is the concrete subjected to tension and not cracked-concrete (tension-not cracked zone), and the third zone is the concrete subjected to tension and cracked (tension-cracked zone). Figure 5.3 shows the three zones of the CFFT section.

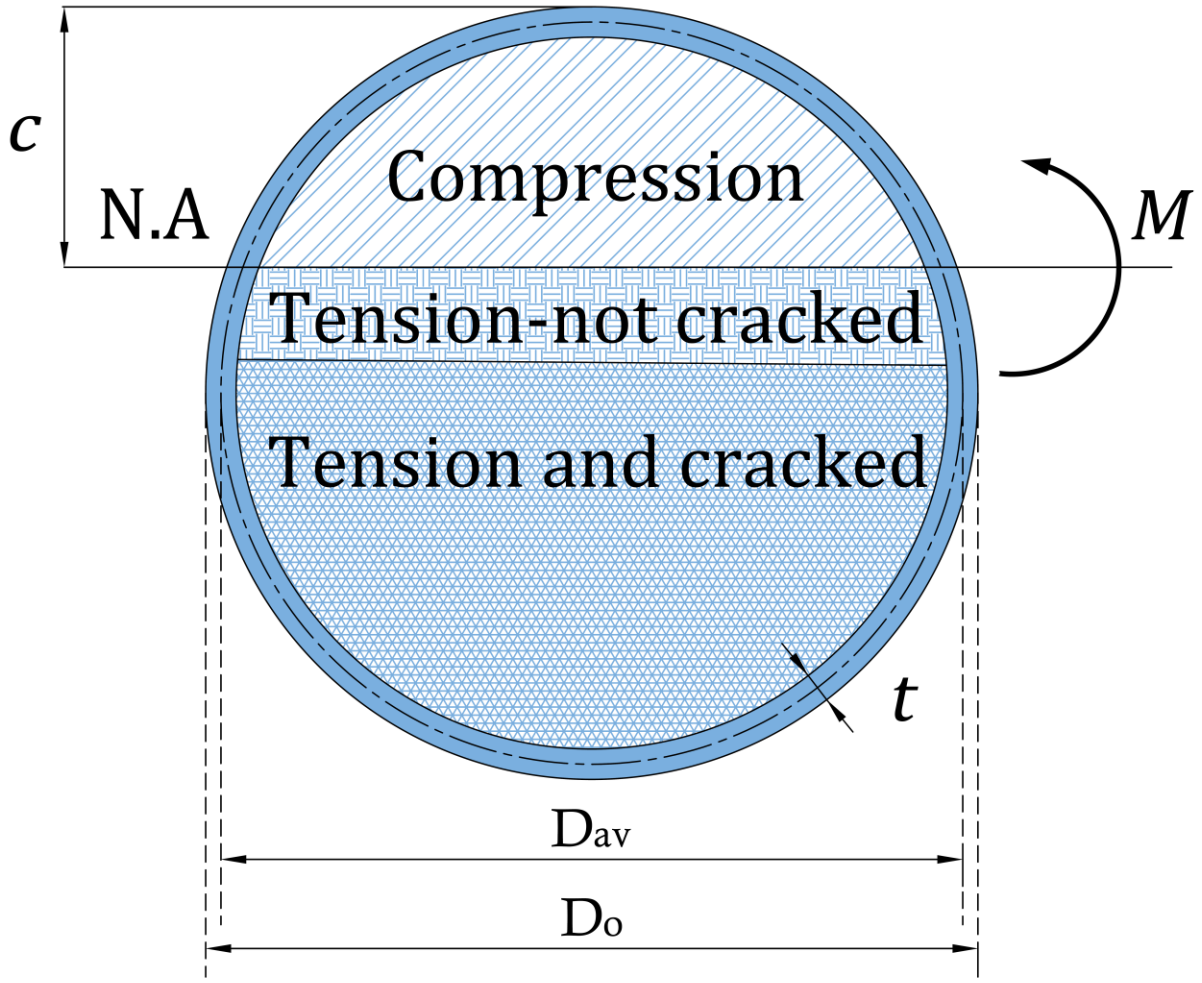

Figure 5.3: Zones of the CFFT member subjected to flexural load

The reinforcement of the CFFT member is the FRP tube. The tube is a continuous surface extended straight the depth. The tube is subjected to tension and compression stresses at the same time. The stress of the tube is varied along the cross-section depth from tensile stress to compressive stress. Figure 5.4 shows the geometry of the CFFT cross-section and the idealized geometry to apply the layer-by-layer approach. Each zone is divided into a certain number of layers to implement the numerical integration over the cross-section area. The compression zone is divided into n number of layers and the layer thickness is h_i. The tension-not cracked zone is divided into one-layer and the layer thickness is h_t. The tension-cracked zone is divided into m number of layers and the layer thickness is h_j. To establish the idealized geometry, Equation 5.6 to Equation 5.15 present the required parameters for the compression zone, Equation 5.16 to Equation 5.24 present the required parameters for the tension-not cracked zone, and Equation 5.25 to Equation 5.33 present the required parameters for the tension-cracked zone.

For a given layer i the compression zone:

$$D_{av} = D_o - t \tag{5.6}$$

$$h_i = \frac{c - 0.5t}{n} \tag{5.7}$$

$$Yc(i) = h_i(i - 0.5) \tag{5.8}$$

$$\phi(i) = \cos^{-1}\left[\frac{0.5D_{av} - Yc(i)}{0.5D_{av}}\right] \tag{5.9}$$

$$\phi1(i) = \cos^{-1}\left[\frac{0.5D_{av} - Yc(i) + 0.5h_i}{0.5D_{av}}\right] \tag{5.10}$$

$$\phi2(i) = \cos^{-1}\left[\frac{0.5D_{av} - Yc(i) - 0.5h_i}{0.5D_{av}}\right] \tag{5.11}$$

$$L(i) = 0.5D_{av}[\phi2(i) - \phi1(i)] \tag{5.12}$$

$$B(i) = D_{av}\sin\phi(i) \tag{5.13}$$

$$A_f(i) = 2tL(i) \tag{5.14}$$

$$A_c(i) = h_iB(i) - 0.5A_f(i) \tag{5.15}$$

`

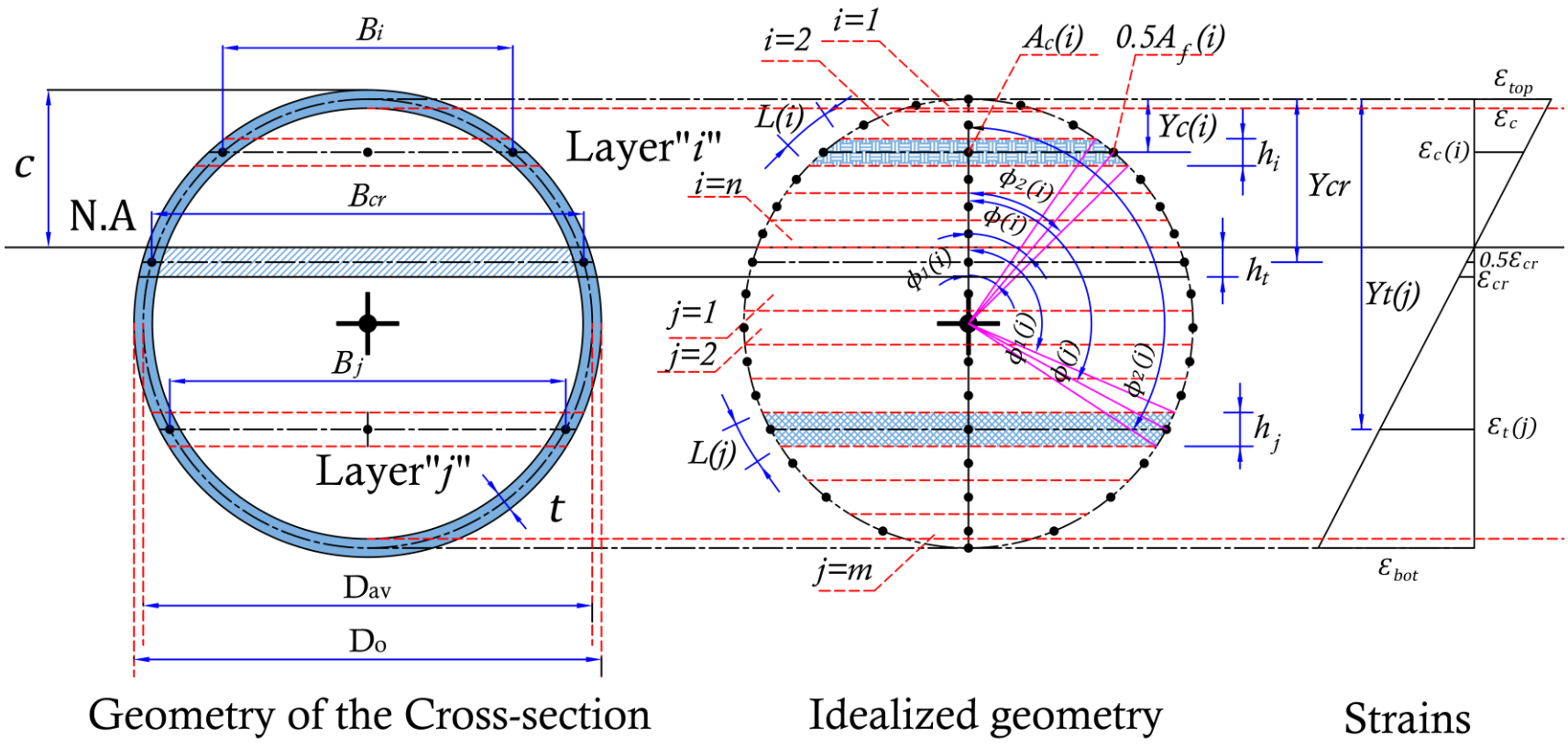

Figure 5.4: Geometry of the CFFT cross-section

For the layer of the tension-not cracked zone:

$$h_t = \frac{\varepsilon_{cr}(c - 0.5t)}{\varepsilon_{top}} \tag{5.16}$$

$$Ycr = c - 0.5(h_t - t) \tag{5.17}$$

$$\phi(t) = \cos^{-1}\left[\frac{0.5D_{av} - Ycr}{0.5D_{av}}\right] \tag{5.18}$$

$$\phi 1(t) = \cos^{-1}\left[\frac{0.5D_{av} - Ycr + 0.5h_t}{0.5D_{av}}\right] \tag{5.19}$$

$$\phi 2(t) = \cos^{-1}\left[\frac{0.5D_{av} - Ycr - 0.5h_t}{0.5D_{av}}\right] \tag{5.20}$$

$$L(t) = 0.5D_{av}[\phi 2(t) - \phi 1(t)] \tag{5.21}$$

$$B(t) = D_{av} \sin \phi(t) \tag{5.22}$$

$$A_f(t) = 2tL(t) \tag{5.23}$$

$$A_c(t) = h_t B(t) - 0.5A_f(t) \tag{5.24}$$

For a given layer j tension-cracked zone:

$$h_j = \frac{D_{av} + 0.5t - c}{m} \tag{5.25}$$

$$Yt(j) = c - 0.5t + \ h_j(j - 0.5) \tag{5.26}$$

$$\phi(j) = \cos^{-1}\left[\frac{0.5D_{av} - Yt(j)}{0.5D_{av}}\right] \tag{5.27}$$

$$\phi 1(j) = \cos^{-1}\left[\frac{0.5D_{av} - Yt(j) + 0.5h_j}{0.5D_{av}}\right] \tag{5.28}$$

$$\phi 2(j) = \cos^{-1}\left[\frac{0.5D_{av} - Yt(j) - 0.5h_j}{0.5D_{av}}\right] \tag{5.29}$$

$$L(j) = 0.5D_{av}[\phi 2(j) - \phi 1(j)] \tag{5.30}$$

`

$$B(j) = D_{av} \sin \phi(j) \quad (5.31)$$

$$A_f(j) = 2tL(j) \quad (5.32)$$

$$A_c(j) = h_j B(j) - 0.5A_f(j) \quad (5.33)$$

Where, (i) refers to the compression zone layers, (t) refers to the tension-not cracked layer, and (j) refers to the tension-cracked zone layers. D_o is the outer diameter and t is the thickness of the tube. D_{av} is the average diameter of the tube. $L(i)$ or $L(t)$ or $L(j)$ is the length of the part of the perimeter of the tube within the layer on one side. $Yc(i)$ or Ycr or $Yt(j)$ is the depth of the centre of the layer from the top level. $\phi 1(i)$ or $\phi 1(t)$ or $\phi 1(j)$ and $\phi 2(i)$ or $\phi 2(t)$ or $\phi 2(j)$ are the angles in radians between the vertical centre line of the section and the two radiuses bounding the length of the arc $L(i)$ or $L(t)$ or $L(j)$. $A_f(i)$ or $A_f(t)$ or $A_f(j)$ is the area of the part of the tube at the two sides within the layer. $A_c(i)$ or $A_c(t)$ or $A_c(j)$ is the net area of concrete within the layer. $B(i)$ or $B(t)$ or $B(j)$ is the width of the layer at its mid-thickness. $\phi(i)$ or $\phi(t)$ or $\phi(j)$ is the angle between the vertical centre line of the section and the radius reaching to the perimeter at the level of the mid thickness of the layer. c is the depth of the compression zone from the top surface of the tube. ε_{top} the strain at the extreme fibers of the tube in compression.

5.4. Equilibrium of Internal Forces and Moments

The internal forces (compression or tension) of each layer at any zone in the cross-section consist of forces in the concrete and forces in the FRP. The internal force is calculated simply by multiplying the area of the layer ($A_f(i)$ or $A_f(t)$ or $A_f(j)$ or $A_c(i)$ or $A_c(t)$ or $A_c(j)$) by the stress corresponding stress at the level of the mid thickness of the layer ($f_{fc}(i)$ or $f_f(t)$ or $f_{ft}(j)$ or $f_c(i)$ or $0.5\ f_{cr}$ or $f_t(j)$). Figure 5.5 shows the stress and the strain distribution along the depth of the CFFT cross section. The stress corresponding to each layer is mainly depending on the stain. The following equations present the stain at each layer as a function in the depth of compression zone c, level of the layer mid-thickness, the average diameter of the tube. D_{av}, and the strain at the extreme fibers of of the tube in compression ε_{top}.

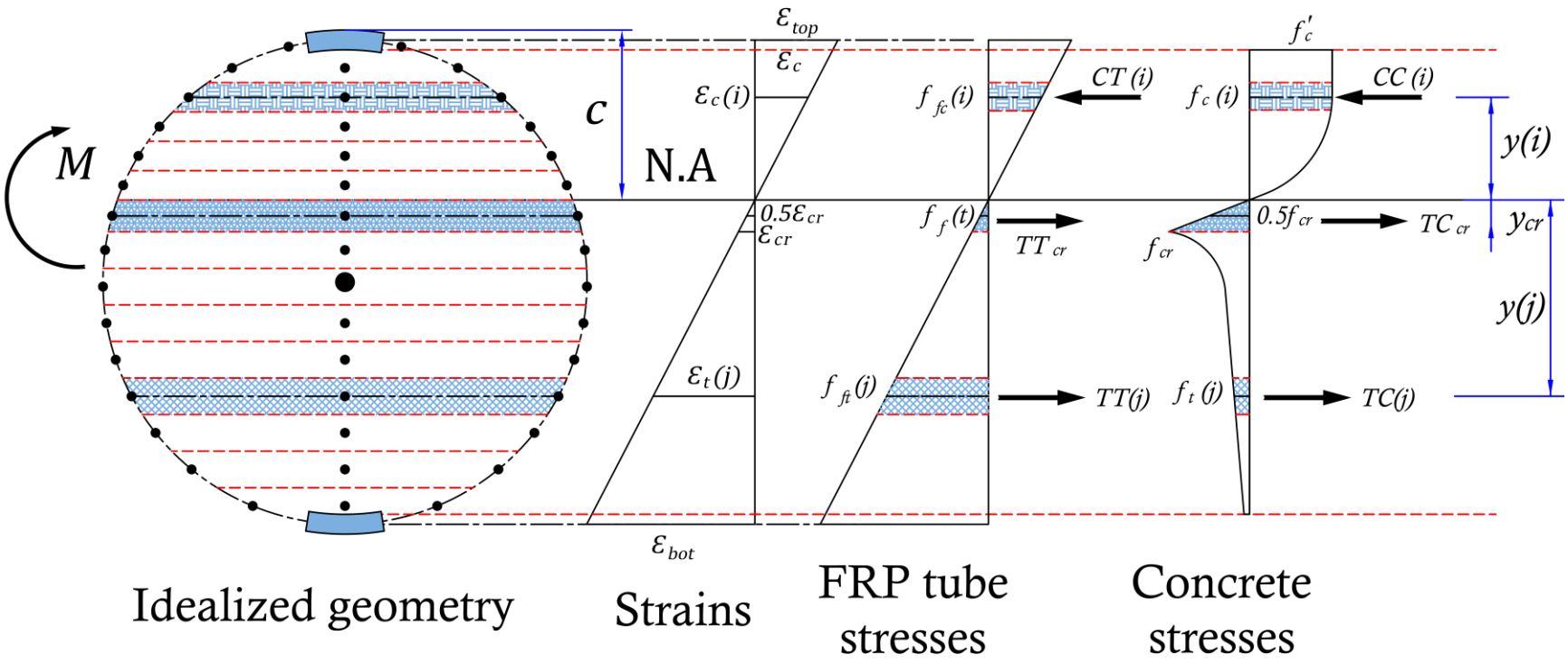

Figure 5.5: Stress and strain distribution along the depth of the cross-section

For a given layer i the compression zone:

$$\varepsilon_c(i) = \varepsilon_{top}\frac{c - 0.5t - Yc(i)}{c - 0.5t} \quad \leq \quad \varepsilon_{fuc} \tag{5.34}$$

The stress in the FRP at the layer level in the compression zone $f_{fc}(i)$ is calculated as:

$$f_{fc}(i) = E_l\, \varepsilon_c(i) \quad \leq \quad f_{cl} \tag{5.35}$$

The compression force in the FRP tube for a given layer i in the compression zone is $CT(i)$ and is calculated as:

$$CT(i) = f_{fc}(i)\, A_f(i) = E_l\, \varepsilon_c(i)\, A_c(i) \tag{5.36}$$

The stress in the concrete at the layer level in the compression zone $f_c(i)$ is calculated according to the equation 5.1 if $(\varepsilon_c(i) \geq \varepsilon_c')$ or following the equation 5.2 if $(0 \leq \varepsilon_c(i) \leq \varepsilon_c')$.

The compression force in concrete for a given layer i in the compression zone is $CC(i)$ and calculated as:

$$CC(i) = f_c(i)\, A_c(i) \tag{5.37}$$

The total compression force in the concrete and the FRP tube in the compression zone is C_{total} calculated according to the following equation:

$$C_{total} = C_{tube} + C_{concrete} = \sum_{i=n}^{i=1} CT(i) + \sum_{i=n}^{i=1} CC(i) \tag{5.38}$$

For the layer of the tension-not cracked zone:

$$\varepsilon(t) = 0.5\, \varepsilon_{cr} \;= 0.5\, \frac{f_{cr}}{E_{co}} \;= 0.5\, \frac{0.62\sqrt{f_c'}}{E_{co}} = \frac{0.31\sqrt{f_c'}}{E_{co}} \tag{5.39}$$

The stress in the FRP at the layer level in the tension-not cracked zone $f_f(t)$ is calculated as:

$$f_f(t) = E_l\, \varepsilon(t) \quad \leq \quad f_{tl} \tag{5.40}$$

The tension force in the FRP tube for the layer of the tension-not cracked zone is TT_{cr} and is calculated as:

$$TT_{cr} = f_f(t)\, A_f(t) \qquad (5.41)$$

The stress in the concrete at the layer of the tension-not cracked zone is $0.5\, f_{cr} = 0.31\sqrt{f_c'}$.

The tension force in concrete for the layer of the tension-not cracked zone is TC_{cr} and is calculated as:

$$TC_{cr} = 0.5\, f_{cr}\, A_c(t) \qquad (5.42)$$

The total tension force in the concrete and the FRP tube in the tension-not cracked zone is T_{cr} calculated according to the following equation:

$$T_{cr} = TC_{cr} + TT_{cr} = 0.5\, f_{cr}\, A_c(t) \;\; + E_l\, \frac{0.31\sqrt{f_c'}}{E_{co}}\, A_f(t) \qquad (5.43)$$

For a given layer j in the tension-cracked zone:

$$\varepsilon_t(j) = \varepsilon_{top} \frac{Yt(j) - (c - 0.5t)}{c - 0.5t} \quad \leq \quad \varepsilon_{fut} \qquad (5.44)$$

The stress in the FRP at a given layer j in the tension-cracked zone $f_{ft}(j)$ is calculated as:

$$f_{ft}(j) = E_l\, \varepsilon_t(j) \;\; \leq \;\; f_{tl} \qquad (5.45)$$

The tension force in the FRP tube at a given layer j in the tension-cracked zone is $TT(j)$ and is calculated as:

$$TT(j) = f_{ft}(j)\, A_f(j) \;\; = E_l\, \varepsilon_t(j) \;\; A_f(j) \qquad (5.46)$$

The stress in the concrete at a given layer j in the tension-cracked zone $f_t(j)$ is calculated according to the equation 5.4 if $(0 \leq \varepsilon_t(j) \leq \varepsilon_{cr})$ or following the equation 5.5 if $(\varepsilon_t(j) \geq \varepsilon_{cr})$.

The tension force in concrete at a given layer j in the tension-cracked zone is $TC(j)$ and is calculated as:

`

$$TC(j) = f_t(j)\, A_c(j) \tag{5.47}$$

The total tension force in the concrete and the FRP tube in the tension-not cracked zone is T_{total} calculated according to the following equation:

$$T_{total} = T_{tube} + T_{concrete} = \sum_{j=m}^{j=1} TT(j) + \sum_{j=m}^{j=1} TC(j) \tag{5.48}$$

The Equilibrium of the internal forced should satisfy the following condition:

$$C_{total} = T_{total} + T_{cr} \tag{5.49}$$

If this condition is fulfilled, the moments of each force can be calculated by multiplying the force of the strip by its distance away from the neutral axis of the cross section.

The moment of tube in the compression zone M_{CT} is calculated as the summation of the moments of all strips in the compression zone where, $M_{CT}(i) = CT(i)\, y(i)$ is the moment for one strip.

$$M_{CT} = \sum_{i=n}^{i=1} M_{CT}(i) = \sum_{i=n}^{i=1} [CT(i)\, y(i)] \tag{5.50}$$

The moment of concrete in the compression zone M_{Cc} is calculated as

$$M_{CC} = \sum_{i=n}^{i=1} M_{CC}(i) = \sum_{i=n}^{i=1} [CC(i)\, y(i)] \tag{5.51}$$

Where, $y(i)$ is the distance between the force and the neutral axis and is calculated as:

$$y(i) = c - 0.5t - Yc(i) \tag{5.52}$$

The moment of tube in the tension-not cracked zone M_{Tcr} is calculated as

$$M_{Tcr} = TT_{cr} * \frac{1}{2}\ h_t \tag{5.53}$$

The moment of concrete in the tension-not cracked zone M_{Ccr} is calculated as

$$M_{Ccr} = TC_{cr} * \frac{1}{2} h_t \quad (5.54)$$

The moment of tube in the tension-cracked zone M_{TT} is calculated as

$$M_{TT} = \sum_{j=m}^{j=1} M_{TT}(j) = \sum_{j=m}^{j=1} [TT(j)\, y(j)] \quad (5.55)$$

The moment of concrete in the tension-cracked zone M_{TC} is calculated as

$$M_{TC} = \sum_{j=m}^{j=1} M_{TC}(j) = \sum_{j=m}^{j=1} [TC(j)\, y(j)] \quad (5.56)$$

Where, $y(j)$ is the distance between the force and the neutral axis and is calculated as:

$$y(j) = Yt(j) - (c - 0.5t) \quad (5.57)$$

The total moment of the cross section M_{total} is calculated as:

$$M_{total} = M_{CC} + M_{CT} + M_{Ccr} + M_{Tcr} + M_{TC} + M_{TT} \quad (5.58)$$

The curvature (κ) of the section is the slope of the strain profile along the cross section and is calculated as:

$$\kappa = \frac{\varepsilon_{top}}{c - 0.5t} \quad (5.59)$$

5.5. Procedure of Analysis

The procedure of the model can be concluded in the following steps:

(1) Determine the dimensions and the mechanical of the tube and the concrete. Specify the number of layers at each zone (n and m).

`

(2) Assume the strain value of the top strain (ε_{top}) at the mid-thickness of the extreme fibers of the tube in compression. This value should consider the condition of ($\varepsilon_{top} \leq \varepsilon_{fuc}$).

(3) Assume the compression zone depth (c).

(4) Calculate the strain value of the bottom strain (ε_{bot}) at the mid-thickness of the extreme fibers of the tube in tension. Check the condition of ($\varepsilon_{bot} \leq \varepsilon_{fut}$), if it is satisfied go to the next step. If this condition did not satisfy go to step 3 and reassume another value for c.

(5) Calculate the internal force and establish the equilibrium equation. If the equilibrium is satisfied, go to the next step. If the equilibrium is not satisfied go back to step number 3 and reassume another value for c. Repeat this step until the equilibrium accomplished.

(6) Once the equilibrium is accomplished, calculate the internal moments and the corresponding curvature.

(7) Repeat this process from step 2 till the response of the moment-curvature is completed

(8) Determine the failure by comparing the strains at the failure with the strength of the tube. If $[\varepsilon_{top} \geq \varepsilon_{fuc}]$ and $[\varepsilon_{bot} < \varepsilon_{fut}]$that means compression failure. If $[\varepsilon_{top} < \varepsilon_{fuc}]$ and $[\varepsilon_{bot} \geq \varepsilon_{fut}]$that means tension failure.

5.6. Validation of the Model

The proposed model estimates the failure mode, flexural capacity (M_{total}), curvature (κ), and compression zone depth (c). The results of the model are validated with the experimental results of the specimen C12S. The model results showed a good agreement comparing to the experimental results. The model estimated compression failure as the experimental failure mode. The predicted flexural capacity of the section by the model was 525 kN.m. The estimated flexural capacity is the same as the maximum experimental recorded moment for C12S which was also 525 kN.m. The analytical moment-curvature ($M_{total} - \kappa$) response is close to the experimental one as shown in Figure 5.6. Figure 5.7 shows comparison between the experimental and the analytical compression zone depth-moment ($c - M_{total}$) response of C12S.

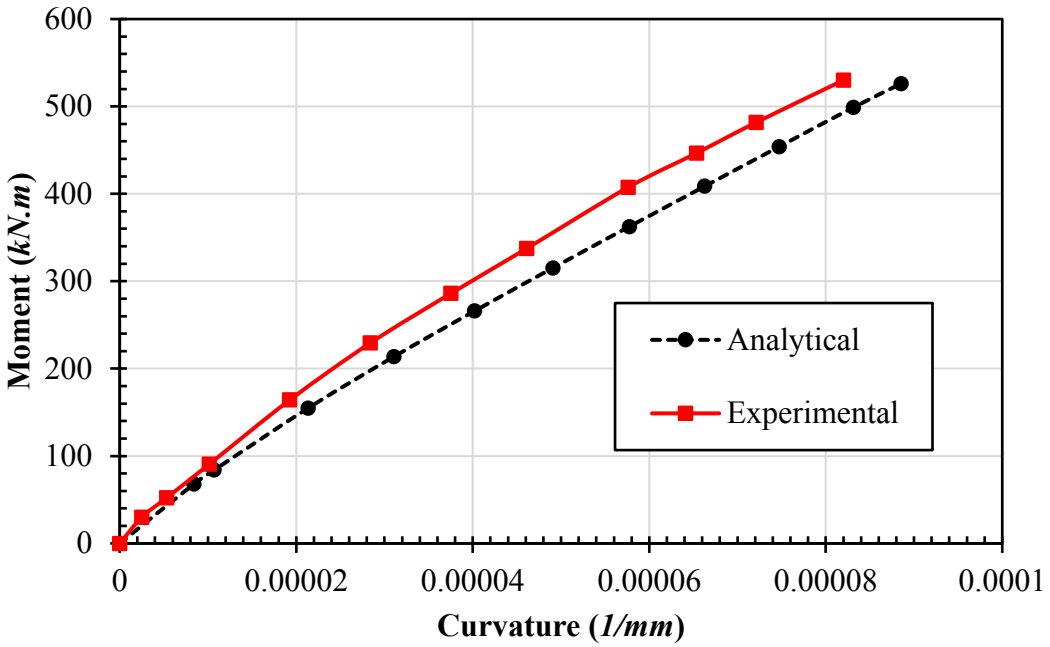

Figure 5.6: Comparison between the analytical and the experimental Moment-curvature response

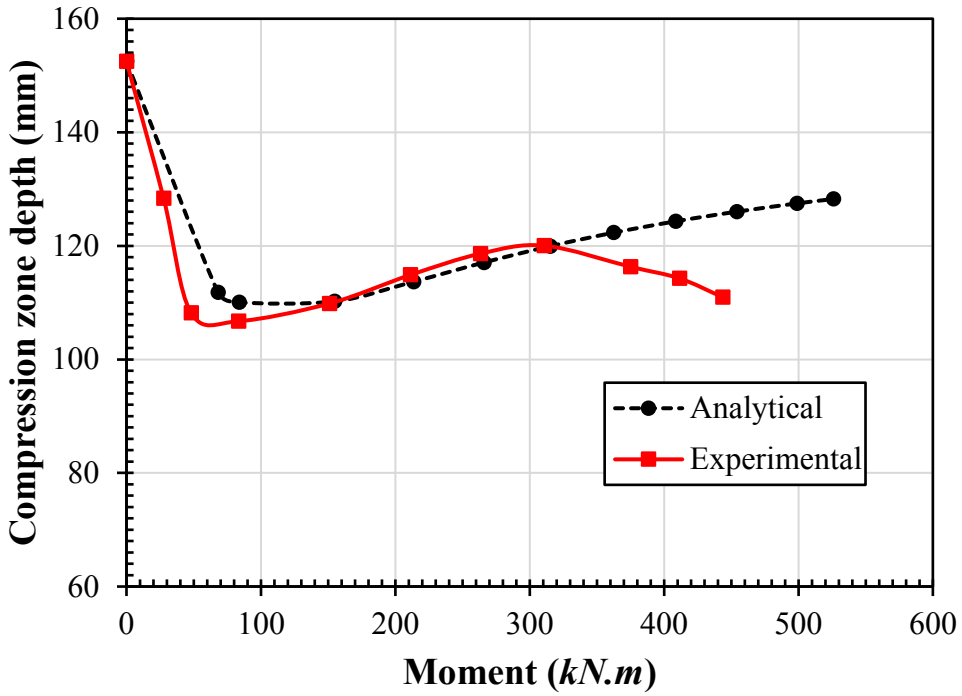

Figure 5.7: Comparison between the analytical and the experimental Moment-compression zone depth response

`

5.7. Conclusions

This chapter proposed an analytical model to predict the flexural behavior of the fully bonded CFFT members. The FRP tube material assumed as elastic isotropic. The compressive stress and forces of the concrete were estimated by using the layer-by-layer approach. The analytical results showed a good agreement comparing by the experimental results. This model estimated the failure mode, flexural capacity, compression zone depth, and curvature. The analytical model was used to plot the analytical moment-curvature ($M_{total} - \kappa$) response which is close to the experimental response.

6. EXPERIMENTAL AND ANALYTICAL INVESTIGATION OF NEW CONCRETE FILLED FRP TUBE BEAM-COLUMN CONNECTIONS

Foreword

Authors and Affiliation

- **Ahmed M. Ali:** Ph.D. candidate in the Department of Civil Engineering at Sherbrooke University, Sherbrooke, J1K 2R1, Quebec, Canada.
  E-mail: Ahmed.Ali3@usherbrooke.ca

- **Radhouane Masmoudi:** Professor at the University of Sherbrooke, Sherbrooke, J1K 2R1, Quebec, Canada.
  E-mail: Radhouane.Masmoudi@usherbrooke.ca

Journal Title: Elsevier— Journal of Engineering Structures

Submitted at: 30 June 2018

Acceptance Status: Under Review

Reference: A. M. Ali and R. Masmoudi, (2018). "Experimental and analytical investigation of new concrete filled FRP tube beam-column connections", *Journal of Engineering Structures*, Elsevier, (submitted).

6.1. Abstract

Researchers focused on investigating the behavior of concrete-filled fiber reinforced polymer (FRP) tube (CFFT) beams and/or columns individually, while the beam-column connections of such elements still obscure. The current study aimed at developing and investigating a simple and practical CFFT beam-column connection. The developed steel connection comprises hollow rectangular steel head supporting the CFFT beam using high-performance epoxy grout to provide an adequate bond. The hollow head was welded to steel end-plate, while the end-plate was fixed to the CFFT columns using eight high-strength bolts. Four different connection lengths were examined to investigate the required embedded length of the CFFT beams inside the connection and ensure adequate transmission of the loads through the connection. The experimental results showed that the optimal embedded depth required to induce flexural failure of the CFFT beam is two times the CFFT beam depth (i.e. FRP tube depth). An analytical model was developed to calculate the flexural capacity of the CFFT beam and estimate the optimal embedded depth required to achieve nominal flexural capacity.

Keywords

Fiber-reinforced polymer, Concrete-filled FRP tubes, CFFT connection, Beam-column connection, Monotonic loading, Bond, Embedment Length

[1] Ph.D. candidate, Department of Civil Engineering, University of Sherbrooke, Sherbrooke, QC, Canada, J1K 2R1. E-mail: Ahmed.Ali3@usherbrooke.ca

[2] Professor, Department of Civil Engineering, University of Sherbrooke, Sherbrooke, QC, Canada, J1K 2R1. E-mail: Radhouane.Masmoudi@usherbrooke.ca

6.2. Introduction

Steel-reinforced concrete elements are exposed to aggressive environments in northern climates, causing extensive damage and resulted in the need for costly rehabilitation due to corrosion of the steel reinforcement. Corrosion of steel is considered the main cause motivated the use of fiber-reinforced polymer (FRP) bars, due to the FRP-immunity to corrode (Benmokrane et al. 1996). During the last two decades, researchers developed different approached to overcome the damages caused by the harsh environmental conditions. One of the widely accepted approaches was using concrete-filled FRP tubes (CFFT) covering the exterior surface of the steel-RC members to increase the durability of the element. In CFFT members, the FRP tube is considered as a permanent lightweight formwork and provides longitudinal and transverse reinforcement. In addition, the FRP tube confines the concrete core which in turn increases the strength and the ductility of the member.

Extensive research has been conducted to address the behavior of the concrete-filled FRP tubes under axial (Fam and Rizkalla 2001; Mohamed and Masmoudi 2010d, 2008; Ozbakkaloglu 2013; Wang et al. 2017), flexural (Abouzied and Masmoudi 2015, 2017; Fam and Rizkalla 2002; Mohamed and Masmoudi 2010c, 2011, 2012), and axial-flexural loading (Fam et al. 2001, 2004). Limited studies attempted to investigate the connection between CFFT and RC-footing. For an instant, Zhu et al. (Zhu 2004; Zhu et al. 2006a) examined CFFT-footing connections with several configurations as precast, post-tensioned, and cast-in-place CFFT-footing connection. Another technique by using adhesive bond between the CFFT tube and steel-RC stub protruded from the footing top was also examined by Lai (Lai 2010). Additionally, Zakaib et al. (Zakaib and Fam 2012) implemented a moment connection of circular CFFT beams by embedding steel I-beam into circular CFFT section. The other end of the steel I-beam was welded to a steel plate fixed to a rigid steel assembly by four steel anchors to provide end fixation. Zakaib detailed that, the optimal embedment length of the steel section inside the CFFT member to attain the CFFT member flexural strength is 17% of the CFFT span (Zakaib and Fam 2012). To the authors' knowledge, no published study attempted to address the CFFT beam-column connection, a crucial step to implement the CFFT beams/columns in practice.

`

This chapter aims at developing a new assembly of CFFT beam-column connection for rectangular CFFT members. The connection was investigated experimentally and analytically to be widely utilized in the practice. The chapter also proposes design equations to calculate the flexural capacity of rectangular CFFT beams and the required embedded depth to achieve its flexural capacity.

6.3. Experimental Program

This section presents the properties of materials that were used in the construction of connections, preparation steps of test-specimens, test setup, and instrumentation.

6.3.1. Material Properties

6.3.1.1. FRP Tubes

The aim of the study was to develop and investigate CFFT beam-column connection, hence, beams and columns were fabricated using glass FRP (GFRP) tubes. The CFFT beam was fabricated using glass continues fibers impregnated in a polymeric polyester resin mixture (Pultrusion method) (Creative Pultrusions 2016). The pultruded tube's cross-section dimensions are 101.67 mm (4 inches) width, 152.5 mm (6 inches) depth, 7.67 mm (0.3 inch) flange thickness and 6.4 mm (0.25 inch) web thickness. The CFFT column consists of a filament winding GFRP tube fabricated using glass fiber impregnated with vinyl-ester resin. The filament winding machine in the Composite Material Reinforcement Laboratory of the University of Sherbrooke was used to fabricate the tube column with stacking sequences of 90/±30/90. The CFFT column tube's cross-section dimensions are 325 mm width, 426 mm depth, and 9.40 mm wall thickness. The mechanical properties of the fabricated tubes were measured by testing ten coupon specimens under axial tension and compression following the requirement of ASTM D3039/D3039M (2014) (ASTM D3039 2014) and ASTM D695 (2010) (ASTM D695 2010), respectively. Table 6-1 presents the dimensions and mechanical properties of the fabricated tubes, where B, H, t_f, t_w, E_l, f_{tl}, and f_{cl} are the tube width, tube depth, flange thickness, web thickness, modulus of elasticity, tensile strength, and compressive strength in the longitudinal direction, respectively. The interior sides of tubes were covered by sand-coating to provide an adequate bond, hence, the full composite action between the tube and the surrounding concrete core was fulfilled (Ali et al. 2017b).

Table 6-1: Tubes mechanical properties

	Type	*B (mm)*	*H (mm)*	t_f *(mm)*	t_w *(mm)*	E_l *(GPa)*	f_{tl} *(MPa)*	f_{cl} *(MPa)*
Beam tube	Pultrude filament winding	102	152.5	7.6	6.4	37.6	450	380
Column tube		325	426	9.4	9.4	13	115	95

6.3.1.2. Concrete

The tubes were filled with ready-mixed normal-weight concrete with 35 MPa target compressive strength; the concrete has aggregate size between 5-20 mm and slump of 80 ± 20 mm. For each specimen, a minimum of six concrete cylinders and three prisms were tested on at the same day of specimen testing, following the standard compressive test ASTM C39/C39M (ASTM C39 2016) and standard modulus of rupture test ASTM C78/C78M (ASTM C78M-16 et al. 2016), respectively. The average concrete compressive strength of the cylinders was equal to 37 MPa ± 2 MPa and the average modulus of rupture of prisms was 4.0 MPa ± 0.2 MPa.

6.3.1.3. Steel Reinforcement

The CFFT columns were internally reinforced using six 15M steel bars (15 mm diameter), distributed equivalently on each side. Three M10 stirrups were used at column extremities for fabrication purposes. Based on the data provided by the manufacturer, the steel reinforcement had a modulus of elasticity and yield tensile strength equal to 200 GPa, 420 MPa, respectively.

6.3.1.4. Steel Connection

Connections between CFFT beams and columns were developed using prefabricated steel assembly designed to transmit the loads between the two elements without experiencing any deformation. The steel connections consist of HSS head (A500 Grade C) welded to rigid steel end-plate. The yielding and ultimate strength of the HSS head as provided by the manufacturer were 317 MPa and 427 MPa, respectively, while the end-plate had yielding and ultimate strength of 300 MPa and 450 MPa, respectively. To support the flanges of the HSS head, two steel stiffeners with 13 mm thickness were used. Different heights of the HSS head (ranged between 200 mm to 450

`

mm) were used to investigate the adequate length required to induce failure at the CFFT beams. Details of the steel connections are depicted in Figure 6.1.

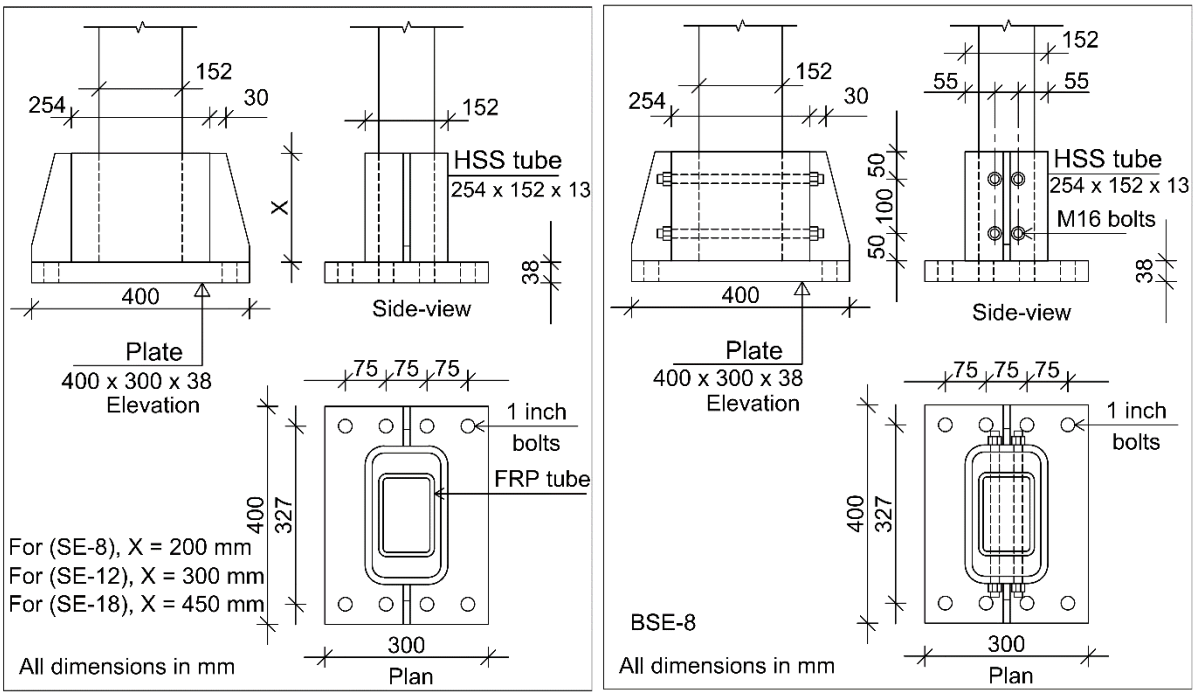

Figure 6.1: Details of the proposed connections

6.3.1.5. Epoxy Grout

The CFFT beam-column connection was designed to allow rotation of the CFFT beams yet providing adequate bonding to transmit the loads between the connection elements. Hence, high-performance epoxy grout was used to fill the hiatus between the CFFT beam and the HSS heads. The epoxy grout had a bond and tensile strength of 17 MPa and 14 MPa, respectively. The bond strength was sufficient to prevent failure due to debonding at the CFFT beam/epoxy grout interface.

6.3.2. Preparation and Description of the Test Specimens

Four CFFT beam-column connections were tested to investigate the behavior of the new connection (Figure 6.1). Three CFFT beams (SE-8, SE-12, and SE-18) aimed at determining the minimum required embedded depth to achieve the CFFT beam flexural capacity. Figure 6.2 shows

the preparation of the three specimens, at which the tubes were filled with concrete, then, aligned in the steel connection to pour the epoxy grout between the tube and connection. The fourth specimen (BSE-8) was fabricated with the smaller embedded depth of SE-8, however, reinforced with four threaded steel rods to prevent the slippage of the beams. The rods were fixed in the position shown in Figure 6.1 before pouring the grout or filling the CFFT beam with concrete for assemblage purpose. Figure 6.3 shows the preparation process of BSE-8.

Preparation of the CFFT columns started by drilling the holes and inserting the threaded rods required for fixing the connection assembly prior casting the concrete, as shown in Figure 6.4. Afterward, the connections assembly were aligned with the pre-drilled holes to insert the threaded rods, while another steel end-plate was fixed on the other side of columns to avoid the tube local failure under the steel nuts. Table 6-2 summarizes the specimens' details.

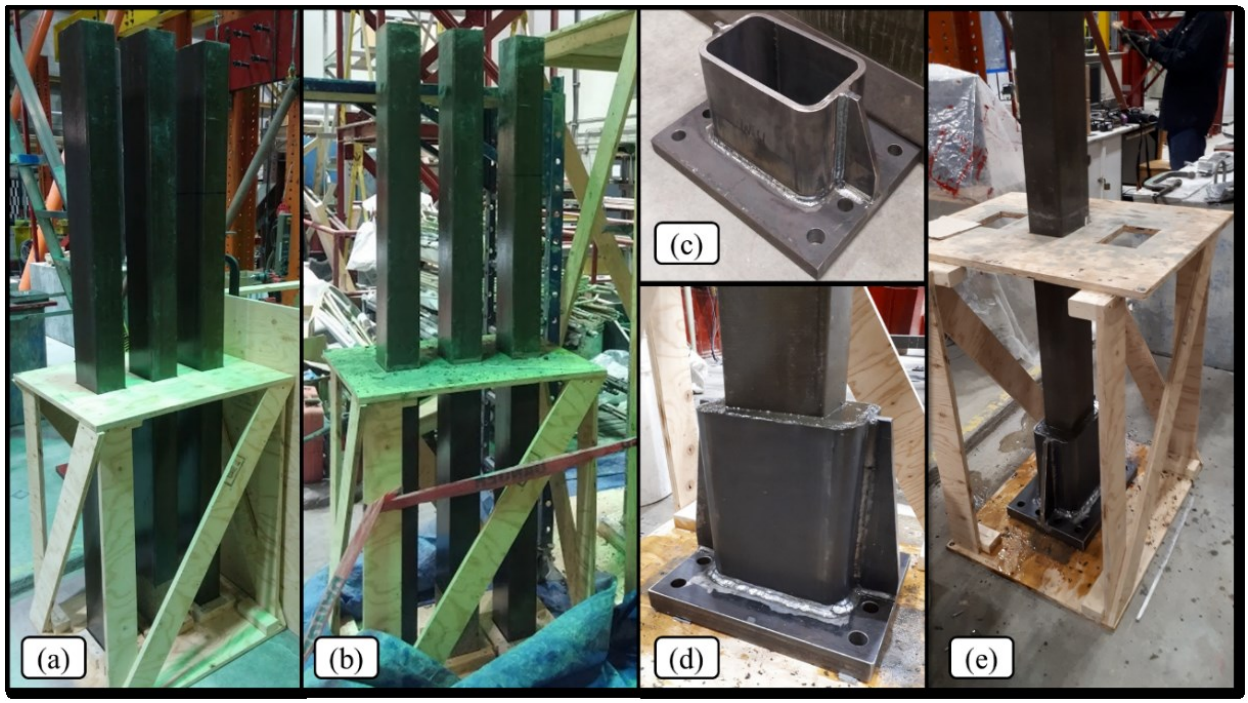

Figure 6.2: Preparation steps of the CFFT-beams: (a) GFRP tubes before casting. (b) During casting of concrete. (c) The steel connection (d) inserting the GFRP tube in the steel connection and casting epoxy grout in the gap. (e) The CFFT beam

`

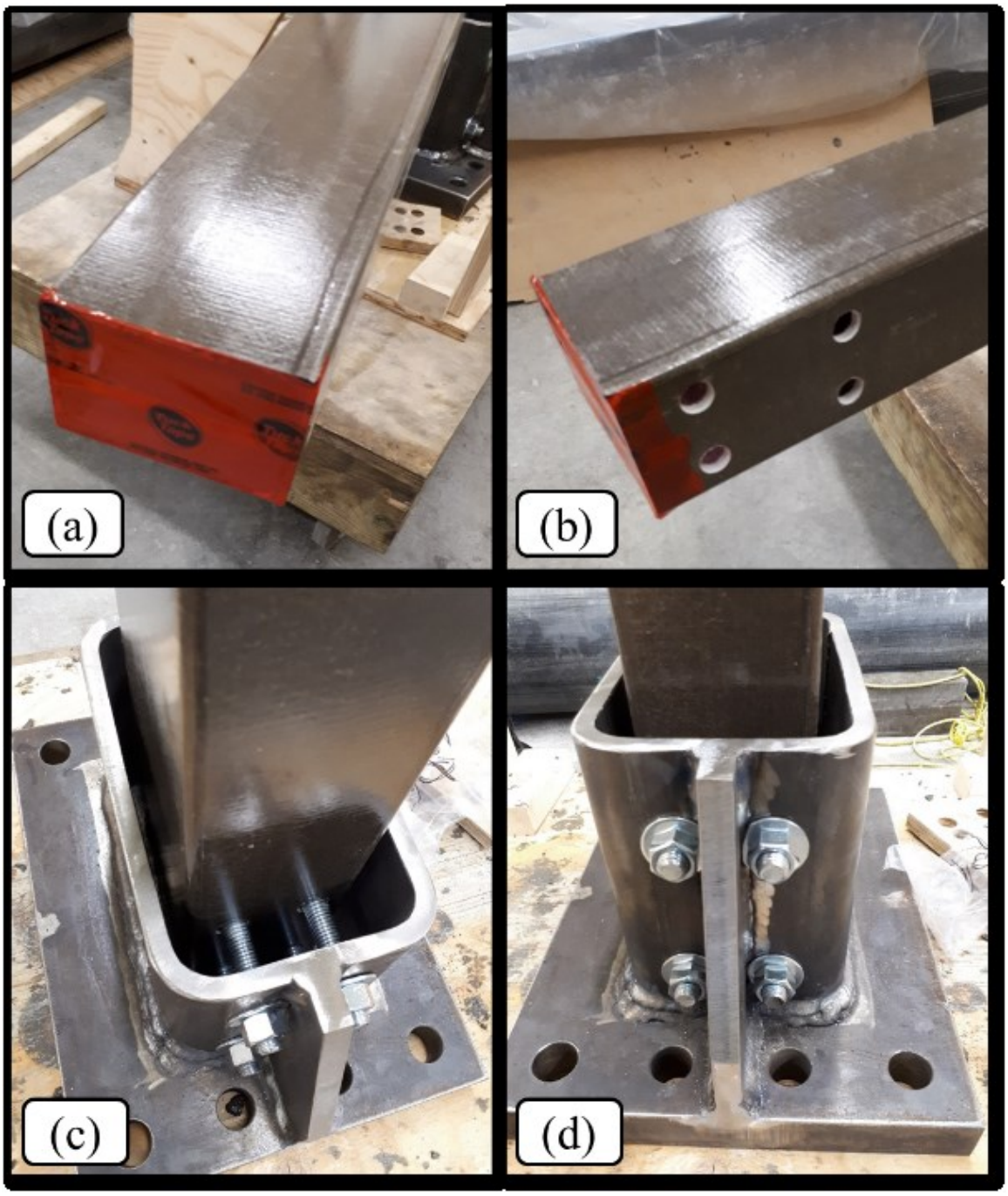

Figure 6.3: Preparation steps of the CFFT Beam BSE-8: (a) closing the bottom end of the tube. (b) Holes on the tube wall. (c) & (d) inserting the tube in the steel connection and passing four M16 threaded-bars through the steel connection and the tube

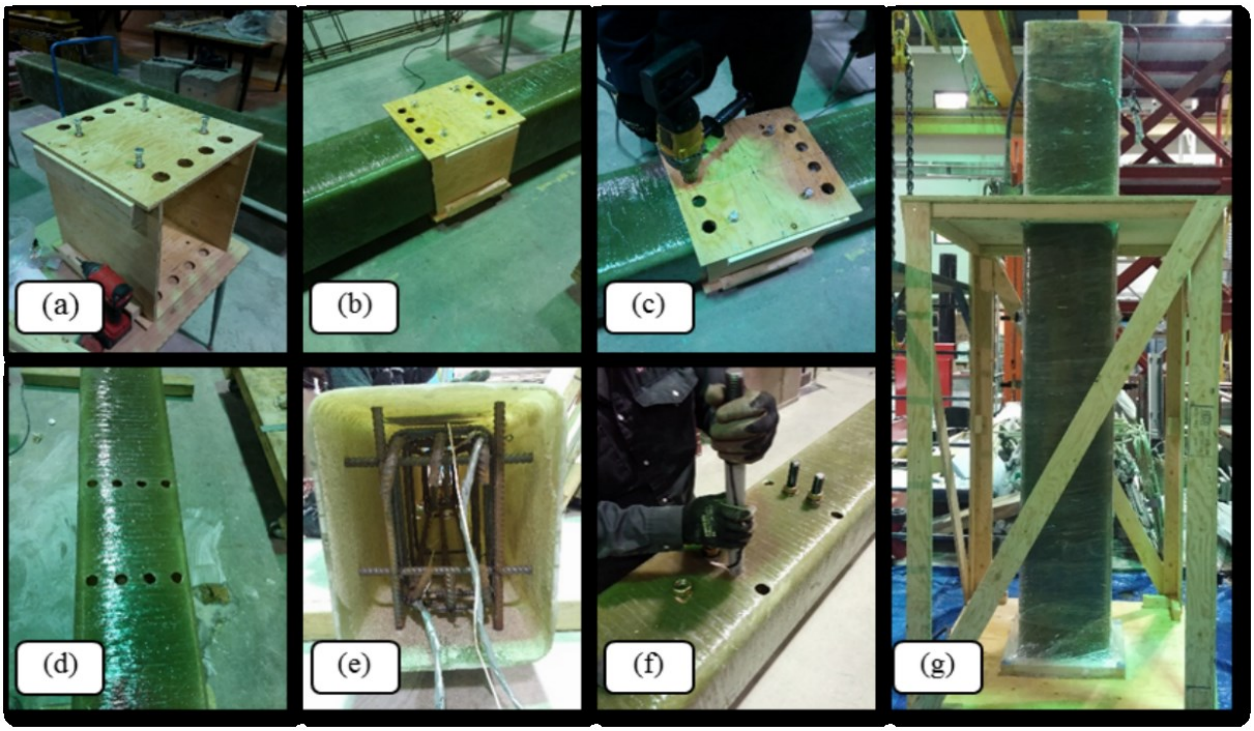

Figure 6.4: Preparation steps of the CFFT column: (a) wooden form with holes. (b) Inserting the GFRP tube in the wood form. (c) Drilling the holes in the GFRP tube. (d) The GFRP after drilling the holes. (e) Inserting of the steel cage. (f) Inserting the PVC plastic pipes in the holes. (g) Casting the concrete on the GFRP tube

Table 6-2: Details of the specimens

	d (mm)	*L_s (mm)*	*L_e (mm)*	*Notes*
SE-8	200	1838	1600	…..
SE-12	300		1500	…..
SE-18	450		1350	…..
BSE-8	200		1600	The beam tube is bolted to the steel connection using 4 threaded-bars M16.

Where *d is* the embedded depth of the CFFT beam into the steel connection
L_s is the shear-span of the CFFT beam (from loading point to the column face)
L_e is the CFFT clear span (from the loading point to the top surface of the grout), respectively.

`

6.3.3. Test Setup and Instrumentation

A typical view of the testing setup is shown in Figure 6.5. Testing of the samples was conducted by placing the CFFT columns horizontally on two fixed-like rigid steel supports. The steel supports were fixed to the rigid laboratory floor using four high strength threaded Dywidag bars. Each Dywidag bar was pre-tensioned to the rigid floor with 300 kN tensile force. The force was sufficient to prevent any deformation of the column ends during testing. Furthermore, the lateral movement of the CFFT was prevented through another lateral support attached to vertical rigid frames (see Figure 6.5).

Loads were applied laterally to the CFFT beams using 500-kN capacity hydraulic actuator. The actuator reaction was resisted using vertical steel frames attached to the laboratory floor and stiffened laterally against any horizontal deformation using four-inclined steel trusses. The loads were applied in displacement control using a constant rate of 1 mm/min up to failure.

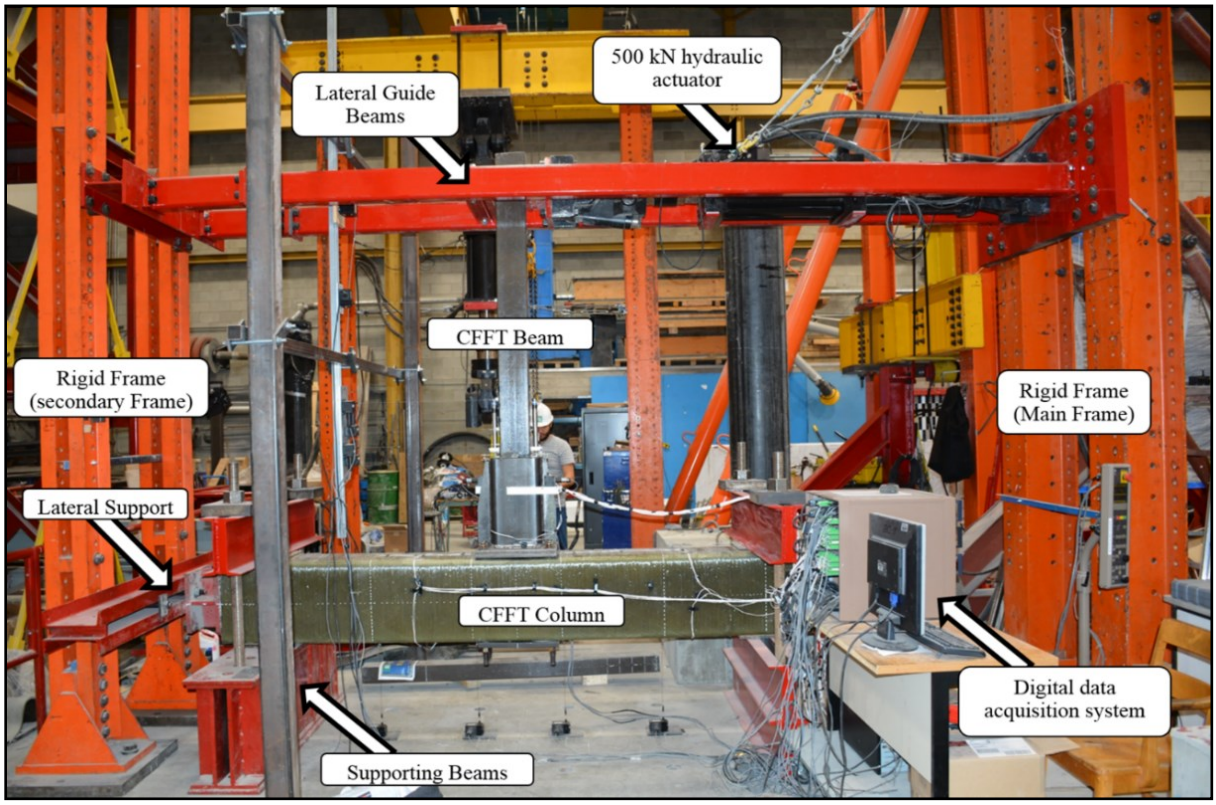

Figure 6.5: Test setup

Six potentiometers were used to measure the lateral displacement of the CFFT beam at different heights above the grout surface at levels of 0 mm, 76 mm, 153 mm, 305 mm, 813 mm, and the

loading-point. The vertical displacement of the CFFT column was measured by another four potentiometers at 525 mm, 1030 mm, 1470 mm, and 1975mm measured from the support. The slippage between the steel connections and the epoxy grout was measured on each side using two potentiometers. Two linearly variable displacement transducers (LVDTs) were used to measure the slippage between the beam and the epoxy grout on the tension and the compression sides.

The vertical and the horizontal strains of CFFT beams were measured using electrical strain gauges placed at different heights on the tension and the compression sides of the beam. Furthermore, deformations of the CFFT columns were measured using eight electrical strain gauges attached to different sections at the top and the bottom face of the columns. Additionally, strains in steel reinforcement were measured using electrical strain gauges attached to different locations of steel bars. A general layout of the instrumentation and instrumentation details of connection zone are shown in Figure 6.6 and Figure 6.7, respectively. Measurements of the potentiometers and LVDTs, electrical strain gauges, and actuator were recorded using a data acquisition system.

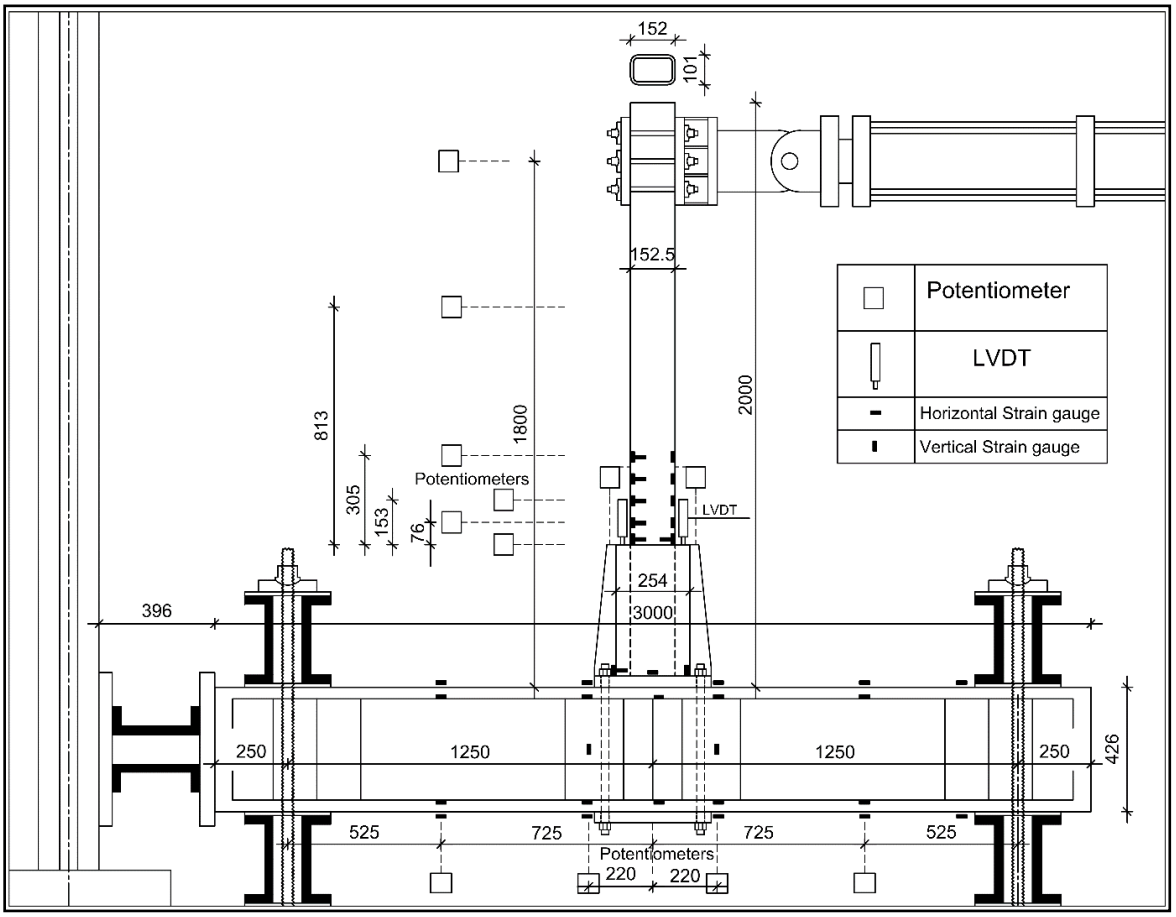

Figure 6.6: Instrumentation layout

`

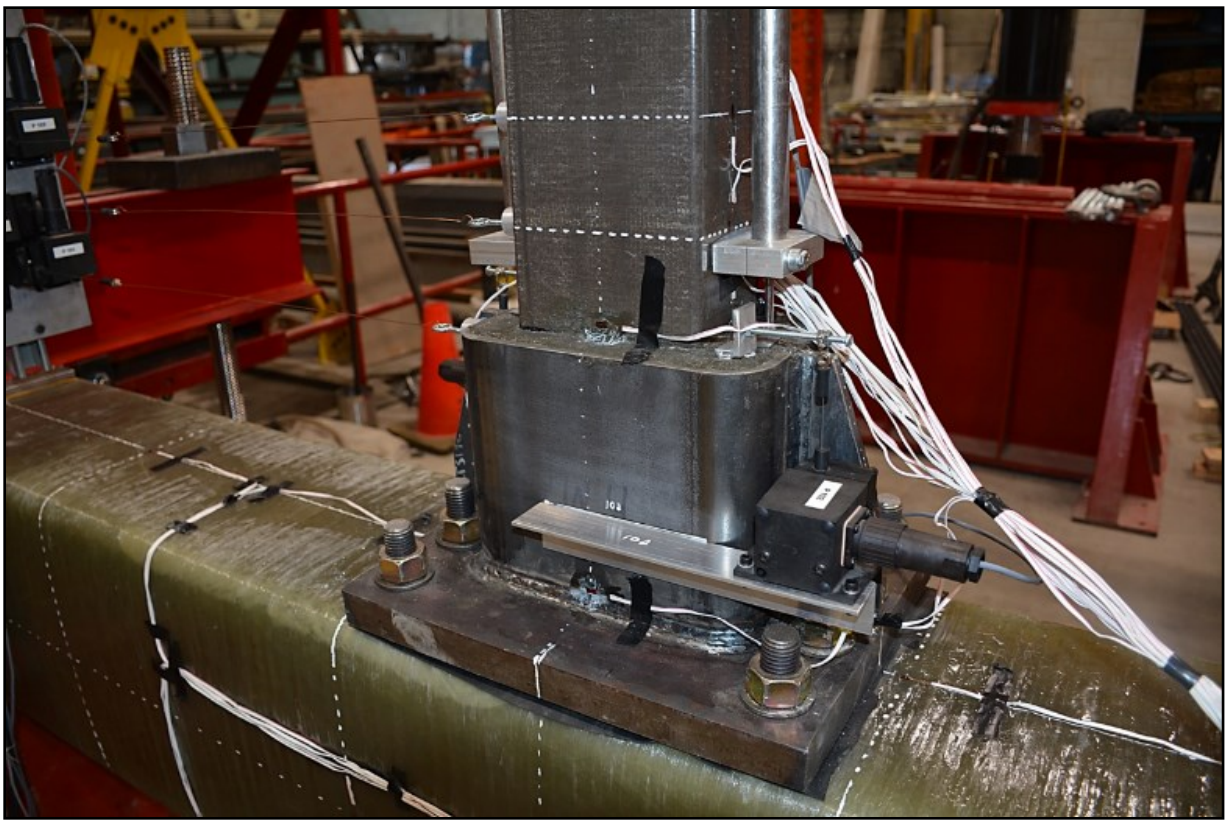

Figure 6.7: Instrumentation of the connection-zone

6.4. Experimental Results and Discussions

Summary of the experimental results is presented in Table 6-3, in terms of ultimate strength, stiffness, failure mode, curvature, and slippage measurements for each CFFT beam.

Table 6-3: Test results

	Failure Load (kN)	*Failure top displacement (mm)*	*Failure moment at grout surface (kN.m)*	*Transferred moment to the CFFT column (kN.m)*	*Max. curvature at failure (1/mm)*	*Location of the max. curvature above grout level (mm)*
SE-8	22	109	35.7	40.4	0.85E-4	0
SE-12	45.5	150	63.7	83.5	1.35E-4	76
SE-18	48.5	123	65.3	89	1.44E-4	0
BSE-8	30	113	48.1	55.1	0.91E-4	76

6.4.1. Failure Mode

As indicated previously, steel connections and the CFFT columns were designed to induce failure on the CFFT beam or on the interfacial bond between the CFFT beam and the epoxy grout. The minimum embedded depth required to achieve the flexural capacity of the CFFT beam is identified herein as optimal embedded depth. Generally, small optimal embedded depth induced failure on the interfacial bond between beam and grout indicates lower connection strength comparing to CFFT beam flexural strength. Contrarily, the connection succeeded when the failure occurred on the CFFT beam rather than any other components of the connection. Specimen SE-8 (with the smallest embedded depth of 200 mm) failed due to collapse on the interface between the CFFT beam and the epoxy grout, identified as slippage failure (Figure 6.8(a)). Slippage failure in SE-8 occurred due to degradation of bond strength between the CFFT beam and steel connection accompanied with hair cracks observed on the epoxy grout. Figure 6.9 shows the moment-slip relationship of SE-8 at the interface between the CFFT tube and epoxy grout, at which slippage started at early loading stage and continue until complete debonding with spacing of 5.4 mm between the CFFT tube and the surrounded epoxy grout at an ultimate load. Hence, it can be deduced that the embedded depth of SE-8 was not sufficient to produce a successful beam-column connection.

`

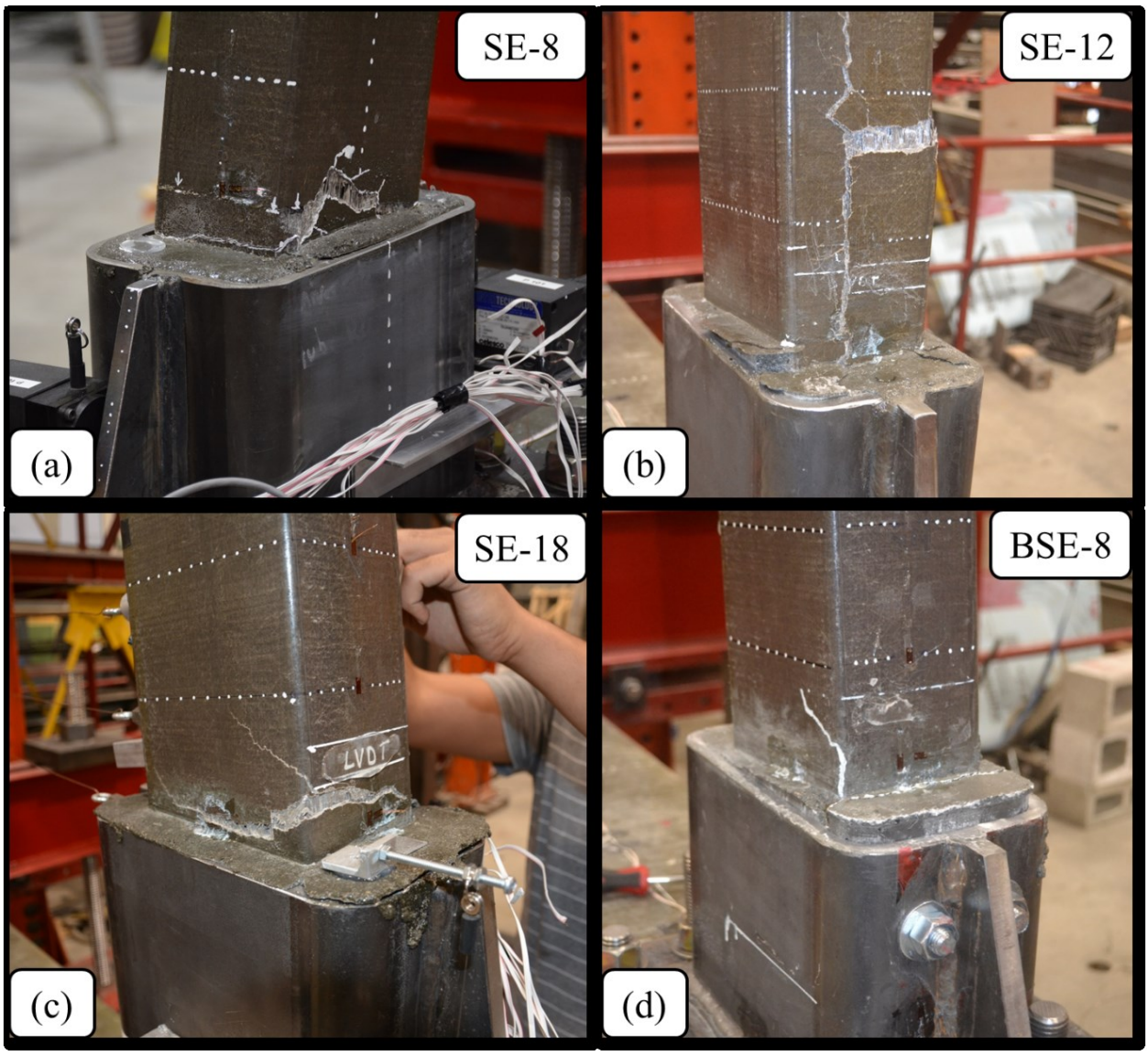

Figure 6.8: Failure mode of the tested specimens

Specimen SE-12 had a 50% increase in the embedded depth (300 mm) comparing to SE-8, yet attained more than twice the lateral load of SE-8 (with a 107% increase in the connection flexure capacity). Failure of the specimen SE-12 initiated by slippage between the CFFT beam and the grout, followed by vertical cracks on the GFRP tube, leading to horizontal rupture and flexural failure of the CFFT tube. Figure 6.8(b) shows the failure mode of SE-12, at which the failure mode was considered as a balanced failure of CFFT beam slippage associated with flexural failure. Slippage of the SE-12 tube was noticeable as shown in Figure 6.9, however, increased linearly with increasing the flexure capacity. Hence, the embedded depth of SE-12 was slightly less than or approximately equal to the optimal embedded depth.

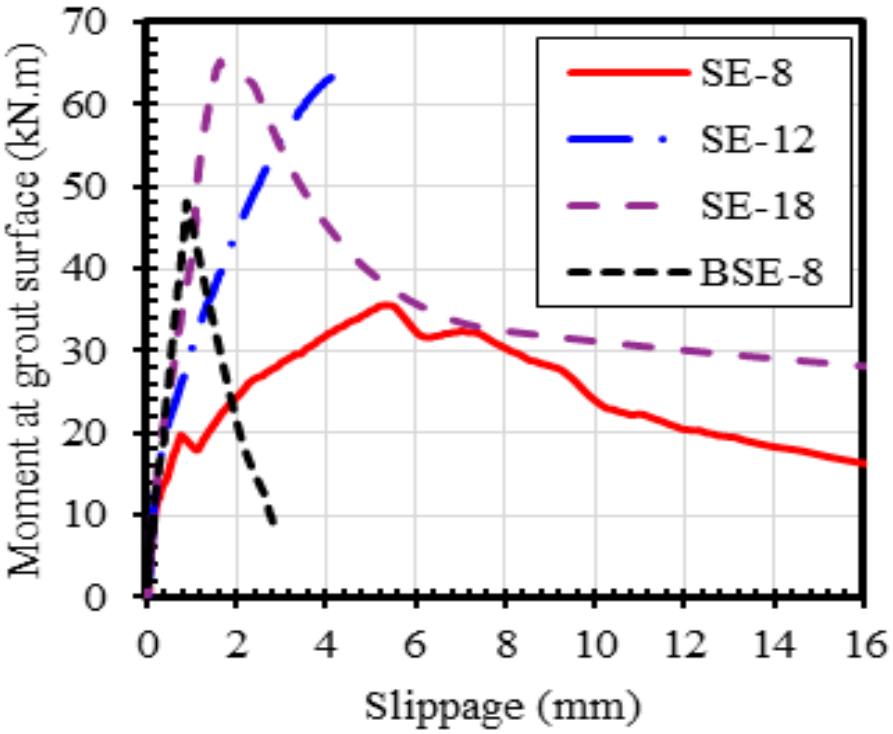

Figure 6.9: Relationship between moment at the grout level and slippage between the CFFT beam

Failure of SE-18 occurred due to flexural rupture in the CFFT beam, as shown in Figure 6.8(c) with insignificant slippage at ultimate load (Figure 6.9). The SE-18 embedded depth of 450 mm was sufficient to achieve a full flexural capacity of the CFFT beam. On the other hand, specimen SE-18 exhibited 6.6% higher lateral capacity comparing to SE-12, however, with a 50% increase in embedded depth. This slight increase in the flexure capacity comparing to SE-12 confirm also that any increase of the embedded depth beyond the depth of SE-12 is not required for flexure strength.

Specimen BSE-8 had the same embedded depth as that of SE-8, however, anchored using four bolts installed through the CFFT tube and the steel connection. Using anchorage bolts in specimen BSE-8 increased the lateral load capacity by more than 35% comparing to SE-8. Nevertheless, drilling holes in specimen BSE-8 to install the bolts reduced the cross-sectional area of the tubes and caused stress concentration around the hole. Hence, BSE-8 failed on the embedded part of the CFFT tube inside the steel connections (Figure 6.8(d)). Therefore, using anchorage bolts in the

`

current pattern to minimize the embedded depth had negatively affected the flexural strength of the CFFT beam. More investigation is required to address other configurations of anchorage bolts.

6.4.2. Load-Displacement Response

Figure 6.10 shows the load-displacement response of the CFFT beams for the four specimens. The response of the specimens started in similar behave until the cracking of the concrete. The failure loads and displacement of the specimens are shown in Table 6.4. The failure load of SE-12 was approached to the failure load of SE-18. Specimen SE-18 accomplished the highest capacity, which considers the full flexural strength of the CFFT beam. The response of specimen SE-8 illustrates that the failure of SE-8 ensued a ductile manner due to the slippage effect, while the other specimens failed in brittle demeanor. The samples showed very elastic behavior with very high deformation at ultimate load, which reflect the effect of the FRP tube properties on the CFFT beam flexural behavior. The clear span-variation of the specimens generated differences in the stiffness of the beams, so the evaluation of beams stiffness cannot be realized from the load-displacement response. The beams stiffnesses are illustrated in the following section.

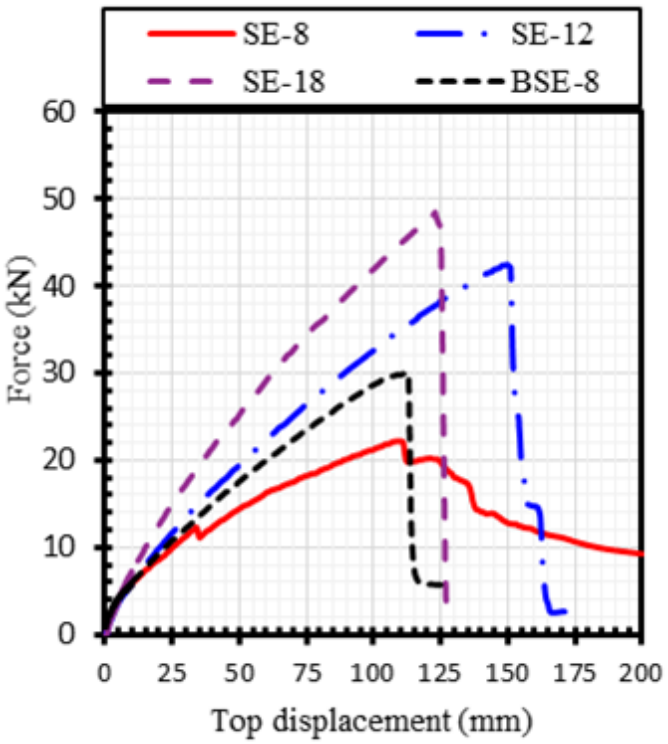

Figure 6.10: Force-displacement of CFFT beams

6.4.3. Moment Curvature Relationship

The moment-curvature relationship is used to evaluate the stiffness and the flexural capacity for each beam. Figure 6.11 shows the moment-curvature responses of the tested specimens at four different sections. The moment and curvature were calculated at 0 mm, 76 mm, 153 mm, and 229 mm above the grout levels to compare the results of the specimens. The moment-curvature responses at the four sections have similar behavior with different failure moments. The maximum moment achieved for SE-8, SE-12, SE-18, and BSE-8, at the failure, was 35.7 kN.m, 63.7 kN.m, 65.3 kN.m, and 48.1 kN.m, respectively. The beams exhibited the same flexural stiffness because the properties and cross-section of the tube are the same. In addition, the tubes were filled with the same concrete.

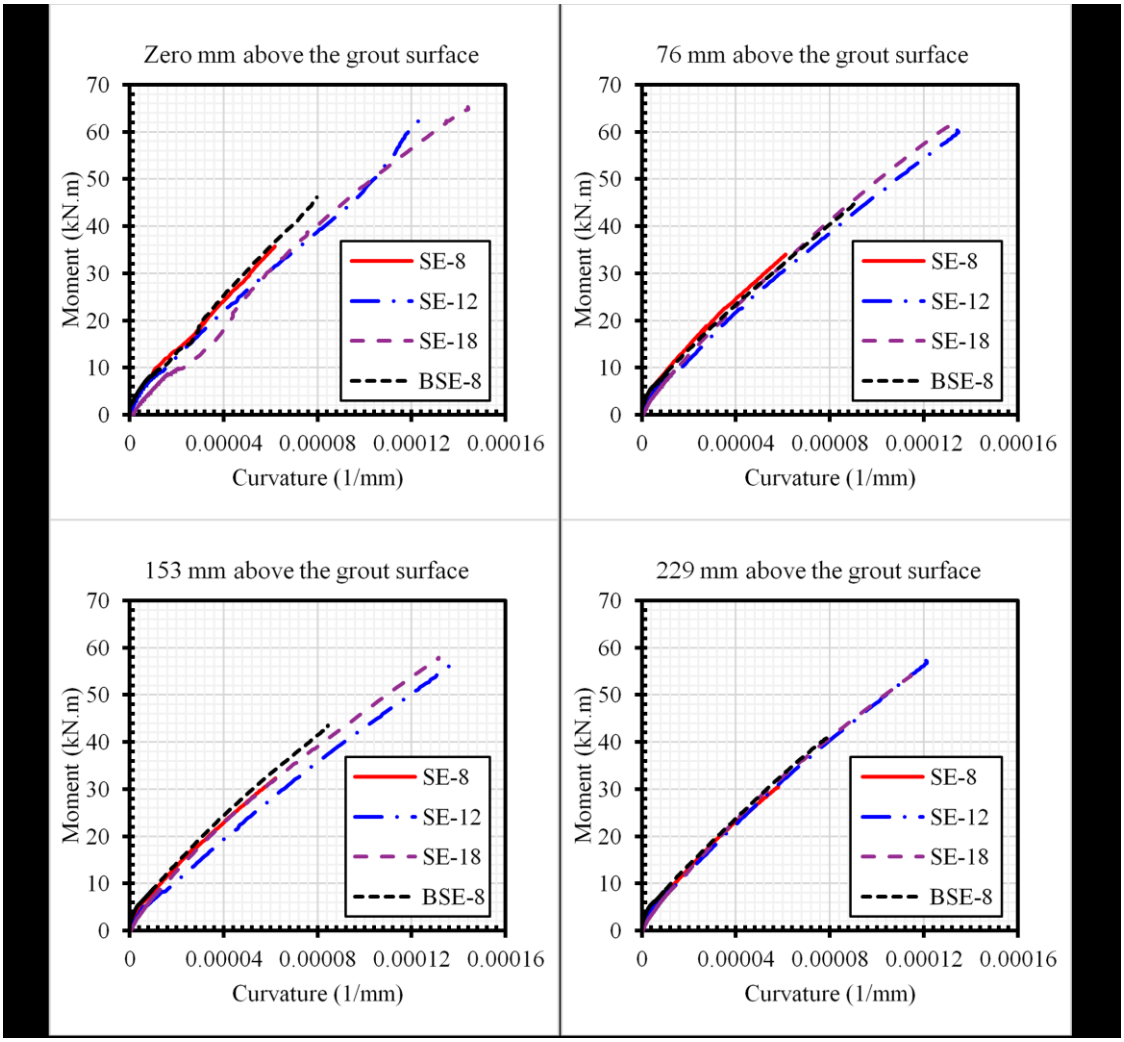

Figure 6.11: Moment-curvature relationship

6.4.4. Curvature and Plastic Hinge

The curvature distribution along the height of the element is an experimental method to determine the plastic hinge length. Developing of the plastic hinge is required for any structural elements to resist seismic loads. The curvature was calculated from the difference in the longitudinal strain measurements between the tension and the compression strain gauges divided by the depth of CFFT beam (H). The curvature is calculated at distances of 0H, 0.5H (76 mm), H (153 mm), 1.5H (229 mm), and 2H (305 mm) above the grout surface to envelop the curvature distribution on the critical zone of the CFFT beam. Figure 6.12 shows the curvature distribution along the height of the CFFT beams. The curvature of all specimens showed a nearly linear distribution along the height of the CFFT beam at the earlier stage until the curvature reached 2E-5, then the curvature developing rate was increased on the sections above the steel connection. SE-18 achieved the highest curvature of 1.44E-4 at the grout surface. The failure mode affected the curvature distribution of SE-8, SE-12, and BSE-8 along the plastic hinge zone. SE-8 failed before attaining any plastic deformation due to excessive slip of the CFFT beam, hence, the curvature distribution of SE-8 was almost linear up to failure. Hence, it can be deduced that the plastic hinge of SE-12 and SE-18 was equal approximately to 153 mm (corresponding to 1.5H); although SE-12 and SE-18 exhibited different curvature distribution on the plastic hinge zone. This could be attributed to the slight slippage of SE-12 (see Figure 6.9), while SE-18 exhibited no slippage at failure.

6.4.5. Connections Strength and Stiffness

The determination of the connection's strength depends on several parameters, and most importantly the flexural strength of the CFFT beam and bond strength of the epoxy grout which are critical parameters to transfer the loads from the CFFT beam to the steel connection. Additionally, the strength of the steel-connection and CFFT column has a significant effect on the performance of the connections. The moment-curvature response (Figure 6.11) was used to evaluate the strength and the stiffness performances of the tested connections. The strengths of specimens SE-8, SE-12, and BSE-8 are lower than SE-18 by 45%, 3%, and 26%, respectively. As expected, by increasing the embedded depth inside the steel connection, the flexural strength of the overall connection is increased until reaching the optimal embedded depth. Beyond this optimal anchorage depth, the flexural strength attained its full capacity. Based on the results of

SE-8, SE-12, and SE-18, the optimal embedded depth for the tested connection can be estimated as 305 mm (2*H*). Figure 6.11 shows that the moment-curvature response of all specimens was approximately linear and parallel together, indicating identical stiffness of the specimens.

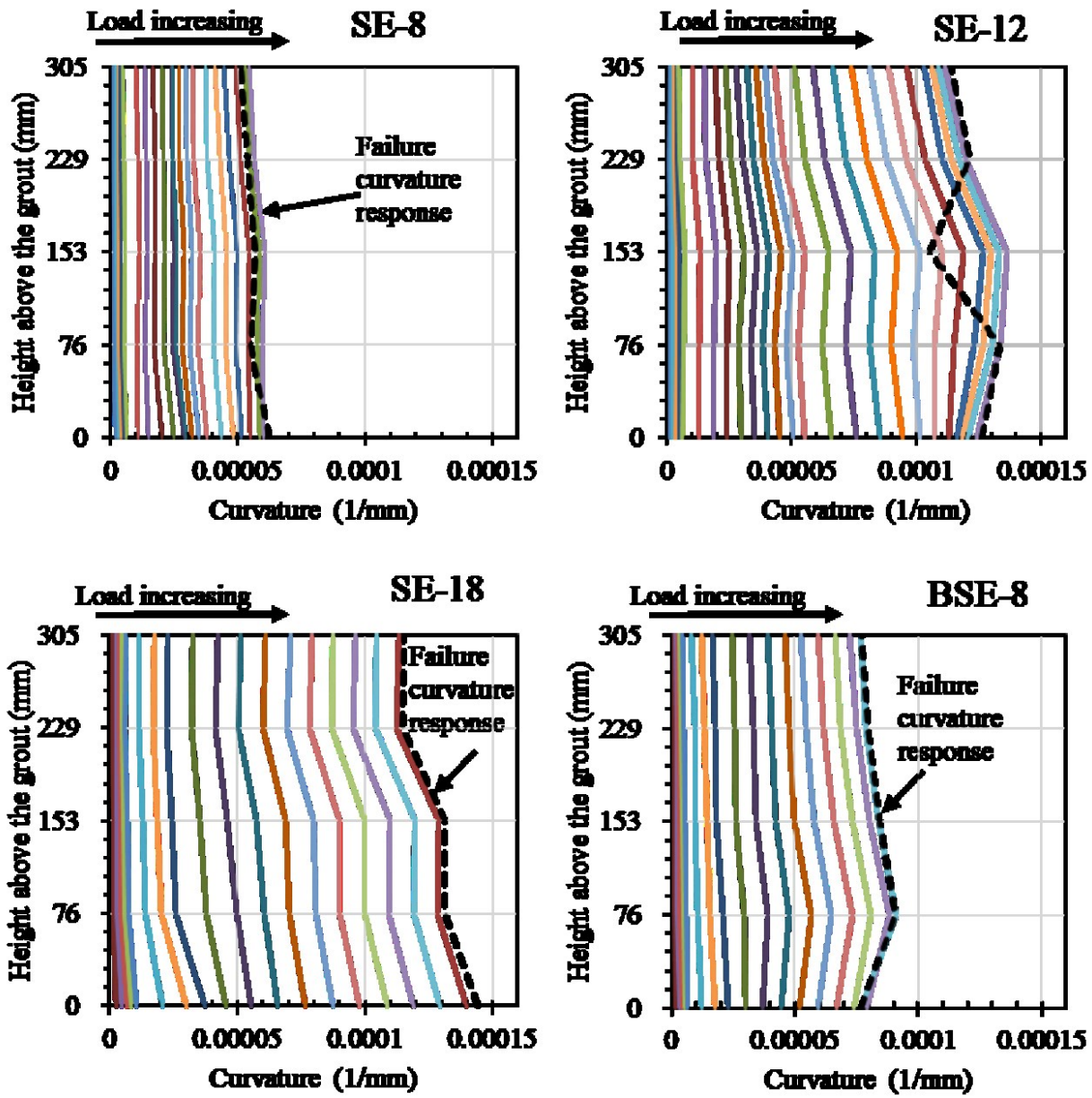

Figure 6.12: Curvature distribution along the height of the CFFT beams

6.4.6. Steel Connections and the CFFT Column

No deformation or failure was observed, as expected, on all the steel connections and the CFFT column. The transferred loads to the CFFT column was inconsiderable if it is compared to the high capacity of the CFFT column. Consequently, the maximum vertical deformation of the CFFT column was less than 0.2 mm and the measured strains on the steel reinforcement bars were less than 2.2E-4. Figure 6.13 shows the relationship between the moment and the axial-strain of steel connections at the top of the end plate. The maximum strain recorded on the HSS steel tube was 0.0004, which equals one-quarter of the yield strain of the HSS section. These results confirmed the ability of the connection to transfer the loads from the CFFT beams to the CFFT column.

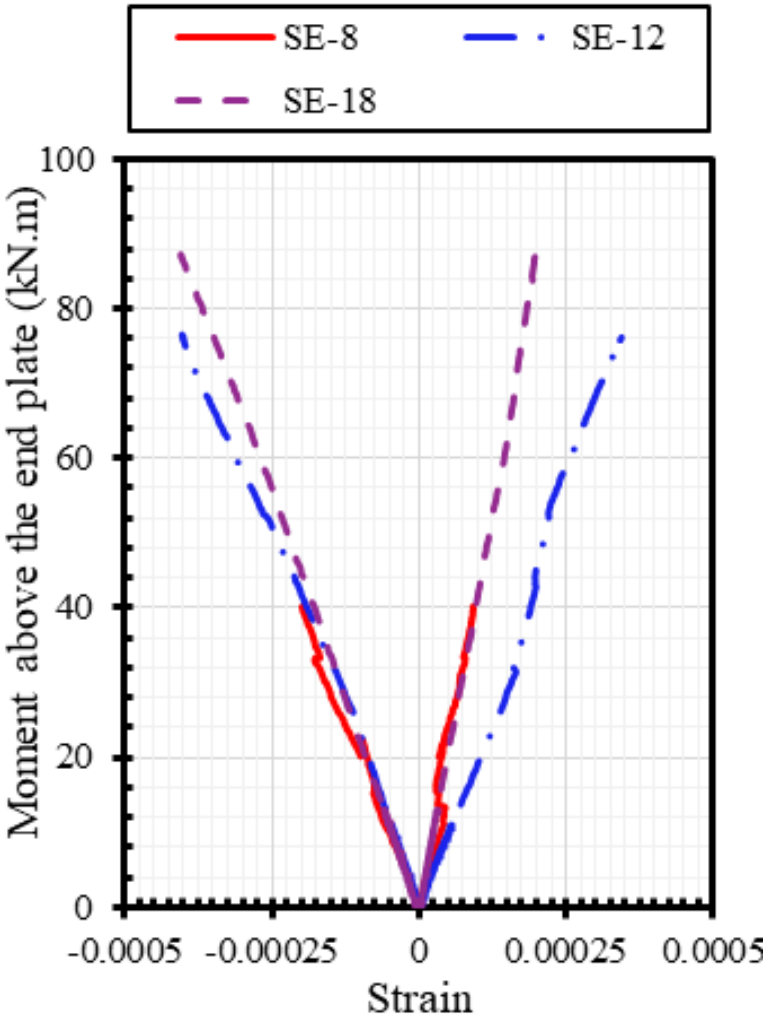

Figure 6.13: Moment-axial strain relationship of steel connections at the top surface of the end plate

6.5. Analytical Model

An analytical model was conducted to estimate the flexural capacity of the CFFT beam, consequently, an equation to calculate the optimal embedded depth was established. The assumptions of this model can be summarized as follows:

1- Strain distribution is linear across the CFFT beam section (plane sections remain plane); the tensile strength of concrete is neglected, and the equivalent rectangular stress-strain block is used according to the ACI 318-14 (American Concrete Institute 2014), as shown in Figure 6.14.

2- The bond-stress distribution is linear until reaching the maximum bond stress (Nelson et al. 2008b). Figure 6.15 shows the assumed bond stress distribution on the tension zone of the embedded part (*d*) of the CFFT beam.

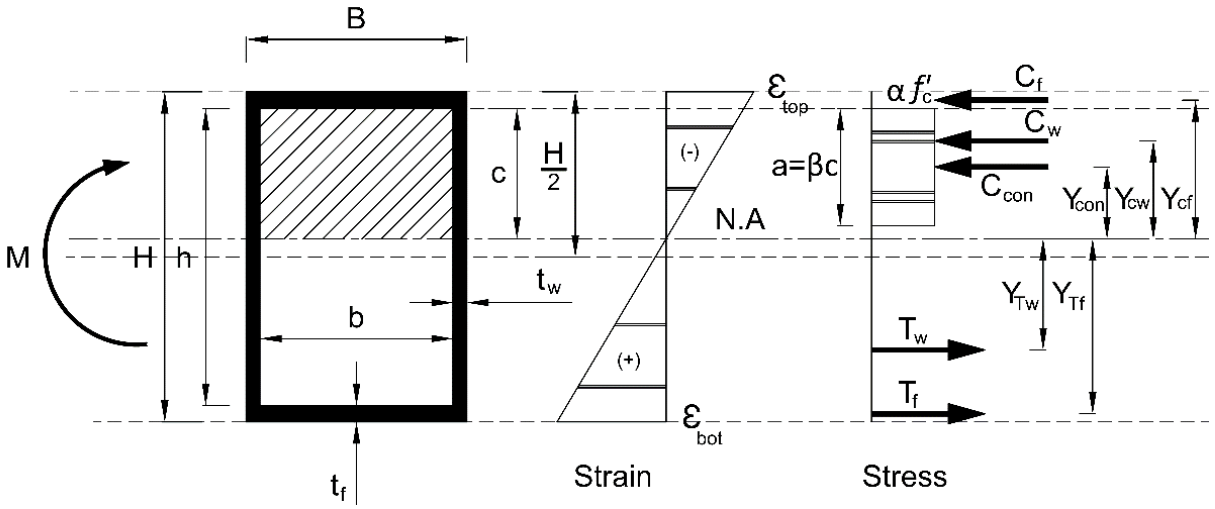

Figure 6.14: Section analysis of rectangular CFFT member under flexure

Three types of the flexural failure can occur on the CFFT members: tension, compression, balanced failure. The tension failure occurs when the tensile strain (bottom strain = ε_{bot}) of the GFRP tube attained its ultimate tensile failure strain (ε_{fut}) and the compression strain (top strain = ε_{top}) is less than the ultimate compressive failure strain (ε_{fuc}), ($\varepsilon_{bot} \geq \varepsilon_{fut}$ and $\varepsilon_{top} < \varepsilon_{fuc}$). On the contrary, the compression failure ensues when $\varepsilon_{bot} < \varepsilon_{fut}$ and $\varepsilon_{top} \geq \varepsilon_{fuc}$. In the balanced failure case, the tensile and the compressive strains should equal with the ultimate strains simultaneously ($\varepsilon_{bot} = \varepsilon_{fut}$ and $\varepsilon_{top} = \varepsilon_{fuc}$).

`

The procedure of this model depends on assuming the type of failure, consequently, calculating the compression zone depth (c) from the equilibrium of the forces. Thereafter, check the assumption validity. If the assumption was valid, calculate the moment at the neutral axis of the section. If the assumption was not valid, re-assume another type of failure. The bottom strain (ε_{bot}) is assumed according to the failure type in Eq. (6.1).

$$\varepsilon_{bot} = \begin{cases} \varepsilon_{fut} = \frac{f_{tl}}{E_l} \quad \dots\dots\dots\dots\dots\dots\dots\dots\dots\dots for\ tension\ failure \\ \left(\frac{H-t_f-c}{c+t_f}\right)\varepsilon_{fuc} = \left(\frac{H-t_f-c}{c+t_f}\right)\frac{f_{cl}}{E_l} \dots\dots\dots\dots for\ compression\ failure \end{cases} \tag{6.1}$$

The tension forces on the tube can be formulated on two-forces (T_w) and (T_f) acting on the tension part of the tube web and flange, respectively. The compression forces acting on the concrete compression zone and the compression part of the tube web and flange are (C_{con}), (C_w), and (C_f), respectively. The value of the web/flange tube compression/tension force can be calculated by multiplying the tube cross-sectional area of this part by the tube elastic modulus and the strain corresponding to the centroid of this part, as shown in Eq. (6.2) to (6.5). The compression concrete force (C_{con}) was calculated, as shown in Eq. (6.6). The compression depth (c) can be calculated from the equilibrium of the section, where the total compression force is equal to the total tension force ($T_{total} = C_{total}$). Eqs. (6.7a) and (6.7b) present equations to calculate the compression depth (c) for tension and compression failure, respectively.

$$T_w = t_w \times E_l \times \left[\frac{(h-c)^2}{H-t_f-c}\right]\varepsilon_{bot} \tag{6.2}$$

$$T_f = B \times t_f \times E_l \times \left[\frac{H-1.5t_f-c}{H-t_f-c}\right]\varepsilon_{bot} \tag{6.3}$$

$$C_w = t_w \times E_l \times \left[\frac{c^2}{H-t_f-c}\right]\varepsilon_{bot} \tag{6.4}$$

$$C_f = B \times t_f \times E_l \times \left[\frac{c+0.5t_f}{H-t_f-c}\right]\varepsilon_{bot} \tag{6.5}$$

$$C_{concrete} = \alpha \times f_c' \times \beta \times c \times b \tag{6.6}$$

For tension failure

$$c = \left(\frac{H-t_f}{2}\right) + \frac{A\,f_{tl}}{2\,\alpha\,f_c'\,\beta\,b} - 0.5\sqrt{t_f^2 + H^2 + \frac{2\,A\,f_{tl}\,t_f}{\alpha\,f_c'\,\beta\,b} - 2Ht_f + \left(\frac{A\,f_{tl}}{\alpha\,f_c'\,\beta\,b}\right)^2} \tag{6.7a}$$

For compression failure

$$c = \left(-\frac{t_f}{2}\right) - \frac{A\, f_{cl}}{2\,\alpha\, f_c'\,\beta\, b} + 0.5\sqrt{t_f^2 - \frac{2\,A\, f_{cl}\, t_f}{\alpha\, f_c'\,\beta\, b} + \frac{2AHf_{cl}}{\alpha\, f_c'\,\beta\, b} + \left(\frac{A\, f_{cl}}{\alpha\, f_c'\,\beta\, b}\right)^2} \quad (6.7a)$$

Where H and B are the outer tube depth and width; respectively; h and b are the depth and the width of the concrete core; A is the cross sectional area of the tube ($A = HB - hb$); E_l is the modulus of elasticity of the FRP tube in the longitudinal direction; t_f is the thickness of the tube flange; ε_{bot} is the stain at the tube-bottom fiber ; β and α are parameters defining a rectangular stress block in the concrete equivalent to the nonlinear distribution of stress, ($\beta = 0.85 - \frac{f_c' - 28}{140}$), ($\alpha = 0.85$) (ACI 318-14)(American Concrete Institute 2014).

The validity of the failure type assumption was checked each time by calculating the strains at the top and bottom of the beam and comparing it with the ultimate strains of the GFRP tube. In the case of tension failure assumption, the strain at the beam top (ε_{top}) was calculated and compared to the ultimate failure compressive strain (ε_{fuc}). If ε_{top} was lower than ε_{fuc}, that means the assumption was valid. Otherwise the tension failure assumption was not valid and reassume compression failure. In the case of the compression failure assumption, the bottom strain (ε_{bot}) of the beam was calculated and compared to the ultimate failure tensile strain (ε_{fut}). If ε_{bot} was lower than ε_{fut}, that means the assumption is valid. Otherwise the compression failure assumption was not valid and reassume tension failure.

In the tension failure assumption case ($\varepsilon_{bot} = \varepsilon_{fut}$)

$$If\ \left[\varepsilon_{top} = \left(\frac{c + t_f}{H - c - t_f}\right)\varepsilon_{bot} < \varepsilon_{fuc}\right] \ldots\ldots \begin{cases} True \ldots tension\ failure\ assumption\ is\ valid \\ False. \ldots reassumme\ compresstion\ failure \end{cases}$$

In the compression failure assumption case ($\varepsilon_{top} = \varepsilon_{fuc}$)

$$If\ \left[\varepsilon_{bot} = \left(\frac{H - c - t_f}{c + t_f}\right)\varepsilon_{top} < \varepsilon_{fut}\right] \ldots \begin{cases} True \ldots compression\ failure\ assumption\ is\ valid \\ False \ldots\ldots\ldots\ldots\ldots\ldots reassumme\ tension\ failure \end{cases}$$

Each force was concentrated at its acting location based on the strain diagram. Eq. (6.8) shows how to calculate the theoretical moment by multiplying each force by its distance from the neutral

`

axis of the section. The distances from the neutral axis to the forces (T_w), (T_f), (C_{con}), (C_w), and (C_f) are equal to (Y_{Tw}), (Y_{Tf}), (Y_{Con}), (Y_{Cw}), and (Y_{Cf}), respectively.

$$M_{th} = T_w \times Y_{Tw} + T_f \times Y_{Tf} + C_w \times Y_{Cw} + C_f \times Y_{Cf} + C_{con} \times Y_{conc}$$

$$M_{th} = T_w\left(\frac{2(h-c)}{3}\right) + T_f(H - 1.5t_f - c) + C_w\left(\frac{2c}{3}\right) + C_f\left(c + \frac{t_f}{2}\right) + C_{con}\left(c - \frac{c\beta}{2}\right) \quad (6.8)$$

The slippage occurred on the tension side of the CFFT beam. It develops when the tension force on the GFRP tube wall is higher than the bond strength between the tube and the surrounding material (epoxy grout in our case). To prevent the slippage failure, the bond strength should be higher than or equal the tensile stress transferred from the tube to the surrounding material. Based on the assumed bond stress distribution in Figure 6.15, the maximum bond force (T_{bond}) was represented in Eq. (6.9). Where τ_{max} is the maximum bond strength between the GFRP tube and the surrounding material and *d* is the embedded depth of the CFFT beam on the surrounding material.

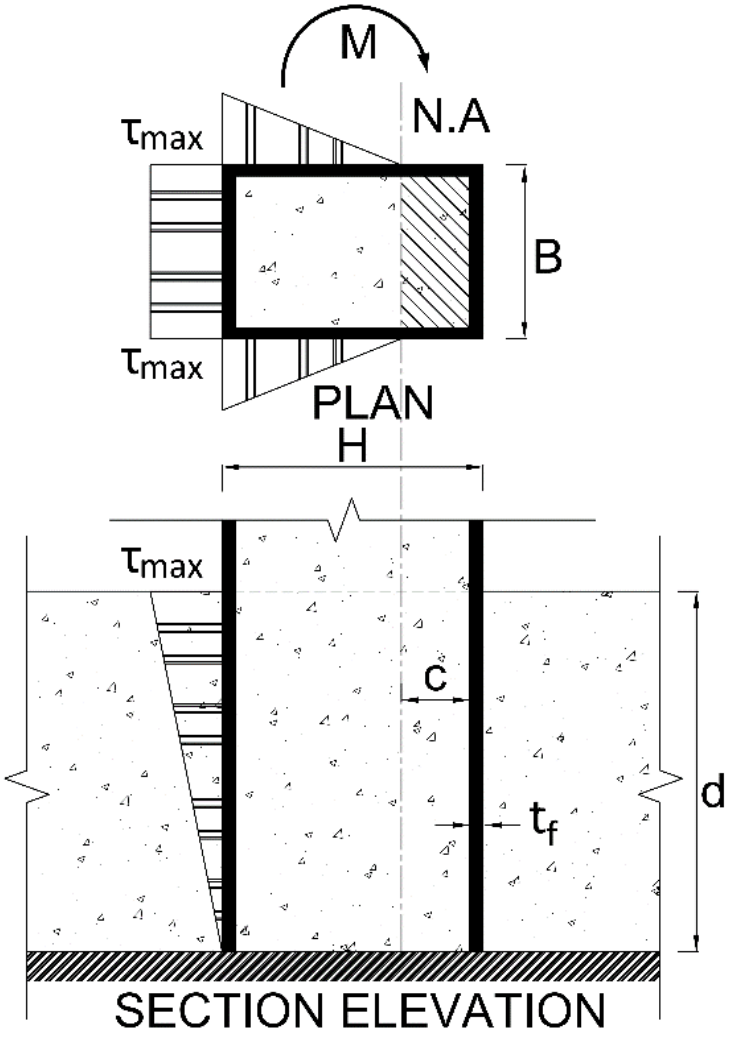

Figure 6.15: The assumed bond stress distribution on the tension zone of the embedded part (d) of the CFFT beam

$$T_{bond} = 0.5\, d\, \tau_{max}\, (B + H - c - t_f) \quad (6.9)$$

The tension force on the tube wall had the same distribution as the bond force, so it was acceptable to compare the absolute values of the two forces together to decide the failure occurred due to the slippage or due to the flexural. To achieve the flexural capacity of the CFFT beam, the force T_{bond} should be higher than the total tension force on the tube wall ($T_{total} = T_w + T_f$). The optimal embedded depth (d_{opt}) is illustrated in Eq. (6.10).

$$d_{opt} = \frac{T_{total}}{0.5\ \tau_{max}\,(B+H-c-t_f)} = \frac{T_w+T_f}{0.5\ \tau_{max}\,(B+H-c-t_f)} \quad (6.10)$$

`

The moment capacity of the CFFT beam should consider the effect of embedded depth, so the theoretical moment in Eq. (6.8) should multiply by the embedment effect factor (ψ). Where ψ equals the embedded depth divided by the optimal embedded depth and ψ is less than or equal to one. The moment capacity of the CFFT beam is shown in Eq. (6.11).

$$M = \psi\, M_{th} \quad \ldots\ldots\ldots\ldots \text{ Where } \psi = \frac{d}{d_{opt}} \leq 1.00 \tag{6.11}$$

6.5.1. Validation of the Analytical Model

The model accomplished adequate results compared to the experimental results. The model determined the flexural strength of the CFFT beam of 64 kN.m. That was less than the experimental value of SE-18, which attained the full flexural capacity of the CFFT beam, by 2%. The predicted failure mode was tension failure like the experimental. Table 6.4 shows a comparison between the results of the model and SE-18, in terms of maximum curvature, its distance from the fixation, flexural capacity, neutral axis depth measured from the compression side, and the max compressive strain of the tube. The bond-model estimated the optimal embedded depth of the CFFT beam, which was 337 mm and higher than the experimental by 10.5%. The effect of the embedded depth on the flexural capacity of the connection was adaptable with the experimental results as shown in Figure 6.16. The flexural capacity of SE-8, SE-12, and SE-18 were 38 kN.m, 57 kN.m, and 64 kN.m, respectively. The model estimated, the flexural strength of SE-8 was higher than the experimental by 6%, while the flexural strength of SE-12 and SE-18 were less than the experimental by 10.5% and 2%, respectively.

Table 6-4: Comparing the model results with the experimental results of SE-18

	Flexural strength (kN.m)	*Max. curvature at failure (1/mm)*	*Location of the max. curvature above grout level (mm)*	*Neutral axis depth (mm)*	*Max. compressive strain*	*Failure Mode*
Analytical	64	1.43E-4	0	68.7	0.0098	Tension
Experimental	65.3	1.44E-4	0	72.9	0.011466	Tension

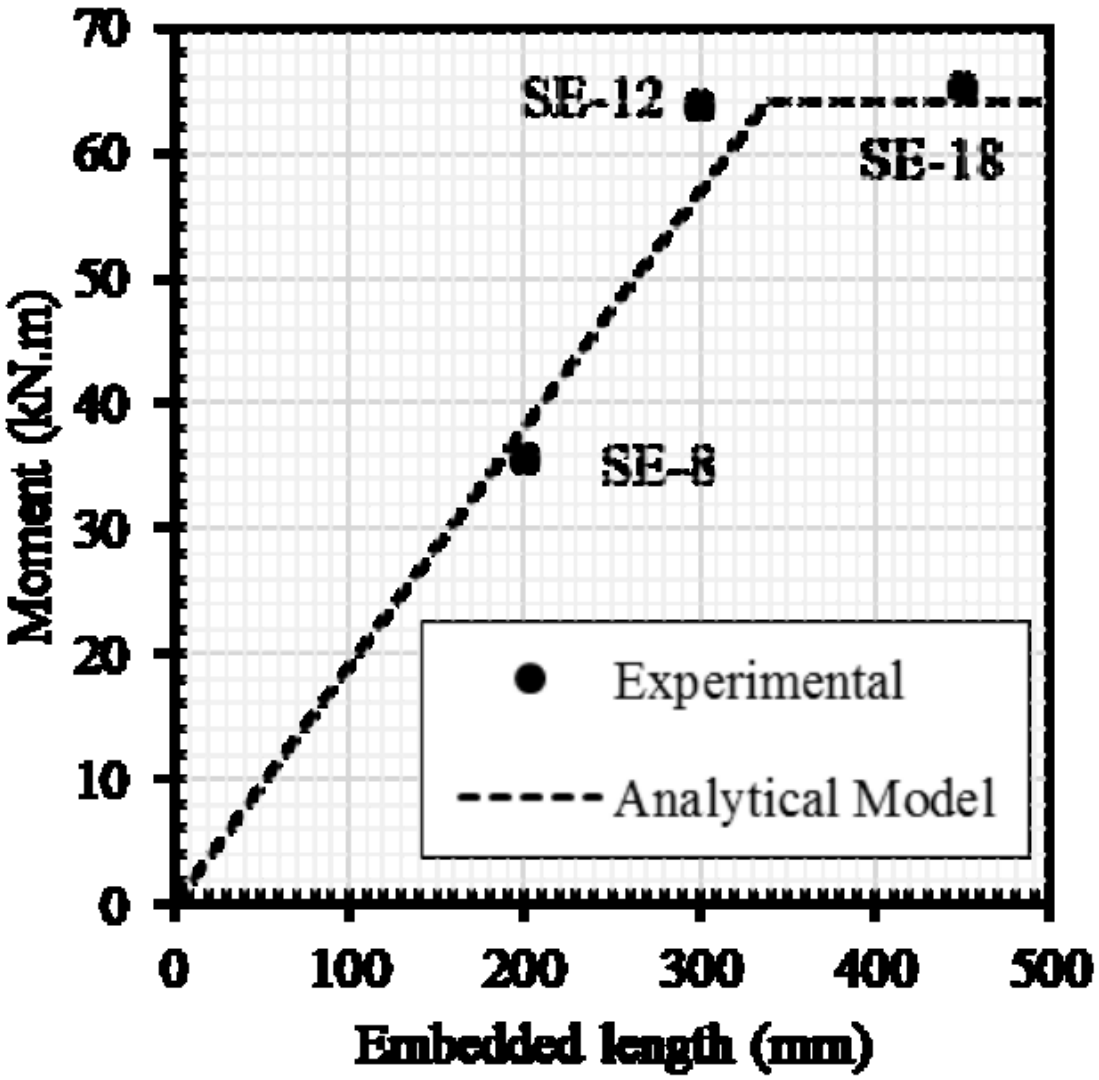

Figure 6.16: Effect of the embedded depth on the flexural capacity of the connection

6.6. Conclusions

A new CFFT beam-column connection was investigated experimentally and analytically to cover a research gap related to connecting CFFT beams to columns. The proposed connection successfully transferred the moment from the CFFT beam to the CFFT column. An analytical model was established to estimate the flexural capacity of the CFFT beam. The model also calculated the optimal embedded depth required to accomplish the CFFT beam flexural strength, in addition to considering the effect of the embedded depth on the flexural strength of the CFFT

`

beam-column connection. Conclusions of this investigation are summarized in the following points:

- The embedded depth had a significant effect on the flexural capacity of the connection. Increasing the embedded depth by 50% (SE-8 to SE-12) increases the flexural capacity by 78%. The flexural capacity was increased by increasing the embedded depth until the embedded depth attain the optimal embedded depth and consequently the full flexural capacity of the CFFT beam is realized.
- The optimal embedded depth of the tested CFFT beam (the minimum embedded depth required to reap the flexural strength of the CFFT beam) into the epoxy grout was 305 mm, which is practically two times the depth of the CFFT beam (2H). The optimal embedded depth depends on the flexural strength of the CFFT beam and the interfacial bond strength between the CFFT tube and the surrounding material (epoxy grout).
- Slippage failure occurred when the embedded depth was shorter than the optimal embedded depth, which adversely affected the flexural capacity of the connection.
- Using transverse anchorage bolts to minimize the optimal embedded depth was a profitable suggestion; it increased the flexural capacity of the connection with small-embedded depth by 35%. On the other hand, the presence of the holes on the GFRP tube wall decreased its flexural strength. Wherefore, more investigations are needed to find the effective bolts pattern, which does not affect the flexural strength of the CFFT beam.
- The proposed analytical equations successfully predicted the flexural strength of the CFFT beam, the failure mode, the optimal embedded depth, and the effect of the embedded depth on the flexural capacity of the connection with high accuracy (maximum difference 10.5%).

.

7. ANALYTICAL STUDY OF THE PROPOSED CFFT BEAM-COLUMN CONNECTION

7.1. Introduction

This chapter proposing an analytical study of the investigated beam-column connection. In the previous chapter, an analytical model was established based on the stress block approach, equilibrium, and strain compatibility to calculate the flexural capacity of unreinforced rectangular CFFT member and predict the optimal embedded length required to accomplish the flexural strength of the CFFT member. The model was exhibited excellent agreement with the experimental results. This chapter presents another analytical model based also strain compatibility, and equilibrium but this model uses the layer-by-layer approach to determine the flexural strength of CFFT members.

A comparison between the two models was implemented to evaluate their accuracy comparing to the experimental results. A parametric study has been conducted to investigate the effect of tube thicknesses, the material properties (FRP tube, concrete), and the grout bond strength.

7.2. Model with Stress-Block approach

This model was discussed at length in the previous chapter. The model neglected the concrete tension stiffening effect in the tension zone. Linear strain distribution over the cross-section was assumed based on the full composite action between the FRP tube and the concrete core; which insured by the sand-coating bond enhancer. The effect of shrinkage in the CFFT small sections is very limited and can be neglected. The parameters of the stress block were determined according to ACI 318-14 (ACI Committee 318 2014). The following chart (Figure 7.1) explains briefly the solution sequence of this model.

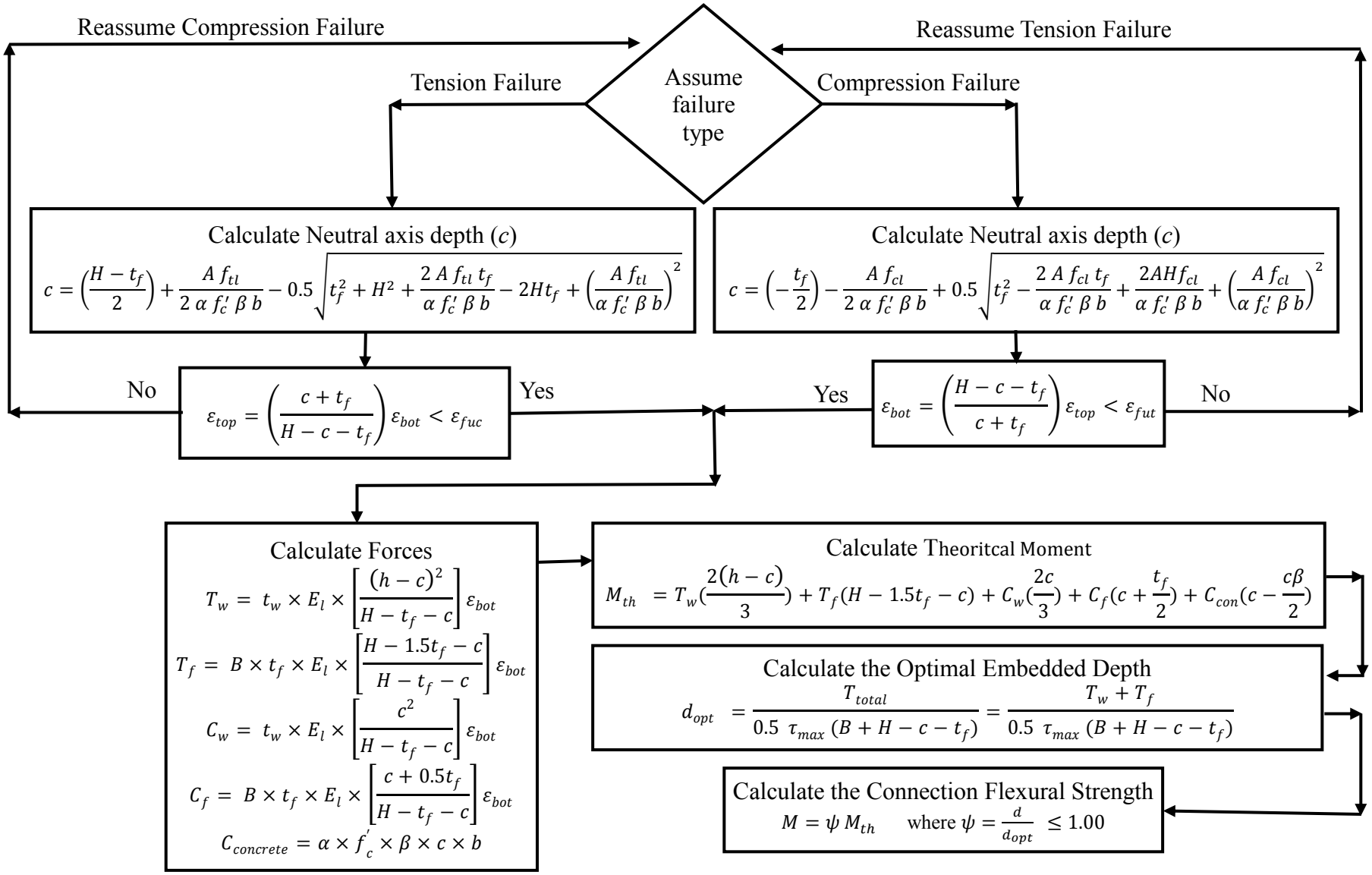

Figure 7.1: Flowchart of the analytical model with stress block approach

The model predicted the flexural strength of the rectangular CFFT member with an accuracy of 2% less than the experimental results. The optimal embedded depth calculated from the model was higher than the experimental results by 10.5%. The model determined the effect of the embedded depth on the flexural strength of the connection with accuracy varied from -6% to +10.5%.

7.3. Model with layer-by-layer approach

This model was implemented to estimate the flexural strength of rectangular CFFT element based on a section analysis to calculate the internal forces in the concrete using numerical integration. The assumptions of this model are the first principle design assumptions for reinforced concrete section under flexural and can be summarized as; the plain section remain plain after deformation and the strain distribution over the cross-section is linear (no slip ensues). This model has considered the concrete tension stiffening effect in the tension zone conversely the other model with stress block approach. This model was established based on trials and errors by assuming the compression zone depth (c) to calculate the internal forces. The actual compression zone depth is reached when the equilibrium of forces occurs.

7.3.1. Materials constitutive models

7.3.1.1. FRP tube material model

The FRP tube material is considered a linear elastic material in tension and compression and has a constant modulus of elasticity (Young's modulus) E_l . Both stress and strain distribution along the cross-section are linear and proportionate together. Figure 7.2 shows the utilized constitutive model for the FRP tube; where f_{cl} and ε_{fuc} are the ultimate compressive strength and strain, respectively. The ultimate tensile strength and strain are expressed using f_{tl} and ε_{fut} , respectively. Due to the linear stress strain relationship of the FRP tube, stress at any point is calculated as: $f_i = E_l \varepsilon_i$.

`

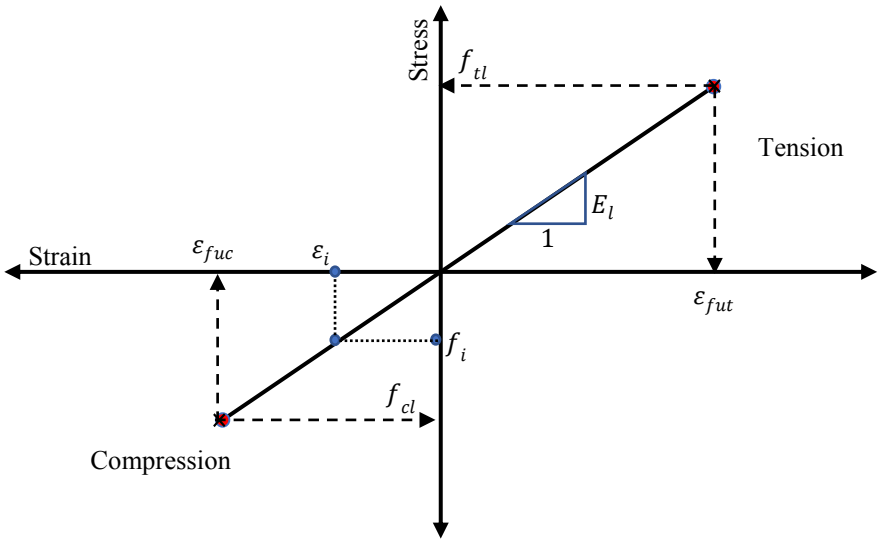

Figure 7.2: Material constitutive model of FRP tube

7.3.1.2. Concrete material model

The partially confined concrete model is used as proposed by (Abouzied and Masmoudi 2017). For concrete in compression, the model is established from the Popovics's model until the compressive stress f_c reaches f_c' pursued by plastic behavior with constant compressive strength equals f_c'; as shown in Figure 7.3. This model is nominated to provide an intermediate confinement level, that is appropriate for rectangular sections of CFFT beams. The model is described in Eqns. (7.1) and (7.2). ε_c presents the compressive strain at any point along the cross-section. Where f_c' and ε_c' are the maximum compressive strength and its corresponding strain, as shown in Figure 7.3. The tangent modulus $E_{co} = 5000\sqrt{f_c'}$ and the secant modulus of concrete $E_{sec} = \frac{f_c'}{\varepsilon_c'}$ are required to calculate the factor r in Eq. (7.3).

$$f_c = f_c' \qquad \text{For } (\varepsilon_c \geq \varepsilon_c') \tag{7.1}$$

$$f_c = \frac{f_c' \, (\varepsilon_c/\varepsilon_c') \, r}{r-1+(\varepsilon_c/\varepsilon_c')^r} \qquad \text{For } (0 \leq \varepsilon_c \leq \varepsilon_c') \tag{7.2}$$

$$r = \frac{E_{co}}{E_{co} - E_{sec}} \tag{7.3}$$

Where f_c' and $\varepsilon_c' = \frac{2f_c'}{E_{co}}$ are the maximum compressive strength and its corresponding strain, as shown in Figure 7.3.

While the model represented by Vecchio and Collins (Collins and Mitchell 1997) used to model the participation of concrete in tension in Eqns. (7.4) and (7.5). Where ($f_{cr} = 0.62\sqrt{f_c'}$) and ($\varepsilon_{cr} = \frac{f_{cr}}{E_{co}}$) are the tensile strength of the concrete and the corresponding tensile strain.

$$f_c = \frac{f_{cr}\,\varepsilon_t}{\varepsilon_{cr}} \quad \text{For } (0 \le \varepsilon_t \le \varepsilon_{cr}) \tag{7.4}$$

$$f_c = \frac{\alpha_1\,\alpha_2\,f_{cr}}{1+\sqrt{500(\,\varepsilon_t - \varepsilon_{cr})}} \quad \text{For } (\varepsilon_t \ge \varepsilon_{cr}) \tag{7.5}$$

Where ε_t presents the tensile strain at any point along the cross-section; (α_1) is a factor accounting for the bond characteristics. The bond factor ranges in value from zero to 1.0, (α_2) is a factor accounting for the nature of loading and was taken as 1.0 for monotonic loading.

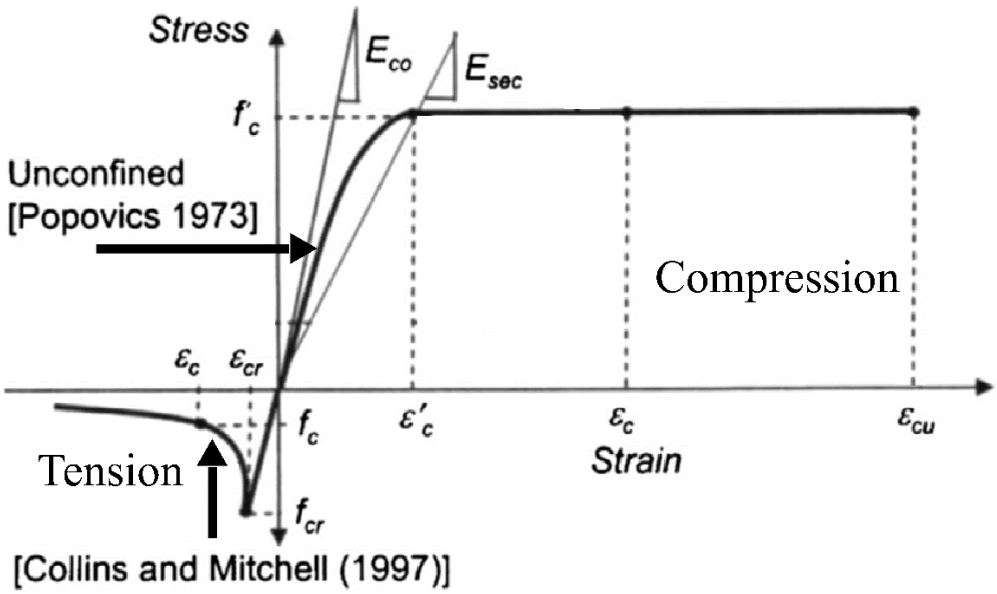

Figure 7.3: Material constitutive model of concrete

`

7.3.2. Equilibrium of internal forces and moments

The internal equilibrium accomplishes when the balance between the internal compression and tension force occurs. The internal tension/compression force in a part of the FRP tube is calculated by multiplying the area of this part by the corresponding stress. The forces in the FRP tube are calculated like the model with stress block approach. The tension forces on the tube can be divided on two-forces (T_w) and (T_f) acting on the tension part of the tube web and flange, respectively. The compression forces acting on the compression part of the tube web and flange are (C_w), and (C_f), respectively, as shown in Figure 7.4.

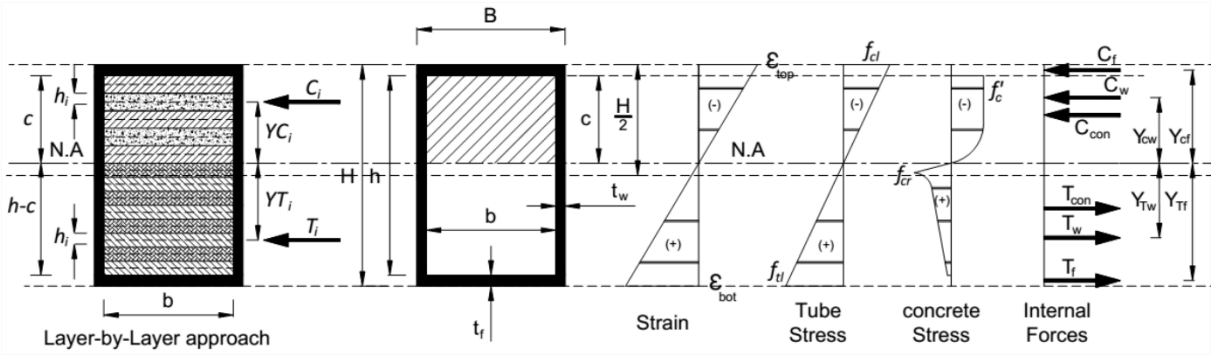

Figure 7.4: Section analysis using layer-by-layer approach

$$T_w = t_w \times E_l \times \left[\frac{(h-c)^2}{H-t_f-c}\right] \varepsilon_{bot} \quad (7.6)$$

$$T_f = B \times t_f \times E_l \times \left[\frac{H-1.5t_f-c}{H-t_f-c}\right] \varepsilon_{bot} \quad (7.7)$$

$$C_w = t_w \times E_l \times \left[\frac{c^2}{H-t_f-c}\right] \varepsilon_{bot} \quad (7.8)$$

$$C_f = B \times t_f \times E_l \times \left[\frac{c+0.5t_f}{H-t_f-c}\right] \varepsilon_{bot} \quad (7.9)$$

Where H and B are the outer tube depth and width; respectively; h and b are the depth and the width of the concrete core; E_l is the modulus of elasticity of the FRP tube in the

longitudinal direction; t_f is the thickness of the tube flange; t_w is the thickness of the tube web; c is the compression zone depth; and ε_{bot} is the stain at the tube-bottom fiber.

While the concrete internal force is determined using the stress numerical integration along the cross-section area due to the nonlinear behavior of the material model of concrete. The compression zone (area over the neutral axis) is divided into number of layer, n. Each layer has the same thickness h_i, which equals the compression zone depth (c) divided by n, ($h_i = c/n$). The tension zone is also divided following the same manner and the thickness of the layer ($h_i = (h - c)/n$). Each layer has centroid located at its mid-thickness. To calculate the strain corresponding to its centroid, the distance from the layer centroid to the neutral axis should be determined. This distance for the compression and tension layers are YC_i and YT_i, respectively. These distances are calculated in Eqns. (7.10) and (7.11). The strain corresponding to the layer centroid is determined in Eqns. (7.12) and (7.13) for layers in compression and tension zone, respectively.

$YC_i = \frac{c}{n}(i - 0.5)$ For the layers in the compression zone (7.10)

$YT_i = \frac{h-c}{n}(i - 0.5)$ For the layers in the tension zone (7.11)

$\varepsilon_{ci} = \frac{YC_i}{c}\varepsilon_{bot}$ For the layers in the compression zone (7.12)

$\varepsilon_{ti} = \frac{YT_i}{c}\varepsilon_{bot}$ For the layers in the tension zone (7.13)

The compression (C_i) or tension (T_i) force for each concrete layer can be calculated according to Eqns. (7.14) and (7.15).

$C_i = b\ h_i\ (f_c)_i$ Where $(f_c)_i$ from Eq. (7.1) or Eq. (7.2) based on the value of $(\varepsilon_c)_i$ (7.14)

$T_i = b\ h_i\ (f_c)_i$ Where $(f_c)_i$ from Eq. (7.4) or Eq. (7.5) based on the value of $(\varepsilon_t)_i$ (7.15)

Summation of forces acting on all the layers located above and below the neutral axis are presenting the total compression force in concrete C_{con} and T_{con} is the total tension force in concrete, respectively.

`

$$C_{con} = \sum_{i=1}^{i=n} C_i \tag{7.16}$$

$$T_{con} = \sum_{i=1}^{i=n} T_i \tag{7.17}$$

The equilibrium of internal forces fulfills when the total compression forces (C_{total}) equal to the total tension forces (T_{total}), which is presented in Eq. (7.18).

$$C_{total} = T_{total} = T_w + T_f + T_{con} = C_w + C_f + C_{con} \tag{7.18}$$

Moment due to the concrete forces M_{con} is calculated as the summation of moments acting on all the layers, as shown in Eq. (7.19). Each layer has a moment M_i equal the force C_i or T_i multiplied by the distance YC_i or YT_i, respectively.

$$M_{con} = \sum_{i=1}^{i=n} M_i = \sum_{i=1}^{i=n} (C_i\, YC_i) + \sum_{i=1}^{i=n} (T_i\, YT_i) \tag{7.19}$$

For the FRP tube, each force was concentrated at its acting location based on the strain diagram. Eq. (7.20) shows how to calculate the theoretical moment by multiplying each force by its distance from the neutral axis of the section. The distances from the neutral axis to the forces (T_w), (T_f), (C_{con}), (C_w), and (C_f) are equal to (Y_{Tw}), (Y_{Tf}), (Y_{Con}), (Y_{Cw}), and (Y_{Cf}), respectively.

$$M_{th} = T_w \times Y_{Tw} + T_f \times Y_{Tf} + C_w \times Y_{Cw} + C_f \times Y_{Cf} + M_{con}$$

$$M_{th} = T_w\left(\frac{2(h-c)}{3}\right) + T_f(H - 1.5t_f - c) + C_w\left(\frac{2c}{3}\right) + C_f\left(c + \frac{t_f}{2}\right) + M_{con} \tag{7.20}$$

7.3.3. Procedure of analysis

The following strides summarize the procedure of analysis:

1- Assign the dimensions and the mechanical properties of the concrete and the FRP tube.

2- Assume the type of failure and the compression zone depth (c). Calculate the strain at bottom fiber of the tube (ε_{bot}) according to the assumption of the failure type, as illustrated in Eq. (7.21).

$$\varepsilon_{bot} = \begin{cases} \varepsilon_{fut} = \frac{f_{tl}}{E_l} \quad \dots\dots\dots\dots\dots\dots\dots\dots\dots\dots for\ tension\ failure \\ \left(\frac{H-t_f-c}{c+t_f}\right)\varepsilon_{fuc} = \left(\frac{H-t_f-c}{c+t_f}\right)\frac{f_{cl}}{E_l} \dots\dots\dots\dots for\ compression\ failure \end{cases} \quad (7.21)$$

3- Check the validity of the failure type assumption by calculating the strain at top fiber of the tube (ε_{top}) tracking the following conditions:

In the tension failure assumption case ($\varepsilon_{bot} = \varepsilon_{fut}$)

$$If\ \left[\varepsilon_{top} = \left(\frac{c+t_f}{H-c-t_f}\right)\varepsilon_{bot} < \varepsilon_{fuc}\right] \dots\dots \begin{cases} True \dots tension\ failure\ assumption\ is\ valid \\ False. \dots reassumme\ compresstion\ failure \end{cases}$$

In the compression failure assumption case ($\varepsilon_{top} = \varepsilon_{fuc}$)

$$If\ \left[\varepsilon_{bot} = \left(\frac{H-c-t_f}{c+t_f}\right)\varepsilon_{top} < \varepsilon_{fut}\right] \dots \begin{cases} True \dots compression\ failure\ assumption\ is\ valid \\ False \dots\dots\dots\dots\dots\dots reassumme\ tension\ failure \end{cases}$$

4- Specify the number of layers (n) in compression and tension zone, for each layer determine the strain at the mid-thickness of the layer (ε_{ci} or ε_{ti})(Eq. 7.12 or Eq. 7.13) and the corresponding compressive or tensile stress f_{ci} (Eq. 7.1 or Eq. 7.2 or Eq. 7.4 or Eq. 7.5).

5- Calculate the internal compression (C_i) or tension force (C_i) on each layer from Eq. (7.14) or Eq. (7.15).

6- Determine the total compression (C_{con} from Eq. 7.16) and tension (T_{con} from Eq. 7.17) force acting on concrete. Calculate the tension (T_w and T_f from Eqns. 7.6 and

`

7.7) and compression (C_w and C_f from Eqns. 7.8 and 7.9) forces acting on the tube forces.

7- Establish the forces equilibrium condition by calculating C_{total} and T_{total}. By comparing the absolute values of C_{total} and T_{total}. If $C_{total} = T_{total}$, that means the equilibrium is fulfilled. If the equilibrium is not satisfied, betake to step no.2 and reassume the compression zone depth (c).

8- Merely the equilibrium condition is satisfied, calculate the theoretical moment from Eq. (7.20).

9- The rest of the steps are like the model with block stress approach and concluded in the following equations:

Calculate the optimal embedded depth (d_{opt}).

$$d_{opt} = \frac{T_{total}}{0.5\ \tau_{max}\ (B + H - c - t_f)} = \frac{T_w + T_f + T_{con}}{0.5\ \tau_{max}\ (B + H - c - t_f)}$$

Calculate the connection flexural strength (M).

$M = \psi\ M_{th}$ where $\psi = \frac{d}{d_{opt}} \leq 1.00$

10- Calculate the failure strains and the curvature (κ) as following:

For compression failure, $\varepsilon_{top} = \varepsilon_{fuc}$ and $\varepsilon_{bot} = \left(\frac{H-c-t_f}{c+t_f}\right)\varepsilon_{top}$

For tension failure, $\varepsilon_{top} = \left(\frac{c+t_f}{H-c-t_f}\right)\varepsilon_{bot}$ and $\varepsilon_{bot} = \varepsilon_{fut}$

$$\kappa = \frac{|\varepsilon_{top}| + |\varepsilon_{bot}|}{H}$$

Figure 7.5 illustrates the solution sequence chart of this model.

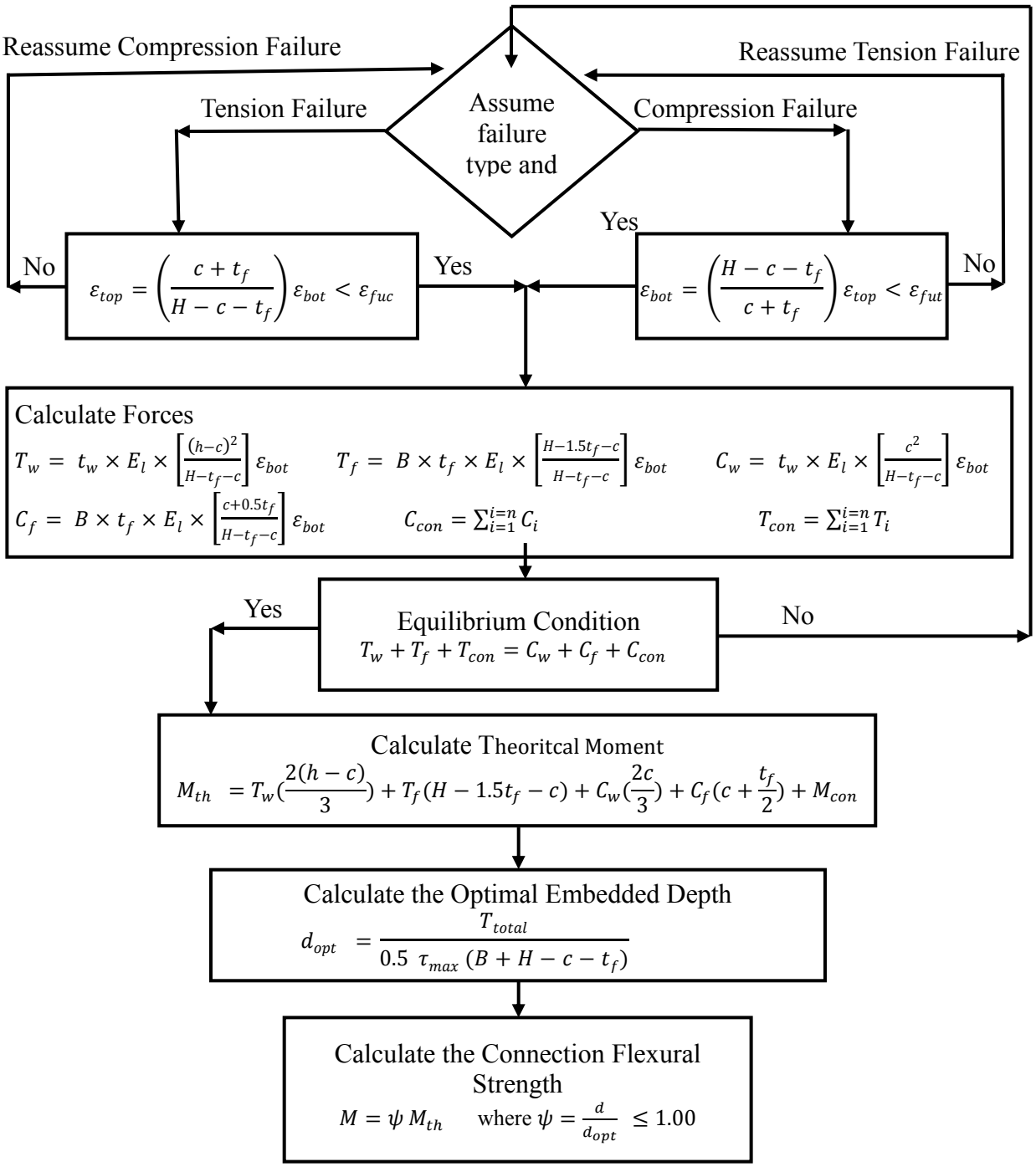

Figure 7.5: Flowchart of the analytical model with layer-by-layer approach

7.3.4. Validation of the model

The section analysis model was established based on the layer-by-layer approach to estimate the flexural capacity of the rectangular CFFT section, the optimal embedded depth, and the

`

influence of the embedded depth on the flexural capacity of the presented CFFT beam-column connection. The layer-by-layer approach achieved approximately identical results compared to the experimental results and the model with the stress-block approach. The flexural strength of the tested section (SE-18) equals 64.35 kN and 64 kN using the layer-by-layer approach and the stress-block approach. While the two approaches are estimated the flexural strength lower than the experimental by 2%. The two models estimated the failure type as a tension failure like the experimental. The two approaches accomplished approximately the same results in terms of neutral axis depth, curvatures, failure strain, and flexural strength.

7.4. Parametric study

A parametric study was conducted to determine the influence of the tube dimensions, mechanical properties of the tube and concrete, and the bond-strength of the surrounding material (the epoxy-grout) on the flexural capacity hence on the optimal embedded depth. This parametric study was established on the model with the layer-by-layer approach. However, the two models attained the same results. The layer-by-layer model was chosen because it is a comprehensive approach and includes more details than the block-stress model.

7.4.1. Effect of the tube flange-thickness

The flexural capacity and the optimal embedded depth were calculated using the same section dimensions and mechanical properties of the tested specimens but with different tube flange-thicknesses to study its effect. As shown in Figure 7.6, the tube with a thin flange fails in tension failure mode. Generally, increasing the tube flange-thickness increases the flexural capacity and the optimal embedded depth. Furthermore, transfers the failure mode from tension to compression failure. In the tension failure case, the increasing rate of the flexural capacity is linear, whereas it behaves nonlinearly in the compression failure case.

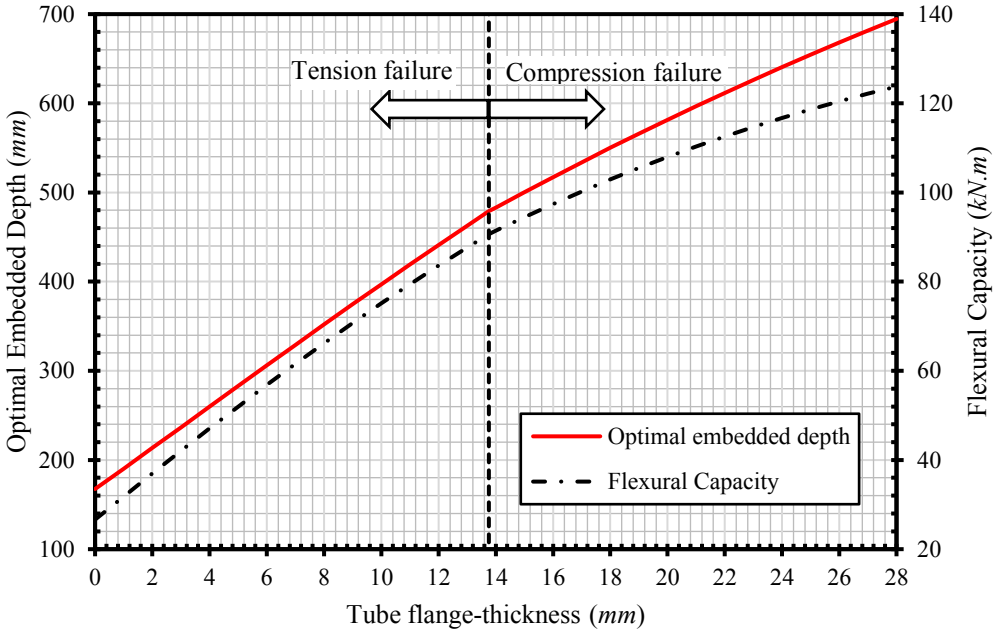

Figure 7.6: Effect of the tube flange-thickness

7.4.2. Effect of the tube web-thickness

The tube web-thickness effect was studied, as shown in Figure 7.7. Increasing the tube web-thickness leads to increase the flexural capacity linearly. Thereby, increases also the optimal embedded depth. The failure mode is transformed from tension to compression failure by increasing the tube web-thickness.

`

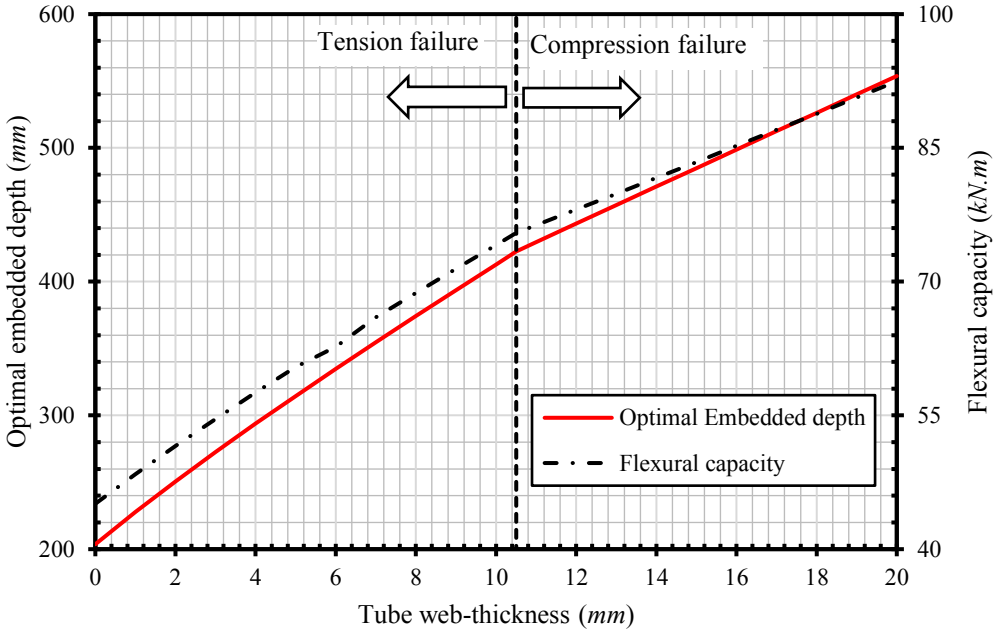

Figure 7.7: Effect of the tube web-thickness

7.4.3. Effect of the beam depth

The depth of the beam (*H*) has a significant effect on its flexural capacity and the optimal depth, as shown in Figure 7.8. Increasing the beam depth transforms the failure type from compression to tension failure. In the compression failure stage, the increasing rate of the flexural capacity and the optimal embedded depth is linear and higher than the rate in the tension failure stage which behaves nonlinearly.

7.4.4. Effect of the beam width

The width of the beam (*B*) affect significantly on its flexural capacity and the optimal depth, as shown in Figure 7.9. Increasing the beam width converts the failure type from compression to tension failure. The increasing rate of the flexural capacity is linear in the compression failure stage while it behaves in nonlinear manner in the tension failure stage. The increasing rate of the optimal embedded depth is linear in whatever the failure mode.

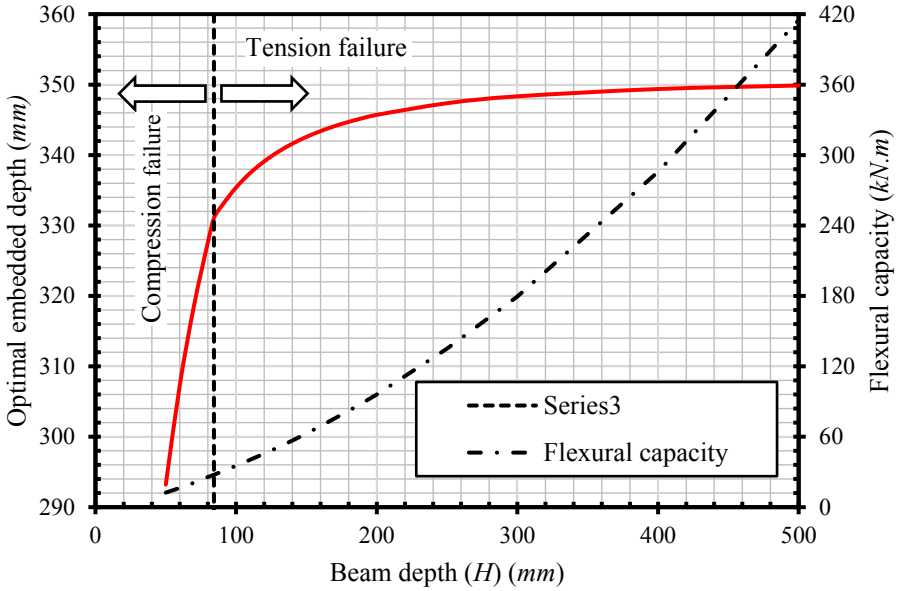

Figure 7.8: Effect of the beam depth (*H*)

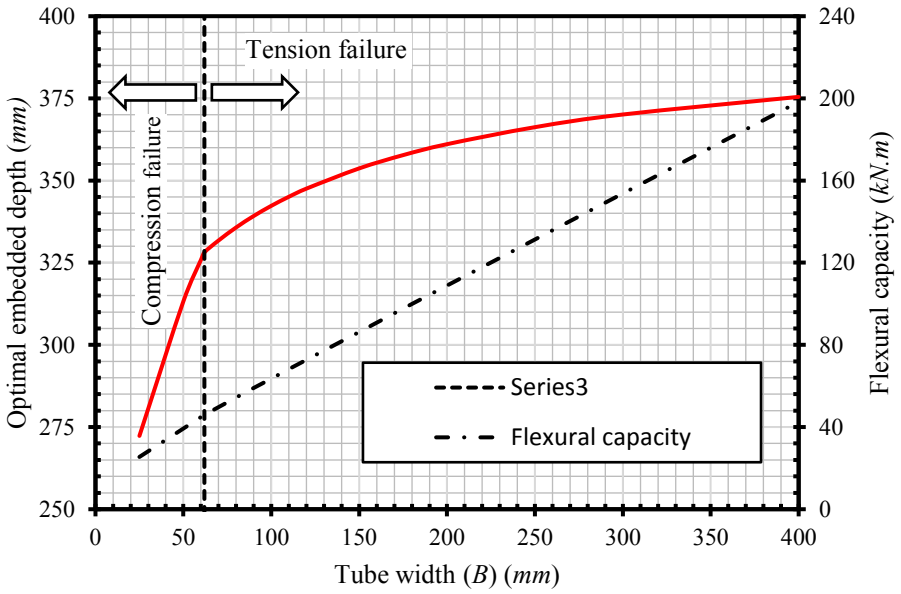

Figure 7.9: Effect of the beam width (*B*)

7.4.5. Effect of the tube mechanical properties

Figure 7.10 to Figure 7.12 show the effect of tube compressive strength, tensile strength, and modulus of elasticity, respectively. As expected, increasing the tube mechanical properties increases its flexural capacity besides its optimal embedded depth. In case of tension failure, the flexural capacity and the optimal embedded depth affected by the tube tensile strength while the tube compressive strength has no effect. The tube compressive strength also influences its flexural capacity as well its optimal embedded depth in compression failure case only. The effect of tube modulus of elasticity is extremely small and can be neglected; as shown in Figure 7.12.

7.4.6. Effect of the concrete compressive strength

In compression failure case, the concrete compressive strength (f_c') significantly influences the connection flexural capacity and its optimal embedded depth, as shown in Figure 7.13. While in the tension failure case, the effect of f_c' became less effective.

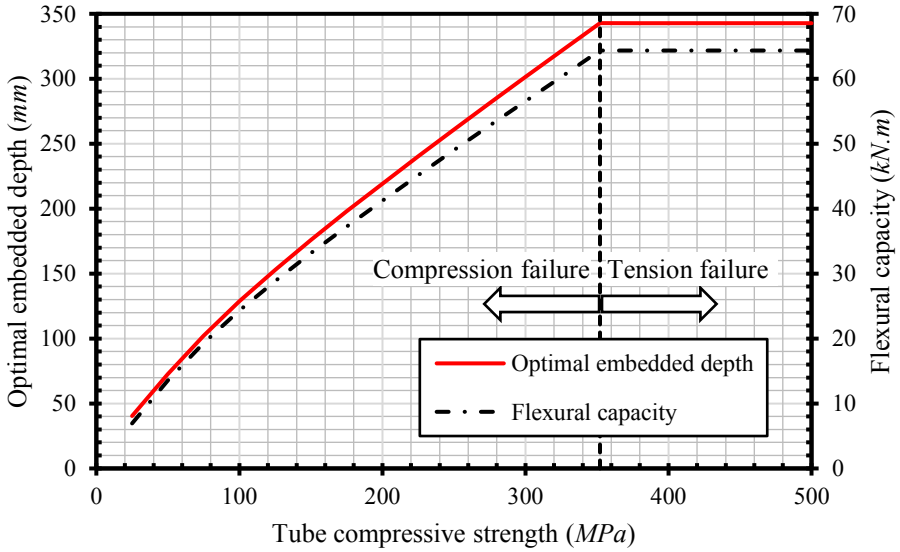

Figure 7.10: Effect of the tube compressive strength (f_{cl})

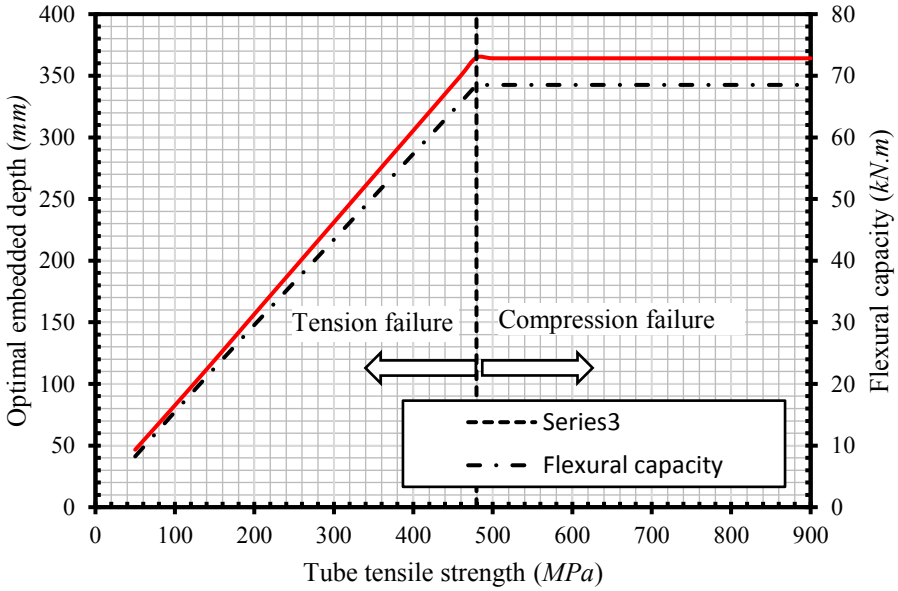

Figure 7.11: Effect of the tube tensile strength (f_{tl})

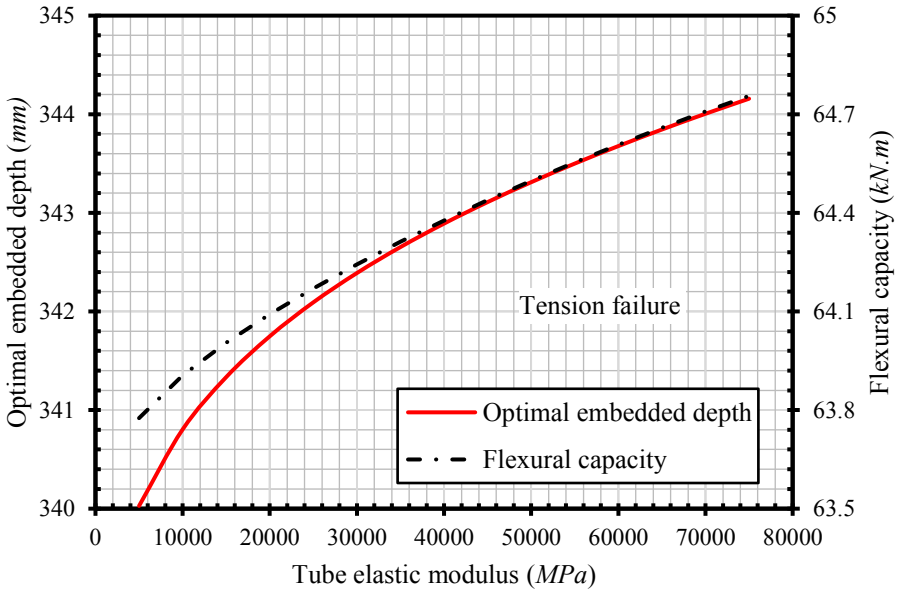

Figure 7.12: Effect of the tube elastic modulus (E_l)

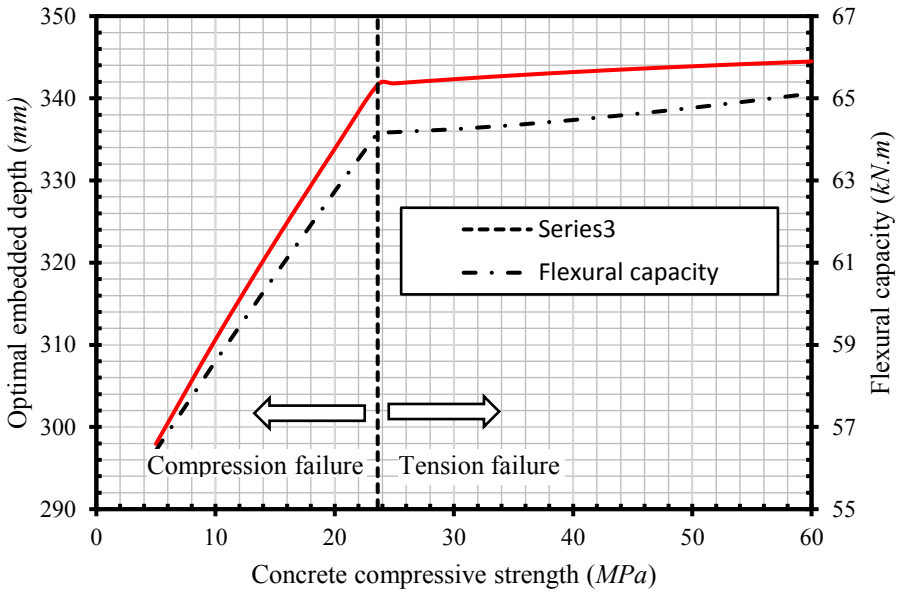

Figure 7.13: Effect of the concrete compressive strength (f_c')

7.4.7. Effect of the bond strength of the surrounding material

Bond strength of the surrounding material (epoxy grout in the tested specimens) is a principle parameter in the determination of the connection flexural strength and its optimal embedded depth. Increasing the bond strength of the surrounding material decreases the required embedded depth to attain the connection flexural strength (optimal embedded depth), as shown in Figure 7.14.

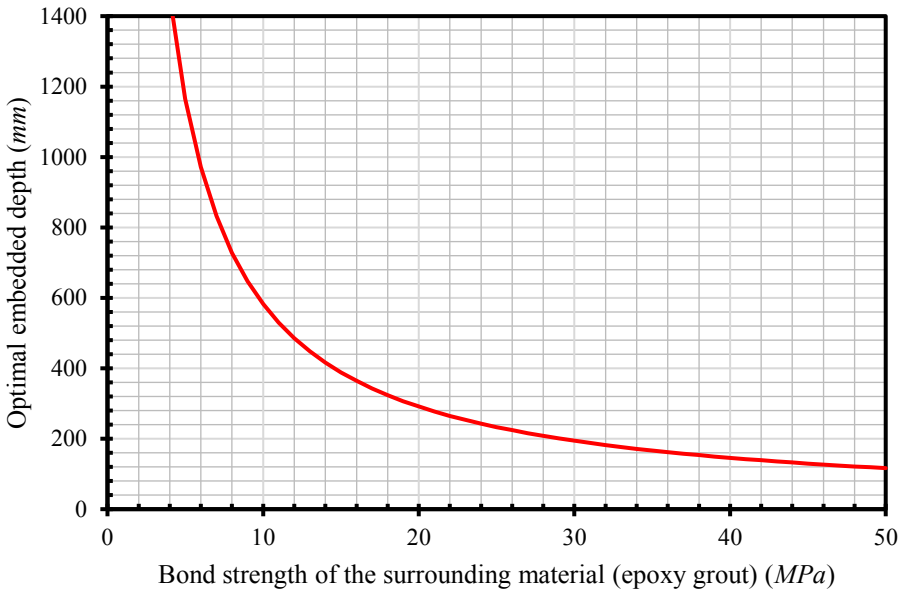

Figure 7.14: Effect of the bond strength of the surrounding material (epoxy grout) (τ_{max})

7.5. Conclusions

This Chapter proposed analytical equations based on the stress block approach which successfully predicted the flexural strength of the CFFT beam, the failure mode, the optimal embedded depth, and the effect of the embedded depth on the flexural capacity of the connection with relatively good accuracy (maximum difference 10.5%).

This chapter also presents an analytical model based on the layer-by-layer approach. Using the layer-by-layer approach to estimate the concrete internal forces provides almost identical results equal to the stress-block results interims of flexural strength of the CFFT beam and the optimal embedded depth.

`

A parametric study; based on the results of the layer-by-layer approach; was conducted to determine the influence of the tube dimensions, mechanical properties of the tube and concrete, and the bond-strength of the surrounding material (the epoxy-grout) on the flexural capacity hence on the optimal embedded depth.

8. GENERAL CONCLUSIONS AND RECOMMENDATIONS

8.1. Summary

This thesis presented two investigations of significant topics related to the CFFT technology. The first topic is the composite action and the interfacial bond between the FRP tube and the concrete core on the flexural behavior of CFFT columns under lateral cyclic. This topic was investigated experimentally and analytically in the first part. While the second part introduced a new beam-column connection for rectangular CFFT members. This beam-column connection was investigated experimentally and analytically.

8.2. Conclusions

8.2.1. First Part: Effect of Bond performance between the FRP tube and the concrete core on the flexural behavior of CFFT under cyclic load

An experimental investigation was incurred to study the effect of the interfacial bond between the FRP tube and the concrete core on the flexural behavior of CFFT columns under lateral cyclic load. The tested columns consisted of two different sizes to examine the column size effect on the tube-concrete interfacial bond performance. The evaluation of the composite action was established based on a novel approach rather than the previous imprecisely approaches, which depended only on the slippage between the concrete core and the FRP tube. This novel approach mainly relies on comparing the strains inside the concrete core with its corresponding strains on the tube skin at the same alignment. Composite action analysis of four full-scale CFFT columns demonstrated the following points:

1. Failure of all columns was detected by FRP tube rupture at the column base on the compression side due to the buckling of the FRP tube-wall. The slippage of the columns out the footings was significantly observed for the specimens with 406 mm diameter.

2. Increasing column size increased the interface gap size. The interface gap generated on the contact between the concrete core and the FRP tube due to the shrinkage of the concrete core and the deficiency in the bond between the FRP tube and its concrete core.

3. Absence of the interfacial bond between the FRP tube and its concrete core increased the interface gap, reduced the flexural strength and stiffness of CFFT columns. In addition, the confinement of the concrete core squandered. The flexural strength of the CFFT column without sand-coating was approximately equal to the flexural capacity of the empty tube.

4. Slippage between the FRP tube and the concrete core at the ends of the CFFT member considers an evidence of the debonding has occurred. On the other hand, no-slippage at the ends of the member cannot be considered as a confirmation for achieving the full composite action in CFFT members.

5. Columns without sand-coating suffered from early debonding before the testing due to the shrinkage of the concrete core that was confirmed by the initial stiffness of the tested columns.

6. The column “C12S” (with 305 mm diameter and sand-coating) achieved the full composite action until the failure, while the column C16S achieved full composite action until 1% drift ration after that the debonding ensued. So that using sand-coating as a bond enhancer improved the flexural strength, stiffness, initial stiffness, and cracking moment of the tested-columns. Sand-coating achieved full composite action in the column with 305 mm diameter, while minimized the adverse effect of the interface gap in the column with 406 mm diameter due to the large size of its concrete core.

7. The results of the analysis were supported by cutting of the FRP tube after the test to examine the interface between the FRP tube and the concrete core. Some parts from the concrete core stuck on the removed part of the tube in the column C12S who

accomplished the full composite action. While the removed parts of the tubes from the other columns were smooth without any stuck concrete.

8. In the column with sand-coating and 406 mm diameter, sand-coating abandoned the FRP tube and stuck on the concrete core.

9. An analytical model was developed to predict the flexural behavior of the fully bonded CFFT members. The analytical results showed a good agreement comparing by the experimental results. This model estimated the failure mode, flexural capacity, compression zone depth, and curvature.

8.2.2. Second Part: Design, Fabrication and Testing of New Beam/Column connection for CFFT rectangular structural members

A new CFFT beam-column connection was investigated experimentally and analytically to cover a research gap related to connecting CFFT beams to columns. The proposed connection successfully transferred the moment from the CFFT beam to the CFFT column. An analytical model was established to estimate the flexural capacity of the CFFT beam. The model also calculated the optimal embedded depth required to accomplish the CFFT beam flexural strength, in addition to considering the effect of the embedded depth on the flexural strength of the CFFT beam-column connection. Conclusions of this investigation are summarized in the following points:

10. The embedded depth had a significant effect on the flexural capacity of the connection. Increasing the embedded depth by 50% (SE-8 to SE-12) increases the flexural capacity by 78%. The flexural capacity was increased by increasing the embedded depth until the embedded depth reached the optimal embedded depth and consequently the full flexural capacity of the CFFT beam is reached.
11. The optimal embedded depth of the tested CFFT beam (the minimum embedded depth required to reap the flexural strength of the CFFT beam) into the epoxy grout was 305 mm, which is practically two times the depth of the CFFT beam (2H). The optimal embedded depth depends on the flexural strength of the CFFT beam and the

`

interfacial bond strength between the CFFT tube and the surrounding material (epoxy grout).

12. Slippage failure between the CFFT beam and the epoxy-grout occurred when the embedded depth was shorter than the optimal embedded depth, which adversely affected the flexural capacity of the connection.
13. Using transverse anchorage bolts to minimize the optimal embedded depth was a good suggestion; it increased the flexural capacity of the connection with small-embedded depth by 35%. On the other hand, the presence of the holes on the GFRP tube wall decreased its flexural strength. Therefore, more investigations are needed to find the effective bolts pattern and sizes, which do not much affect the flexural strength of the CFFT beam.
14. The proposed analytical equations successfully predicted the flexural strength of the CFFT beam, the failure mode, the optimal embedded depth, and the effect of the embedded depth on the flexural capacity of the connection with relatively good accuracy (maximum difference 10.5%).
15. Using the layer-by-layer approach to estimate the concrete internal forces provides almost identical results equal to the stress-block results interims of flexural strength of the CFFT beam and the optimal embedded depth.

8.3. Recommendations for Future Work

This study opened the way to investigate new topics. Based on the findings of the presented study, Additional research and studies are recommended to cover the following point:

8.3.1. First Part

1- Investigation of more sizes and shapes of FRP tube (different tube diameters from 100mm to 1000 mm).
2- Determine the bond strength between the FPR tube and the concrete core (push-through tests).
3- Investigate the bond-effect using the proposed approach for the internally reinforced CFFT members.

4- Develop a unified method to measure the interface gap.
5- Use of high-strength concrete, non-shrinkable concrete, and expansive concrete to fill the FRP tube.
6- Monitor the strains of the concrete core and the FRP tube just after the concrete casting until the end of the test to capture the shrinkage effect.
7- Establish flexural design equations to consider the bond condition and the size effect.
8- Develop a finite element model to implement a parametric study and establish design charts for CFFT members.

8.3.2. Second Part

1- Investigate other types of beam/Colum connections for CFFT: for example, directly connected by hooked steel-rebars with joints-sections bigger than the beam section
2- Investigate the effect of holes in the CFFT column.
3- Investigate the bolt pattern of the bolted connection.
4- Investigate the effect of minimizing the void between the CFFT beam and the steel connection.
5- Investigate the cyclic behavior the proposed connection.

`

8.4. Conclusions (en Français)

Cette thèse a présenté l'étude de deux sujets importants dans le domaine de la technologie des tubes en PRF remplis de béton (TPRFB). Le premier sujet porte sur l'action composite et l'adhérence entre le tube en PRF et le noyau de béton sur le comportement en flexion des colonnes TPRFB sous charge cyclique latéral. Ce sujet a été étudié expérimentalement et théoriquement dans la première partie. Alors que la deuxième partie a porté sur la conception, la fabrication et la mise à l'essai d'une nouvelle connexion poutre-colonne pour les membrures TPRFB de sections rectangulaires. Cette nouvelle connexion poutre-colonne a été étudiée expérimentalement et analytiquement.

8.4.1. Première partie : Évaluation de la performance de l'adhérence entre le tube en PRF and le noyau de béton

Une étude expérimentale a été réalisée pour étudier l'effet de la performance de l'adhérence entre le tube en PRF et le noyau de béton sur le comportement en flexion des colonnes TPRFB sous charge cyclique latérale. Les colonnes testées ont deux tailles différentes pour examiner l'effet de la taille de la colonne sur la performance l'adhérence à l'interface tube en PRF-béton. L'évaluation de l'action composite a été établie sur la base d'une nouvelle approche plutôt que sur les approches antérieures imprécises, qui ne dépendaient que du glissement entre le noyau en béton et le tube en PRF. Cette approche novatrice repose principalement sur la comparaison des déformations à l'intérieur du noyau de béton avec les déformations correspondantes du tube en PRF à la même hauteur. L'analyse de l'action composite de quatre colonnes TPRFB grandeur nature a démontré les points suivants:

1. Le mode de rupture de toutes les colonnes a été détecté par la rupture du tube PRF à la base de la colonne du côté compression en raison du flambage du mur du tube en FRP. Le glissement des colonnes (406 mm de diamètre) sur les semelles était significatif.

2. L'augmentation de la taille des colonnes a augmenté l'effet de retrait du béton et par conséquent, une réduction de la capacité d'adhérence du béton sur la paroi intérieure du tube en PRF.
3. Le vide généré par le retrait du béton a réduit la résistance à la flexion et la rigidité des colonnes TPRFB. De plus, le confinement du noyau de béton par le tube en PRF n'a pas été optimal. La résistance à la flexion de la colonne TPRFB avec un grand écart de retrait était inférieure à la capacité de flexion du tube vide.
4. Le glissement différentiel entre le tube en PRF et le noyau de béton est une preuve pour confirmer le décollement et la perte de l'adhérence.
5. Les colonnes sans enrobage de sable souffraient de décollement avant le début des essais en raison du retrait du noyau de béton.
6. La colonne C12S (avec un diamètre de 305 mm et un revêtement en sable) a atteint l'action composite complète jusqu'à la rupture, tandis que la colonne C16S a obtenu une action composite complète jusqu'à un taux de déplacement latéral de 1%. Ainsi, l'utilisation du revêtement de sable améliore tout d'abord l'adhérence entre le béton et le tube en PRF et par conséquent; il améliore la résistance à la flexion, la rigidité, la rigidité initiale et le moment de fissuration des colonnes testées. Le revêtement en sable n'a pas été aussi optimum pour la colonne C16S. Nous pensons que ceci est dû à la grande taille de la colonne, qui a fait augmenter l'effet du retrait du béton.
7. Les résultats de l'analyse ont été soutenus par la coupe du tube en PRF après l'essai pour examiner l'interface entre le tube de PRF et le noyau de béton. Certaines parties du noyau de béton arraché sont collées sur la face intérieure du tube dans la colonne C12S où l'action composite a été complète. Cependant, les parties enlevées du tube de la colonne C16S étaient lisses sans aucun béton arraché.
8. Dans la colonne C16S avec revêtement de sable (406 mm de diamètre), l'enrobage de sable a décollé du tube en PRF, et s'est collé sur le noyau de béton.
9. Un modèle analytique a été développé pour prédire le comportement en flexion des colonnes TPRFB ayant une adhérence parfaite entre le tube en PRF et le noyau de béton. Les résultats analytiques ont montré un bon accord avec les résultats

`

expérimentaux. Ce modèle permet de prédire le mode de rupture, la capacité de flexion, la profondeur de la zone de compression et la courbure.

8.4.2. Deuxième Partie: Conception, fabrication et la mise à l'essai d'une nouvelle connexion poutre-colonne pour les membrures TPRFB de sections rectangulaires

Une nouvelle connexion poutre-colonne TPRFB a été étudiée expérimentalement et analytiquement pour contribuer à combler partiellement un vide dans la recherche liée aux connexions des poutres aux colonnes TPRFB. La connexion proposée a transféré avec succès le moment de la poutre TPRFB à la colonne TPFRP. Un modèle analytique a été établi pour prédire la capacité en flexion de la poutre TPRFB. Le modèle prédit également la profondeur d'encastrement optimale requise pour atteindre la pleine résistance à la flexion de la poutre TPFRP. Outre ces conclusions générales, les conclusions de cette deuxième partie sont résumées dans les points suivants:

10. La profondeur encastrée a un effet significatif sur la capacité en flexion de la connexion. L'augmentation de la profondeur encastrée de 50% (SE-8 à SE-12) a résulté en une augmentation de la capacité en flexion de 78%. La profondeur optimale dans le coulis de ciment/époxy est de 305 mm, soit pratiquement deux fois la profondeur de la poutre TPFRP (2H). Cette profondeur optimale dépend de la résistance à la flexion de la poutre TPFRP et de la résistance à l'adhérence entre le tube TPFRP et le coulis de ciment/époxy.
11. Une rupture par glissement s'est produite lorsque la profondeur encastrée était plus courte que la profondeur optimale, ce qui a résulté en une réduction de la capacité en flexion de la connexion.
12. L'utilisation de boulons d'ancrage transversaux pour minimiser la profondeur optimale est une suggestion viable. Ce type de connexion (ayant une longueur encastrée réduite) a permis l'augmentation de la capacité en flexion de la connexion de 35%. D'autre part, la présence des trous sur la paroi du tube en FRP a diminué sa résistance à la flexion. Par conséquent, plus d'investigations sont nécessaires pour

trouver la taille et les espacements des boulons optimums, de manière à atténuer la réduction de la résistance à la flexion de la poutre TPFRP.

13. Les équations analytiques proposées ont prédit avec succès la résistance à la flexion de la poutre TPFRP le mode de rupture, la profondeur optimale d'encastrement et l'effet de la profondeur encastrée sur la capacité en flexion de la connexion avec une précision relativement bonne (différence maximale de 10,5%).
14. L'utilisation de l'approche d'analyse couche par couche pour évaluer les forces internes dans le béton fournit des valeurs presqu'identiques aux valeurs de l'approche des blocs de contrainte de la résistance à la flexion de la poutre TPFRP et de la profondeur optimale d'encastrement.

8.5. Recommandations pour des Travaux Futurs

Cette étude a ouvert la voie à l'étude de ces deux nouveaux sujets. Sur la base des résultats de l'étude présentée, des recommandations pour des travaux de recherche futurs concernent les points suivants:

8.5.1. Première Partie:

1- Étudier plus en profondeur l'effet de la taille des tubes en PRF (différents diamètres de tubes de 300 mm à 1000 mm).
2- Étudier en profondeur la résistance à l'adhérence entre le béton et le tube en PRF (essais sur des anneaux de béton avec force sur le noyau de béton).
3- Développer une méthode unifiée pour mesurer l'écart à l'interface.
4- Utilisation d'un béton ayant peu ou pas de retrait ou d'un béton expansif pour remplir le tube en PRF.
5- Développer un modèle d'éléments finis pour mettre en œuvre une étude paramétrique et établir des organigrammes pour les membrures des TPFRP.

`

8.5.2. Deuxième Partie:

1- Étudier d'autres types de connexion comme par exemple : connecter la poutre TPRFB directement à la colonne TPRFB à l'aide d'armature en acier pliées dans le béton.
2- Étudier l'effet de la taille des boulons et leurs distributions dans la connexion poutre/colonne.
3- Étudier l'effet de la réduction du vide entre la poutre TPFRP et la connexion en acier.
4- Étudier le comportement cyclique de la connexion proposée.
5- Développer un modèle numérique par éléments finis où plusieurs paramètres seront simulés.

9. REFERENCES

AASHTO. (2012). *Aashto Lrfd Guide Specifications for Design of Concrete-Filled Frp Tubes for Flexural and Axial Members*.

Abouzied, A. (2016). "Flexural behaviour of rectangular FRP tubes fully or partially filled." Sherbrooke University.

Abouzied, A., and Masmoudi, R. (2014). "Flexural Behavior of New Partially Concrete-Filled Filament-Wound Rectangular Frp Tube Beams." *4th International Structural Specialty Conference, Canadian Society of Civil Engineering*.

Abouzied, A., and Masmoudi, R. (2015). "Structural performance of new fully and partially concrete-filled rectangular FRP-tube beams." *Construction and Building Materials*.

Abouzied, A., and Masmoudi, R. (2017). "Flexural behavior of rectangular FRP-tubes filled with reinforced concrete: Experimental and theoretical studies." *Engineering Structures*.

ACI Committee 318. (2014). *Building Code Requirements for Structural Concrete (ACI 318-14) and Commentary (ACI 318R-14). Aci 318-14*.

Ahmad, I. (2004). "Shear Response and Bending Fatigue Behavior of Concrete-Filled Fiber Reinforced Polymer Tubes." North Carolina State University, USA.

Ali, A. M., and Masmoudi, R. (2017). "Flexural strength and behavior of circular sand-coated concrete-filled FRP tubes under cyclic load." *ACI Special Publication*, SP-79, Under Press.

Ali, A. M., Masmoudi, R., and Khan, M. I. (2017a). "EFFECT OF SAND-COATING BOND PERFORMANCE ON THE FLEXURAL CAPACITY OF CIRCULAR

CONCRETE-FILLED FRP TUBES." *6th International Conference on Engineering Mechanics and Materials*, EMM608–(1–10).

Ali, A. M., Robillard, D., Masmoudi, R., and Khan, I. M. (2017b). "Experimental investigation of bond and tube thickness effect on the flexural behavior of concrete-filled FRP tube under lateral cyclic loading." *Journal of King Saud University - Engineering Sciences*.

American Concrete Institute. (2014). "Building code requirements for structural concrete and commentary." *Aci 318-14*.

ASTM. (2013). "ASTM D6109. Standard Test Methods for Flexural Properties of Unreinforced and Reinforced Plastic Lumber and Related Products." 1–7.

ASTM C39. (2016). "Standard Test Method for Compressive Strength of Cylindrical Concrete Specimens." *American Society for Testing and Materials*.

ASTM C78M-16, Test, C. C., Drilled, T., Concrete, C., ASTM C78M-16, ASTMC78/C78M, and ASTM C78M-16. (2016). "Standard Test Method for Flexural Strength of Concrete (Using Simple Beam with Third-Point Loading) 1." *ASTM C78M-16*.

ASTM D3039. (2014). "Standard Test Method for Tensile Properties of Polymer Matrix Composite Materials1." *Annual Book of ASTM Standards*.

ASTM D695. (2010). "Standard test method for compressive properties of rigid plastics." *ASTM International. Designation: D*.

Bažant, Z. P., and Sandeep, B. (1995). "Creep and shrinkage prediction model for analysis and design of concrete structures-model B3." *Materials and Structures*.

Belzer, B. E., Robinson, M. J., and Fick, D. R. (2013). "Composite Action of Concrete-Filled Rectangular GFRP Tubes." *American Society of Civil Engineers*.

Benmokrane, B., Chaallal, O., and Masmoudi, R. (1996). "Flexural response of concrete beams reinforced with FRP reinforcing bars." *ACI Structural Journal*.

Boumarafi, A., Abouzied, A., and Masmoudi, R. (2015). "Harsh environments effects on the axial behaviour of circular concrete-filled fibre reinforced-polymer (FRP) tubes." *Composites Part B: Engineering*, 83, 81–87.

Burgueno, R., Davol, A., and Seible, F. (1998). "The carbon shell system for modular bridge components." *Second International Conference on Composites in Infrastructure*, Tucson, Arizona, 341–354.

Chopra, A. K. (2007). "Dynamics of structures : theory and applications to earthquake engineering." *Pearson Education*.

Clough, R. W., and Penzien, J. (2013). *Dynamics of Structures*. *Dynamics of Structures*.

Cole, B., and Fam, A. (2006). "Flexural load testing of concrete-filled FRP tubes with longitudinal steel and FRP rebar." *Journal of Composites for Construction*.

Collins, M. P., and Mitchell, D. (1997). *Prestressed concrete structures / Michael P. Collins, Denis Mitchell*. Response Publications, Toronto, Ontario.

Creative Pultrusions, I. (2016). *Data sheet of Fiberglass Reinforced Polymer (FRP) Powertrusion Cross Arm*.

Creative Pultrusions Inc. (2015). *PRODUCT BROCHURE SUPERPILE^{TM} FIBERGLASS REINFORCED POLYMER (FRP) PIPE PILES*. Alum Bank, PA.

ElGawady, M. A., and Dawood, H. M. (2012). "Analysis of segmental piers consisted of concrete filled FRP tubes." *Engineering Structures*.

Fam, A., Flisak, B., and Rizkalla, S. (2001). "FRP tubes filled with concrete and subjected to axial loads, bending and combined loads." *International Conference on FRP Composites in Civil Engineering (CICE2001)*.

`

Fam, A., Qie, F. S., and Rizkalla, S. (2004). "Concrete-filled steel tubes subjected to axial compression and lateral cyclic loads." *Journal of Structural Engineering*.

Fam, A., and Rizkalla, S. (2003). "Large scale testing and analysis of hybrid concrete/composite tubes for circular beam-column applications." *Construction and Building Materials*, 17(6–7), 389–403.

Fam, A. Z., and Rizkalla, S. H. (2001). "Behavior of axially loaded concrete-filled circular fiber-reinforced polymer tubes." *ACI Structural Journal*.

Fam, A. Z., and Rizkalla, S. H. (2002). "Flexural Behavior of Concrete-Filled Fiber-Reinforced Polymer Circular Tubes." *Journal of Composites for Construction*.

Fam, A. Z., Schnerch, D., and Rizkalla, S. H. (2005). "Rectangular Filament-Wound Glass Fiber Reinforced Polymer Tubes Filled with Concrete under Flexural and Axial Loading: Experimental Investigation." *Journal of Composites for Construction*.

Hadi, M. N. S., Khan, Q. S., and Sheikh, M. N. (2016). "Axial and flexural behavior of unreinforced and FRP bar reinforced circular concrete filled FRP tube columns." *Construction and Building Materials*, 122, 43–53.

Helmi, K., Fam, A., and Mufti, A. (2005). "Field installation, splicing, and flexural testing of hybrid FRP/concrete piles." *ACI Special Publication*, Vol. SP-23, 1103–1120.

Honickman, H., and Fam, A. (2009). "Investigating a Structural Form System for Concrete Girders Using Commercially Available GFRP Sheet-Pile Sections." *Journal of Composites for Construction*.

Idris, Y., and Ozbakkaloglu, T. (2013). "Seismic Behavior of High-Strength Concrete-Filled FRP Tube Columns." *Journal of Composites for Construction*, 17(6), 04013013.

Ji, G., Ouyang, Z., and Li, G. (2009). "Experimental investigation into the interfacial shear

strength of AGS-FRP tube confined concrete pile." *Engineering Structures*.

Lai, Y. C. (2010). "MOMENT CONNECTIONS OF CONCRETE-FILLED FIBRE REINFORCED POLYMER TUBES TO REINFORCED CONCRETE FOOTINGS." Queen‟s University Kingston, Ontario, Canada.

Mirmiran, A., Samaan, M., Cabrera, S., and Shahawy, M. (1998a). "Design, manufacture and testing of a new hybrid column." *Construction and Building Materials*.

Mirmiran, A., Shahawy, M., El Khoury, C., and Naguib, W. (2000). "Large beam-column tests on concrete-filled composite tubes." *ACI Structural Journal*.

Mirmiran, A., Shahawy, M., Samaan, M., Echary, H. El, Mastrapa, J. C., Pico, O., and Shahawy. (1998b). "Effect of column parameters on FRP-confined concrete." *Journal of Composites for construction*.

Mohamed, H. M., and Masmoudi, R. (2010a). "Axial Load Capacity of Concrete-Filled FRP Tube Columns: Experimental versus Theoretical Predictions." *Journal of Composites for Construction*.

Mohamed, H. M., and Masmoudi, R. (2010b). "Flexural strength and behavior of steel and FRP-reinforced concrete-filled FRP tube beams." *Engineering Structures*.

Mohamed, H. M., and Masmoudi, R. (2010c). "Flexural strength and behavior of steel and FRP-reinforced concrete-filled FRP tube beams." *Engineering Structures*, 32(11), 3789–3800.

Mohamed, H. M., and Masmoudi, R. (2010d). "Axial Load Capacity of Concrete-Filled FRP Tube Columns: Experimental versus Theoretical Predictions." *Journal of Composites for Construction*, 14(2), 231–243.

Mohamed, H. M., and Masmoudi, R. (2011). "Deflection Prediction of Steel and FRP-Reinforced Concrete-Filled FRP Tube Beams." *Journal of Composites for*

`

Construction, 15(3), 462–472.

Mohamed, H. M., and Masmoudi, R. (2012). "Effect of test parameters on flexural strength of circular fiber-reinforced polymer-confined concrete beams." *Journal of Reinforced Plastics and Composites*.

Mohamed, H., and Masmoudi, R. (2008). "Compressive behavior of reinforced concrete-filled FRP tubes." *American Concrete Institute, ACI Special Publication*.

Nelson, M., Lai, Y. C., and Fam, A. (2008a). "Moment Connection of Concrete-Filled Fiber Reinforced Polymer Tubes by Direct Embedment into Footings." *Advances in Structural Engineering*, 11(5), 537–547.

Nelson, M., Lai, Y. C., and Fam, A. (2008b). "Moment Connection of Concrete Filled Fiber Reinforced Polymer Tubes by Direct Embedment into Footings." *Advances in Structural Engineering*, 11(5), 537–547.

Ozbakkaloglu, T. (2005). "Seismic performance of high-strength concrete columns in FRP stay-in-place formwork." Tucson, AZ : Department of Civil Engineering and Engineering Mechanics, University of Arizona, [1998], Ottawa, ON, CANADA.

Ozbakkaloglu, T. (2013). "Compressive behavior of concrete-filled FRP tube columns: Assessment of critical column parameters." *Engineering Structures*, 51, 188–199.

Ozbakkaloglu, T., and Idris, Y. (2014). "Seismic Behavior of FRP-High-Strength Concrete–Steel Double-Skin Tubular Columns." *Journal of Structural Engineering*, 140(6), 04014019.

Ozbakkaloglu, T., and Saatcioglu, M. (2004). "Seismic performance of high-strength concrete columns cast in stay-in-place FRP formwork." *13 th World Conference on Earthquake Engineering*.

Ozbakkaloglu, T., and Saatcioglu, M. (2006). "Seismic Behavior of High-Strength

Concrete Columns Confined by Fiber-Reinforced Polymer Tubes." *Journal of Composites for Construction*.

Priestley, M., Calvi, G. M., and Kowalsky, M. J. (2007). "Displacement-based seismic design of structures." *Building*.

Priestley, M. J. N., Seible, F., and Calvi, G. M. (1996). *Seismic-Design-and-Retrofit-of-Bridges.pdf*. A Wiley interscience publication.

Roeder, C. W., Cameron, B., and Brown, C. B. (1999). "Composite Action in Concrete Filled Tubes." *Journal of Structural Engineering*.

Sadeghian, P., and Fam, A. Z. (2010). "Bond-Slip Analytical Formulation toward Optimal Embedment of Concrete-Filled Circular FRP Tubes into Concrete Footings." *Journal of Engineering Mechanics*.

Sadeghian, P., and Fam, A. Z. (2011). "Closed-Form Model and Parametric Study on Connection of Concrete-Filled FRP Tubes to Concrete Footings by Direct Embedment." *Journal of Engineering Mechanics*.

Sadeghian, P., Lai, Y. C., and Fam, A. (2011). "Testing and Modeling of a New Moment Connection of Concrete-Filled FRP Tubes to Footings under Monotonic and Cyclic Loadings." *Journal of Composites for Construction*.

Samaan, M. S. (1997). "An Analytical and Experimental Investigation of Concrete-Filled-Fiber Reinforced Plastics (FRP) Tubes." University of Central Florida.

Shao, Y., and Amir Mirmiran. (2005). "Experimental Investigation of Cyclic Behavior of Concrete-Filled Fiber Reinforced Polymer Tubes." *Journal of Composites for Construction*.

Wang, W., Sheikh, M. N., Hadi, M. N. S., Gao, D., and Chen, G. (2017). "Behaviour of concrete-encased concrete-filled FRP tube (CCFT) columns under axial

`

compression.” *Engineering Structures*, 147.

Youm, K. S., Cho, J. young, Lee, Y. H., and Kim, J. J. (2013). “Seismic performance of modular columns made of concrete filled FRP tubes.” *Engineering Structures*.

Youssef, J., and Hadi, M. N. S. (2017). “Axial load-bending moment diagrams of GFRP reinforced columns and GFRP encased square columns.” *Construction and Building Materials*.

Zakaib, S., and Fam, A. (2012). “Flexural Performance and Moment Connection of Concrete-Filled GFRP Tube–Encased Steel I-Sections.” *Journal of Composites for Construction*.

Zhu, Z. (2004). “Joint construction and seismic performance of concrete-filled fiber reinforced polymer tubes.” North Carolina State University.

Zhu, Z., Ahmad, I., and Mirmiran, A. (2006a). “Seismic Performance of Concrete-Filled FRP Tube Columns for Bridge Substructure.” *Journal of Bridge Engineering*.

Zhu, Z., Ahmad, I., and Mirmiran, A. (2006b). “Splicing of precast concrete-filled FRP tubes.” *Journal of Composites for Construction*.

Zhu, Z., Mirmiran, A., and Shahawy, M. (2004). “Stay-in-Place Fiber Reinforced Polymer Forms for Precast Modular Bridge Pier System.” *Journal of Composites for Construction*.